

The Pennsylvania State University

The Graduate School

ADDITIVE MANUFACTURING OF FUNCTIONALLY GRADED MATERIALS BETWEEN  
FERRITIC AND AUSTENITIC ALLOYS

A Dissertation in

Materials Science and Engineering

by

James S. Zuback

© 2019 James S. Zuback

Submitted in Partial Fulfillment

of the Requirements

for the Degree of

Doctor of Philosophy

December 2019

The dissertation of James S. Zuback was reviewed and approved\* by the following:

Tarasankar DebRoy  
Professor of Materials Science and Engineering  
Dissertation Advisor  
Chair of Committee

Todd A. Palmer  
Professor of Engineering Science and Mechanics

Allison M. Beese  
Assistant Professor of Materials Science and Engineering

Reginald F. Hamilton  
Associate Professor of Engineering Science and Mechanics

John C. Mauro  
Professor of Materials Science and Engineering  
Chair of Intercollege Graduate Degree Program

\*Signatures are on file in the Graduate School

## ABSTRACT

Ferritic steels and austenitic alloys are used extensively as structural materials in power generation facilities such as fossil-fired and nuclear power plants. Currently, these alloys are joined using common fusion welding processes. However, dissimilar metal welds between ferritic and austenitic alloys are susceptible to premature failure due to a variety of simultaneously operating metallurgical issues, including carbon migration, localized creep strain, and coefficient of thermal expansion mismatch. Although improvements have been made to alloy selection and weld design over the past few decades, the root causes that ultimately lead to failure persist. As many of the power plants responsible for the worldwide production of electricity have exceeded or are nearing their designed lifetimes, an engineering solution that directly addresses the underlying metallurgical challenges is of great interest.

Dissimilar metal welds between ferritic and austenitic alloys are an attractive application for the design of a functionally graded material system capable of preventing premature failure. Functionally graded materials represent a class of advanced materials designed to achieve a function by locally controlling density, composition, or microstructure to engineer site-specific properties. Problems arising from abrupt changes in chemical composition, microstructure, and properties in dissimilar welds can be overcome by implementing a functionally graded material that gradually transitions from a ferritic steel to an austenitic alloy. Additive manufacturing is well-suited for the design and fabrication of spatially dependent material combinations to achieve specific functions by grading chemical composition in a layer by layer manner.

Carbon migration in dissimilar metal welds between ferritic and austenitic materials has been identified as a major cause for poor creep performance and premature failures in nuclear applications. Steep composition gradients and abrupt microstructural changes result in a large thermodynamic driving force that facilitates carbon diffusion away from the ferritic material, leading to negative impacts on creep strength. An appropriately graded transition joint effectively reduces the driving force for carbon diffusion by lowering the carbon chemical potential gradient. Theoretical calculations show that negligible amounts of carbon diffusion occur under typical service conditions in a functionally graded material between 2.25Cr-1Mo steel and Alloy 800H compared to its dissimilar weld counterpart. The functionally graded material fabricated using

laser-based directed energy deposition was then experimentally tested for its effectiveness in reducing carbon diffusion and was shown to significantly outperform the dissimilar weld.

Microstructural characterization indicated that a full composition gradient from 2.25Cr-1Mo steel and Alloy 800H may not be necessary, and a shorter transition joint will suffice. When the microstructure becomes fully austenitic, there is little change in microhardness and further compositional grading provides no benefits in reducing carbon diffusion. Additionally, a soft zone formed at the beginning of the functionally graded material near the ferritic steel, leading to an abrupt change in properties. If this region is excluded from the functionally graded material, however, the designed function of the transition joint for reducing carbon diffusion is negatively impacted. This finding indicates that tradeoffs between the function and unexpected microstructure exist during the design and fabrication of functionally graded materials.

Lack of fusion defects, which are detrimental to properties and performance, formed in specific regions of the functionally graded material. The formation of defects was traced to changes in molten pool geometry due to variations in chemical composition. The presence of minor alloying elements changes the activity of surface-active elements, namely oxygen, in discrete regions throughout the functionally graded material. The thermodynamic activities of surface-active elements significantly impact the magnitude and direction of liquid metal flow during processing due to surface tension driven effects. The simulated molten pool geometries were found to be deep and narrow for compositions close to the ferritic steel and become shallower and wider as composition is graded towards the austenitic alloy. To avoid lack of fusion defects, process parameters such as laser power or hatch spacing may need to be adjusted in-situ to account for the variations in molten pool geometry.

Changes in chemical composition during compositional grading can lead to the formation of unexpected secondary phases that can significantly alter mechanical properties and sometimes lead to build failures. The precipitate morphology in additively manufactured nickel base superalloys with slight changes in chemical composition was investigated with the goal of establishing connections between chemical composition and precipitate type. Although the as-deposited alloys exhibited similar precipitate distributions, the differences in precipitate type and morphology were striking. Variations in minor alloying elements were found to be an important driver for secondary phase formation in both the as-deposited and hot isostatic pressed conditions.

## TABLE OF CONTENTS

LIST OF FIGURES .....	ix
LIST OF TABLES .....	xviii
ACKNOWLEDGEMENTS .....	xix
Chapter 1 INTRODUCTION.....	1
1.1 Structural material challenges in power generation facilities .....	1
1.2 Opportunities for advanced manufacturing of multifunctional materials .....	4
1.3 Research Objectives .....	6
1.4 Thesis Structure.....	7
1.5 References .....	8
Chapter 2 LITERATURE REVIEW.....	10
2.1 Metallurgical challenges in ferritic to austenitic dissimilar welds .....	10
2.1.1 Carbon migration .....	10
2.1.2 Microstructure and property evolution .....	16
2.1.2.1 As-welded condition .....	16
2.1.2.2 After heat treatment and aging.....	20
2.1.3 Summary.....	26
2.2 Background of functionally graded materials and additive manufacturing .....	27
2.2.1 Overview of functionally graded materials .....	27
2.2.2 Types of additive manufacturing processes.....	29
2.2.3 Functionally graded materials in additive manufacturing .....	31
2.2.3.1 Single material functionally graded materials .....	32
2.2.3.2 Multi-material functionally graded materials .....	34
2.3 Factors affecting properties of additively manufactured materials .....	36

2.3.1 Influence of process variables .....	37
2.3.1.1 Energy input.....	37
2.3.1.2 Cooling rates .....	41
2.3.2 Effects of microstructure .....	46
2.3.2.1 Iron based alloys .....	49
2.3.2.2 Aluminum alloys.....	52
2.3.2.3 Nickel alloys .....	55
2.3.2.4 Titanium alloys .....	60
2.3.2.5 Grain size .....	62
2.3.2.6 Dislocations in AM materials .....	67
2.3.3 Compositional variables .....	70
2.3.3.1 Iron alloys .....	70
2.3.3.2 Aluminum alloys.....	72
2.3.3.3 Nickel alloys .....	74
2.3.3.4 Comparison with other processes .....	76
2.3.4 Summary.....	80
2.4 References .....	81
<b>Chapter 3 USING FUNCTIONALLY GRADED MATERIALS TO LIMIT CARBON DIFFUSION BETWEEN FERRITIC AND AUSTENITIC ALLOYS.....</b>	<b>99</b>
3.1 The problem of carbon diffusion in dissimilar welds .....	99
3.2 Thermodynamic and kinetic modeling of carbon diffusion .....	101
3.2.1 Model background and calculation setup .....	101
3.2.2 Influence of chemical composition on thermodynamic driving force.....	104
3.2.3 Predicting carbon diffusion during service.....	104
3.2.4 Testing model with literature data .....	105

3.3 Experimental methods and materials .....	107
3.3.1 Powder feedstock and compositional grading .....	107
3.3.2 Specimen fabrication and preparation .....	109
3.3.3 Chemical composition profile measurements.....	109
3.4 Testing the effectiveness of FGM .....	110
3.4.1 Calibrating carbon measurements .....	110
3.4.2 Initial chemical concentration profiles .....	112
3.4.3 Selecting an effective heat treatment.....	115
3.4.4 Carbon concentration profiles after heat treatment .....	116
3.5 Minimizing the driving force for carbon diffusion .....	118
3.6 Summary and conclusions.....	124
3.7 References .....	126
Chapter 4 MICROSTRUCTURAL EVOLUTION IN A FUNCTIONALLY GRADED 2.25CR-1MO STEEL AND ALLOY 800H SYSTEM .....	128
4.1 Chapter overview .....	128
4.2 Experimental methods and theoretical calculations .....	129
4.2.1 Sample fabrication and preparation.....	129
4.2.2 Characterization techniques.....	129
4.2.3 Predictions of microstructure and phase transformations.....	130
4.3 As-deposited microstructure in FGM.....	132
4.4 Phase transformations in single alloy samples .....	142
4.5 Revisiting the carbon diffusion problem.....	148
4.6 Summary and conclusions.....	155
4.7 Reference.....	156
Chapter 5 DEFECT FORMATION DURING THE FABRICATION OF FUNCTIONALLY GRADED ALLOYS .....	157

5.1 Introduction .....	157
5.2 Theoretical modeling and experimental procedures .....	159
5.2.1 Surface tension calculations .....	159
5.2.2 Thermodynamic calculations.....	161
5.2.3 Heat transfer and fluid flow model.....	162
5.2.4 Specimen fabrication and characterization.....	165
5.3 Lack of fusion defects in functionally graded material.....	167
5.4 Characterization of single bead deposits .....	169
5.5 Effect of chemical composition on surface tension .....	173
5.6 Simulated bead shape in single pass deposits .....	176
5.7 Summary and conclusions.....	183
5.8 Reference.....	184
<b>Chapter 6 THE IMPACT OF COMPOSITION ON PRECIPITATE FORMATION IN AN ADDITIVELY MANUFACTURED NICKEL BASE SUPERALLOY .....</b>	<b>186</b>
6.1 Introduction .....	186
6.2 Materials and methods .....	188
6.3 Solidification structure and segregation behavior.....	190
6.4 Precipitate characterization in as-deposited condition .....	193
6.5 Predicting precipitate morphology from chemical composition .....	197
6.6 Effects of HIP on precipitate morphology .....	200
6.7 Summary and conclusions.....	206
6.8 References .....	207
<b>Chapter 7 CONCLUDING REMARKS .....</b>	<b>210</b>

## LIST OF FIGURES

Figure 1.1. A comparison of the worldwide electricity production by various sources in 1973 and 2016, with most electricity now being produced using coal, natural gas, and nuclear sources. Reproduced from [1].....	1
Figure 1.2. An example of the structural materials used in the primary and secondary circuits of a pressurized water reactor in a nuclear power plant [2]. Reprinted with permission from Elsevier. ....	2
Figure 1.3. Failures in ferritic/austenitic dissimilar welds often begin with crack formation, such as that seen in (a) a failed thermowell between Grade 91 steel and SS316 [8]. In laboratory creep experiments, microscopic cracks repeatedly form near the weld interface in the ferritic steel for a variety of alloy combinations, including (b) 2.25Cr-1Mo ferritic steel and Alloy 800 [9] (Reprinted with permission from Springer Nature) and (c) P92 ferritic steel and nickel superalloy Inconel 740H [10] (Reprinted with permission from Elsevier).....	3
Figure 1.4. Abrupt changes of both (a) chemical composition and (b) microhardness across the fusion line of a dissimilar weld between 2.25Cr-1Mo steel and Alloy 800 using Inconel 182 filler metal [15] introduce many metallurgical issues that lead to premature failure. Reprinted with permission from Springer Nature.....	5
Figure 2.1. The carbon concentration profile across a weld of two steels, one containing 3.80 wt% Si and the other with 0.05 wt% Si, after a 10 day heat treatment at 1050°C [7].....	11
Figure 2.2. Although the carbon concentration is roughly uniform across dissimilar welds between ferritic and austenitic alloys (a), the abrupt changes in chemical composition lead to a large thermodynamic driving force for carbon diffusion (b). ....	13
Figure 2.3. The measured carbon concentration profile across a dissimilar weld between 2.25Cr-1Mo steel and Inconel filler metal that was taken out of service. The operating temperature range for this weld was approximately 540-565°C. Data from figure acquired from [12]. ....	14
Figure 2.4. A comparison of the carbon concentration profiles in laboratory experiments across a dissimilar metal weld between a 5Cr-0.5Mo ferritic steel and a 21Cr-12Ni austenitic alloy (a) in the as-welded condition and (b) after heat treatment at 500°C for 1000 h [13]. Reprinted with permission from Springer Nature.....	15
Figure 2.5. Microstructures in a dissimilar weld between 18MND5 ferritic steel and SS309L (a) in the as welded condition and (b) after post weld heat treatment at 610°C for 8 h showing the formation of carbon depleted and enriched zones [14]. Reprinted with permission from Springer Nature.....	16
Figure 2.6. A schematic diagram of the different regions of a heat affected zone in a P91 steel with the accompanying approximated phase diagram [20]. ....	17
Figure 2.7. The as-welded microstructure of a 2.25Cr-1Mo steel/OE-S3 NiMo-1 filler weld showing (a) the macroscopic view of the FZ, HAZ, and BM, (b) the interface between the FZ and CGHAZ, (c) the FGHAZ, (d) the ICHAZ, and (e) the unaffected BM [25]. Reprinted with permission from Elsevier. ....	18

Figure 2.8. A series of hardness indentations across the fusion line of a dissimilar weld between 2.25Cr-1Mo steel and SS309L, where the Vickers hardness values are shown by their respective indents [30].	19
Figure 2.9. Variations in calculated martensite start temperature using measured chemical composition as a function of distance across a weld interface between a ferritic steel and (a) SS309L and (b) Inconel® 625 [30].	20
Figure 2.10. Hardness indentations across the fusion line of a dissimilar weld between 2.25Cr-1Mo steel and SS309L after post weld heat treatment at 720°C for 10 h, where the Vickers hardness values are shown by their respective indents [30].	21
Figure 2.11. Hardness measurements across a dissimilar clad between A508 low alloy ferritic steel and a SS309L after post weld heat treatment at 607°C [15]. Reprinted with permission from Springer Nature.	22
Figure 2.12. The evolution of as-welded microhardness in a dissimilar weld between 5Cr-0.5Mo ferritic steel and 21Cr-12Ni austenitic alloy after aging at 500°C [13]. Reprinted with permission from Springer Nature.	23
Figure 2.13. A comparison of creep testing results on 2.25Cr-1Mo steel (Base), a 2.25Cr-1Mo steel/2.25Cr-1Mo steel weld (Similar weld), and a 2.25Cr-1Mo steel/Alloy 800 weld (Dissimilar weld). Reproduced from [39] with permission from Elsevier.	24
Figure 2.14. The distribution of strain across a dissimilar weld between 2.25Cr-1Mo steel and Alloy 800H using IN82 filler metal at different times during creep testing [39]. Reprinted with permission from Springer Nature.	25
Figure 2.15. The localized creep strain measured by digital image correlation in a dissimilar weld between 2.25Cr-1Mo steel and Alloy 800H aged at 600°C for 4000 h during an accelerated creep test at 625°C and 50 MPa [45]. Reprinted with permission from Elsevier.	26
Figure 2.16. Functionally graded materials can have (a) a stepwise or (b) smooth variations in properties as a function of location. The changes in properties in can result from variations in (c) composition, (d) grain orientation, (e) secondary phase fraction, (f) grain size, (g) fiber length and orientation, or (h) particle density [51]. Reprinted with permission from Elsevier.	28
Figure 2.17. The variation in hardness of a carburized duplex stainless steel due to a gradient in carbon concentration, where high hardness corresponds to high carbon concentration [53].	29
Figure 2.18. Schematic illustration of the different types of AM processes used for fabricating metallic components, including (a) DED-L, (b) DED-EB, (c) DED-GMA [59], and (d) PBF-L [60].	30
Figure 2.19. Prosthetic hip implants made of titanium fabricated by DED-L with designed variations in porosity [82].	32
Figure 2.20. A gradient in grain structure and orientation was fabricated by Popovich et al. [87] by changing the laser power in selected regions of an Inconel® 718 part fabricated by PBF-L as shown by the electron backscatter diffraction image.	34

Figure 2.21. Schematic description of a DED-L processes used for the fabrication of a compositionally graded alloy where powders of Alloy A and B are blown into a melt pool at different feed rates along the build height [104]. Reprinted with permission from Elsevier. ....	35
Figure 2.22. The composition and hardness variations as a function of distance from the baseplate in FGMs fabricated by DED-L for (a) SS304L to Inconel® 625 [79] and (b) Ti-6Al-4V to Invar [90]. Reprinted with permission from Elsevier. ....	36
Figure 2.23. Hardness measurements for austenitic stainless steels deposited by AM as a function of linear heat input [108-116]. ....	38
Figure 2.24. Vickers hardness as a function of linear heat input for titanium alloys where solid black dots correspond to Ti-6Al-4V and open points are marked otherwise [68, 117-127]. ....	39
Figure 2.25. The relationship between computed cooling rates and a dimensionless heat input parameter for the DED-L of (a) SS316L validated from experimental data [132] and (b) common AM alloys under typical process conditions [131]. ....	41
Figure 2.26. Hardness data as a function of reported cooling rates for (a) steels [133-138], (b) aluminum alloys [139-143] and (c) nickel alloys [144-148] in which no post-processing heat treatment was used. ....	42
Figure 2.27. Hardness data for Jominy end quench experiments for (a) various steels with similar carbon concentrations and (b) 8600 series steels (0.55Ni, 0.50Cr, 0.20Mo) with varying carbon concentrations [149]. ....	43
Figure 2.28. Computed thermal histories at the mid-length and mid-heights of selected layers during a single pass, nine layer simulation of DED-L of SS316 [150]. ....	44
Figure 2.29. Hardness variations as a function of location within a DED-L single pass, multilayer build of IN718 [154] showing (a) a longitudinal cross section (X-Z plane), (b) a transverse cross section (Y-Z plane), and (c) a horizontal cross section (X-Y plane) where X is the travel direction, Y is the track width direction, and Z is the build direction. ....	46
Figure 2.30. Columnar dendritic microstructure of SS316L deposited by DED-L [116]. ....	50
Figure 2.31. Vickers microhardness as a function of secondary arms spacing for stainless steels fabricated by AM from [108, 116, 132, 199, 200]. Error bars represent the standard deviation in measurements. ....	51
Figure 2.32. As-deposited microstructure of AlSi10Mg alloy fabricated by selective laser melting showing a fine cellular/dendritic structure with small amounts of eutectic [204]. ....	53
Figure 2.33. Microstructure of laser deposited Al 4047 showing dendritic and equiaxed structures at different locations within the same layer [205]. ....	54
Figure 2.34. Vickers microhardness as a function of secondary arms spacing for aluminum alloys fabricated by AM from [165, 205, 210, 211] and selected data for directional solidification of Al-3Si from Kaya et al. [206]. Error bars represent the standard deviation in measurements. ....	55

Figure 2.35. Vickers microhardness as a function of secondary arms spacing for nickel alloys fabricated by AM from [200, 214-218]. Error bars represent the standard deviation in measurements.....	56
Figure 2.36. The precipitation and growth of $\delta$ phase at various times in PBF-L IN625 subjected to a standard stress relief heat treatment at 870°C [219]. .....	57
Figure 2.37. Box and whisker plot showing the variation in Vickers hardness of IN718 parts fabricated by DED-L [181, 221-224], PBF-L [129, 225-231], and PBF-EB [232, 233] AM and subjected to various post process heat treatments.....	58
Figure 2.38. Measured Vickers hardness during PBF-EB of IN718 subjected to different cooling cycles and in-situ heat treatment [234]. .....	59
Figure 2.39. A portion of the Ti-Al-V phase diagram [236] for a constant aluminum concentration of 6 wt%.....	60
Figure 2.40. Representative micrographs of Ti-6Al-4V fabricated by (a) DED and (b) PBF after stress relieving [153]. Components fabricated by DED typically display coarse lamellar $\alpha$ -laths with small amounts of $\beta$ while PBF components have much finer acicular martensite ( $\alpha'$ ). .....	61
Figure 2.41. Vickers microhardness as a function of alpha lath width for Ti-6Al-4V fabricated by AM from [117, 215, 238-243]. Error bars, where available, represent the standard deviation in measurements.....	62
Figure 2.42. Comparison between the correlation developed by Keist and Palmer [153] and independent experimental data [117-121, 247-249] for yield strength and hardness measurements spanning multiple AM processes. ....	64
Figure 2.43. A collection of independent experimental data showing a comparison between measured yield strength and Vickers hardness for SS316L fabricated by AM [109, 111, 112, 251, 252]. .....	65
Figure 2.44. The relationship between cooling rate, average grain diameter, and Vickers hardness for the AM of SS316L [151, 251]. The cooling rate on the horizontal axis is plotted with a logarithmic scale and black arrows indicate the y-axis for each data set. ....	66
Figure 2.45. An analysis of anisotropic behavior [60] through a comparison between the transverse and longitudinal tensile strengths in additively manufactured (a) stainless steels [108, 109, 111, 253, 254] (b) aluminum alloy AlSi10Mg [168, 169, 255-259] (c) Ti-6Al-4V [62, 69, 117, 119, 260-271] and (d) nickel alloys [272-277]. Data points deviating from the dashed one-to-one line are exhibit more anisotropy compared to those lying close to the line. ..	67
Figure 2.46. TEM micrograph of dislocations in nickel-based superalloy CMSX-4 processed by PBF-EB AM [279]......	68
Figure 2.47. Dislocation structures in nickel-based superalloy CM247LC fabricated by PBF-L [281] showing (a) high dislocation density in the as-deposited condition, especially near cell edges and (b) reduced dislocation density after heat treatment at 1230°C for 2h followed by air cooling. ....	69
Figure 2.48. Experimentally measured hardness [74, 155-162] vs. $P_{cm}$ of iron-based alloys for AM. ....	71

Figure 2.49. Experimentally measured [163-171] and calculated HV of aluminum alloys fabricated by AM using Equation (2.12). .....	73
Figure 2.50. As-deposited HV [129, 172-186, 188, 294] as a function of $\phi$ , which depends on the chemical composition of nickel-based AM alloys.....	75
Figure 2.51. Comparison between measured as-deposited hardness values of iron-based alloys in AM, TMAZ hardness values of FSW and as-welded hardness from fusion welding. ....	77
Figure 2.52. Comparison between measured and calculated hardness values using Equation (2.12) for AM and FSW data [306]. .....	79
Figure 3.1. Hardenability curves for Jominy end-quench experiments on 8600 series steels (0.55Ni, 0.50Cr, 0.20Mo) with carbon concentrations of 0.20, 0.30, 0.40, and 0.60 wt% C [1, 4]. For any given distance from the quenched end, i.e. positions having similar cooling rates, a stark increase in hardness is measured as the carbon concentration increases. ....	99
Figure 3.2. A visual representation of the one-dimensional diffusion flux of a species, k, in a multicomponent material along an axis, z. ....	102
Figure 3.3. Schematic diagram of the calculation region for carbon diffusion calculations and initial composition profiles for C, Cr, Mo and Ni in (a) a dissimilar metal weld and (b) a functionally graded material between 2.25Cr-1Mo steel and Alloy 800H. The (a) double geometric and (b) linear grid spacings are shown by the solid black dots. ....	103
Figure 3.4. The abrupt change of the carbon chemical potential in (a) dissimilar metal welds results in a much larger thermodynamic driving force for carbon diffusion than the gradual change in (b) functionally graded materials. ....	104
Figure 3.5. Changes in the carbon concentration profile as a function of time for (a) a dissimilar metal weld and (b) a functionally graded material between 2.25Cr-1Mo steel and Alloy 800H.....	105
Figure 3.6. Comparison of simulated carbon diffusion profiles with experimental measurements between a 5Cr-0.5Mo/21Cr-12Ni weld heat treated at 773 K for 500 h. ....	106
Figure 3.7. Illustration showing the steps for achieving blended mixtures using a combination of elemental (Fe, Cr) and pre-alloyed powder (800H).....	108
Figure 3.8. Schematic diagram of the build dimensions in the functionally graded material between 2.25Cr-1Mo steel and Alloy 800H.....	108
Figure 3.9. For quantitative carbon concentration measurements, carbon counts per second were recorded during line scans on standard reference materials of (a) low alloy steel, (b) Incoloy 800, and (c) Cr-Mo steel with known carbon concentrations. (d) A linear interpolation between data points was then used to determine the carbon concentration of unknown samples.....	111
Figure 3.10. The measured concentrations of Fe, Ni, and Cr show that a gradual, stepwise change in chemical composition was achieved in the functionally graded material close to the expected variations calculated using a simple rule of mixtures.....	112

Figure 3.11. The calculated variation in carbon chemical potential at 773 K (500°C) as a function of distance using the measured chemical compositions in Figure 3.10 shows a gradual change in the thermodynamic driving force for carbon diffusion. ....	113
Figure 3.12. The smooth changes in the initial carbon concentrations of the (a) dissimilar weld and (b) functionally graded material in the as-welded and as-deposited conditions, respectively, indicate that both samples experienced dilution during processing.....	114
Figure 3.13. The variation of the Larson-Miller parameter with time and temperature calculated from equation (3.4) ( $C=20$ ) with two equivalent LMP values at different times and temperatures shown by the red circles. ....	116
Figure 3.14. A comparison of the carbon concentration profiles in the (a) DMW and (b) FGM after an accelerated heat treatment at 998 K (725°C) for 235 h demonstrate that carbon diffusion is significantly suppressed in the FGM compared to the DMW.....	117
Figure 3.15. Carbon potential as a function of distance at 500°C for a linear composition change (blue) and a composition change modeled to minimize carbon potential gradient (green) from 2.25Cr-1Mo steel ( $x=0$ ) to Alloy 800H ( $x=5$ ).....	121
Figure 3.16. Chromium concentration as a function of distance at 500°C for a linear composition change (blue) and a composition change modeled to minimize carbon potential gradient (green) from 2.25Cr-1Mo steel (position=0) to Alloy 800H (position=5). ....	122
Figure 3.17. Carbon potential gradient as a function of length of transition joint at four different temperatures within the typical service range.....	123
Figure 4.1. EPMA data were converted to nickel and chromium equivalents and plotted on the Schaeffler constitution diagram to determine the main microstructural phases across the gradient. ....	133
Figure 4.2. Vickers hardness measurements along the compositionally graded sample. Regions of martensite, austenite and a mixture of austenite and martensite predicted by the Schaeffler diagram are separated by dotted lines. ....	134
Figure 4.3. SEM micrograph taken approximately 3 mm from the baseplate in the build direction, corresponding to the 3 <sup>rd</sup> deposited layer and a composition of 10% 800H. ....	135
Figure 4.4. Continuous cooling diagram for the austenite transformation of steel-rich compositions (10 and 20% 800H) within the FGM calculated from JMatPro®. ....	136
Figure 4.5. (a) SEM micrograph approximately 7 mm from the baseplate in the build direction, corresponding to the 7 <sup>th</sup> deposited layer and a composition of 20% 800H and (b) a higher magnification image outlined by the white box in (a) showing martensite and austenite. ....	137
Figure 4.6. SEM micrographs taken approximately (a) 11 mm and (b) 15 mm from the baseplate in the build direction. The microstructures correspond to the 11 <sup>th</sup> and 15 <sup>th</sup> deposited layers and compositions of 30 and 40% 800H, respectively.....	138
Figure 4.7. Changes in the martensite start ( $M_s$ ), 50% completion ( $M_{50}$ ) and finish ( $M_f$ ) temperatures for the martensite transformation as a function of composition in terms of percent 800H.....	138

Figure 4.8. SEM micrographs approximately (a) 19 mm and (b) 34 mm from the baseplate in the build direction. The microstructures correspond to the 19 <sup>th</sup> and 34 <sup>th</sup> deposited layer, and compositions of 50 and 100% 800H, respectively.....	139
Figure 4.9. EDS map showing elemental segregation along the grain boundaries and interdendritic regions in the 90% 800H region of the composition gradient. ....	140
Figure 4.10. Thermodynamic calculations in the 90% 800H region showing (a) stable carbides as a function of temperature and (b) mass fractions of solidified phases from Scheil simulation .....	141
Figure 4.11. The measured XRD patterns show the change from a fully BCC to a fully FCC microstructure for alloy compositions ranging from 10 to 70% 800H. The circle and square symbols correspond to BCC and FCC peaks, respectively.....	143
Figure 4.12. Calculated lattice parameters for the BCC and FCC phases as a function of alloy composition show that the unit cell of each phase is largely unaffected by changes in chemical composition. ....	144
Figure 4.13. (a) The relative length change as a function of temperature for a sample extracted from the SAE387 Gr. 22 steel baseplate with a magnified view of the phase transformations shown in (b). ....	145
Figure 4.14. The changes in dilation as a function of temperature for the (a) 10%, (b) 20%, (c) 30%, and (d) 40% 800H alloy compositions, where a constant heating and cooling rates of 5°C/min were used.....	146
Figure 4.15. Calculated and measured transformation temperatures for the 10 to 40% 800H alloy compositions, including $A_{c1}$ and $A_{c3}$ upon heating, and $M_s$ upon cooling. ....	148
Figure 4.16. The corresponding (a-b) compositional variations (c-d) carbon chemical potential and (e-f) carbon diffusion profiles where only a partial composition gradient from 10% to 70% 800H (b, d, f) is used between 2.25Cr-1Mo steel and Alloy 800H compared to a full composition gradient (a, c, e).....	150
Figure 4.17. The corresponding (a-b) compositional variations (c-d) carbon chemical potential and (e-f) carbon diffusion profiles when a partial composition gradient up to 70% 800H starts from 20% 800H (b, d, f) compared to 10% 800H (a, c, e). ....	152
Figure 5.1. Cracks are often observed in a variety of FGM systems fabricated by AM, such as (a) Ti-6Al-4V to Invar 36 [7], (b) Inconel® 82 to SS316L [9], (c) Ti-6Al-4V to Inconel® 718 [10], and (d) Ti-6Al-4V to SS304L [8]. Reprinted with permission from Elsevier. ....	158
Figure 5.2. Schematic diagram of metallurgical cross section with the quantified parameters labeled. ....	166
Figure 5.3. (a) Low magnification light optical micrograph of the periodic vertical alignment of lack of fusion defects, indicated by the red arrows. The defects were found at the junctions between subsequent passes and layers, indicated by the light optical micrograph with the approximate pool boundaries indicated in (b). Higher magnification images show the consequences of lack of fusion defects, such as (c) oxide filling and (d) cracking.....	167
Figure 5.4. Image analysis measurements indicate that both the average individual lack of void size and total void area decrease as more 800H alloy is added to the FGM.....	168

Figure 5.5. Bead geometry changes as a function of alloy composition and laser power as seen in the optical micrographs of transverse cross-sections of the single bead deposits. The percentages along the left axis represent the amount of 800H added to the alloy.....	170
Figure 5.6. The effects of alloy composition and laser power on (a) the total melted area of the deposit, (b) the maximum dilution depth, and (c) the percent dilution calculated from Equation (5.15). .....	171
Figure 5.7. The chemical composition and laser power have significant effects on the experimentally measured deposit (a) height and (b) width.....	172
Figure 5.8. The calculated activity as a function of composition for (a) oxygen and (b) sulfur for different alloy compositions at 1600°C. ....	174
Figure 5.9. Changes in the (a) surface tension and (b) temperature coefficient of surface tension ( $d\sigma/dT$ ) as a function of temperature for different alloy compositions.....	175
Figure 5.10. The critical temperature, defined as the temperature at which the temperature coefficient of surface tension ( $d\sigma/dT$ ) changes from positive to negative, changes significantly with alloy composition.....	176
Figure 5.11. The calculated deposit geometries for the 10% 800H alloy compositions (a) ignoring surface-active elements and (b) considering the effects of oxygen and sulfur show considerable differences in shape. In contrast, the changes in deposit geometries for the 60% 800H alloy compositions (c) ignoring surface-active elements and (d) considering the effects of oxygen and sulfur are much less sensitive. Experimentally measured deposit geometries are shown by the dotted black lines.....	179
Figure 5.12. Three-dimensional isometric views of the temperature and velocity fields for (a) 10% 800H and (b) 60% 800H when surface-active elements are considered in the calculation. The red regions in the plots represent temperatures above $T_{crit}$ .....	180
Figure 5.13. The calculated deposit (a) width, (b) depth, and (c) height as a function of alloy composition and oxygen concentration for a 2000 W laser power. All other parameters used in the simulations were the same as experimental conditions. ....	182
Figure 6.1. Some precipitates in Inconel® 625 are undesirable in terms of mechanical properties due to their brittle nature, where can initiate cracks as shown by the white arrow in a Laves phase precipitate in low Fe Inconel® 625. ....	186
Figure 6.2. Small variations in chemistry can lead to significant differences in grain structures in as-deposited (a) low Fe and (b) high Fe Inconel® 625 and the corresponding grain structures after HIP in the (c) low Fe and (d) high Fe materials. Consequently, uniaxial tension tests and resulting (e) engineering and (f) true stress-strain curves for each material and condition show significant differences in material properties. Reprinted with permission from Elsevier. ....	187
Figure 6.3. The measured chemical compositions in XEDS line scans across multiple dendrites in the as-deposited (a) low Fe and (b) high Fe Inconel® 625 show the spatial enrichment and depletion of alloying elements. ....	190

Figure 6.4. The optical micrographs of as-deposited (a) low Fe and (b) high Fe Inconel® 625 show the columnar dendritic solidification structures and secondary phase precipitates in interdendritic regions. ....	194
Figure 6.5. Laves phase in Inconel® 625 exhibits an irregular morphology derived from a eutectic transformation near the end of solidification, such as the cluster shown in as-deposited low Fe Inconel® 625. ....	195
Figure 6.6. HAADF-STEM micrograph of the precipitate morphology in the as-deposited low Fe sample along with the corresponding XEDS maps of Ni, Cr, Mo, Si, Nb and N.....	196
Figure 6.7. HAADF-STEM micrograph showing the precipitate morphology in the as-deposited high Fe Inconel® 625 sample along XEDS maps corresponding to the enclosed area showing enrichment in Ti, Nb, and N and depletion in Ni, Cr, and Mo.....	197
Figure 6.8. Significant differences in the fractions of secondary phases as a function of temperature are predicted for the (a) low Fe and (b) high Fe Inconel® 625 during Scheil solidification. ....	198
Figure 6.9. The Laves phase volume fraction under Scheil solidification conditions is influenced by the amount of Fe and Si in the alloy composition as shown by the contour plot. The dotted lines represent constant volume fractions with values indicated by labels.....	199
Figure 6.10. The effects of Si and Ti contents on the temperature at which Laves phase forms in Inconel® 625 with a constant Fe concentration of 2.5 wt%. ....	199
Figure 6.11. The binary diffusion coefficients [1] of various alloying elements in FCC nickel as a function of temperature. ....	200
Figure 6.12. The calculated concentration profiles as a function of distance and time show that the spatial variation of Mo, the slowest diffusing element, quickly homogenizes in both the (a) low Fe and (b) high Fe Inconel® 625 at the HIP temperature (1160°C). The starting concentration profile is calculated from Scheil solidification and the domain corresponds to half a secondary dendrite. ....	201
Figure 6.13. Precipitate distribution in (a) low Fe and (b) high Fe Inconel® 625 after HIP at 1160C for 4 h. ....	202
Figure 6.14. HAADF-STEM micrograph of precipitates rich in Mo, Nb, and N along a grain boundary in the low Fe Inconel® 625 sample after HIP. ....	204
Figure 6.15. HAADF-STEM micrograph and corresponding XEDS composition maps showing the combination of M <sub>2</sub> N and Laves precipitates at a grain boundary in the low Fe Inconel® 625 after HIP. ....	204
Figure 6.16. The calculated phase equilibria at 1160°C for a chemical composition corresponding to the measured Laves phase chemistry (a) considering all available phases in the Ni-superalloy database of JMatPro® V8 and (b) suspending the M(C,N) phase. ....	205
Figure 6.17. HAADF-STEM micrograph of a Ti and Nb rich nitride in the high Fe Inconel® 625 sample after HIP. ....	206

## LIST OF TABLES

Table 2.1. Interaction coefficients between carbon and other common alloying elements in steels in liquid iron at 1600°C. ....	13
Table 2.2. A comparison between AM processes and their characteristics [60]. ....	31
Table 2.3. A summary of functionally graded material systems fabricated by additive manufacturing. ....	33
Table 2.4. Process parameters for iron, aluminum and nickel alloys .....	47
Table 2.5. Process and resulting as-deposited microstructures for iron, aluminum and nickel alloys .....	48
Table 2.6. A summary of dislocation densities reported for AM alloys.....	70
Table 2.7. Compositions (in wt%), $P_{cm}$ values and average HV numbers for iron-based alloys..	72
Table 2.8. Compositions (in wt%) and HV ranges used for aluminum-based alloys .....	74
Table 2.9. Compositions (in wt%) and range of HV numbers for nickel alloys.....	76
Table 2.10. Reported cooling rates for FSW, fusion welding and AM .....	78
Table 3.1. Composition (in wt%) of materials used in the DED-L process. Single values in the baseplate composition represent the maximum allowable concentration. ....	107
Table 3.2. Chemical compositions at various positions along a hypothetical functionally graded material, where the chromium concentration is to be determined at each location and all other elements vary linearly between 2.25Cr-1Mo steel and Alloy 800H. ....	119
Table 4.1. Carbides in equilibrium for different alloy compositions at 773 K. ....	142
Table 4.2. Comparison of computed diffusion fluxes ( $\text{mol/m}^2\text{-s}$ ) and carbon depletion at 773 K after different service times in dissimilar joints between 2.25Cr-1Mo steel and Alloy 800H. ....	154
Table 5.1. Values for the enthalpy of segregation ( $\Delta H_i^\circ$ ), entropy of segregation factor ( $ki$ ), and surface excess at saturation ( $\Gamma i_0$ ) of element $i$ for binary Fe-O and Fe-S alloys [12]....	160
Table 5.2. First order binary interaction coefficients between surface-active and other alloying elements in liquid iron at 1600°C [14, 29]. ....	175
Table 5.3. Calculated thermophysical properties of alloy compositions ranging from 10 to 60% 800H.....	178
Table 6.1. Chemical composition (wt%) of Inconel® 625 powder feedstock.....	189
Table 6.2. A comparison between measured and predicted chemical compositions (wt %) of the dendrite core ( $C_{core}$ ), interdendritic region ( $C_{ID}$ ), initial alloy composition ( $C_{avg}$ ) or instantaneous liquid composition ( $C_L$ ), and partition coefficients ( $k_i$ ) during solidification for low and high Fe Inconel® 625. ....	191
Table 6.3. Comparison between the average measured chemical compositions (wt%) of secondary phases in Inconel® 625. ....	196

## ACKNOWLEDGEMENTS

I would first like to thank my academic advisors, Prof. Tarasankar DebRoy and Dr. Todd Palmer, for their support, guidance, and willingness to help during my graduate studies. They have shown me the path for achieving scholarship, helped develop invaluable research skills, and taught me how to disseminate reusable insight to the academic community and upcoming researchers. I will forever be grateful for the mentorship and advice, and without them, many of my achievements would not have been possible.

Secondly, I would like to thank my group members Dr. Jared Blecher, Dr. Huiliang Wei, Mr. Tuhin Mukherjee, Mr. Gerry Knapp, Mr. Andrew Iams, Mr. Scott Meredith, Mr. Zakariya Khayat, Ms. Marissa Brennan, Mr. Titus Reed, Mr. Derek Shaffer, Mr. Skyler Hilburn, Mr. Mingze Gao and Ms. Selda Nayir for your help, technical discussions, and overall kindness. I would also like to thank visiting scholars Dr. Leilei Wang, Dr. Tong Liu, Dr. Zhongmei Gao, Dr. Wenmin Ou, Ms. Yang Du, Ms. Qianru Wu, and Mr. Meng Jiang for instilling aspects of your cultures in me.

I am grateful for my committee members Dr. Allison Beese and Dr. Reginald Hamilton for their useful comments and suggestions.

Lastly, I would like to express my gratitude for the love and support my family and friends have provided during my graduate career. Your patience, encouragement, and faith in me are second to none.

This research was funded by the Nuclear Energy University Program of the US Department of Energy under grant number DE-NE0008280.

# Chapter 1

## INTRODUCTION

### 1.1 Structural material challenges in power generation facilities

The worldwide generation of electricity from various fuel sources has risen steadily over the past 40 to 50 years. In 2016, about 25 petawatt-hours (1 petawatt =  $10^{15}$  watts) were generated from a combination of coal, oil, natural gas, hydroelectricity, nuclear, and other forms of renewable energy; amounting to an approximate fourfold increase from 1973 [1]. To put these numbers into perspective, 25 petawatt-hours would be equivalent to the power consumed if every human on Earth (~7.5 billion) each simultaneously operated 150 incandescent lightbulbs (60 W) for a full year. The use of natural gas, coal, and nuclear energy constitutes about 72% of the total electricity generation, as shown in Figure 1.1, much of which comes from large power generation facilities located in developed countries [1]. These power generation facilities typically operate at the highest temperatures possible for the best efficiency while maintaining a low risk of catastrophic failure that would otherwise jeopardize the safety of workers or public citizens.

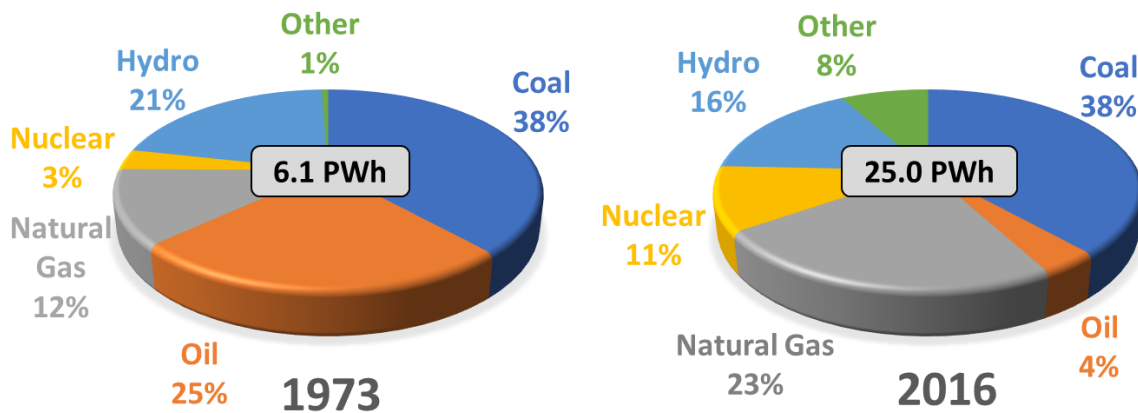


Figure 1.1. A comparison of the worldwide electricity production by various sources in 1973 and 2016, with most electricity now being produced using coal, natural gas, and nuclear sources. Reproduced from [1].

A variety of materials are used in power generation facilities, as seen in Figure 1.2, which shows an example of the structural materials used in a pressurized water reactor in a nuclear power plant [2]. The integrity of structural alloys is an important factor that determines the service conditions of plant operation and ultimately the efficiency of energy generation. A general trade-off between performance and cost exists during material selection, and for this reason, the most economical and safe choice is to use a combination of a wide variety of alloys. Inexpensive, low

alloy ferritic steels have good strength and corrosion resistance and are a popular choice for low temperature environments like steam generator vessels and piping [3]. Meanwhile, austenitic stainless steels and nickel-base superalloys exhibit excellent corrosion resistance and creep strength, making them suitable for the most extreme service conditions such as those found in steam generators and superheaters.

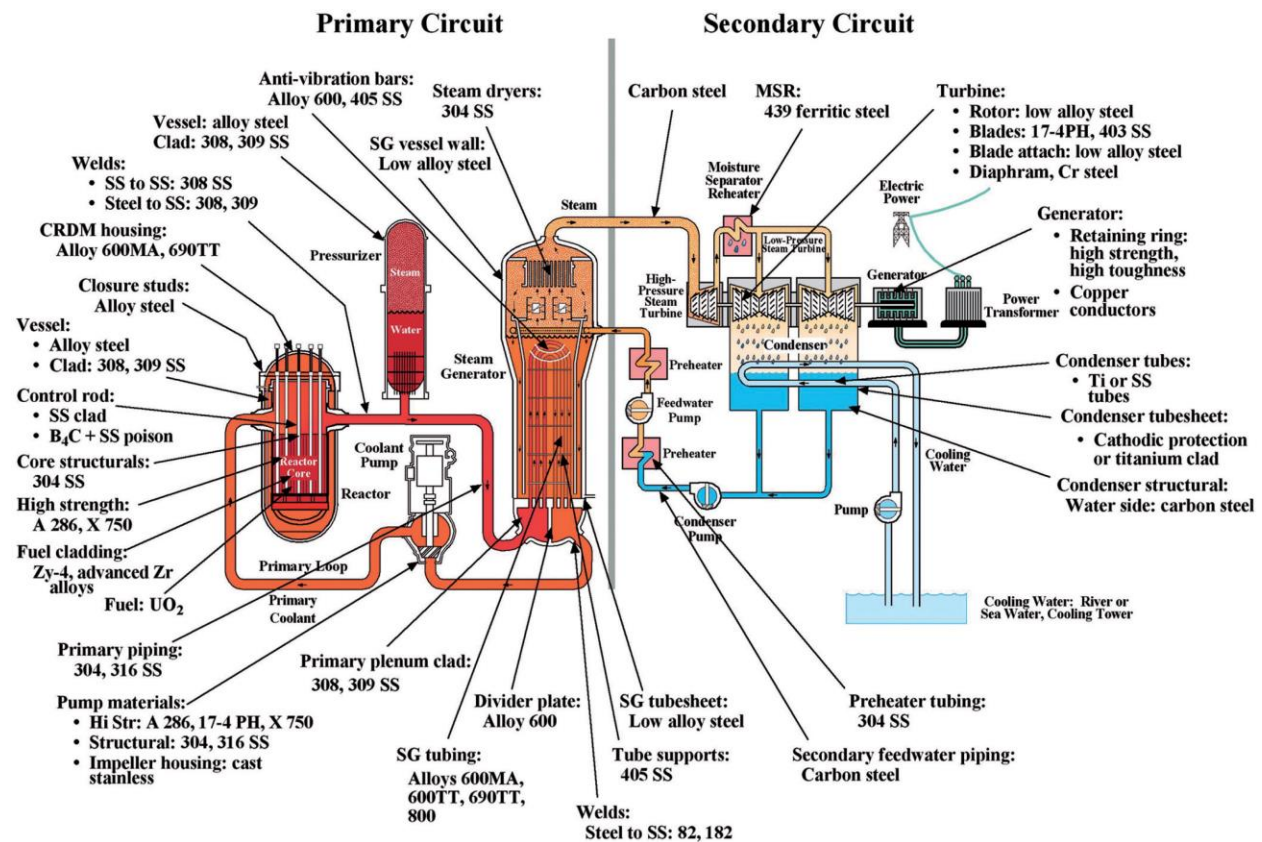
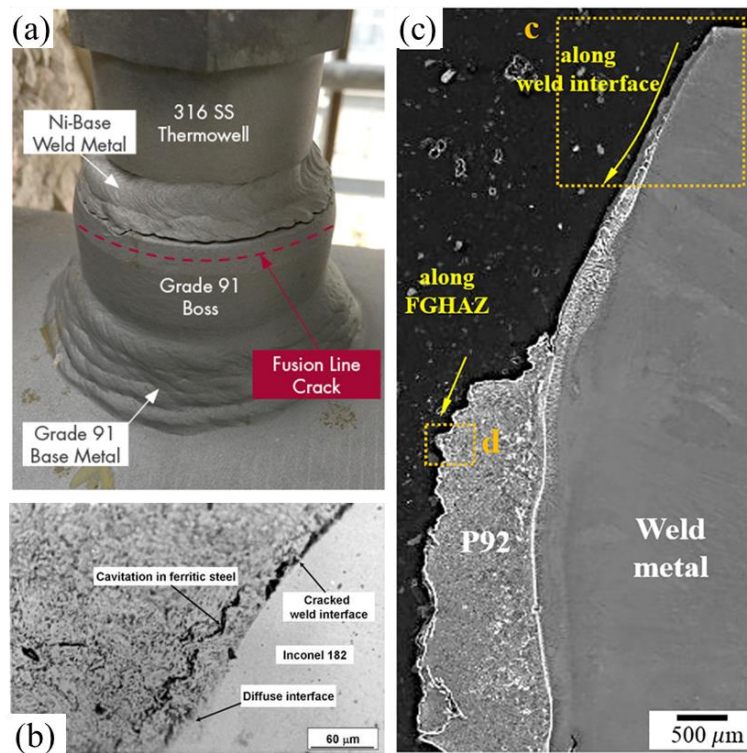


Figure 1.2. An example of the structural materials used in the primary and secondary circuits of a pressurized water reactor in a nuclear power plant [2]. Reprinted with permission from Elsevier.

Alloys of all types need to be joined, often by fusion welding, which can result in unintended consequences that may not be realized until after years of plant operation. Depending on engineering design, power generation facilities can contain thousands of dissimilar metal welds [4]. The premature failure in the transition regions between dissimilar alloys is both an economic and a safety concern. It has been reported that the SG costs of plant outages caused by the repair and replacement of dissimilar welds can reach nearly \$1 million per day [5]. Often found in steam generators and superheater sections, these welds operate under a wide range of service

temperatures of approximately 400-600°C [6]. A leakage in these regions of the plant can damage surrounding materials and, more importantly, cause severe bodily harm to workers on site.

The issue of dissimilar weld failures is well-known and established. Based on a 1982 industry survey [7], about 19% of plants had reported cracks and leakage of dissimilar welds between low alloy ferritic and austenitic stainless steels in boiler applications similar to that shown in Figure 1.3. The time to failure ranged between 29,000 to 125,000 hours (~3 to 14 years) and the average time to failure was estimated around 80,000 hours (9 years). These times fall well short of designed plant lifetimes of approximately 30 to 40 years. Interestingly, a striking correlation between failure and filler metal type was observed, as welds using stainless steel filler wire constituted about 63% of all reported failures. Most failures occurred in the heat affected zone of the ferritic steel adjacent to the fusion line and were exacerbated by thermal cycling during plant shut down and start up.



*Figure 1.3. Failures in ferritic/austenitic dissimilar welds often begin with crack formation, such as that seen in (a) a failed thermowell between Grade 91 steel and SS316 [8]. In laboratory creep experiments, microscopic cracks repeatedly form near the weld interface in the ferritic steel for a variety of alloy combinations, including (b) 2.25Cr-1Mo ferritic steel and Alloy 800 [9] (Reprinted with permission from Springer Nature) and (c) P92 ferritic steel and nickel superalloy Inconel 740H [10] (Reprinted with permission from Elsevier).*

With the worldwide demand for energy on the rise, global efforts are being undertaken to meet these demands in economically and environmentally friendly ways. Until major breakthroughs are made to use renewable energy sources, humans will continue to rely on electricity generation via current fuel consumption methods. However, many fossil-fired and nuclear power plants in operation are either approaching or have reached the limits of their design lifetime [11]. Since constructing entirely new power plants alone is not cost-effective, scientists and engineers have been tasked with the material challenges associated with keeping old plants in operation. Furthermore, new fossil-fired and nuclear power plants are being designed to last longer (up to 80 years) in much harsher environments than plants currently in operation [12, 13]. These energy needs raise an important question for practicing engineers: how can we advance the science and technology of materials engineering to ensure efficient operation and plant safety?

## **1.2 Opportunities for advanced manufacturing of multifunctional materials**

Many individual research efforts [10, 14-19] and major review articles [3, 7, 20, 21] have investigated the issues leading to premature failures in ferritic to austenitic weldments. While degradation during service cannot reliably be traced to a single root mechanism, the following interdependent factors contribute to failure in dissimilar metal welds:

- Carbon migration from the ferritic steel to the austenitic filler metal
- Creep cavitation voids forming around carbides near the fusion line
- Mismatch in coefficient of thermal expansion between alloys and filler metals
- Selective oxidation at the weld interface due to changes in chemistry
- Localized stress concentrations caused by changes in material properties

Nearly all the listed factors arise from an abrupt change in chemical composition, microstructure, or properties over a relatively short distance associated with regions near the weld interface. Examples of the scale of these spatial changes are shown in Figure 1.4 for a dissimilar ferritic-to-austenitic weld. Some approaches to mitigate these metallurgical issues include the selection of various filler metal compositions, improving the joint design, introducing intermediate alloys, and modifying the chemical composition of the alloys. Even after decades of realization and research, however, a comprehensive, cost-effective solution to prevent premature failure in dissimilar metal welds between ferritic and austenitic alloys has remained elusive.

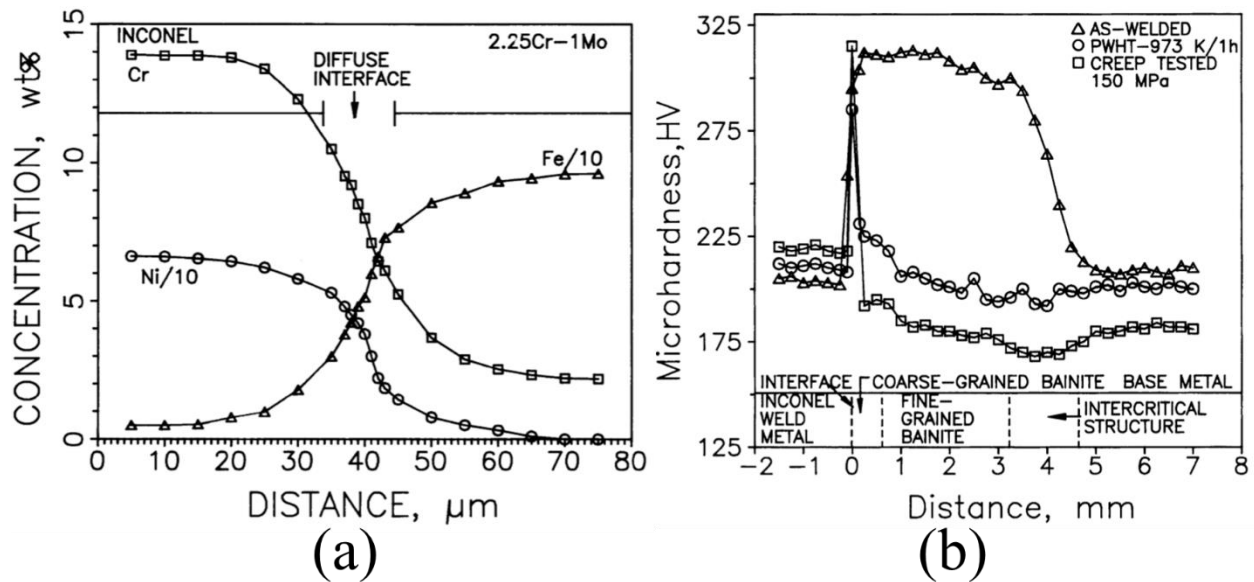


Figure 1.4. Abrupt changes of both (a) chemical composition and (b) microhardness across the fusion line of a dissimilar weld between 2.25Cr-1Mo steel and Alloy 800 using Inconel 182 filler metal [15] introduce many metallurgical issues that lead to premature failure. Reprinted with permission from Springer Nature.

The core solution to overcoming the challenges found in dissimilar welds between ferritic and austenitic alloys resides in the ability to eliminate abrupt changes in chemical composition and the resulting microstructure and properties. Instead, it is reasonable to assume that a gradual change extending over a much larger distance, coined as a graded transition joint or, more commonly, a functionally graded material, would mitigate these problems. In fact, the current best practices use this concept, albeit on a larger scale than where problems occur, by utilizing a trimetallic weld joint configuration. An intermediate alloy, usually a nickel alloy, is inserted between ferritic and austenitic stainless steels to reduce the coefficient of thermal expansion mismatch [3]. Although these configurations have shown to improve the lifetime of joints, they simply buy more time and are still prone to failure before the expected plant lifetime [4].

The recent emergence and development of additive manufacturing technologies provides a promising approach to fabricate graded transition joints with a controlled variation in chemical composition, microstructure, and properties. Laser-based, powder-blown directed energy deposition, a popular additive manufacturing process, offers a means for selectively varying chemical composition in a layer-by-layer manner on a length scale of 0.5 to 1 mm [22]. Both pre-alloyed and elemental powders can be combined in predefined ratios to spatially tailor chemical

composition profiles. When engineered with a specific function, it is hypothesized that these functionally graded materials can overcome the existing challenges associated with the fusion welding of ferritic and austenitic alloys.

### **1.3 Research Objectives**

Dissimilar metal welds between ferritic and austenitic alloys used in energy generation applications are susceptible to failure before their expected lifetime due to a variety of metallurgical issues related to a sharp change of chemical composition, microstructure, and properties over a short distance at the weld interface. A gradual change in material from the ferritic steel to austenitic alloy over a length scale orders of magnitude larger than that found in welds is proposed to overcome the challenges associated with dissimilar metal joining. This research investigates the science and metallurgy of additively manufactured functionally graded materials between ferritic and austenitic alloys for improving the service life of dissimilar metal joints. Specifically, this research seeks to quantitatively understand how compositional changes influence the processing, microstructure, and properties of alloys used in functionally graded materials. The following are areas of focus in this thesis:

1. The theory and design of compositional profiles that serve a function during service, and experimentally testing the effectiveness of the material.
2. Characterization of the changes in microstructure and properties when changing from a ferritic to austenitic alloy.
3. Unforeseen challenges in the additive manufacturing of functionally graded materials and the effects of chemical composition on their printability.
4. The effects of composition on precipitate formation in austenitic alloys relevant to functionally graded material applications.

The scope of the thesis, which employs a suite of experimental and computational tools, includes the design, fabrication, and testing of functionally graded materials intended for service in power generation applications. Computational thermodynamic and kinetic simulations serve as an invaluable tool to design and predict behavior of functionally graded materials. A laser-based directed energy deposition additive manufacturing process is used to then fabricate functionally graded materials with pre-blended elemental and alloy powders. A numerical heat transfer and fluid flow model is utilized to study the effects of chemical composition on changes in molten pool

geometry. Microstructural characterization is performed with a variety of microscopy techniques on length scales ranging from tens of nanometers to millimeters. The combination of these tools allows for comprehensive research that lays the groundwork for the development of structurally sound, functionally graded materials for power generation applications.

#### **1.4 Thesis Structure**

The thesis begins with a brief introduction in Chapter 1 into the fundamental material challenges that have plagued structural materials in nuclear power generation facilities for decades. The motivation for this research is built from the challenges in terms of potential socioeconomic benefits and workplace safety, followed by a detailed list of objectives. Finally, an overview of the methodology used to achieve these research objectives is given.

In Chapter 2, a detailed formulation of metallurgical issues in dissimilar welds introduced in Chapter 1 is developed based on decades of scientific research. To establish the foundation for using advanced materials to overcome these challenges, an overview on functionally graded materials is given where advantages and disadvantages are discussed. Next, the current state-of-the-art of additive manufacturing is reviewed to provide a background into the methodology employed in this research to design, control, and fabricate functionally graded materials. Finally, the influence of additive manufacturing on material properties and performance are addressed.

The specific design for limiting carbon diffusion by using functionally graded materials between ferritic and austenitic alloys is analyzed in Chapter 3. A formulation of multicomponent diffusion in the alloy system is made and the effects of chemical composition on the driving force for carbon diffusion are studied. The tools and methodology for predicting carbon diffusion during long-term service, where laboratory experiments are not feasible, are explained in detail. Accelerated heat treatments are then used to test the effectiveness of using functionally graded materials over dissimilar welds to limit carbon diffusion. Experimental measurements of the resulting carbon diffusion profiles from additively manufactured samples are presented to confirm and validate the hypothesis. Finally, further predictions are given to estimate the advantages gained by replacing conventional dissimilar welds with functionally graded materials.

Chapter 4 evaluates the as-deposited microstructure of the functionally graded material between 2.25Cr-1Mo steel and Alloy 800H. Experimental observations are compared with theoretical predictions to understand the effects of chemical composition variations on phase

transformations. Additional single alloy composition specimens were fabricated to determine the phase composition and transformation behavior in different regions of the functionally graded material with emphasis placed on the regions encompassing the transition from a ferritic to austenitic microstructure.

Upon further evaluation, defects due to improper selection of process parameters were found in the additively manufactured samples, which would compromise the properties and performance of the functionally graded alloy. Chapter 5 develops an understanding into the effects of compositional changes during functional grading on molten pool geometry during additive manufacturing. The chapter begins with an analysis of the experimental methodology and analysis of single-track deposits fabricated from different powder mixtures. The observations and trends in the experimental data are established as a function of chemical composition. The background theory is established and calculations of important thermophysical that affect melt pool geometry are made to explain experimental observations. Rigorous heat transfer and fluid flow calculations that account for free surface deformation and the effects of surface-active elements on fluid flow are used to simulated experimental conditions.

The effects of chemical composition on the formation of secondary precipitates in an additively manufactured nickel superalloy, which is commonly used as a parent alloy in functionally graded alloys, are studied in Chapter 6. Calculations based on both equilibrium and non-equilibrium thermodynamics are made to predict precipitate formation based on chemical composition. The calculations are compared with experimental measurements and guidelines are presented to tailor chemical composition during functional grading to avoid deleterious secondary phases.

Finally, the results of this research are summarized in Chapter 7. The conclusions from the thesis are evaluated based on the contributions to materials science.

## **1.5 References**

- [1] International Energy Agency, Key World Energy Statistics 2018, Paris, France, 2018, [https://doi.org/10.1787/key\\_energ\\_stat-2016-en](https://doi.org/10.1787/key_energ_stat-2016-en).
- [2] T. Allen, J. Busby, M. Meyer, D. Petti, Materials challenges for nuclear systems, *Materials today*, 13(12) (2010) 14-23.
- [3] A.K. Bhaduri, S. Venkadesan, P. Rodriguez, P.G. Mukunda, Transition metal joints for steam generators—An overview, *Int. J. Pres. Ves. Pip.*, 58(3) (1994) 251-265.

- [4] J.N. DuPont, Microstructural evolution and high temperature failure of ferritic to austenitic dissimilar welds, *Int. Mater. Rev.*, 57(4) (2012) 208-234.
- [5] B. Dooley, P.S. Chang, The current state of boiler tube failures in fossil plants, *Power Plant Chemistry*, 2(4) (2000) 197-203.
- [6] R. Viswanathan, J.F. Henry, J. Tanzosh, G. Stanko, J. Shingledecker, B. Vitalis, R. Purgert, U.S. program on materials technology for ultra-supercritical coal power plants, *J. Mater. Eng. Perform.*, 14(3) (2005) 281-292.
- [7] C. Lundin, Dissimilar metal welds-transition joints literature review, *Weld. J.*, 61(2) (1982) 58-63.
- [8] T. Totemeier, Dissimilar metal welds in Grade 91 steel, *News and Views*, Structural Integrity Associates, 2018, pp. 15-18.
- [9] K. Laha, K.S. Chandravathi, P. Parameswaran, S. Goyal, M.D. Mathew, A comparison of creep rupture strength of ferritic/austenitic dissimilar weld joints of different grades of Cr-Mo ferritic steels, *Metall. Mater. Trans. A*, 43(4) (2012) 1174-1186.
- [10] K.-Y. Shin, J.-W. Lee, J.-M. Han, K.-W. Lee, B.-O. Kong, H.-U. Hong, Transition of creep damage region in dissimilar welds between Inconel 740H Ni-based superalloy and P92 ferritic/martensitic steel, *Mater. Charact.*, 139 (2018) 144-152.
- [11] P. Voosen, How long can a nuclear reactor last?, 2009, <https://www.scientificamerican.com> (accessed 11 June 2019.).
- [12] S. Sridhar, P. Rozzelle, B. Morreale, D. Alman, Materials challenges for advanced combustion and gasification fossil energy systems, *Metall. Mater. Trans. A*, 42(4) (2011) 871-877.
- [13] J. DuPont, R. Mizia, Review of dissimilar metal welding for the NGNP helical-coil steam generator, Idaho Falls, ID, 2010,
- [14] R. Klueh, J. King, Elevated-temperature tensile and creep-rupture behavior of alloy 800H/ERNiCr-3 weld metal/2 1/4 Cr-1 Mo steel dissimilar-metal weldments, Oak Ridge, TN, USA, 1982,
- [15] K. Laha, K. Chandravathi, K.B.S. Rao, S. Mannan, D. Sastry, An assessment of creep deformation and fracture behavior of 2.25 Cr-1Mo similar and dissimilar weld joints, *Metall. Mater. Trans. A*, 32(1) (2001) 115-124.
- [16] K. Laha, K.B.S. Rao, S. Mannan, Creep behaviour of post-weld heat-treated 2.25 Cr-1Mo ferritic steel base, weld metal and weldments, *Mater. Sci. Eng. A*, 129(2) (1990) 183-195.
- [17] M.K. Samal, M. Seidenfuss, E. Roos, K. Balani, Investigation of failure behavior of ferritic–austenitic type of dissimilar steel welded joints, *Eng. Fail. Anal.*, 18(3) (2011) 999-1008.
- [18] M. Subramanian, J. Galler, J. DuPont, B. Kombaiah, X. Yu, Z. Feng, S. Babu, Heterogeneous creep deformation in Dissimilar Metal Welds (DMWs), *Mater. Sci. Eng. A*, 749 (2019) 1-13.
- [19] Y. Zhao, J. Gong, Y. Jiang, The effect of carbon diffusion on creep behaviours for a dissimilar joint between P91 and 12Cr1MoV steels, ASME 2016 Pressure Vessels and Piping Conference, American Society of Mechanical Engineers, 2016, p. V005T09A024.
- [20] J. DuPont, Microstructural evolution and high temperature failure of ferritic to austenitic dissimilar welds, *Int. Mater. Rev.*, 57(4) (2012) 208-234.
- [21] D. Roberts, R. Ryder, R. Viswanathan, Performance of dissimilar welds in service, *J. Press. Vess.*, 107(3) (1985) 247-254.
- [22] T. DeRoy, H. Wei, J. Zuback, T. Mukherjee, J. Elmer, J. Milewski, A. Beese, A. Wilson-Heid, A. De, W. Zhang, Additive manufacturing of metallic components–process, structure and properties, *Prog. Mater. Sci.*, 92 (2018) 112-224.

## Chapter 2

### LITERATURE REVIEW

#### 2.1 Metallurgical challenges in ferritic to austenitic dissimilar welds

Dissimilar metal joints between ferritic and austenitic materials are commonly found in sector transitions of fossil-fired and nuclear energy generation facilities [1-4]. Ferritic low-alloy steels are often used in pressure vessels due to their good strength and corrosion resistance at elevated service temperatures. Austenitic stainless steels and Fe-Ni-Cr alloys offer excellent high temperature strength, resistance to oxidation, and creep rupture properties. Fusion welding between these dissimilar materials is typically performed with a stainless steel or nickel-based filler metals, depending on the alloy system. Consequently, abrupt changes in chemical composition, microstructure, and mechanical properties are observed [2, 4-6], leading to a degradation in the performance of the joint during long-term high temperature service [1]. This section reviews some of the metallurgical characteristics and challenges in dissimilar welds with an emphasis on carbon diffusion.

##### 2.1.1 Carbon migration

Mass transfer by diffusional processes is an important topic of interest in materials science and engineering. The amount of mass transported through a unit area per unit area is defined as the flux,  $J$ , and is often used to represent the overall transport. In the simplest form, Fick's first law for one-dimensional, steady state diffusion commonly expresses the flux of a component as,

$$J = -D \frac{dC}{dx} \quad (2.1)$$

where  $D$  is the diffusion coefficient,  $C$  is the concentration of the species, and  $x$  is the direction in space. The diffusion coefficient is a term that represents the kinetics of the process while the concentration gradient ( $dC/dx$ ) represents the driving force for diffusion. Equation (2.1) indicates that a species will move from a region of high to low concentration. This situation is analogous to a ball rolling down a hill, where the ball moves from a location of high to low potential energy. The concentration profile in Equation (2.1) is constant as a function of time, and therefore is not practical for many real-life scenarios that involve diffusional processes. The time evolution of the concentration profile can be written as a partial differential equation,

$$\frac{\partial C}{\partial t} = \frac{\partial}{\partial x} (J) = \frac{\partial}{\partial x} \left( D \frac{\partial C}{\partial x} \right) \quad (2.2)$$

where  $t$  is time. Equation (2.2) is referred to as Fick's second law for non-steady state diffusion in one dimension. In physical processes described by Fick's second law of diffusion, the concentration profile in one dimension evolves as a function of time until it eventually reaches steady state. Consider dropping colored dye into a narrow vial of water. In the beginning moments, the dye is highly concentrated at the dropping location, and eventually the dye spreads out evenly so that the concentration is uniform at all points in the vial. This is a crude example of Fick's second law of diffusion.

Equations (2.1) and (2.2) are taught in many introductory materials science and engineering courses, where the driving force for diffusion is expressed as the concentration gradient of a species. These equations can accurately represent simplified ideal binary systems such as the carburization of pure iron. However, many engineering materials applications are non-ideal and cannot be adequately described by Equations (2.1) and (2.2). For example, a set of experiments in which two steels with roughly similar carbon concentrations, but with different amounts of other alloying elements, were welded and subjected to high temperature heat treatment [7]. According to Fick's first and second laws above, there should be no flux of carbon atoms across the weld interface because the carbon concentration gradient is roughly uniform, and it should remain unchanged. Figure 2.1 shows the measured carbon concentration profile across the weld after a 10 day heat treatment at 1050°C, which indicates that not only was there a change in the concentration profile, but carbon diffused from regions of low to high concentration near the weld interface.

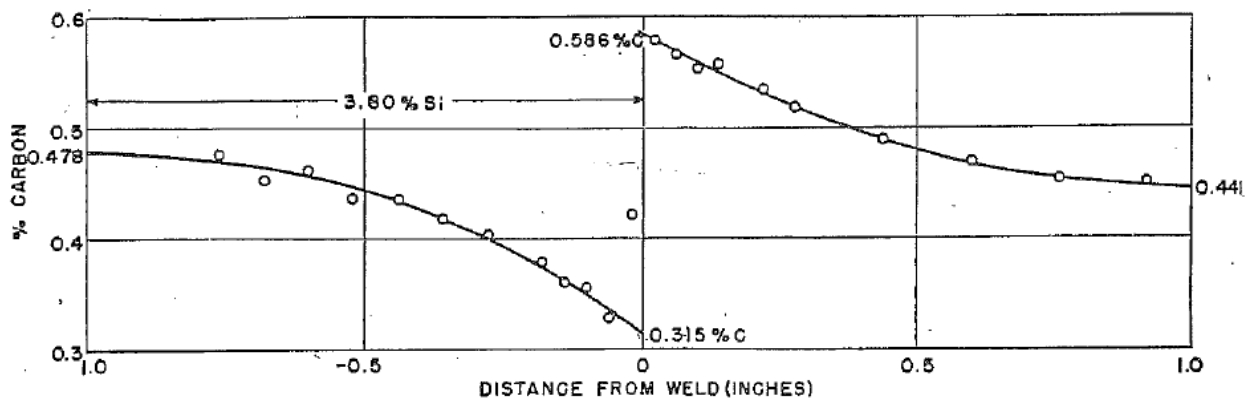


Figure 2.1. The carbon concentration profile across a weld of two steels, one containing 3.80 wt% Si and the other with 0.05 wt% Si, after a 10 day heat treatment at 1050°C [7].

These diffusion experiments are an example of phenomena called uphill diffusion, when the flux of a species opposes the direction of the composition gradient, i.e. the species migrates from areas of low to high concentrations. To account for this phenomenon, it is more general and accurate to represent Fick's equations as,

$$J = -L \frac{d\mu}{dx} \quad (2.3)$$

$$\frac{\partial C}{\partial t} = \frac{\partial}{\partial x}(J) \quad (2.4)$$

where  $L$  is termed as a mobility factor and  $\mu$  is the chemical potential of a species. In Equations (2.3) and (2.4), the driving force for the diffusion of species is now represented by the spatial gradient in the chemical potential of that species.

The chemical potential of a species,  $i$ , is defined as,

$$\mu_i = \mu_i^0 + RT \ln a_i \quad (2.5)$$

where  $\mu_i^0$  is the standard chemical potential defined by the chosen reference state,  $R$  is the universal gas constant,  $T$  is temperature and  $a_i$  is the activity. The activity of an element in dilute alloys is most commonly expressed as,

$$a_i = \gamma_i [\text{wt}\%_i] \quad (2.6)$$

where  $\gamma_i$  is the activity coefficient and  $[\text{wt}\%_i]$  is the weight percent of element  $i$ . Using the Wagner formalism [8], the activity coefficient can be written as,

$$\log \gamma_i = \log \gamma_i^0 + \sum_j \epsilon_i^j [\text{wt}\%_j] \quad (2.7)$$

in which  $\gamma_i^0$  is constant taken to equal unity,  $\epsilon_i^j$  are the first-order interaction coefficients between elements  $i$  and  $j$ , and  $[\text{wt}\%_j]$  is the weight percent of element  $j$ . The magnitude of  $\epsilon_i^j$  indicates the strength of the interaction, while the sign dictates whether element  $j$  increases or decreases the activity of  $i$ . Interaction coefficients for carbon in liquid iron at 1600°C are shown in Table 2.1 as an example. From Equations (2.5)-(2.7), it is evident that the presence of  $j$  alloying elements affects the chemical potential of element  $i$ , which in turn can influence the driving force for diffusion.

Table 2.1. Interaction coefficients between carbon and other common alloying elements in steels in liquid iron at 1600°C.

Element $j$	Al	Cr	C	Mn	Mo	Ni	Si	V
$\epsilon_C^j$	5.3	-5.1	6.9	-2.7	-4.0	2.9	9.7	-16.1

Carbon migration is a major problem that contributes to the premature failure of dissimilar ferritic-to-austenitic weldments in power generation facilities [2, 9]. The problem is similar to that studied in the Darken experiments [7], and a schematic diagram is shown in Figure 2.2. Both the ferritic and austenitic alloys contain roughly 0.1 wt% C, which results in an approximately uniform distribution of carbon across the weld. However, austenitic alloys, such as stainless steels and nickel base filler metals, often contain large amounts of alloying elements that reduce the chemical potential of carbon (Figure 2.2(b)). Consequently, a large drop in the carbon chemical potential over a short distance at the weld interface results in a large thermodynamic driving force for carbon diffusion.

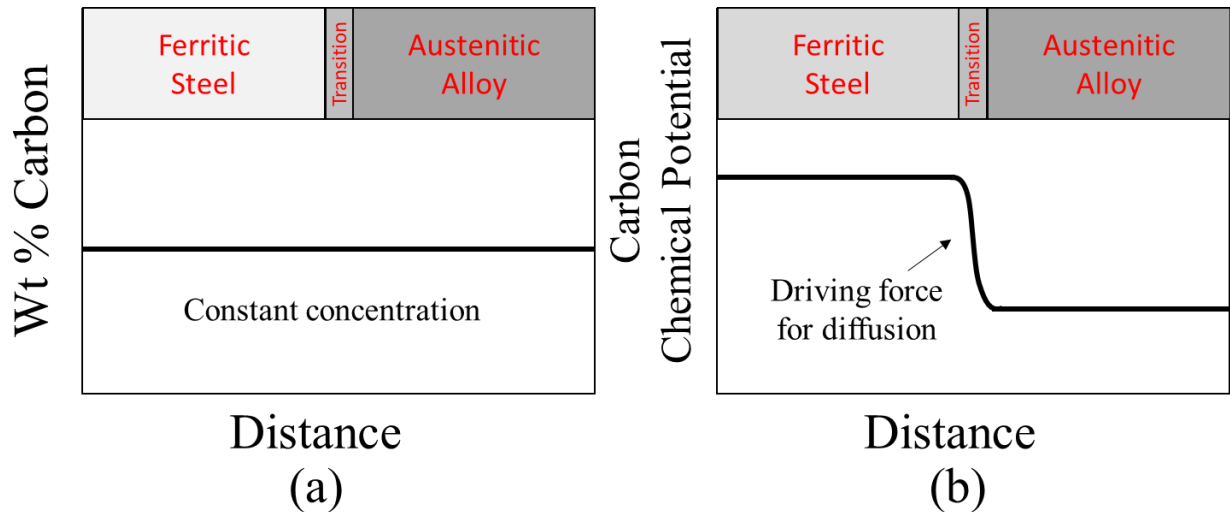


Figure 2.2. Although the carbon concentration is roughly uniform across dissimilar welds between ferritic and austenitic alloys (a), the abrupt changes in chemical composition lead to a large thermodynamic driving force for carbon diffusion (b).

Operating temperature in regions of power generation facilities containing dissimilar welds are typically in the range of 400-600°C [10]. At these temperatures, the diffusion of substitutional alloying elements such as Cr is sluggish, while that of carbon, an interstitial element, is relatively fast [11]. Consequently, the carbon concentration profiles evolve significantly as a function of service time. A carbon concentration profile across a dissimilar weld of 2.25Cr-1Mo steel and

Inconel filler metal taken out of service is shown in Figure 2.3 [12]. The weld was operated in the temperature range of approximately 540-565°C during its lifetime. On the ferritic side of the weld interface, a carbon depleted zone forms, which represents a region where the carbon concentration falls below the initial concentration of the steel. In the austenitic filler metal adjacent to the weld interface, carbon accumulates, and this region is commonly referred to as the carbon enriched zone [4]. In this region, the carbon concentration can often exceed the solubility limit of the alloy, and as a result, various types of carbides form depending on the chemical composition of the alloy.

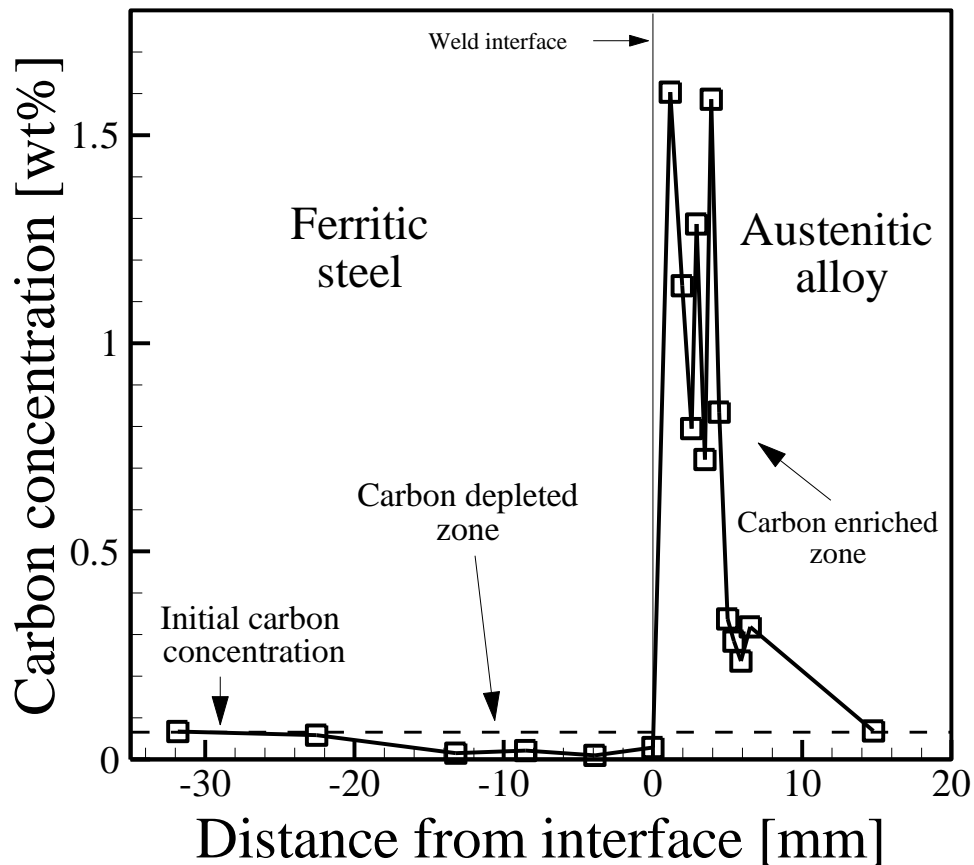


Figure 2.3. The measured carbon concentration profile across a dissimilar weld between 2.25Cr-1Mo steel and Inconel filler metal that was taken out of service. The operating temperature range for this weld was approximately 540-565°C. Data from figure acquired from [12].

Although carbon concentration profile measurements from dissimilar welds placed in service, such as in Figure 2.3, are rather sparse, many efforts have been undertaken to investigate carbon diffusion in laboratory experiments [13-16] and computer simulations [17-19]. The carbon concentration across a dissimilar weld between a ferritic 5Cr-0.5Mo steel and 21Cr-12Ni austenitic in the as-welded condition is shown in Figure 2.4(a). Some fluctuations in the concentration profile

are observed near the fusion line, but the distribution across the weld is roughly uniform. After aging heat treatments at 500°C for 1000 h, large amounts of carbon accumulation are measured in the austenitic alloy adjacent to the weld interface in Figure 2.4(b), similar to the measured profile in Figure 2.3. Although laboratory experiments such as in Figure 2.4 are performed on a time scale of weeks to months, they are often useful for studying the diffusional processes that occur in dissimilar welds over a course of years to decades.

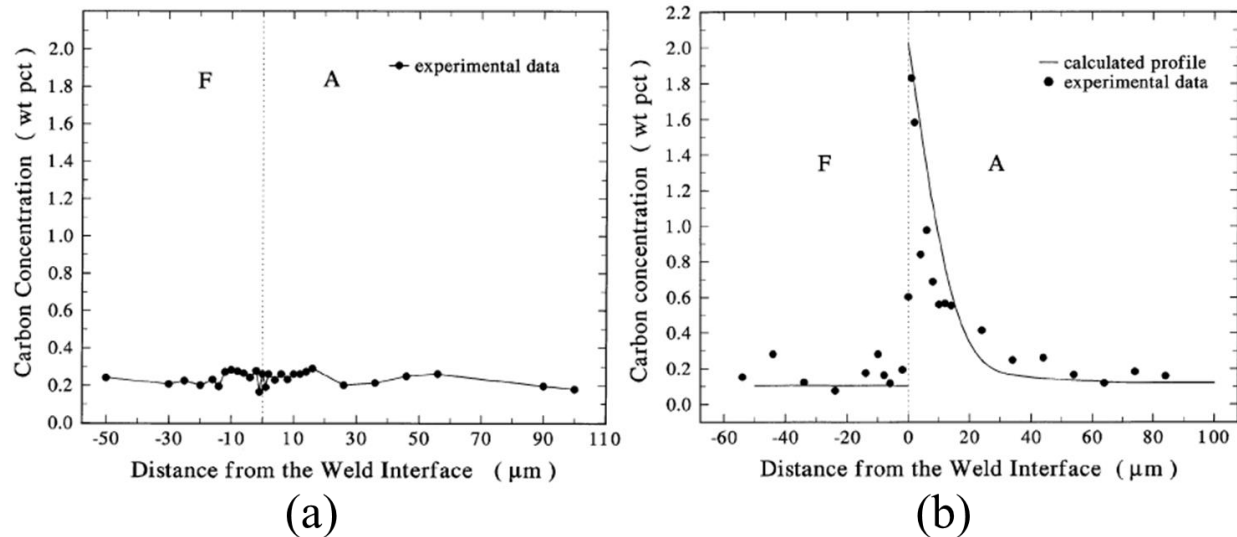


Figure 2.4. A comparison of the carbon concentration profiles in laboratory experiments across a dissimilar metal weld between a 5Cr-0.5Mo ferritic steel and a 21Cr-12Ni austenitic alloy (a) in the as-welded condition and (b) after heat treatment at 500°C for 1000 h [13]. Reprinted with permission from Springer Nature.

Carbon migration can also be analyzed qualitatively through metallographic examination. Chemical etchants can be used to distinguish carbon depleted and carbon rich regions of dissimilar welds under a light optical microscope. Typically, carbon concentration gradients cause contrast in images, where light etching regions typically contain less carbon and dark regions are significantly enriched. For example, the as-welded microstructure in Figure 2.5(a) shows a sharp interface between a ferritic 18MND5 steel and SS309L, and the contrast within each alloy is roughly uniform [14]. After a post weld heat treatment at 610°C for 8 h, a dark band representing carbon enrichment is visible in the austenitic alloy in Figure 2.5(b), while the carbon depleted zone in the ferritic steel etch relatively lightly compared to the remainder of the steel microstructure. Although microscopic techniques do not provide quantitative data, they are an inexpensive alternative for quickly identifying regions of dissimilar welds affected by carbon diffusion.

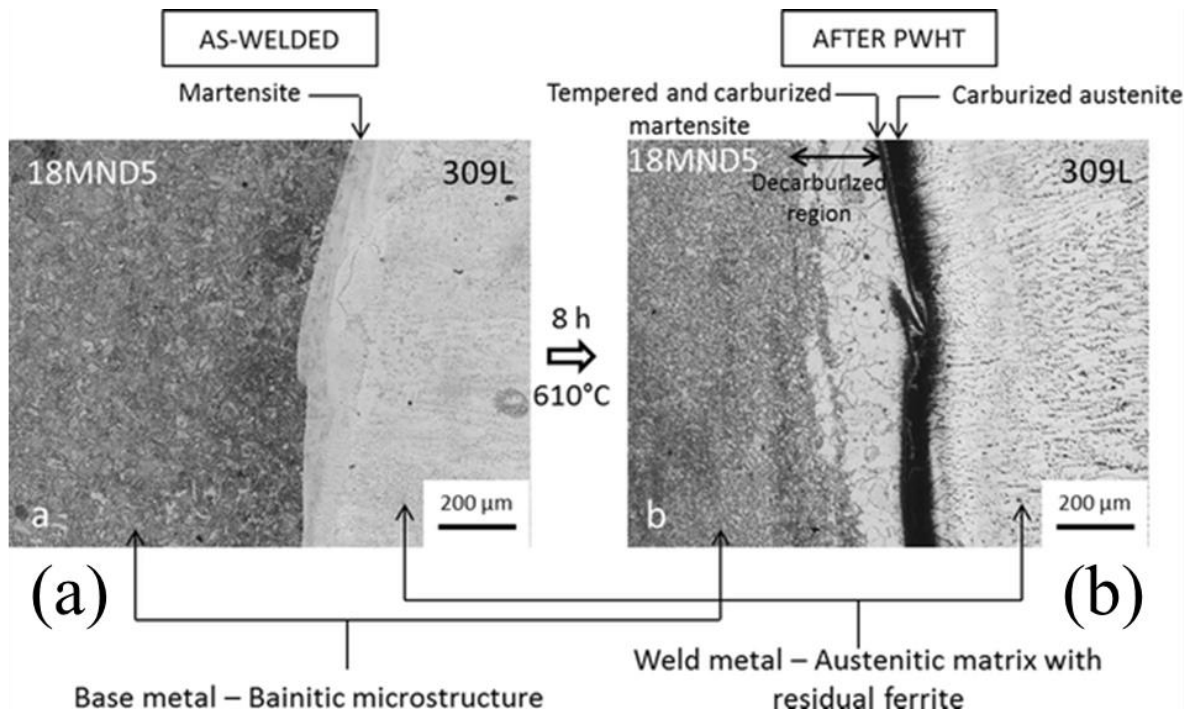


Figure 2.5. Microstructures in a dissimilar weld between 18MND5 ferritic steel and SS309L (a) in the as welded condition and (b) after post weld heat treatment at 610°C for 8 h showing the formation of carbon depleted and enriched zones [14]. Reprinted with permission from Springer Nature.

## 2.1.2 Microstructure and property evolution

### 2.1.2.1 As-welded condition

The microstructures around the weld fusion line between ferritic and austenitic alloys can be complex due to differences in chemical composition and local variations in thermal histories. In ferritic steels, solid-state phase transformations occur in the heat affected zone (HAZ) that affect the phase fractions and grain size. The HAZ is defined here as a region which does not melt during welding, but experiences peak temperatures that can alter the microstructure upon cooling. An example of microstructure evolution for a P91 steel [20] is shown in Figure 2.6. Immediately adjacent to the fusion zone (FZ), the peak temperature remains below the solidus temperature of the steel but remains high enough to induce significant amounts of grain growth. As the peak temperature decreases moving away from the fusion zone, a gradient in grain size results due to the differences in grain growth kinetics. This region is collectively referred to as the coarse grain HAZ (CGHAZ). At the outer boundary of the CGHAZ, the peak temperature reaches a value that causes the recrystallization of new, small austenitic grains. Since the temperature is not high enough to allow for significant grain growth, the grains in this region remain relatively fine, and

this region is called the fine grain HAZ (FGHAZ). The FGHAZ extends until a point is reached where the peak temperature is at the boundary of the two-phase ferrite/austenite region in the phase diagram. The original ferrite grains of the base metal partially transform to austenite within this region, often referred to as the inter-critical HAZ (ICHAZ). Beyond the ICHAZ, the temperatures remain low enough that no phase transformations occur and any grain growth is negligible.

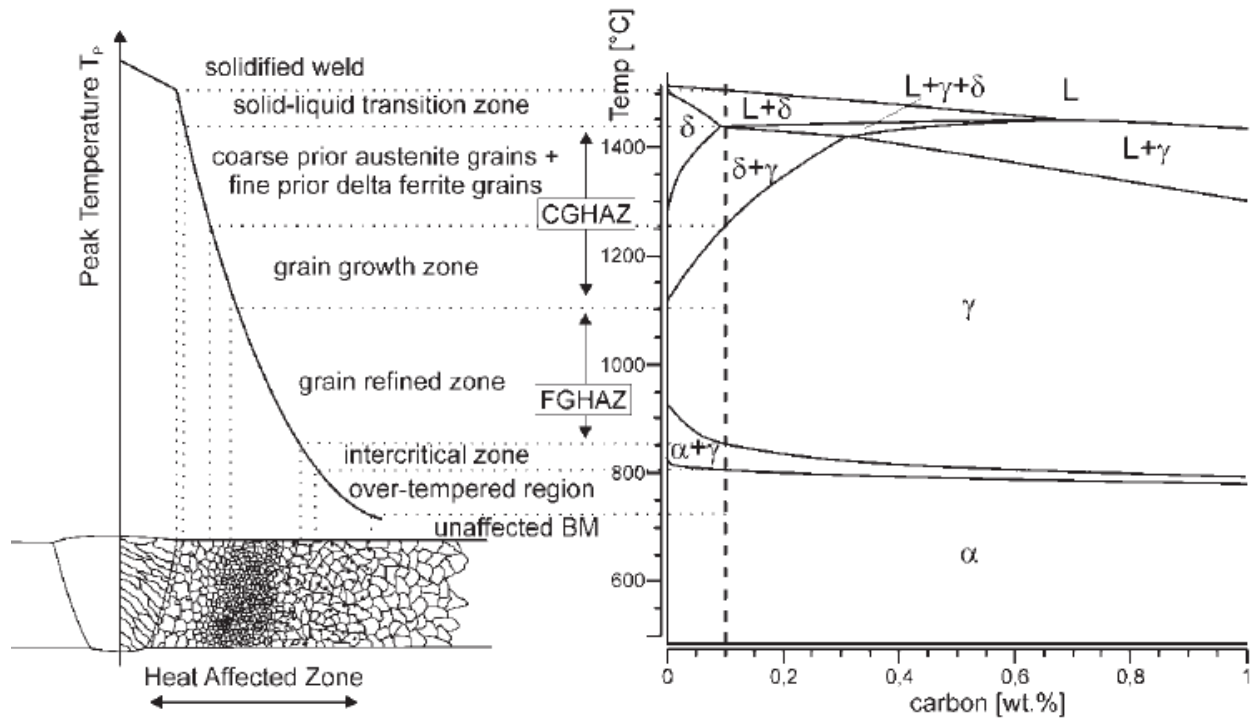


Figure 2.6. A schematic diagram of the different regions of a heat affected zone in a P91 steel with the accompanying approximated phase diagram [20].

The example in Figure 2.6 was described for a P91 steel, however the same concepts apply to many ferritic materials. Optical micrographs of the HAZ in a 2.25Cr-1Mo steel weld using OE-S3 NiMo-1 filler metal are shown in Figure 2.7. These gradients in microstructure in the HAZ of ferritic steels can lead to non-uniform properties. The significant grain growth in the CGHAZ often causes softening due to the Hall-Petch effect [21, 22], which states that a materials strength generally decreases as the grain size increases. The HAZ of ferritic steels is often the region of failure in both similar and dissimilar welds [9, 23, 24]. It should be noted that although gradients in microstructure occur in the HAZ of ferritic steels, the chemical composition remains roughly uniform, and the changes in grain size are caused by local thermal histories during welding.

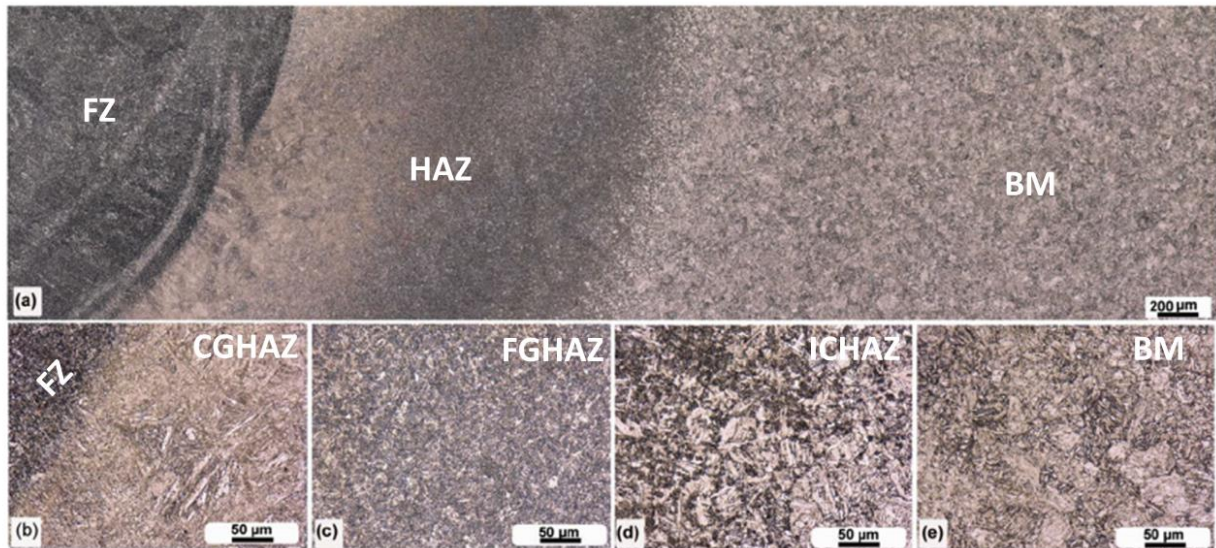


Figure 2.7. The as-welded microstructure of a 2.25Cr-1Mo steel/OE-S3 NiMo-1 filler weld showing (a) the macroscopic view of the FZ, HAZ, and BM, (b) the interface between the FZ and CGHAZ, (c) the FGHAZ, (d) the ICHAZ, and (e) the unaffected BM [25]. Reprinted with permission from Elsevier.

Immediately adjacent to the HAZ of the ferritic steel is the fusion zone, where the melting of material and mixing of alloying elements occurs. The fusion zone can be separated into three distinct regions, namely the partially melted, the partially mixed, and the fully mixed zones. The partially melted zone refers to regions in the ferritic steel where the peak temperature is between the liquidus and solidus temperature of the alloy. In this region, convective flow is negligible, so any changes in chemical composition occur primarily by diffusion processes. Due to the rapid cooling rates during welding, the diffusion distances in the partially melted zone are relatively small, and the chemical composition in this region is similar to the base metal. Similarly, the mixing of alloys is dominated by diffusion in the partially mixed zone, however convective flow also contributes significantly to the mixing of alloying elements. Liquid metal flow driven by Marangoni convection dominates heat and mass transfer in the fully mixed zone [26, 27], resulting in chemical compositions significantly different from either base material.

Martensite formation is common in the partially mixed zone because the mixing of alloying elements increases the hardenability in this region [28]. Regions of martensite are easily identified using microhardness measurements, since the hardness of martensite is typically much higher than ferrite, bainite, and austenite [29]. A microhardness trace across a fusion weld between 2.25Cr-

1Mo steel and SS309L [30] is shown in Figure 2.8. The size of the hardness has an inverse relationship with hardness values, where small indents resist localized plastic deformation resulting in high hardness values. The highest hardness values occur in the partially mixed zone on the austenitic side of the weld interface, which indicate martensite formation. Overall, Figure 2.8 highlights the complexity in property distribution across ferritic to austenitic dissimilar welds, where abrupt variations occur due to the combined effect of changes in chemical composition and microstructure.

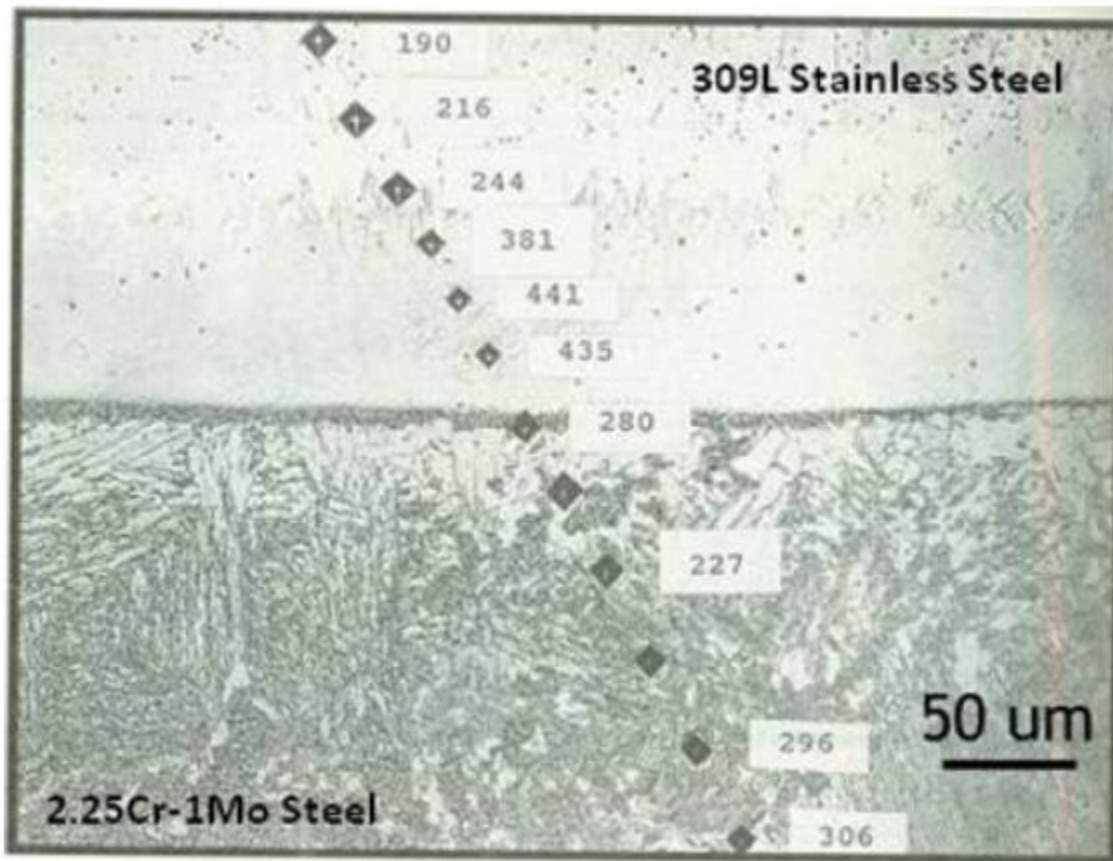


Figure 2.8. A series of hardness indentations across the fusion line of a dissimilar weld between 2.25Cr-1Mo steel and SS309L, where the Vickers hardness values are shown by their respective indents [30].

The overall width of the martensitic regions is dependent on both welding parameters and the type of austenitic alloy or filler metal used. The propensity to form martensite can be most easily evaluated by calculating the martensite start temperature ( $M_s$ ), which indicates the temperature at which the transformation from austenite to martensite begins upon cooling. Many empirical relationships have been established with directly relate chemical composition to  $M_s$  [28,

31-33]. Examples of the calculated martensite distributions across dissimilar welds between a ferritic steel and austenitic alloys SS309L and Inconel® 625 [30] are shown in Figure 2.9. Regions of chemical composition with a martensite start temperature above room temperature are likely to undergo the martensite transformation. From Figure 2.9, a much wider band of martensite is predicted to form in the dissimilar weld using SS309L compared to one using Inconel® 625.

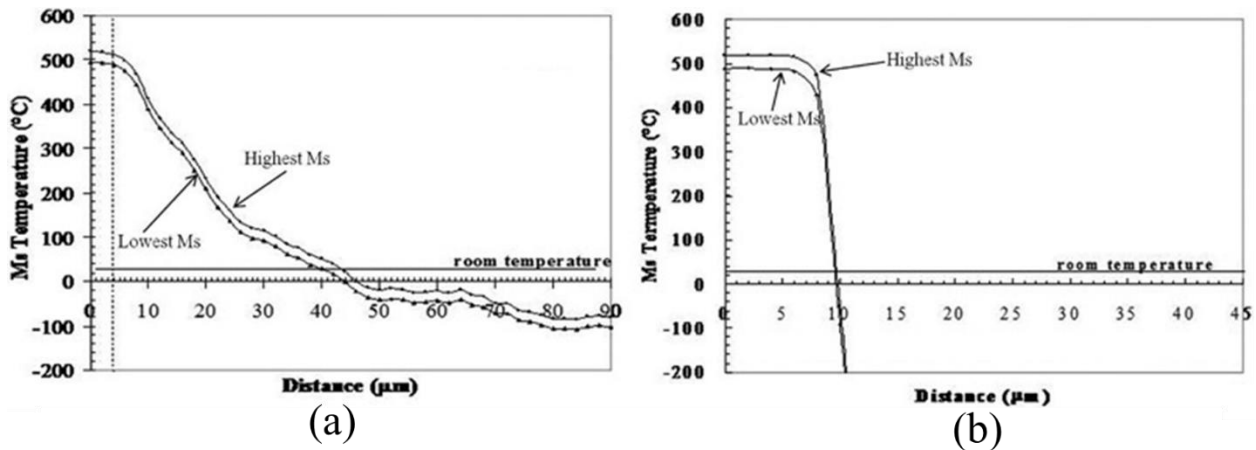


Figure 2.9. Variations in calculated martensite start temperature using measured chemical composition as a function of distance across a weld interface between a ferritic steel and (a) SS309L and (b) Inconel® 625 [30].

#### 2.1.2.2 After heat treatment and aging

Non-uniform heating and cooling coupled with significant differences in thermal expansion coefficients can lead to residual stresses in dissimilar welds in the as-welded condition [34-36]. Post-weld heat treatments are a method to reduce residual stresses at the weld interface that would otherwise contribute to stress concentrations and localized variations in performance [37]. The use of high temperatures can promote carbon diffusion and induce microstructural changes that affect the overall properties of welded joints.

An optical micrograph of a dissimilar weld between 2.25Cr-1Mo steel and SS309L [30] with hardness indentations across the fusion line is shown as an example in Figure 2.10. The dark region at the weld interface corresponds to the carbon-enriched in the austenitic filler metal, which has a significantly higher hardness than surrounding regions in the ferritic steel. Compared to Figure 2.8, the ferritic steel significantly softens after heat treatment in Figure 2.10 due to carbon depletion and grain coarsening. In general, these large gradients in hardness occur over distances of approximately 100 to 200 microns, depending on welding parameters [9].

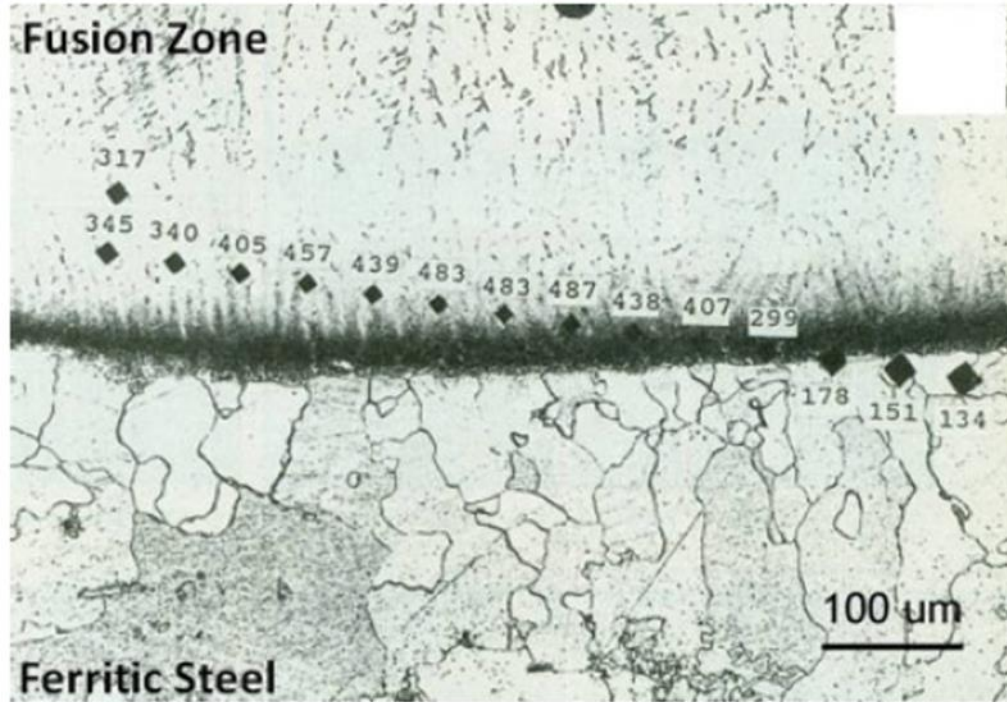


Figure 2.10. Hardness indentations across the fusion line of a dissimilar weld between 2.25Cr-1Mo steel and SS309L after post weld heat treatment at 720°C for 10 h, where the Vickers hardness values are shown by their respective indents [30].

The heat treatment response of dissimilar welds between ferritic and austenitic alloys is dependent on the specific alloy compositions and the time and temperature of the heat treatment. As described in Section 2.1.1, both the driving force for carbon diffusion and the diffusivity of carbon are affected by spatial gradients in chemical composition. Prolonged exposure at high temperatures increase the carbon diffusion flux and contribute to microstructural coarsening. An example of the effects of heat treatment time on the hardness distribution for a clad of SS309L on A508 ferritic steel [15] is shown in Figure 2.11. In the as-deposited condition, an increase in hardness near the fusion line can be attributed to the formation of martensite. When subjected to a heat treatment at 607°C, carbon begins to migrate across the fusion boundary away from the ferritic steel. After 8 hours, carbon-depleted and carbon-enriched zones are clearly observed from the hardness traces. Also, significant softening occurs in both the ferritic and austenitic materials due to grain growth and the annihilation of dislocations. After 20 hours, carbon depletion and microstructural softening become more pronounced, as prolonged exposure allows more time for diffusion.

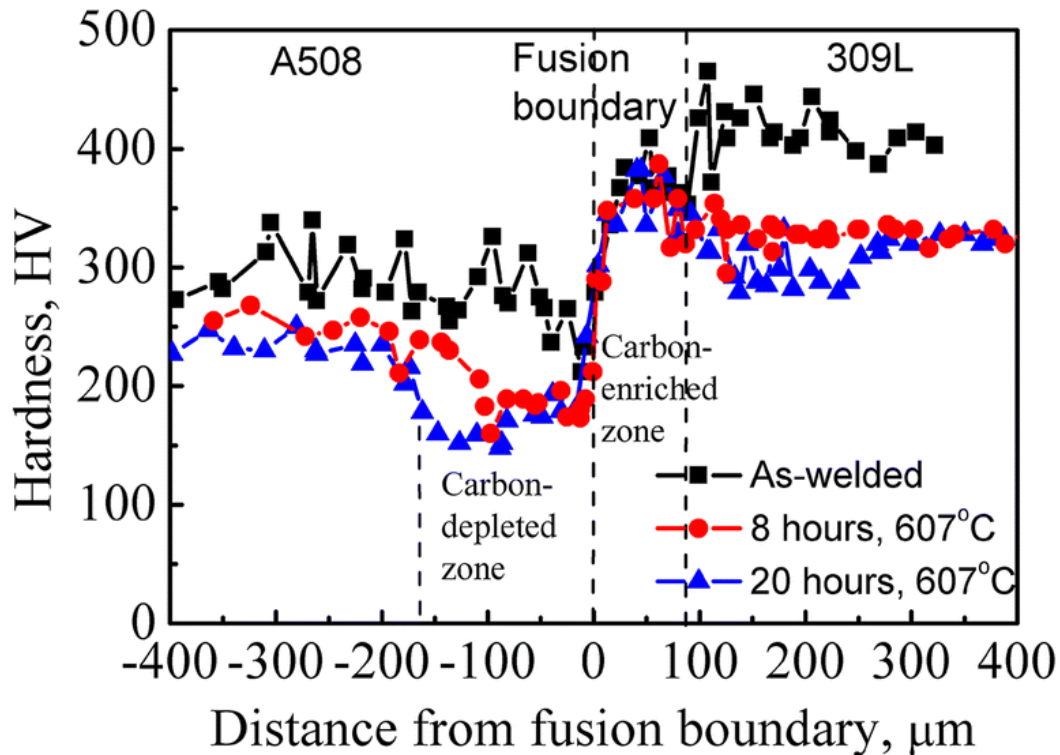


Figure 2.11. Hardness measurements across a dissimilar clad between A508 low alloy ferritic steel and a SS309L after post weld heat treatment at 607°C [15]. Reprinted with permission from Springer Nature.

Like post-weld heat treatments, aging of dissimilar welds leads to microstructural evolution and affects localized and macroscopic properties of the weld. In this context, aging refers to a long-term heat treatment used in laboratory experiments to simulate the microstructural evolution a material will likely experience during service. While post-weld heat treatments are typically conducted at high temperatures for hours, aging is performed at relatively lower temperatures and can last from weeks to months. An example of the effects of aging time at 500°C on the hardness distribution across a dissimilar weld between a ferritic 5Cr-0.5Mo steel and 21Cr-12Ni stainless steel [13] is shown in Figure 2.12. Like post-weld heat treatments, the ferritic steel undergoes significant softening compared to the as-welded condition. On the austenitic side of the weld interface, a hardness peak is measured after 1000 hours, which corresponds to the carbon-enriched zone. Further softening in the ferritic steel and carbon enrichment in the austenitic alloy are measured after an aging time of 20,000 hours. Unlike post-weld heat treatments, however, aging experiments allow for welded materials to undergo important carbide precipitation sequences that influence long-term mechanical properties such as creep [38].

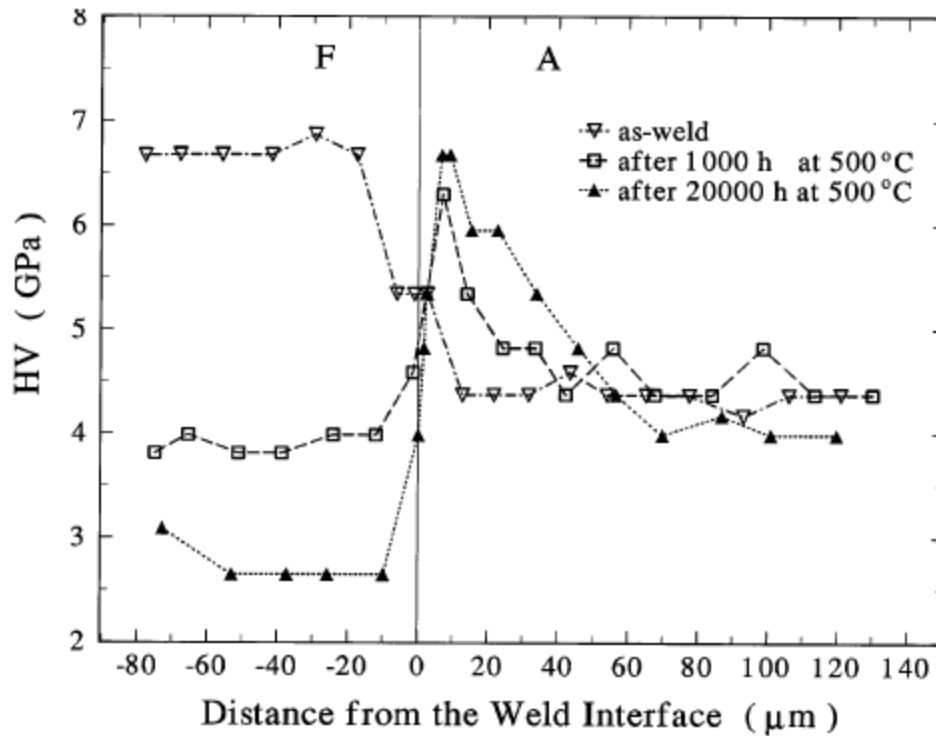


Figure 2.12. The evolution of as-welded microhardness in a dissimilar weld between 5Cr-0.5Mo ferritic steel and 21Cr-12Ni austenitic alloy after aging at 500°C [13]. Reprinted with permission from Springer Nature.

Carbon diffusion and the resulting evolution of microstructure and hardness can deteriorate the performance of dissimilar welds after prolonged exposure to high temperature. The depletion of carbon on the ferritic side of the weld interface results in a locally weak region. The long-term mechanical behavior of dissimilar welds can be evaluated by their creep properties when compared to the properties of the wrought parent materials. The detrimental effects of carbon diffusion in dissimilar welds are manifested in Figure 2.13, which compares the creep strength and time to rupture of a dissimilar weld between 2.25Cr-1Mo steel and Alloy 800 (solid square) to a 2.25Cr-1Mo base material (open circle) and a 2.25Cr-1Mo/2.25Cr-1Mo weld (open triangle) [39]. Up to approximately 1000 hours, the dissimilar weld behaves in a similar manner to the reference materials, as the stress-time to rupture curve lies between the wrought and welded base material. However, a sharp drop in the creep performance occurs after this point, and the properties of the dissimilar weld quickly deteriorate while those of the base and similar weld display consistent behavior. After about 1000 hours, the dissimilar weld can only accommodate a fraction of the applied stress for a constant time to rupture. It is important to note that the results of these

laboratory are particularly concerning because simple extrapolation to times of approximately  $10^5$  hours indicate that dissimilar welds can accommodate only small stress levels ( $\sim 10$  MPa).

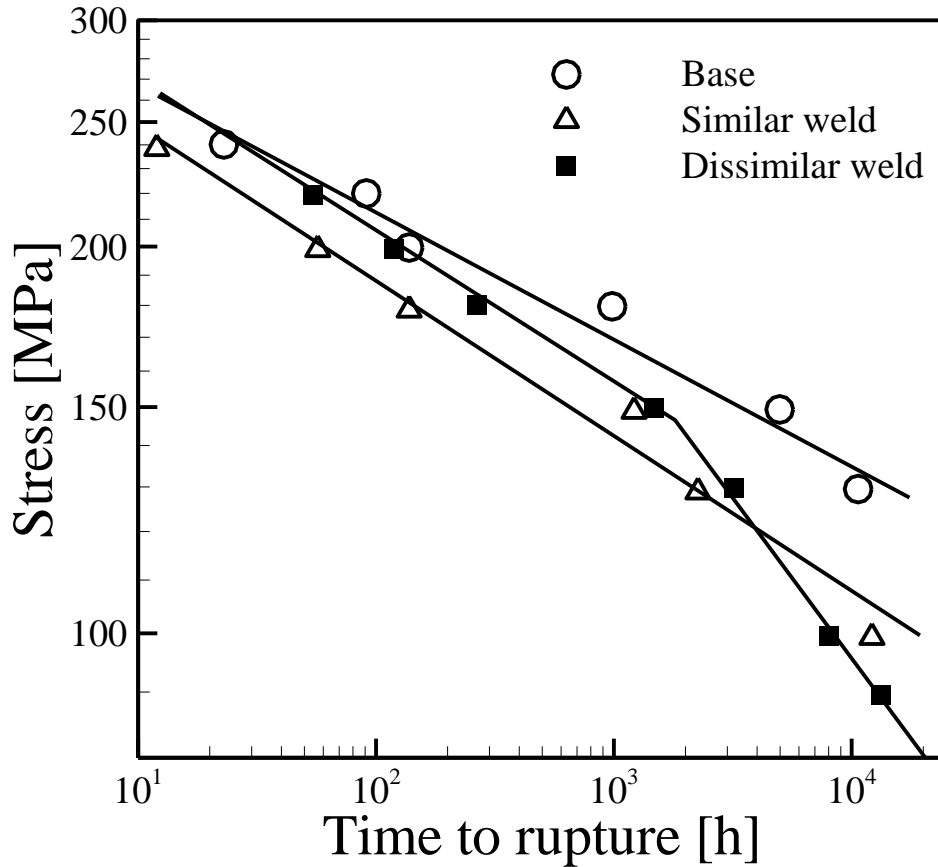


Figure 2.13. A comparison of creep testing results on 2.25Cr-1Mo steel (Base), a 2.25Cr-1Mo steel/2.25Cr-1Mo steel weld (Similar weld), and a 2.25Cr-1Mo steel/Alloy 800 weld (Dissimilar weld). Reproduced from [39] with permission from Elsevier.

The results in Figure 2.13 indicate that the overall creep rupture strength is affected by carbon diffusion and the non-uniform distribution of properties. However, time-to-rupture creep tests do not generally provide information on the localized deformation in the welded joint. Early work [39] to study localized plastic deformation during creep tests introduced periodically-spaced indentations across the weld interface as markers. The distance between each marker could then be measured at various times after interrupting testing using optical techniques. An example of results obtained by this technique is shown in Figure 2.14, where the local strain is plotted as a function of location around the weld interface. For all times, the strain is highly localized in the HAZ of the ferritic steel next to the weld interface. This region experiences enough strain to initiate and propagate cracks that eventually lead to rupturing after 1350 hours. The tendency of dissimilar

welds between ferritic and austenitic alloys to fail on the ferritic side of the weld interface is well-documented and has shown consistency in results [39-44].

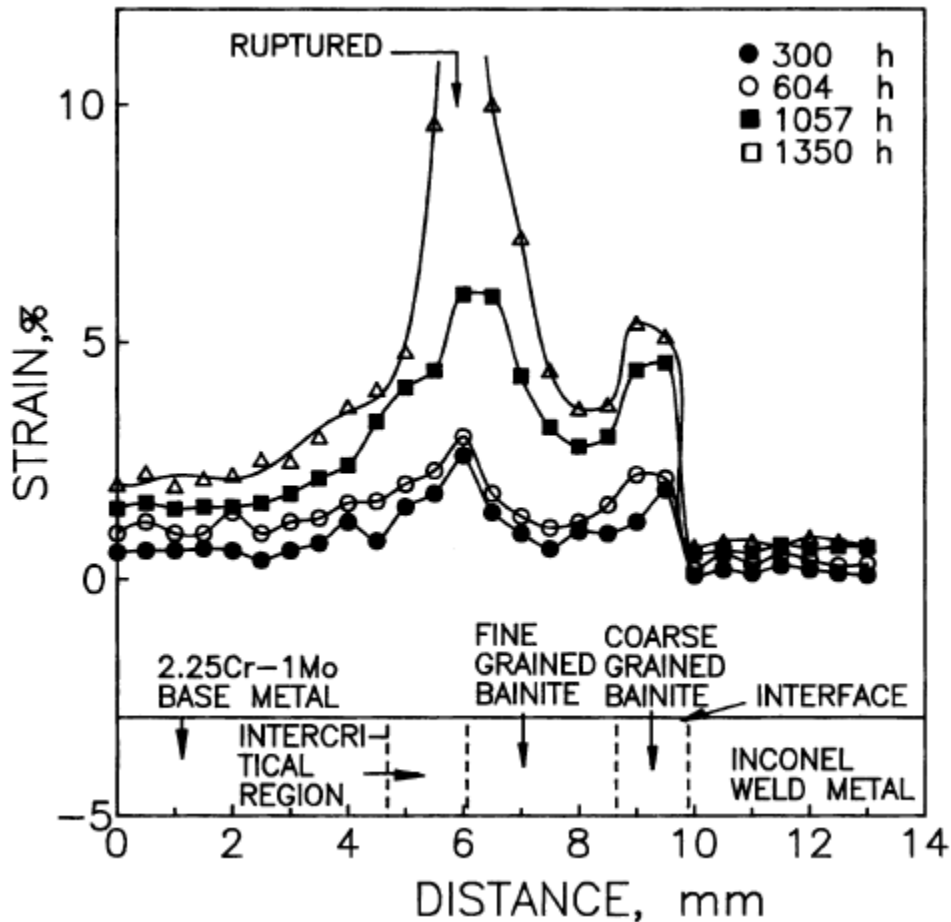


Figure 2.14. The distribution of strain across a dissimilar weld between 2.25Cr-1Mo steel and Alloy 800H using IN82 filler metal at different times during creep testing [39]. Reprinted with permission from Springer Nature.

More recent techniques for measuring localized plastic deformation have utilized digital image correlation, which tracks the motion of individual spots in a speckled pattern of paint introduced to the sample surface using a digital camera. Subramanian et al. [45] used this technique to measure heterogeneous deformation during creep testing of a dissimilar weld between 2.25Cr-1Mo steel and Alloy 800H. Prior to aging, the welds were aged at 600°C for up to 4000 hours to simulate a material that has been placed in service. Consistent with Figure 2.14, the plot in Figure 2.15 shows that strain is highly localized in the HAZ of the ferritic steel, which is located adjacent to the weld fusion zone. Only small amounts of deformation were measured in the austenitic filler metal and alloy.

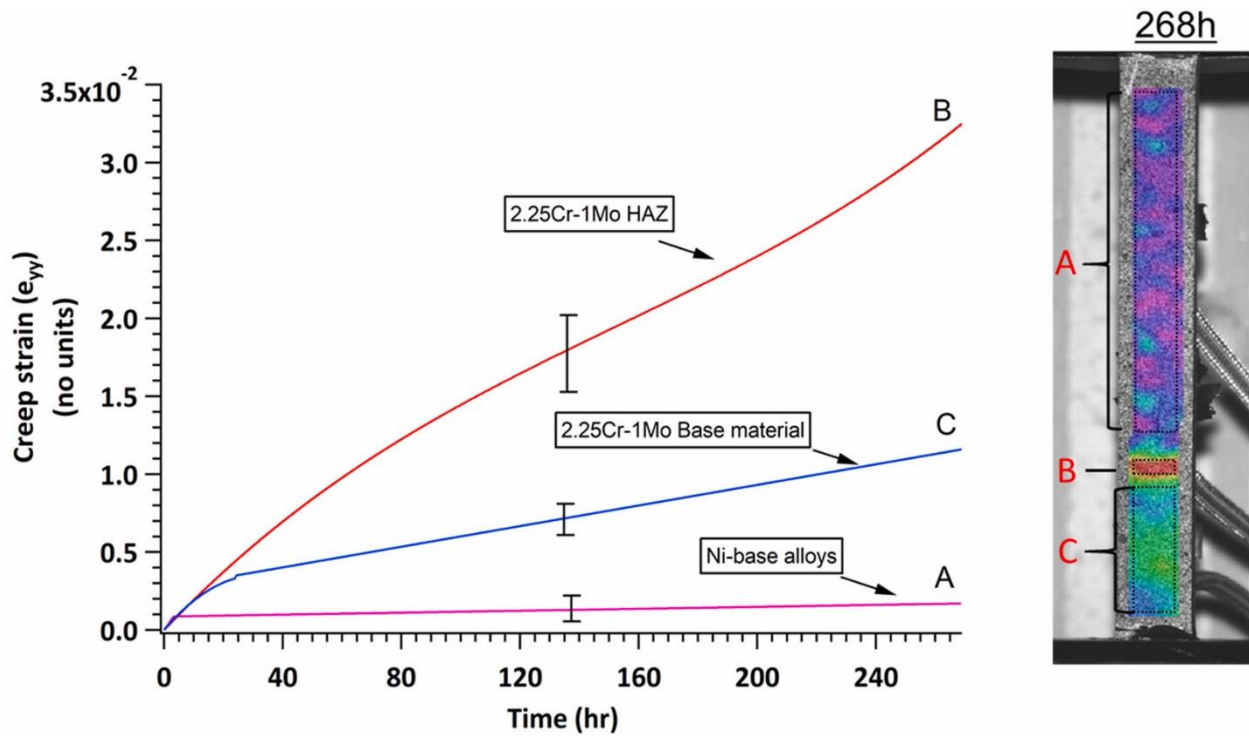


Figure 2.15. The localized creep strain measured by digital image correlation in a dissimilar weld between 2.25Cr-1Mo steel and Alloy 800H aged at 600°C for 4000 h during an accelerated creep test at 625°C and 50 MPa [45]. Reprinted with permission from Elsevier.

### 2.1.3 Summary

The microstructure and property distributions across dissimilar welds between ferritic and austenitic alloys are highly non-uniform, which originate from large differences in chemical composition over a short distance. Gradients in alloying elements lead to a driving force for carbon diffusion away from the ferritic steel when welds are subjected to high temperatures. Carbon migration often leads to softening of the ferritic steel due to carbon depletion, and it hardens the austenitic side of the fusion line as a result of carbon enrichment. The gradients in carbon concentration across the weld fusion line result in abrupt variations in microhardness, and these variations can be exacerbated by other effects such as grain coarsening and martensite formation. After prolonged exposure at high temperatures, differences in chemical composition and microstructure lead to non-uniform, highly localized deformation when the weld is under static load, such as in creep testing. Much of the deformation occurs in the HAZ of the ferritic steel, which coincides with the soft, carbon depleted, coarse-grained region next to the weld interface. Consequently, these areas of relatively low strength are susceptible to large amounts of deformation and favorable locations for crack nucleation and growth and ultimately weld failure.

## 2.2 Background of functionally graded materials and additive manufacturing

A potential solution for overcoming metallurgical challenges associated with dissimilar welds is to eliminate abrupt changes in chemical composition and microstructure by replacing the welds with functionally graded materials. Additive manufacturing is an attractive fabrication technique for producing functionally graded materials with tailored composition profiles. In this section, a brief background is given on functionally graded materials, additive manufacturing process, and literature examples of additively manufactured functionally graded materials.

### 2.2.1 Overview of functionally graded materials

Functionally graded materials (FGMs) are a class of advanced materials with spatial variations in chemical composition, microstructure, density, or porosity engineered to achieve site-specific properties and enhanced performance [46]. The costs of manufacturing FGMs are typically higher than conventional materials, making them useful in applications where the properties of traditional materials are not adequate. A primary goal of FGMs is to eliminate abrupt changes in properties between two or more materials that would result from direct joining using processes such as welding. In contrast to materials with unintended heterogeneities as the result of processing, the spatial variations of composition, structure, or properties in FGMs are fully intended and engineered to achieve a specific function.

The control of the spatial variation of properties in FGMs is highly dependent on the feature of the material that is being graded, as well as the manufacturing method. In layer-wise fabrication methods, such as thin film deposition [47], ultrasonic consolidation [48], or additive manufacturing [49-51], the variation in properties is step-wise and is determined by the thickness of the layer of material. In contrast, diffusion-based processes, like diffusion bonding [52], can achieve variations near the atomic scale and can be viewed as macroscopically continuous. A schematic illustration of the types of property variation and examples of features that can be graded is shown in Figure 2.16 [51]. Note that FGMs can be manufactured from single material systems by controlling site-specific features like grain size and orientation, as well as multi-material systems by grading composition, phases, or particle density.

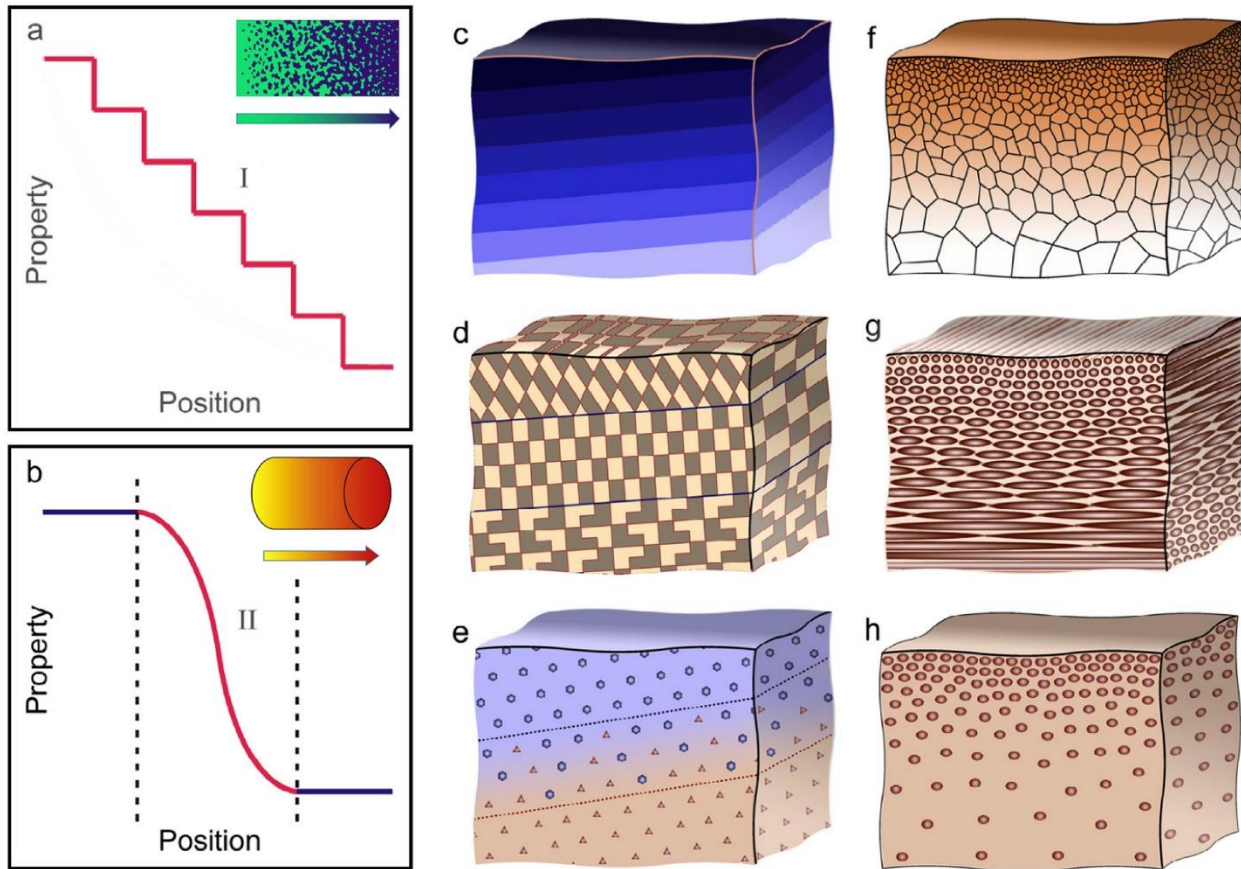


Figure 2.16. Functionally graded materials can have (a) a stepwise or (b) smooth variations in properties as a function of location. The changes in properties in can result from variations in (c) composition, (d) grain orientation, (e) secondary phase fraction, (f) grain size, (g) fiber length and orientation, or (h) particle density [51]. Reprinted with permission from Elsevier.

A classic example of FGMs used in engineering applications is the carburization of steels. In the carburization process, iron alloys are subjected to a controlled, carbonaceous gas environment that allows for carbon to diffuse into the alloy. Since the hardness of steels is directly related to carbon concentration [29], the purpose of carburization is to harden the surface of a part while maintaining the toughness steel underneath. An optical micrograph of a carburized duplex stainless steel with hardness indents is shown in Figure 2.17 as an example [53]. After carburization, high concentrations of carbon at the surface of the steel lead to high hardness, and the spatial variation in hardness as distance from the surface increases is proportional to the carbon concentration gradient. The temperature and time of carburization can be controlled to produce desired hardness variations, usually over distances a few millimeters. Many steel gears are carburized to improve wear resistance without embrittling the alloy.

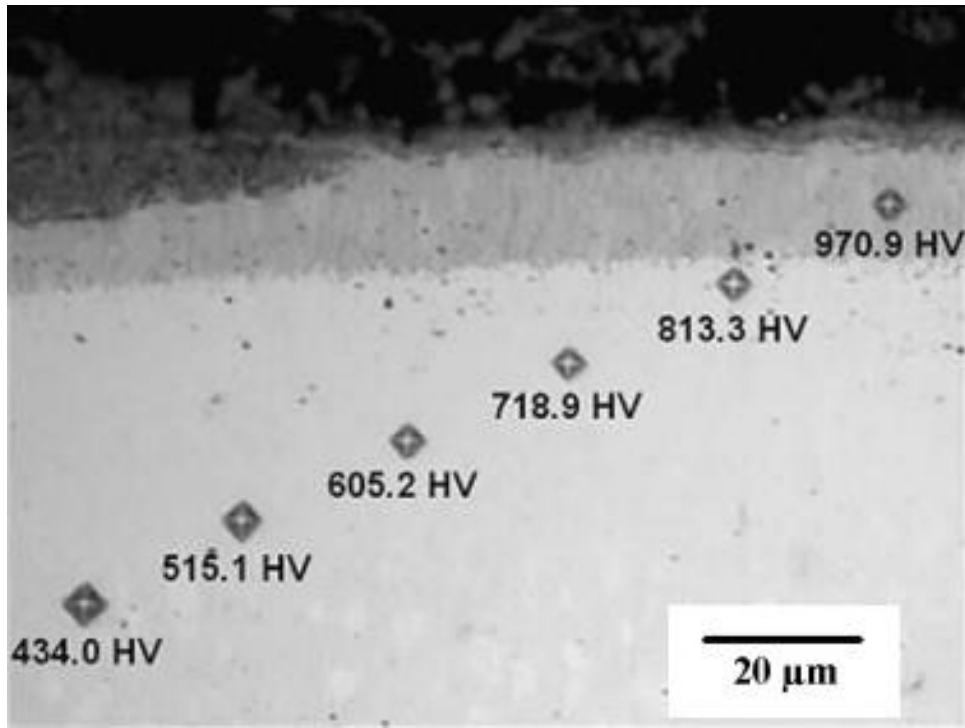


Figure 2.17. The variation in hardness of a carburized duplex stainless steel due to a gradient in carbon concentration, where high hardness corresponds to high carbon concentration [53].

Conventional methods for manufacturing FGMs vary depending on the designed application, material system, and overall length scale of gradient in properties [51]. Gaseous-based techniques, such as chemical vapor deposition, are particularly useful for controlling chemical composition in thin films and coatings [54], although the scale of these FGMs is typically limited to tens of microns. Liquid-phase processes like centrifugal casting [55] are capable of manufacturing bulk composite materials, although the types of gradients are often limited to secondary phases or particles. Other examples of manufacturing techniques include thermal spray [56], directional solidification [57], and powder metallurgy [58].

### 2.2.2 Types of additive manufacturing processes

For metallic components, AM processes generally fall into two main categories depending on the delivery method of the feedstock material. A schematic diagram of the different types of AM processes is shown in Figure 2.18. Powder bed fusion (PBF) consists of spreading a fine layer of powder material across a substrate with a recoating blade or roller. The powder feedstock remains stationary while a heat source is scanned along predefined paths to produce the desired part in a layer-by-layer manner. In directed energy deposition (DED) AM, either powder or wire

feedstock is delivered coaxially with the heat source into a molten pool. In contrast to PBF, the feedstock delivery system moves with the heat source in DED processes. Types of heat sources commonly used include lasers (L), electron beams (EB), plasma arcs (PA) and gas metal arcs (GMA). A distinction between individual studies will be made by defining the specific AM process and type of heat source. For example, a laser based DED process is designated as DED-L. There is a wide range of process parameter combinations used in different AM processes that determine the structure and properties of fabricated components.

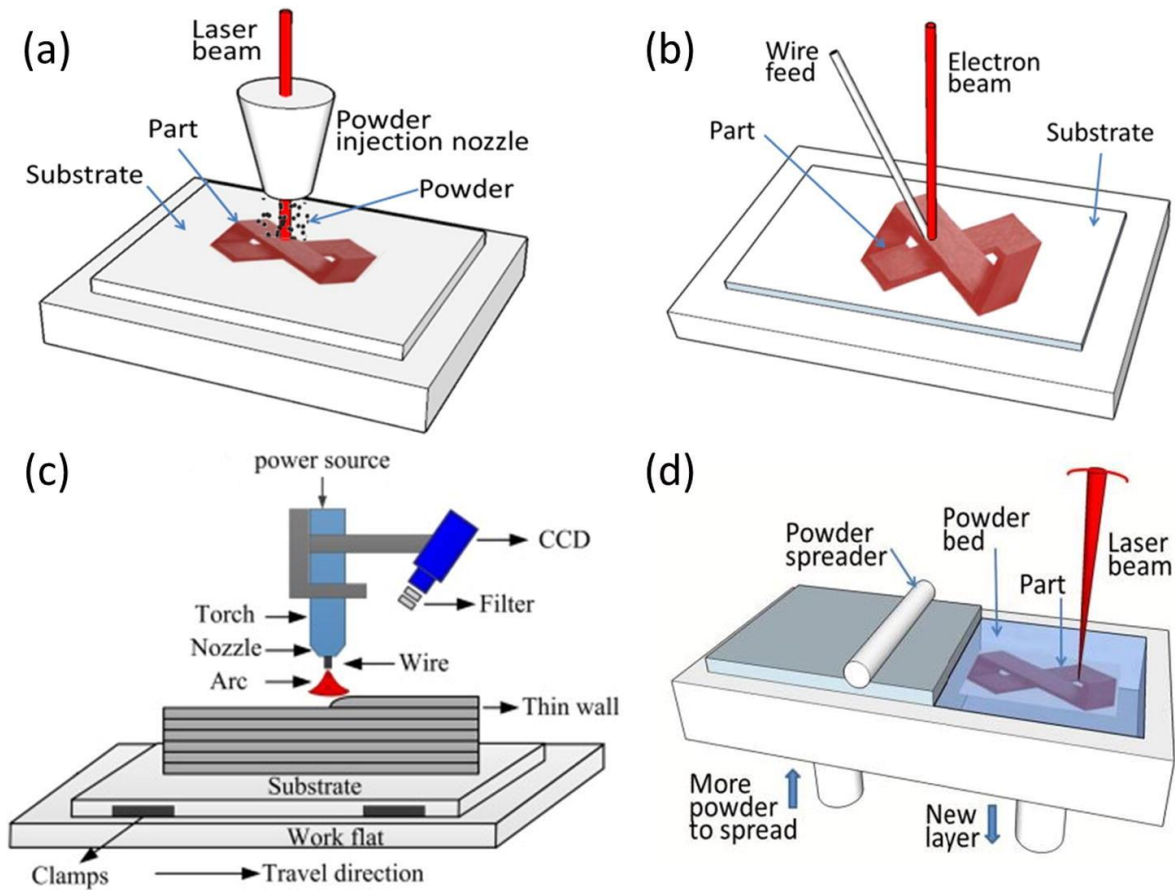


Figure 2.18. Schematic illustration of the different types of AM processes used for fabricating metallic components, including (a) DED-L, (b) DED-EB, (c) DED-GMA [59], and (d) PBF-L [60].

The different AM processes are compared in Table 2.2, which considers typical parameters used, the volume of material deposited, speed of production, and the need for post-processing. In general, PBF processes are used to fabricate intricate parts with high spatial resolution, while DED processes are more targeted towards manufacturing at a relatively larger scale. Although lasers and electron beam heat sources can reach speeds of 1-10 m/s, the overall production time for PBF is relatively high due to small layer thicknesses and beam sizes. The heat sources in DED, namely

electron beams and arcs are designed to deposit large amounts of material to decrease production time.

Table 2.2. A comparison between AM processes and their characteristics [60].

Process	DED			PBF	
	Powder	Wire		Powder	
Heat source	Laser	E-beam	Electric arc	Laser	E-beam
Nomenclature	DED-L	DED-EB	DED-PA/ DED-GMA	PBF-L	PBF-EB
Power (W)	100 to 3000	500 to 2000	1000 to 3000	50 to 1000	
Speed (mm/s)	5 to 20	1 to 10	5 to 15	10 to 1000	
Max. feed rate (g/s)	0.1 to 1.0	0.1 to 2.0	0.2 to 2.8	–	
Max. build size (mm x mm x mm)	2000 x 1500 x 750	2000 x 1500 x 750	5000 x 3000 x 1000	500 x 280 x 320	
Production time	High	Medium	Low	High	
Dimensional accuracy (mm)	0.5 to 1.0	1.0 to 1.5	Intricate features are not possible	0.04 to 0.2	
Surface roughness ( $\mu\text{m}$ )	4 to 10	8 to 15	Needs machining	7 to 20	
Post processing	HIP and surface grinding are seldom required	Surface grinding and machining is required to achieve better finish	Machining is essential to produce final parts	HIP is rarely required to remove the porosities	
References	[61-66]	[67-70]	[59, 71-73]	[74-77]	

### 2.2.3 Functionally graded materials in additive manufacturing

Additive manufacturing (AM) technologies offer an attractive way for producing FGMs in which the chemical composition [78, 79], part density [80], and process parameters [81] can be changed to alter the microstructure and properties with high levels of spatial resolution. Some AM processes are more suitable for various types of FGMs than others depending on the material delivery method and intricacy of the designed parts. A summary of different types of metallic FGMs is given in Table 2.3. In most cases, FGMs fabricated by AM can be classified as either single material or multi-material.

### 2.2.3.1 Single material functionally graded materials

A single material FGM uses only one type of feedstock for fabrication, and the material is not altered during the AM process. In these types of FGMs, process parameters like energy input or scan strategy are varied to manipulate local microstructures. The PBF-L and some DED-L processes are common AM technologies for fabricating single material FGMs because process parameters can be varied quickly, and relatively high dimensional accuracy can be achieved in parts. Features such as grain structure, density or porosity, and crystallographic texture can be graded using PBF-L systems, provided prior knowledge correlating process parameters and material behavior is obtained.

A useful, high-demand application for single material FGMs can be found in the medical industry for producing prosthetics and implants that are customized for individual patients. An example of a titanium hip implant fabricated using DED-L is shown in Figure 2.19 [82]. Gradients in porosity, which are controlled by varying the scan strategy, are used to alter the local density of the orthopedic implant. The designed variation in porosity allows for bone growth while providing load-bearing support. The use of AM to fabricate graded porous structures for biomedical applications is an active area of interdisciplinary research [83-86].

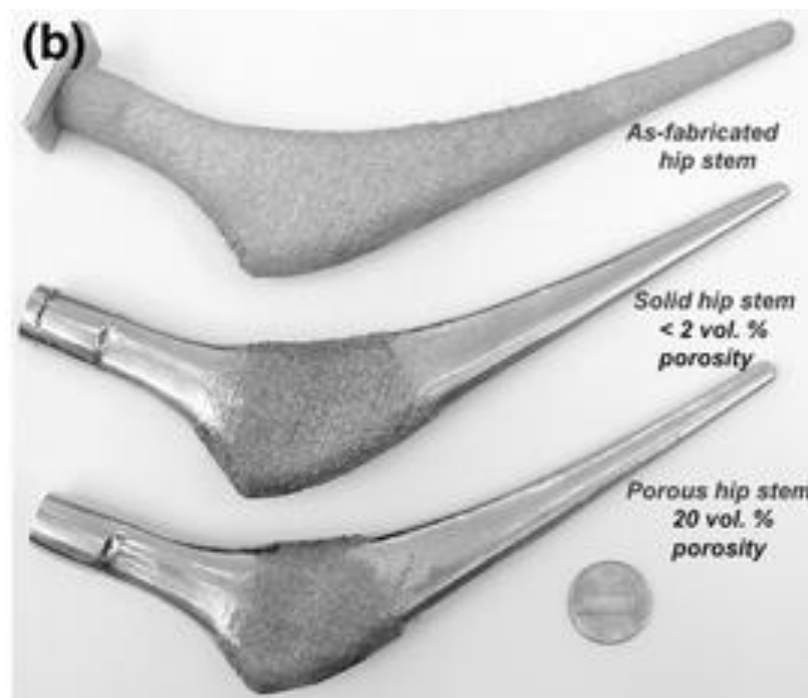


Figure 2.19. Prosthetic hip implants made of titanium fabricated by DED-L with designed variations in porosity [82].

Table 2.3. A summary of functionally graded material systems fabricated by additive manufacturing.

Material system	Process	Feedstock	Heat source	Gradient	Ref.
Inconel® 718	PBF	Powder	Laser	Grain size	[87]
17-4PH SS	PBF	Powder	Laser	Magnetism	[88]
CoCrMo	PBF	Powder	Laser	Porosity	[89]
Titanium	DED	Powder	Laser	Porosity	[82]
Ti-6Al-4V to Invar	DED	Powder	Laser	Composition	[90]
Ti-6Al-4V to V to SS304L	DED	Powder	Laser	Composition	[91]
V to Invar	DED	Powder	Laser	Composition	[92]
Ti to V & Ti to Mo	DED	Powder	Laser	Composition	[93]
SS304L to IN625	DED	Powder	Laser	Composition	[79]
Grade 22 steel to In82	DED	Wire	Arc	Composition	[94]
Grade 22 steel to P87	DED	Wire	Arc	Composition	[94]
Grade 22 steel to 347H	DED	Wire	Arc	Composition	[94]
Pure Ti with N <sub>2</sub> gas	DED	Powder	Laser	Composition	[95]
SS316L to Zr	DED	Powder	Laser	Composition	[96]
SS410 to Ni to Zr	DED	Powder	Laser	Composition	[96]
SS410 to V to Ti to Zr	DED	Powder	Laser	Composition	[96]
SS410 to Cu to Zr	DED	Powder	Laser	Composition	[96]
P21 steel to SS316L	DED	Powder	Laser	Composition	[97]
Fe-Ni-Cr	DED	Powder	Laser	Composition	[98]
Ti to Ti-6Al-4V	DED	Powder	Laser	Composition	[99]
Ti-6Al-4V to Mo	DED	Powder	Laser	Composition	[100]
Ti-6Al-4V to IN718	DED	Powder	Laser	Composition	[101]
SS410 to SS316L	DED	Powder	Laser	Composition	[102]

Popovich et al. [87] have demonstrated that single material FGMs can also be useful for applications involving high temperature structural materials. Figure 2.20 shows an electron backscatter diffraction image of the grain structure of an Inconel® 718 part fabricated by PBF-L in which specific locations have distinct differences in grain size and orientation. The grain

structure was manipulated by adjusting laser power, scanning speed, hatch spacing, beam diameter, and layer thickness, all of which affect the molten pool geometry, heat transfer and fluid flow, solidification parameters, and grain nucleation and growth [60]. Fine equiaxed grain regions were achieved using low laser powers and fast scanning speeds, while the opposite was used for large, textured columnar grains. The differences in grain structure were shown to cause non-uniform strain distributions during tensile testing, which can be most easily described by the Hall-Petch relation [21, 22].

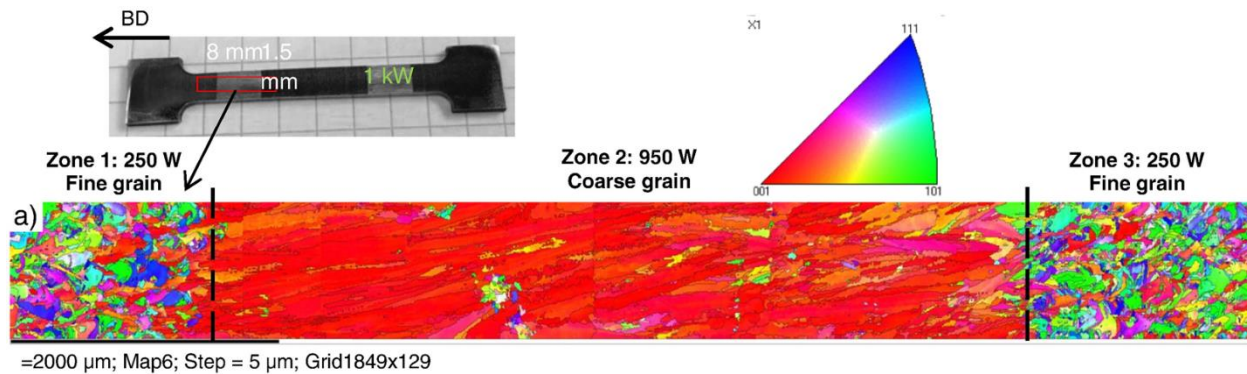


Figure 2.20. A gradient in grain structure and orientation was fabricated by Popovich et al. [87] by changing the laser power in selected regions of an Inconel® 718 part fabricated by PBF-L as shown by the electron backscatter diffraction image.

### 2.2.3.2 Multi-material functionally graded materials

The most common AM process for tailoring composition gradients is DED-L using powder feedstock. The flow rates of different alloy powders can be adjusted such that volume fractions of each feedstock entering the molten pool yield desired chemical composition variations [103]. A schematic diagram of the process is shown in Figure 2.21, which represents a hypothetical composition gradient between Alloys ‘A’ and ‘B’ [104]. In most cases, FGMs such as the one depicted in Figure 2.21 grade composition along the build direction in a layer-by-layer manner. Therefore, the variations in chemical composition generally correspond to roughly the layer thickness, which can range from hundreds of microns to millimeters for DED processes.

Many different material systems have been used to fabricate FGMs using AM, and Table 2.3 shows a summary of previous work. When designing a deposition plan for compositionally graded alloys, the physical properties of the material systems should be carefully considered. Since maintaining a roughly constant molten pool volume during fabrication is a good strategy for controlling build dimensions, the material density of each material plays a crucial role in the design

of FGMs. When two materials with similar density are to be used in a FGM, changes in the mass fraction of each powder entering the molten will not significantly change the molten pool volume as long as the overall mass entering the pool remains constant. Therefore, mass fractions are often used to control the gradients of material systems involving iron and nickel alloys, which have similar densities ( $\sim 7$  to  $8 \text{ g/cm}^3$ ). In contrast, volume fractions are used to control the layer-by-layer material variations for alloys with significantly different densities, such as FGMs involving titanium ( $\sim 4 \text{ g/cm}^3$ ) and nickel alloys, for example. Increments of weight or volume fractions for FGMs fabricated by DED-L have been reported ranging from 3 to 50% [79, 90, 105].

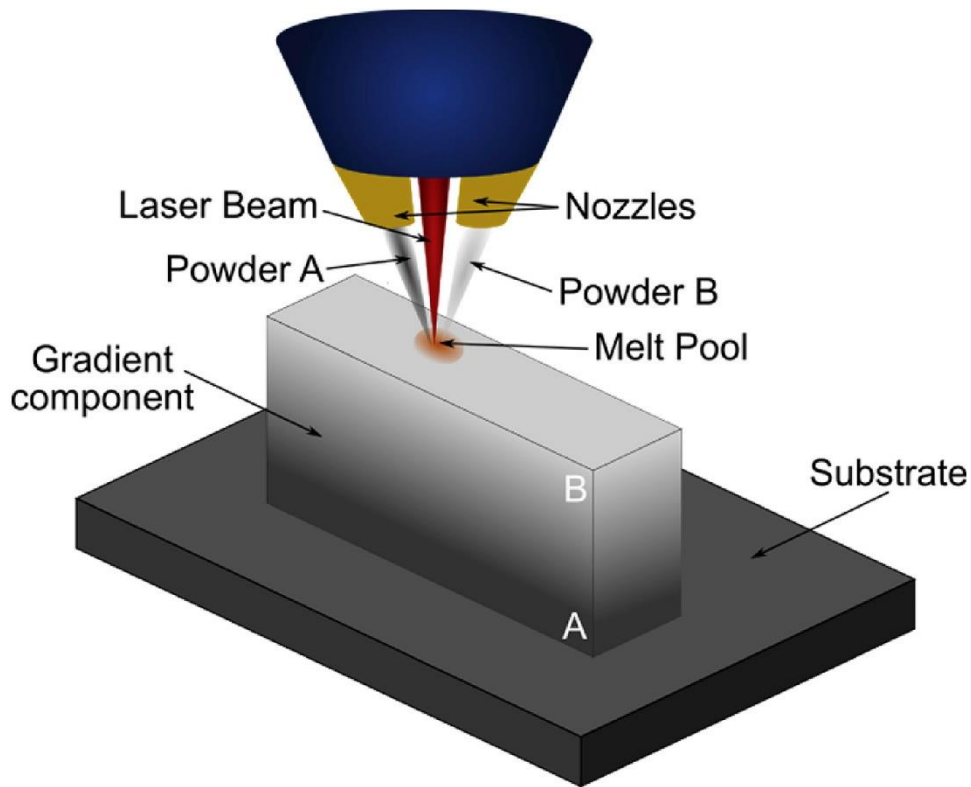


*Figure 2.21. Schematic description of a DED-L processes used for the fabrication of a compositionally graded alloy where powders of Alloy A and B are blown into a melt pool at different feed rates along the build height [104]. Reprinted with permission from Elsevier.*

The types of materials used in metallic FGMs often determine the gradient in the property distribution. While macroscopically smooth gradients in chemical composition are often achieved, both smooth and abrupt changes in properties, namely hardness, have been reported, and two examples are shown in Figure 2.22. In a FGM between SS304L and Inconel® 625 [79], the change in microhardness across the gradient roughly follows a rule-of-mixtures type relation between the

hardness of each end member alloy. In contrast, abrupt variations in microhardness were reported in a FGM between Ti-6Al-4V and Invar 36 [90], although the change in chemical composition was largely monotonic. The microhardness variations could be attributed to the changes in microstructure. The FGM between SS304L and Inconel® 625 largely consisted of a single solid solution strengthened matrix phase while heterogeneous distributions of different brittle intermetallic compounds were characterized in the Ti-6Al-4V to Invar 36 material system.

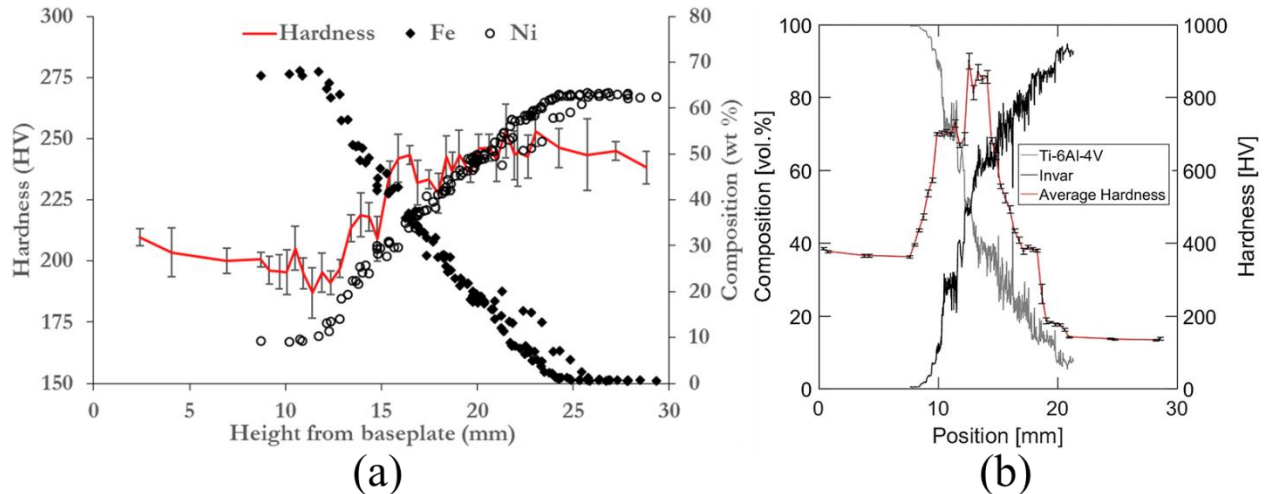


Figure 2.22. The composition and hardness variations as a function of distance from the baseplate in FGMs fabricated by DED-L for (a) SS304L to Inconel® 625 [79] and (b) Ti-6Al-4V to Invar [90]. Reprinted with permission from Elsevier.

### 2.3 Factors affecting properties of additively manufactured materials

The properties and serviceability of additively manufactured components depend on their chemical composition, microstructure, properties and defects. Literature data on some mechanical properties such as the yield strength of additively manufactured components often show significant scatter that can mostly be attributed to the presence of internal defects. In contrast, microhardness data are largely unaffected by internal defects. Hardness is one of the most commonly tested mechanical properties because measurements are quick, relatively inexpensive and provide insight to other properties such as yield strength [106] and wear resistance [107]. As a result, hardness measurements indicate the true effect of microstructural features such as the presence of various phases, precipitate particles, average grain size, and alloy composition. Although extensive research has been undertaken by many investigators, the data on properties such as hardness from individual publications are often fragmented.

In this section<sup>1</sup>, the role of metallurgical variables like cooling rate, microstructure, alloy composition, and post-processing heat treatments on the hardness of multiple alloy components fabricated by AM are examined. The data reviewed allow for the role of AM process variants on the microstructure and component hardness prior to post processing heat treatment to be examined. In many papers, hardness values are reported without any microstructural characterization precluding any direct correlation between microstructure and hardness. In those cases, selection of an effective compositional variable allows examination of the role of important alloying elements on hardness. While such correlations cannot take advantage of the decades of research correlating microstructure with properties, they reveal several immensely useful insights. Furthermore, the findings discussed are useful to determine if a target hardness is attainable either by adjusting AM process variables or selection of an appropriate alloy composition. Finally, they serve as a basis for alloy selection for attaining a target hardness of a component fabricated by AM.

### *2.3.1 Influence of process variables*

#### *2.3.1.1 Energy input*

The thermal histories during AM vary both spatially and temporally. Temperature measurements are limited to specific locations within the substrate when thermocouples are used and the surface of the molten pool when infrared imaging is used. Therefore, it is often difficult to represent the cooling rates and thermal histories of the entire AM process with a single value. An approximate alternative is to compare studies based on the amount of energy is delivered to the deposit in the form of a linear heat input [60],

$$E = \frac{P}{v} \quad (2.8)$$

where  $P$  is the power of the heat source in Watts and  $v$  is the scanning speed in mm/s. While more complex expressions for energy input exist in the literature, they often contain more process variables for the calculation, the details of which are not always reported.

Austenitic stainless steels, such as SS 304L and 316L, and titanium alloy Ti-6Al-4V have received much attention in the AM literature. Figure 2.23 shows the reported Vickers hardness [108-116] for austenitic stainless steels SS 316, SS 316L and SS 304L as a function of linear heat

---

<sup>1</sup> Portions of this section were reproduced from J.S. Zuback and T. DebRoy, ‘The hardness of additively manufactured alloys’, *Materials*, 11 (2018) 2070, doi:10.3390/ma11112070.

input. Generally, a higher heat input results in large molten pools, higher peak temperatures and slower cooling rates. It is expected that hardness will decrease with increases in linear heat input due to more heat accumulation, larger grain sizes and microstructural coarsening. A slight downward trend is observed in Figure 2.23 when all data is collected and plotted together. It should be noted that the scatter in the data can be caused by differences in equipment and techniques from independent researchers. However, it is interesting to note the differences with slight changes in chemical composition between SS316 and SS316L. Although each stainless steel is microstructurally similar, noticeable changes in microhardness are observed due to slight variations in carbon concentration.

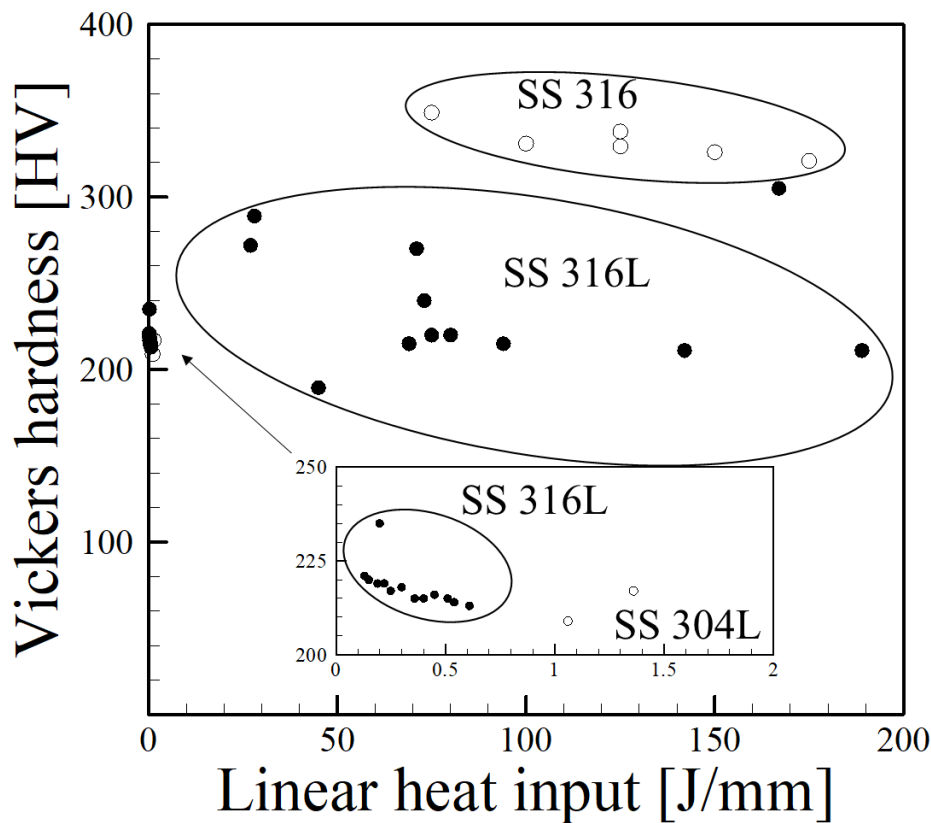


Figure 2.23. Hardness measurements for austenitic stainless steels deposited by AM as a function of linear heat input [108-116].

In a similar manner, average hardness values [68, 117-127] are plotted as a function of linear heat input for Ti-base alloys in Figure 2.24. Small values of linear heat input typically are found in powder bed processes where low powers and high scanning speeds are used. In contrast, DED and wire-based AM processes tend to use higher powers and lower scanning speeds, contributing to higher linear heat inputs. Observed microstructures of Ti-6Al-4V builds depend on

the process used and process variables resulting in different cooling rates. Although there have been individual studies that show decreases in hardness with increases in linear heat input for a single process, no observable trend can be seen when all data is combined. However, the highest values are recorded for low linear heat inputs, which correspond to powder bed processes.

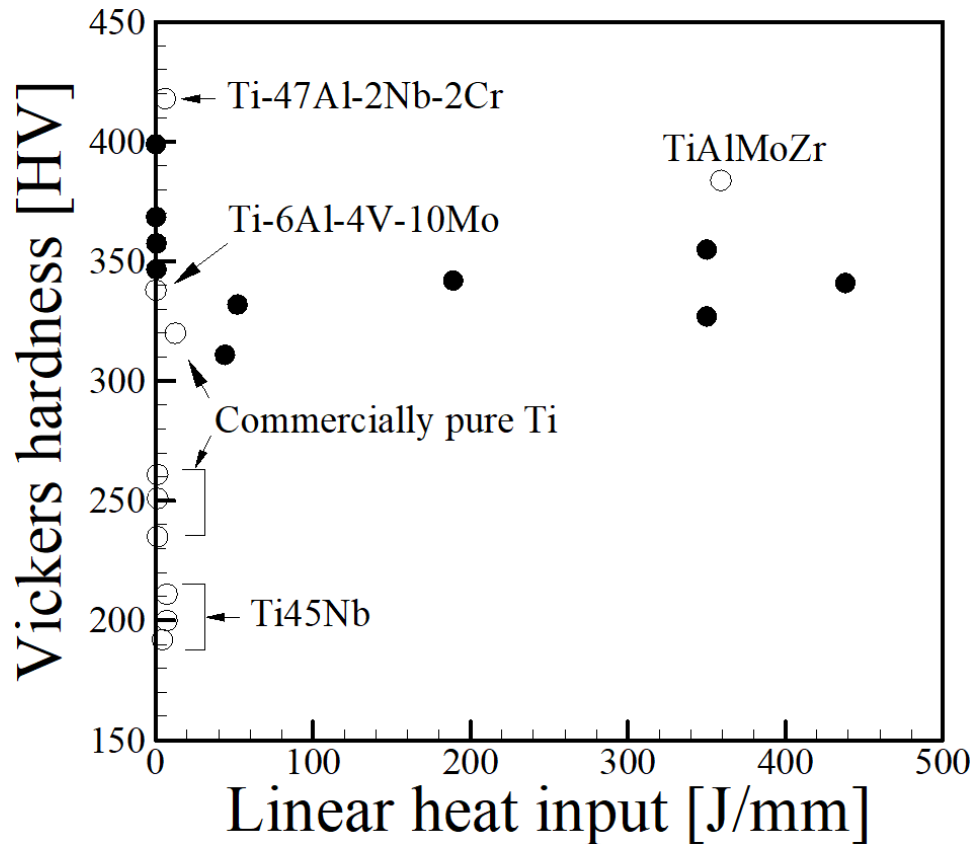
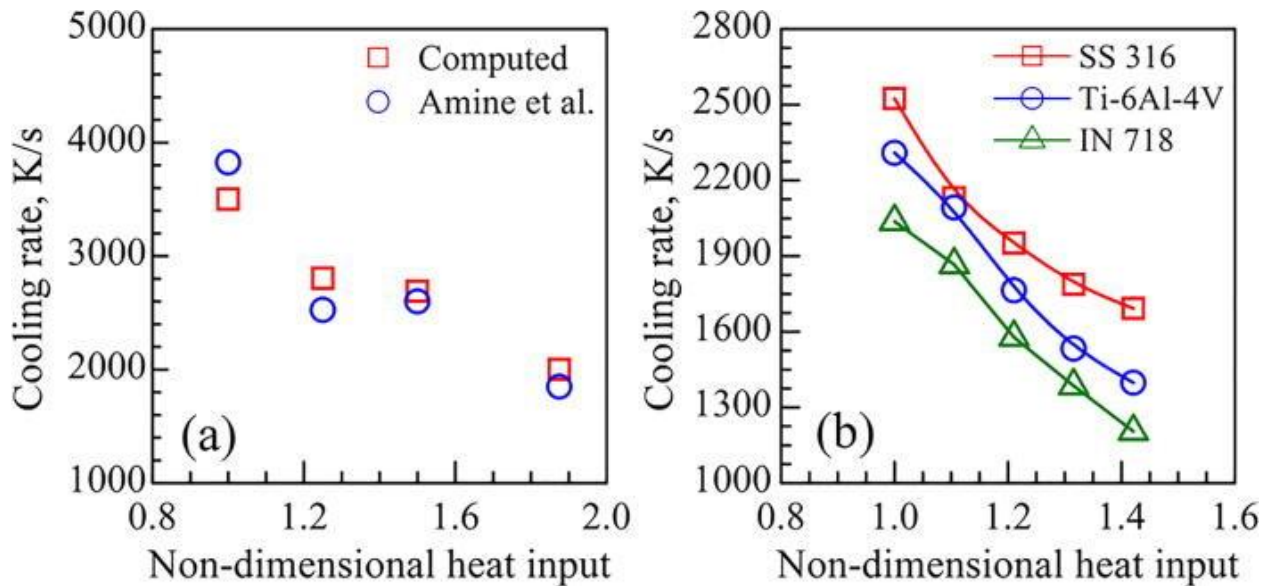


Figure 2.24. Vickers hardness as a function of linear heat input for titanium alloys where solid black dots correspond to Ti-6Al-4V and open points are marked otherwise [68, 117-127].

The use of linear heat input as a process variable has also been used in many studies to determine part density or residual porosity. It is generally accepted that an increase in the density of an AM component will effectively increase hardness measurements. Indeed, multiple investigations [115, 125, 128, 129] have reported positive correlations between part density and hardness. However, it is important to note that most of these studies use a matrix of experiments where multiple process parameters are varied to optimize part density by reducing porosity. Changing process parameters that affect important metallurgical variables like cooling rates and molten pool geometry will often lead to changes in microhardness regardless of residual porosity. In fact, studies that contradict the correlation between part density and microhardness have also been reported [117, 130]. For example, Thijs et al. [130] showed no apparent trend between part

density and microhardness. After PBF-L of Ti-6Al-4V for a constant linear heat input of 0.21 J/mm, a sample with 99.6% density exhibited a Vickers hardness of 409 HV while a value of 426 HV was measured for a sample with approximately 96% density. These changes in microhardness were caused by a difference in hatch spacing that ultimately affects cooling rates and resulting microstructure.

The heat input for a given set of process conditions can be linked to the cooling rate. Larger heat inputs generally result in slower cooling rates due to the large molten pool sizes and higher peak temperatures. Mukherjee et al. [131] used a 3D heat transfer and fluid flow model to show that the computed cooling rates have an inverse relationship with a dimensionless heat input, i.e. low heat inputs yield high cooling rates and vice versa. The dimensionless parameter is similar to Equation (2.8) and was defined as  $Q^*=(P/v)/(P_R/v_R)$  where  $P$  and  $v$  are the laser power and scanning speed, respectively. The terms  $P_R$  and  $v_R$  represent the reference power and scanning speed taken to be the those that give the lowest heat input for the analyzed data set, making  $Q^*$  always greater than unity. The computed cooling rates were validated with experimental data from Amine et al. [132] for the multilayer DED-L of SS316L as shown in Figure 2.25(a). The calculations were then further extended to show the relationship between heat input and cooling rates for other common AM alloys in Figure 2.25(b) under typical processing conditions. For all cases, similar downward trends of cooling rates are observed for higher non-dimensional heat inputs.



*Figure 2.25. The relationship between computed cooling rates and a dimensionless heat input parameter for the DED-L of (a) SS316L validated from experimental data [132] and (b) common AM alloys under typical process conditions [131].*

### 2.3.1.2 Cooling rates

In conventional metals processing, desired microstructures and properties are achieved through precise control of cooling rates and subsequent heat treatments. The controlled cooling rates of bulk materials are approximately spatially uniform and lead to repeatability in microstructure and properties for an alloy of a given chemical composition. For this reason, useful correlations can be developed that directly relate the microhardness of an alloy to cooling rate. Figure 2.26 (a)-(c) shows such relationships between hardness and cooling rates for collected data on steels [133-138], aluminum alloys [139-143] and nickel alloys [144-148] in which plates or bars are cooled at controllable rates. The logarithmic scale on the horizontal axis shows that the cooling rates cover multiple orders of magnitudes. For each of the alloy classes, similar symbols indicate alloys of the same composition. Moving from left to right on the plot for a single composition indicates a change in hardness for an alloy due to an increasing cooling rate whereas moving vertically along the plot for any given cooling rate compares hardness changes due to a change in composition for alloys of the same class. Also, hardness values tend to plateau at high cooling rates for all alloy systems considered.

From Figure 2.26 (a)-(c), it is observed that hardness differences resulting from changes in cooling rates are greatly outweighed by those when comparing alloys in the same class with different compositions. This trend is further supported by Figure 2.27 which shows hardness data for Jominy end quench samples for various grades of steel [149]. In Figure 2.27(a), a comparison is made between different types of alloy steels with similar carbon concentrations. Similarly, Figure 2.27(b) compares 8600 series steels, having small amounts of Ni, Cr, and Mo, with varying carbon contents. In both figures, changes in hardness due to both differences in chemical composition and cooling rates is substantial. Furthermore, increases in carbon concentration represented in Figure 2.27(b) can result in significant increases in hardness, regardless of cooling rate.

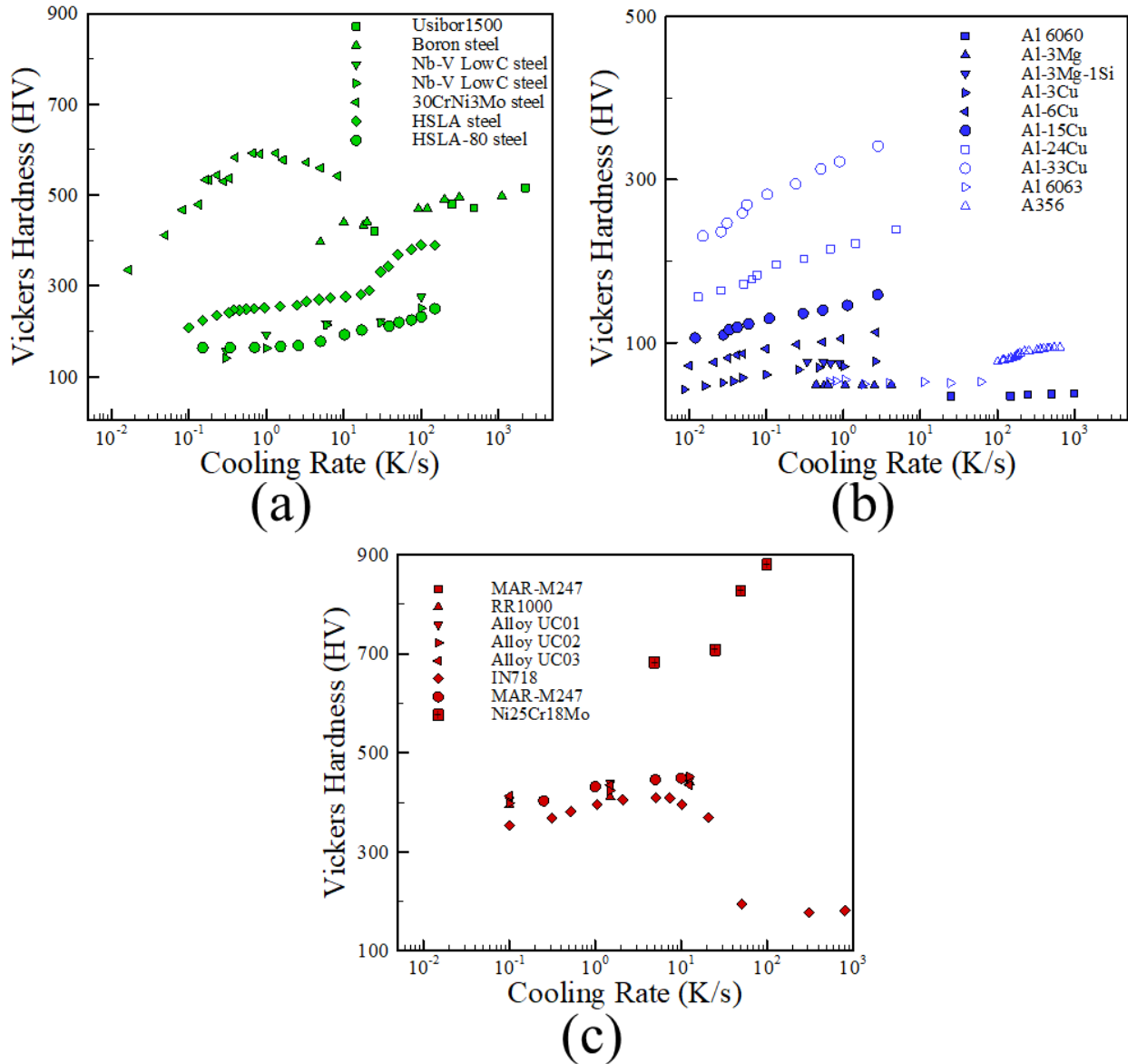


Figure 2.26. Hardness data as a function of reported cooling rates for (a) steels [133-138], (b) aluminum alloys [139-143] and (c) nickel alloys [144-148] in which no post-processing heat treatment was used.

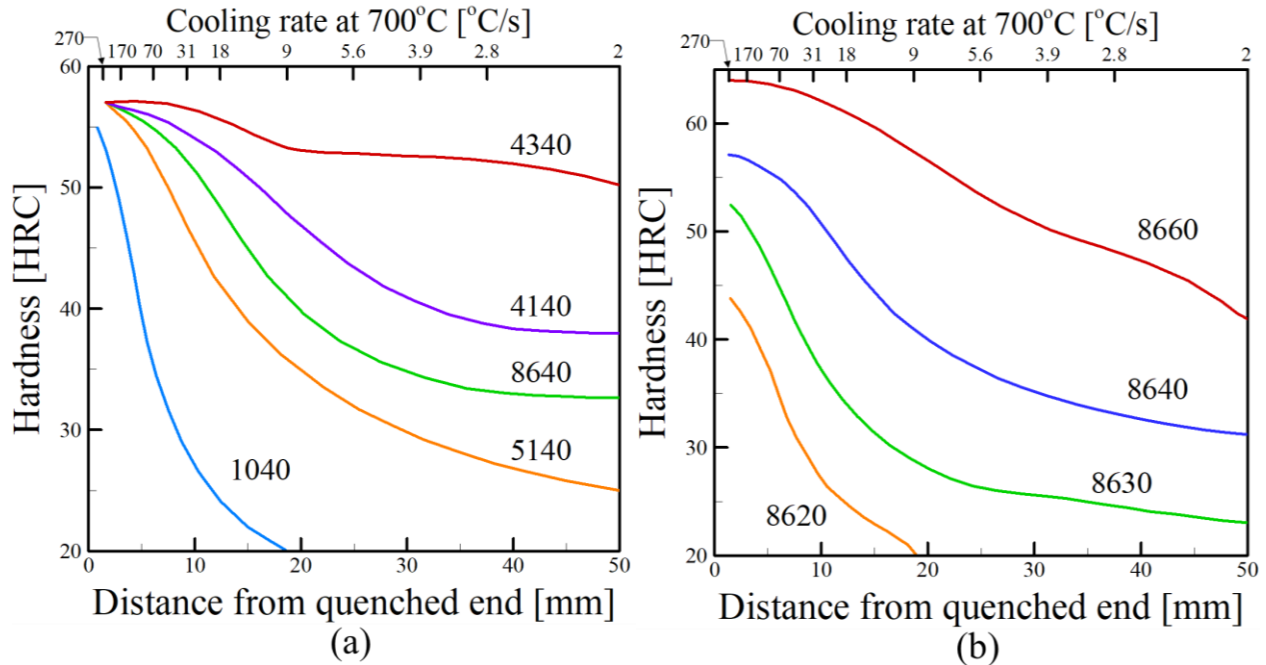


Figure 2.27. Hardness data for Jominy end quench experiments for (a) various steels with similar carbon concentrations and (b) 8600 series steels (0.55Ni, 0.50Cr, 0.20Mo) with varying carbon concentrations [149].

The thermal histories in AM involve multiple cycles of rapid heating and cooling and can span multiple orders of magnitude depending on the process and temperature range at which the cooling rate refers to. Figure 2.28 shows numerically computed temperature cycles from a heat transfer and fluid flow model during DED-L of SS316L for a single track, nine layer deposit [150]. Monitoring locations were selected at the midpoint in the length and width directions for selected layers. Clearly, cooling rates vary drastically both as a function of time and location within a build. For this reason, cooling rates are difficult to quantify for multi-pass, multi-layered AM parts that experience repeated heating and cooling and can make microstructural analyses convoluted.

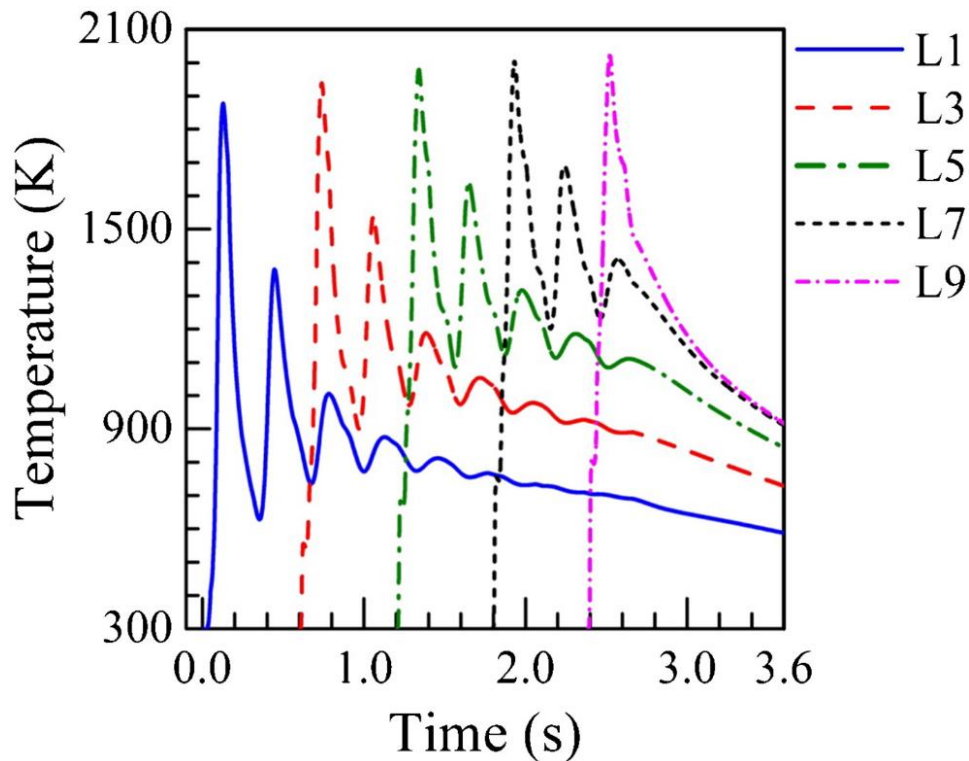


Figure 2.28. Computed thermal histories at the mid-length and mid-heights of selected layers during a single pass, nine layer simulation of DED-L of SS316 [150].

Both experimental and computational efforts have been undertaken for simple AM builds consisting of single passes and few layers to understand the relationship between cooling rates and microhardness for austenitic stainless steels. During the DED-L of SS316L [151], it was shown experimentally that the average cooling rates ranged from 22-764 °C/s for different processing conditions. The corresponding Vickers hardness values measured were approximately 150 HV for the slowest cooling rate and 368 HV for the highest cooling rate. Although it is unclear of the temperature range at which the cooling rate was averaged, the high hardness value was attributed to the formation of martensite. Manvatkar et al. [152] combined a numerical heat transfer and fluid flow model with experiments to correlate cooling rates to microhardness for a single pass, three layer DED-L deposition of SS316. The calculated cooling rates, defined as the average cooling rate through the solidification temperature range, varied from approximately 7000 °C/s in the first layer to 3000 °C/s. The resulting measured hardness values were approximately 230 and 210 HV for the first and third layers, respectively.

Another important process variable that is often overlooked when developing correlations is the geometry of the deposited part. The thermal history at an arbitrary location within a build

will depend on the melting and solidification of material around that location. Also, the heat transfer conditions that govern the temperature history can change as different part geometries are used. Although no simple universal expressions exist to quantify the effects of geometry, a systematic study by Keist and Palmer [62, 153] investigated the effects of geometry on mechanical properties of Ti-6Al-4V fabricated by PBF and DED using both laser and electron beam sources. When comparing measurements between thin and thick L-shaped walls, the Vickers hardness numbers of single pass walls were significantly lower than the hardness of the 3-pass walls.

In geometries consisting of simple shapes, the hardness variations can easily be correlated with location in a build by taking multiple cross sections. In general terms, heat accumulates in a build with an increase in process time. As the build height increases further away from the substrate material, the heat transfer is directed through previously deposited layer which usually results in slower cooling rates. Extended times at elevated temperatures for alloys that are not precipitation hardenable causes coarsening of microstructural features, relaxation of residual stresses, and dislocation motion and annihilation. As a result, hardness measurements tend to be lower at locations further away from the substrate (increasing build height) and higher in areas close to the substrate. Figure 2.29 shows cross sections with different orientations with respect to the build for a single pass wall of IN718 processed with DED-L. The most obvious changes in microhardness occur in the Z-direction as shown in Figure 2.29 (a) and (b) which correspond to the build direction. No significant differences were observed in the X- and Y-directions as observed in Figure 2.29 (b) and (c). Since IN718 is a precipitation-hardened alloy, appreciable changes in hardness at different locations in the build were attributed to aging during processing [154]. Regions near the baseplate experienced more time at high temperatures leading to enhanced precipitation.

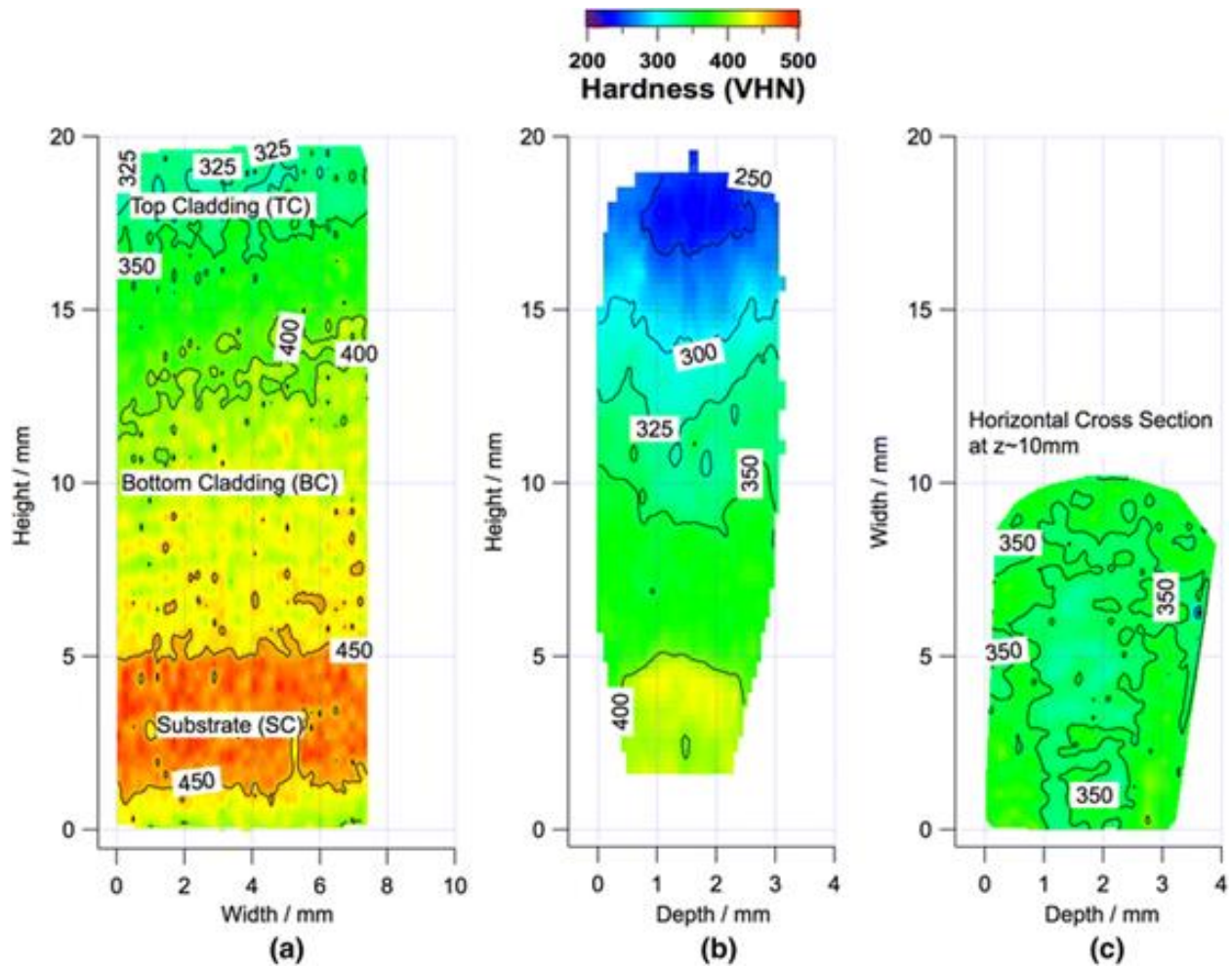


Figure 2.29. Hardness variations as a function of location within a DED-L single pass, multilayer build of IN718 [154] showing (a) a longitudinal cross section (X-Z plane), (b) a transverse cross section (Y-Z plane), and (c) a horizontal cross section (X-Y plane) where X is the travel direction, Y is the track width direction, and Z is the build direction.

### 2.3.2 Effects of microstructure

As-deposited microstructures of alloy components fabricated by AM are direct products of the thermal histories experienced during heating, melting, solidification, and cooling. Microstructure evolution depends on alloy composition and some alloys undergo important phase transformations that can impact the properties and performance of AM parts. Table 2.4 shows a collection of process conditions for steels [74, 155-162], aluminum [163-171], and nickel alloys [129, 172-188] that have been fabricated by AM. Correspondingly, Table 2.5 shows the phases and hardness values reported for the same alloys. In this section, the influence of microstructures on the hardness of AM alloys is discussed below for various types of alloys.

Table 2.4. Process parameters for iron, aluminum and nickel alloys

Iron alloys					Nickel alloys				
Alloy	*Process	†Power [W]	Scanning speed [mm/s]	Ref.	Alloy	*Process	†Power [W]	Scanning speed [mm/s]	Ref.
H13	EBM	(20 mA)	500	[155]	IN718	SLM	200	800-1200	[172]
4340	DMD	500	7.5	[156]	IN718	DMD	750	6.25	[173]
18Ni300	SLM	86-100	180-220	[157]	IN718	SLM	110-130	400-600	[129]
H13	DMD	1000-1400	10.5-19.0	[158]	Rene 142	EBM	Not reported	Not reported	[174]
H13	DMD	2500	5	[159]	Colmonoy 6	LRM	2500	4.2	[176]
ER70S-6	3D GMAW	(14-16 V, 65-76A)	5.23	[160]	IN625	LRM	1000-1500	5.0-13	[175]
M2 steel	DMLS	200	50-175	[161]	Rene 142	LC	550	Not reported	[177]
Tool steel	SLM	75-175	300-450	[162]	Nimonic 263	SLM	200	100	[178]
420 SS	DMLS	283-317	600-1000	[74]	IN718	SLM	170	417	[179]
Aluminum alloys					Experimental	SLM	1000	2	[180]
					IN718	SLM	3000	Not reported	[181]
Al 2139	EBF <sup>3</sup>	1350	8.47	[163]	IN939	SLM	400	540-620	[182]
AlSi10Mg	SLM	195	800	[164]	IN718	SMD	(220A)	5	[183]
Al-12Si	Pulsed SLM	500-4500	1.5-3.0	[165]	Rene 41	LMD	4500-5000	5.00-5.83	[184]
Al-12Si	SLM	200	37-2000	[166]	Rene 80	SLE	1000	~100	[185]
AlSi10Mg	SLM	200	318	[167]	Hastelloy X	SLM	165-195	Not reported	[186]
AlSi10Mg	SLM	200	Not reported	[168]	Hastelloy X	SLM	Not reported	Not reported	[186]
AlSi10Mg	DMLS	120	900	[169]	IN718	SLM	Not reported	Not reported	[187]
Al-12Si	SLS	100-200	80-200	[170]	Ni60A	LMDS	Not reported	Not reported	[188]
Al 2024	SLM	200	83-333	[171]					

\*EBM = Electron beam melting, DMD = Direct metal deposition, SLM = Selective laser melting, 3D-GMAW = Gas metal arc welding 3D printing, DMLS = Direct metal laser sintering, EBF<sup>3</sup> = Electron beam freeform fabrication, DMLS = Direct metal laser sintering, SLS = Selective laser sintering, LRM = Laser Rapid Manufacturing, LC = Laser Cladding, SMD = Shaped Metal Deposition, LMD = Laser Metal Deposition

† Values in parenthesis signify processes where it is more common to report the voltage and current

Table 2.5. Process and resulting as-deposited microstructures for iron, aluminum and nickel alloys

	Alloy	Process	Phases	HV	Ref.
Iron alloys	H13	EBM	Martensite	‡498.5 ± 14.5	[155]
	4340	DMD	Ferrite, Martensite, Cementite	580.5 ± 100.5	[156]
	18Ni300	SLM	Not reported	‡323.5 ± 21.5	[157]
	Maraging steel				
	H13	DMD	Not reported	550 ± 30	[158]
	H13	DMD	Fine martensite, retained austenite, fine carbides	615 ± 35	[159]
	ER70S-6	3D-GMAW	Polygonal ferrite, acicular ferrite	184 ± 15	[160]
	M2 steel	DMLS	Martensite, austenite, fine carbides	800 ± 100	[161]
	FeCrMoVC	SLM	Fine martensite, austenite, carbides	900 ± 12	[162]
	tool steel				
420 SS	DMLS	Martensite, little retained austenite	‡478 ± 20	[74]	
Aluminum alloys	Al 2139	EBF <sup>3</sup>	Not reported	81-103	[163]
	AlSi10Mg	SLM	FCC dendrites, interdendritic eutectic	131-141	[164]
	Al-12Si	Pulsed SLM	FCC dendrites, small eutectic phases	130-140	[165]
	Al-12Si	SLM	FCC Al matrix, nano-sized Si precipitates	107-115	[166]
	AlSi10Mg	SLM	FCC	114	[167]
	AlSi10Mg	SLM	FCC, fine Si precipitates	127	[168]
	AlSi10Mg	DMLS	FCC	103-111	[169]
	Al-12Si	SLS	FCC Al-Si matrix	99-113	[170]
	Al 2024	SLM	FCC	104-118	[171]
Nickel alloys	IN718	SLM	FCC- $\gamma$ , ellipsoidal Ni <sub>3</sub> Nb precipitates	387-398	[172]
	IN718	DMD	FCC- $\gamma$	255	[173]
	IN718	SLM	FCC- $\gamma$ , fine $\gamma'$ precipitates	331.9-395.8	[129]
	Rene 142	EBM	FCC- $\gamma$ , cuboidal $\gamma'$ precipitates	428.1	[174]
	Colmonoy 6	LRM	FCC- $\gamma$ , interdendritic eutectic	700-800	[176]
	IN625	LRM	FCC- $\gamma$	‡474.9-574.1	[175]
	Rene 142	LC	Not reported	410-460	[177]
	Nimonic 263	SLM	$\gamma$ , carbides in interdendritic regions	300	[178]
	IN718	SLM	FCC- $\gamma$	340-380	[179]
	Experimental	SLM	Not reported	650-800	[180]
	IN718	SLM	FCC- $\gamma$	400-450	[181]
	IN939	SLM	FCC- $\gamma$	450	[182]
	IN718	SMD	FCC- $\gamma$ , interdendritic carbides/Laves	245-287	[183]
	Rene 41	LMD	FCC- $\gamma$ , MC carbides	418.1-435.1	[184]
	Rene 80	SLE	FCC- $\gamma$ , fine carbides/ $\gamma'$ particles	489.8	[185]
	Hastelloy X	SLM	FCC- $\gamma$	276.9-284.9	[186]
	Hastelloy X	SLM	FCC- $\gamma$	273.2-281.0	[186]
	IN718	SLM	FCC- $\gamma$	410.8-430.2	[187]
Ni60A	LMDS	FCC- $\gamma$	‡631.1-762.9	[188]	

### 2.3.2.1 Iron based alloys

Due to the high costs of AM compared to conventional casting and forging processes, the use of plain carbon and low alloy steels have not found significant usage for AM applications outside of a few studies [189, 190]. Many of the steels used in AM have been tool steels [191-197], studied for specialized repair applications in which high strength and wear resistance is crucial. Tool steels such as M2 and H13 obtain high strengths and hardness due to their propensity to form martensite even at relatively low cooling rates. Additionally, these alloys contain high amounts of carbon which promote the formation of carbides and increase strength and hardness. Typical microstructures of tool steels processed by AM include a martensitic matrix with some carbide precipitation and retained austenite [192, 197]. After deposition of tool steels, heat treatment is desirable to increase ductility and toughness. A tempered martensitic microstructure with carbide precipitates results from extended times at high temperatures [194].

Austenitic stainless steels, such as SS304L and SS316L exhibit predominantly austenitic microstructure consisting of cells and columnar dendrites, depending on the type of AM technique and the process parameters. Figure 2.30 shows an SEM micrograph of the typical columnar dendritic morphology of the austenitic grains encountered for SS316L fabricated using DED-L. Although austenitic stainless steels are dominated by an austenitic matrix, small amounts of delta ferrite can form as a result of thermal cycles and microsegregation. High cooling rates during solidification favor austenite whereas lower cooling rates tend to yield increasing amounts of delta ferrite [198]. In PBF processes, a fine cellular solidification structure on the order of 1  $\mu\text{m}$  is often observed. As austenitic stainless steels often do not precipitate secondary phases or undergo other solid-state transformations, the strength and hardness depend on the fineness of the solidification structure and chemical composition.

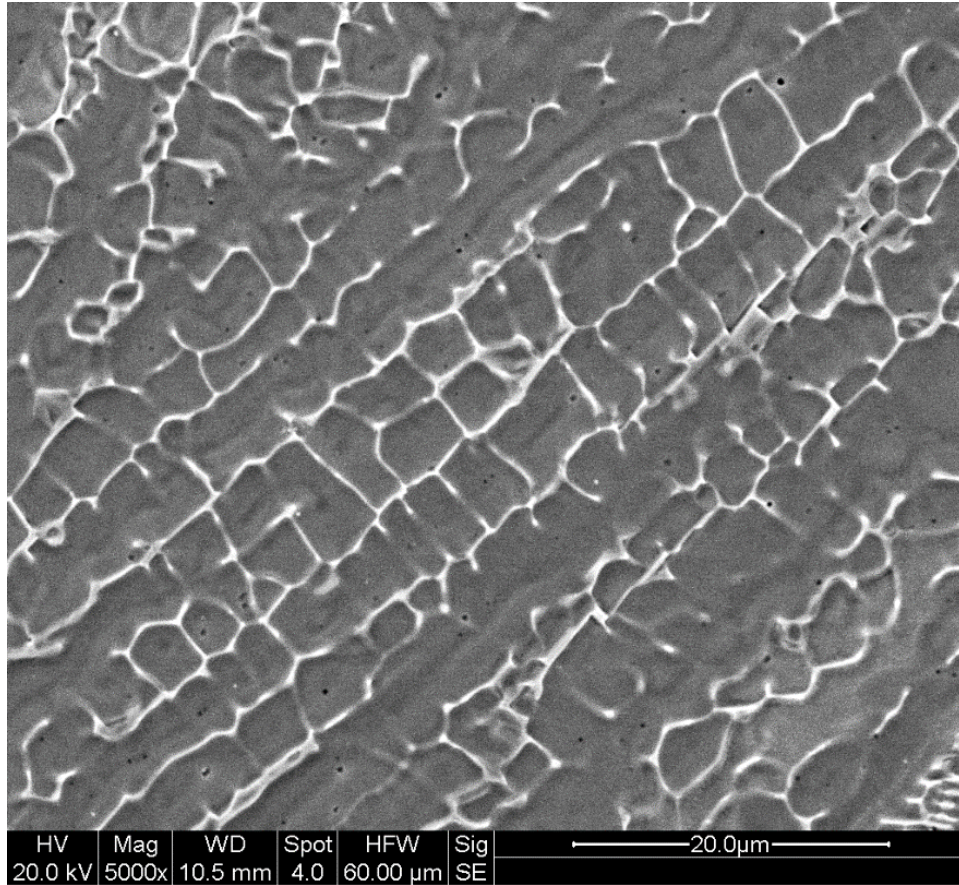


Figure 2.30. Columnar dendritic microstructure of SS316L deposited by DED-L [116].

Figure 2.31 shows a collection of measured HV as a function of secondary dendrite arm spacing (SDAS) for the austenitic stainless steels SS316 and SS316L processed by DED-L. Both alloys typically exhibit large austenitic columnar grains with a dendritic substructure. Although these alloys are chemically similar, SS316L ( $\leq 0.03$  wt% C) contains slightly less carbon than SS316 ( $\leq 0.08$  wt% C) to help improve weldability and prevent sensitization. This small change in composition has pronounced effects on microhardness for roughly the same size SDAS with measurements for SS316, although limited, having a hardness of nearly 100 HV higher than those of SS316L. The same effect was observed in Figure 2.23. Therefore, it is important to perform detailed chemical composition analyses when studying the effects of microstructure on properties as small fluctuations in concentration of carbon can significantly affect hardness.

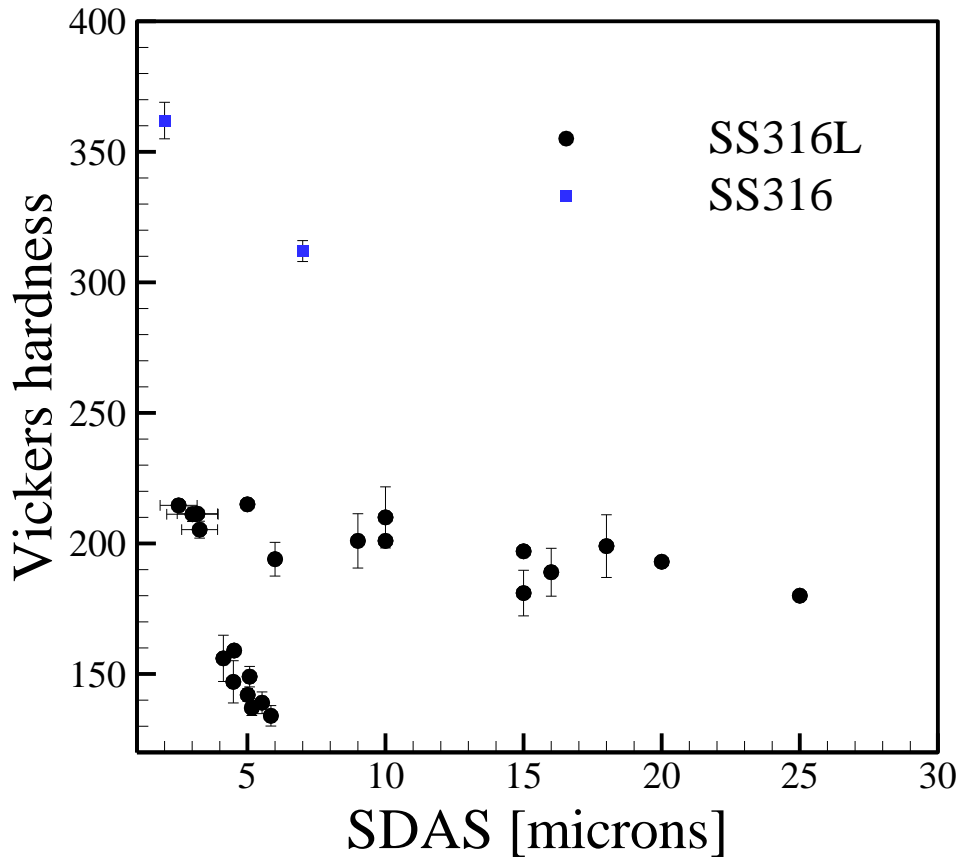


Figure 2.31. Vickers microhardness as a function of secondary arms spacing for stainless steels fabricated by AM from [108, 116, 132, 199, 200]. Error bars represent the standard deviation in measurements.

Precipitation hardened (PH) stainless steels have received considered attention in the AM community with the most commonly processed alloys being 17-4PH and 15-5PH. Nominal compositions for the PH grade stainless steels typically promote the formation of martensite during rapid cooling. Subsequent solutionizing and aging allows for Cu-rich nanoparticles to precipitate in a tempered martensite matrix which determine the final properties. However, microstructures ranging from austenitic/martensitic to primarily martensitic have been reported in the AM literature depending on the atomization condition of the powder feedstock and the type of shielding gas used. Multiple investigations [201, 202] have shown that when Ar-atomized 17-4PH stainless steel was processed under an Ar atmosphere, a primarily martensitic structure was obtained. However, when nitrogen, an austenite-stabilizing element, was used as a processing gas to melt nitrogen atomized powders, a mixture of primarily austenite and martensite was observed. In the as-deposited conditions, substantial differences in microhardness in the two extreme conditions

were measured, as the samples with more austenite exhibited a hardness slightly over 200 HV and the martensitic samples had a hardness slightly less than 400 HV [202].

The microstructure evolution during solutionizing and aging is highly dependent on the as-deposited microstructure. Standard solution heat treatments originally developed for wrought alloys may not be applicable due to the heterogeneous microstructures encountered in AM parts. For example, Cheruvathur et al. [203] found that the Vickers hardness of solutionized 17-4PH grade stainless steel was  $312 \pm 17$  HV compared to a value of  $258 \pm 8$  for the as-deposited condition. Although 17-4PH is classified as a martensitic stainless steel, a mixture of approximately 50% martensite and 50% retained austenite was found in the as-deposited condition with small amounts of NbC. After solutionizing and subsequent air cooling, less retained austenite was found in the microstructure, which was attributed to the increase in hardness.

#### 2.3.2.2 Aluminum alloys

The aluminum alloys most commonly used in AM processes contain large amounts of Si which promote eutectic solidification. The lower melting point of eutectic Al-Si alloys, such as Al-12Si and AlSi10Mg, are easier to process via laser-based AM processes compared to other aluminum alloys due to the low absorptivity of Al over a wide range of wavelengths. Aluminum alloys generally exhibit a cellular or dendritic microstructure consisting of a face centered cubic Al-matrix with fine Si-rich phases in the as-deposited condition when processed by AM. For example, Figure 2.32 shows cubic silicon phase in a fine cellular/dendritic structure within the face centered cubic aluminum matrix of AlSi10Mg after selective laser melting [204]. Eutectic formation was found to form at the triple points of the cellular/dendritic structure. Although cells and dendrites predominate in much of the literature, partial equiaxed microstructures [205] can be observed as shown in Figure 2.33 depending on the solidification parameters.

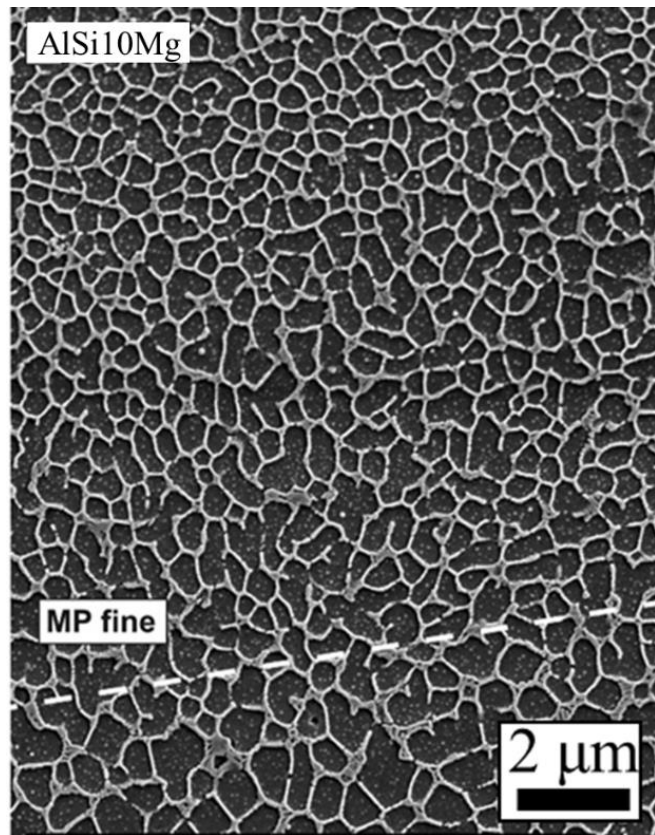


*Figure 2.32. As-deposited microstructure of AlSi10Mg alloy fabricated by selective laser melting showing a fine cellular/dendritic structure with small amounts of eutectic [204].*

As precipitation hardenable aluminum alloys rely on aging heat treatments to achieve enhanced properties, the high strengths and hardness observed in as-fabricated alloys stem from the fine solidification structure. Although there is sparse data fragmented over multiple aluminum alloy systems, Figure 2.34 shows a collection of HV values plotted as a function of SDAS from AM. Selected data from directionally solidified aluminum alloys Al-3Cu, Al-1Ti, and Al-3Si [206] is shown for comparison. A combination of high cooling rates and significant amounts of alloying elements, namely Si, lead to fine secondary dendrite arm spacing and high hardness in the alloys processed by AM. However, any attempts to link microstructure to properties should be limited to single compositions and Figure 2.34 merely shows a collection of data to demonstrate the fineness of AM microstructures in comparison to other processes. Any significant deviations in chemical composition that affect solidification requires separate analysis.

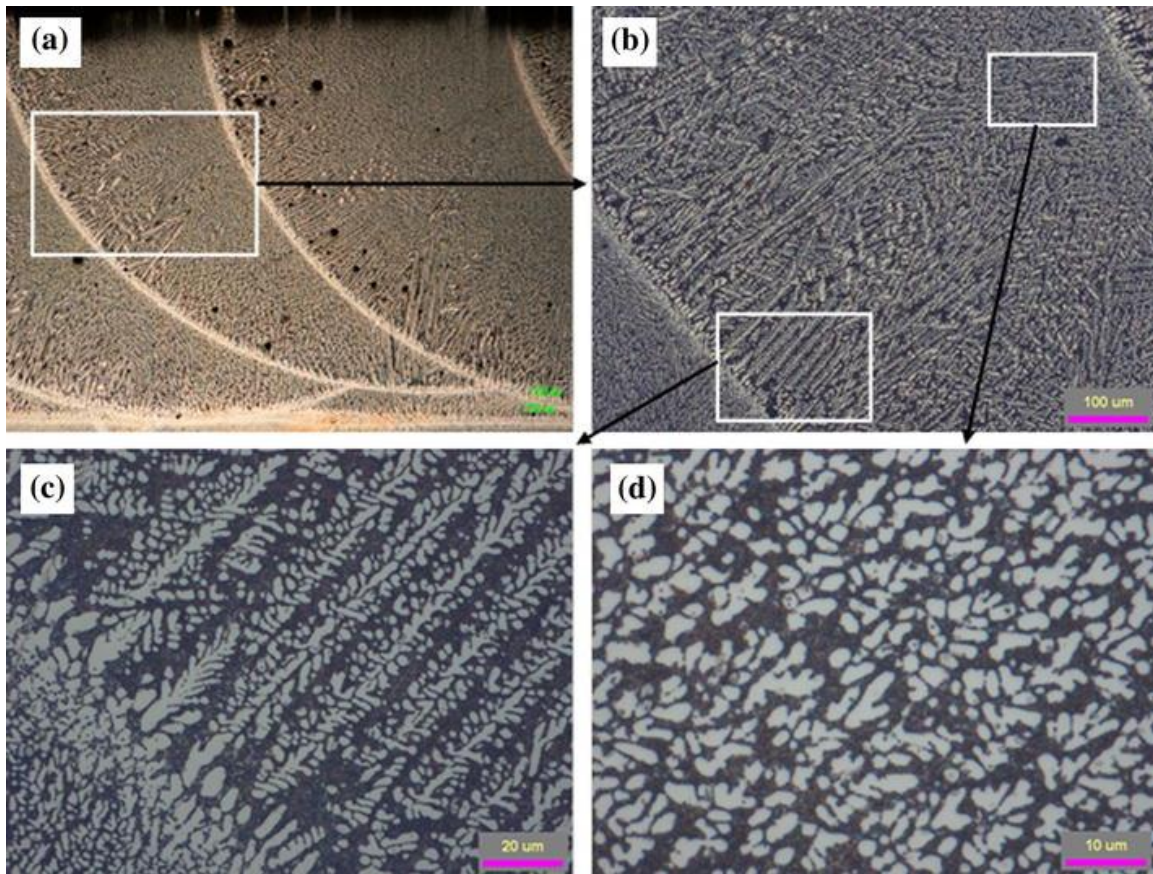


Figure 2.33. Microstructure of laser deposited Al 4047 showing dendritic and equiaxed structures at different locations within the same layer [205].

Although high strengths and hardness have been obtained after the AM of aluminum alloys, as-deposited components typically suffer from poor ductility. Investigations into the effects of post-process heat treatments on the mechanical properties of AlSi10Mg processed by PBF-L have resulted in interesting conclusions. Results from Aboulkhair et al. [207] showed that when applying standard T6 heat treatments (solutionizing + artificial aging) at various solutionization times, the Vickers hardness of heat treated samples (between 75-100 HV) was always less than the hardness in the as-deposited condition (~110 HV). Although Li et al. [208] reported similar findings, their results showed that the hardness after solutionizing was, in fact, greater than the hardness after artificial aging. After microstructural examination, it was found that Si particles formed during solutionizing and subsequent artificial aging coarsened the particles to an extent similar to overaging in commonly processed aluminum alloys. However, Kempen et al. [209] achieved about a 12% increase from the as-deposited hardness ( $136 \pm 9$  to  $152 \pm 5$  HV) when directly applying an artificial aging heat without a solutionizing step.

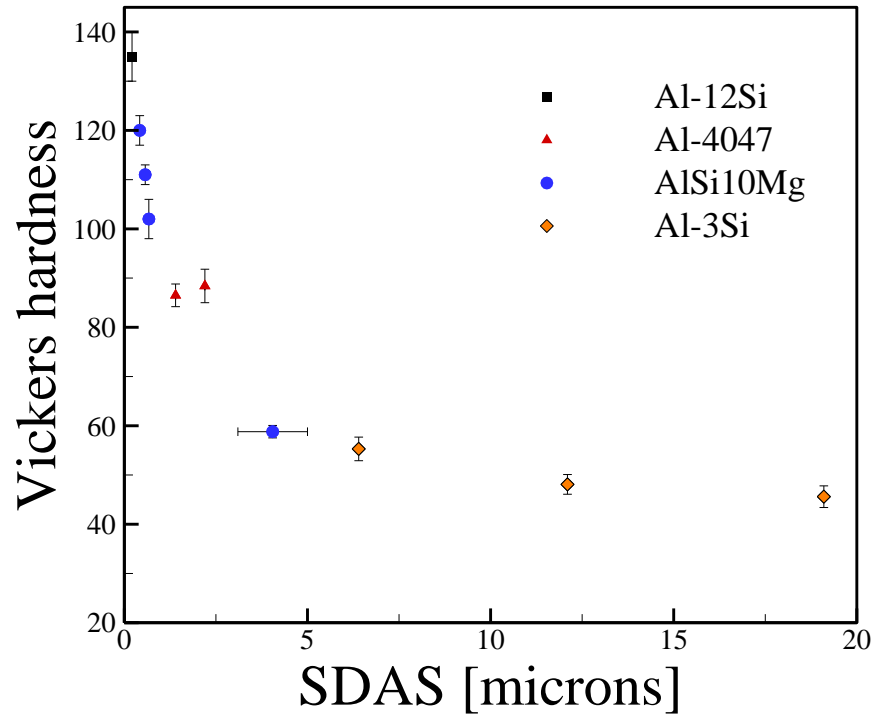


Figure 2.34. Vickers microhardness as a function of secondary arms spacing for aluminum alloys fabricated by AM from [165, 205, 210, 211] and selected data for directional solidification of Al-3Si from Kaya et al. [206]. Error bars represent the standard deviation in measurements.

The use of HIP as a post-processing technique has found widespread use across many different alloys systems used in AM. In most cases, a dramatic effect can be observed when comparing the hardness of as-deposited and post-HIP conditions. During the PBF-L of AlSi10Mg [212], subsequent HIP treatment resulted in a hardness value ( $60 \pm 5$  HV) more than half of that of the as-deposited condition ( $125 \pm 5$  HV) due to significant microstructural coarsening and stress relief. Similarly, Tradowsky et al. [213] found that for machined AlSi10Mg samples fabricated by PBF-L, yield strength decreased by more than 60% after post-process HIP. However, the loss of strength was compensated by a substantial increase in percent elongation from approximately 5% in the as-deposited condition to about 21% after HIP.

### 2.3.2.3 Nickel alloys

Nickel alloys are some of the most complex alloys used in AM applications due to the large amounts of alloying elements that can result in various types of secondary phase precipitation which ultimately affect mechanical properties. The as-deposited microstructure of nickel alloys are highly dependent on thermal histories and chemical composition. Figure 2.35 shows microhardness as a function of SDAS for the DED-L of IN625, IN718 and Waspaloy. In the case

of IN625, data points are confined to a rather tight grouping with an average microhardness and SDAS of approximately 250 HV and slightly less than 4  $\mu\text{m}$ , respectively. Although IN625 is generally classified as a solid solution strengthened alloy, secondary phases often form in both welding and AM due to significant microsegregation. However, these secondary phases (Laves, MC carbide) often form upon solidification and appreciable nucleation and growth in the solid state during AM processing is uncommon.

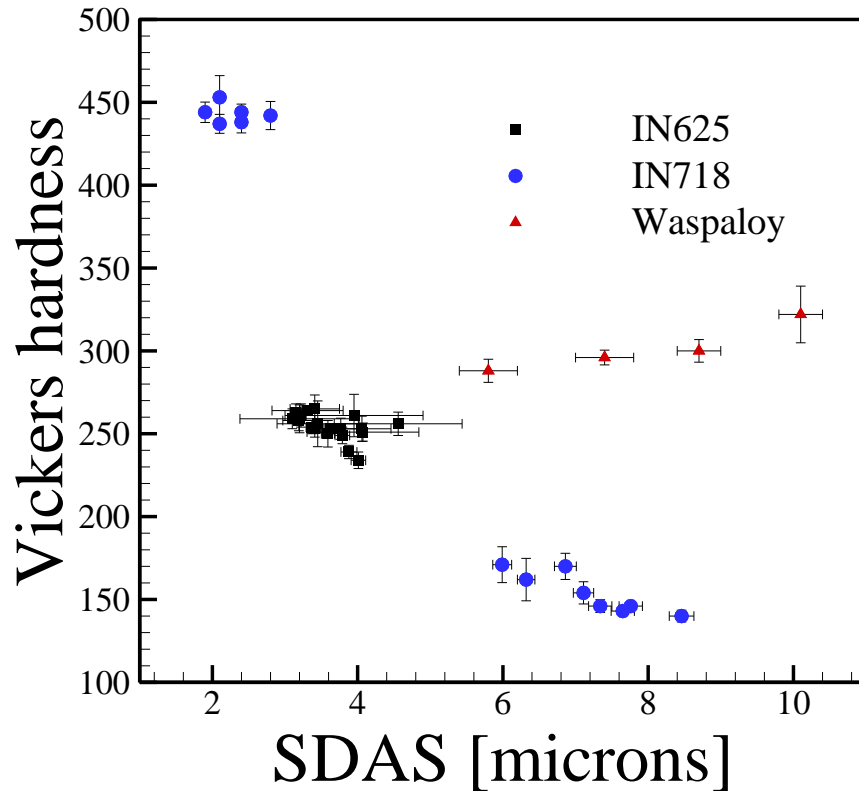
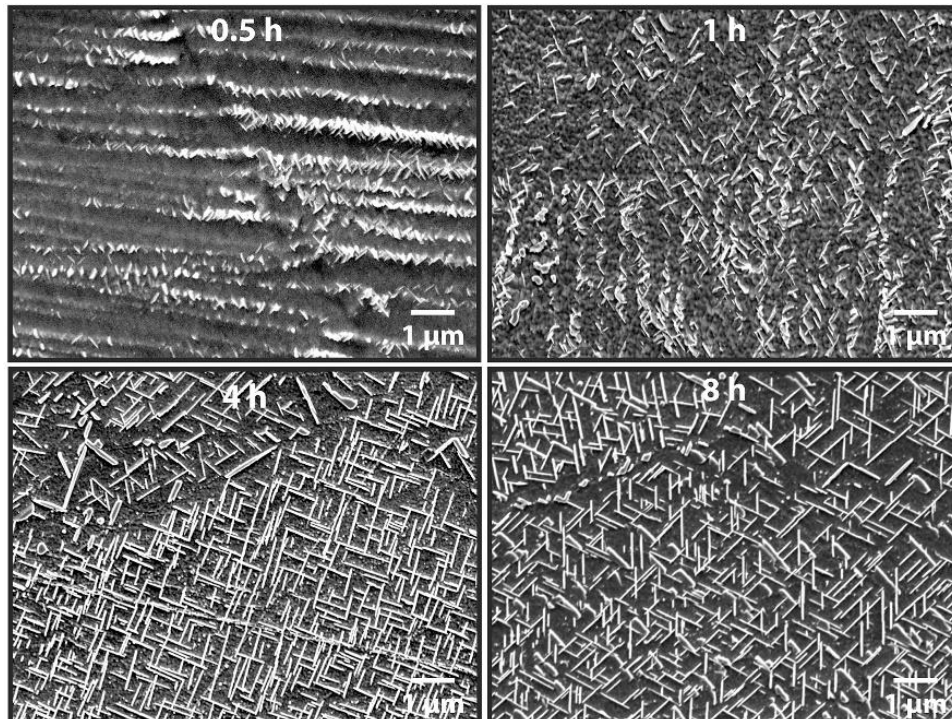


Figure 2.35. Vickers microhardness as a function of secondary arms spacing for nickel alloys fabricated by AM from [200, 214-218]. Error bars represent the standard deviation in measurements.

In the case of IN718, the highest HV values in Figure 2.35 correspond to a post-process heat treatment where the lower values were measured in the as-deposited state. It is clear from this comparison that the changes in hardness due to SDAS is negligible when compared to the effects of precipitation hardening. Interestingly in the case of the Waspaloy data, a positive correlation is observed between HV and SDAS. At first, this may seem counterintuitive, however the increases in SDAS were a result of deposits with different layer numbers with a higher number of layers corresponding to higher SDAS. As more heat was accumulated in the build and cooling rates decreased, microstructural coarsening occurred simultaneously with nucleation and growth of  $\gamma'$

precipitates. Therefore, the observed hardness is contributed by both the coarsening as well as the precipitation of  $\gamma'$  phase.

The as-deposited microstructures in AM alloys vary drastically from those of wrought counterparts for which standard heat treatments were developed. Consequently, large amounts of elemental segregation often observed in AM parts are expected to contribute to heat treatment responses that vary significantly from those of wrought parts. Zhang et al. [219] showed that after just five minutes at the manufacturer recommended stress relief temperature ( $870^{\circ}\text{C}$ ), IN625 processed by PBF-L began to nucleate and grow deleterious  $\delta$ -phase. Figure 2.36 shows the time evolution of the needle-shaped precipitates during stress-relieving. For comparison, an isothermal transformation diagram for wrought IN625 [220] does not predict the formation of  $\delta$ -phase until approximately 10 hours at  $870^{\circ}\text{C}$ . The presence and morphology of intermetallic phases such as those shown in Figure 2.36 act as stress concentrators and can be detrimental to the ductility and toughness of materials. Instances such as these may prompt the need for developing standard heat treatments specially designed for AM materials to avoid undesirable microstructural evolution.



*Figure 2.36. The precipitation and growth of  $\delta$  phase at various times in PBF-L IN625 subjected to a standard stress relief heat treatment at  $870^{\circ}\text{C}$  [219].*

Vilaro et al. [178] reported hardness increases during 8h stress relief heat treatments of PBF-L Nimonic 263 up to approximately 800°C. Even though the residual stresses present in the as-deposited condition were greatly reduced at 600°C, a slight increase in microhardness was observed. It was proposed that the high density dislocation structure was unable to restore due to the presence of very small (<10 nm)  $\gamma'$  particles that pinned dislocation motion at these temperatures which, along with the precipitation M23C6 carbides, increased hardness. It was not until a heat treatment above the  $\gamma'$  solvus temperature (~960°C) was used that the precipitates dissolved, and the dislocation density was reduced.

Although IN718 is a nickel alloy, other elements like Al, Cr, Fe, Mo, Nb, and Ti constitute nearly half of the alloy mass which aid in the nucleation and growth of  $\gamma'$  and  $\gamma''$  precipitates. Although slight variations in time and temperatures have been used, post-processing of IN718 components fabricated by AM generally follow standard heat treatments including solutionization at 980°C for 1 h followed double aging at 720°C for 8h and 620°C for 8h. The box-and-whisker plot in Figure 2.37 shows a collection of literature data for the hardness of IN718 parts at various stages of post-processing after AM fabrication. Individual points in Figure 2.37 represent outlying data. Clearly, significant advantages are gained in post-process heat treating to achieve properties that are otherwise unattainable in as-deposited parts.

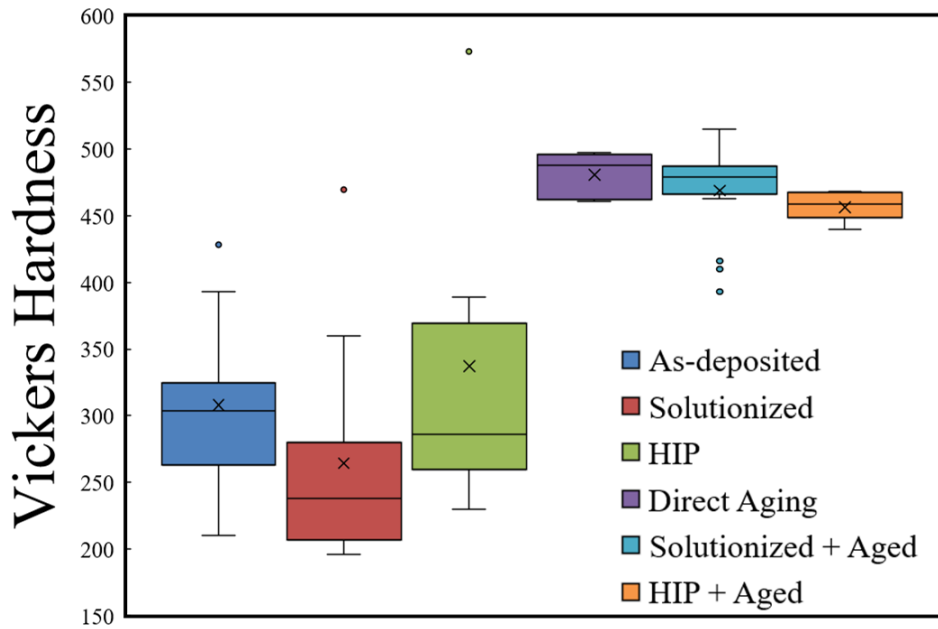


Figure 2.37. Box and whisker plot showing the variation in Vickers hardness of IN718 parts fabricated by DED-L [181, 221-224], PBF-L [129, 225-231], and PBF-EB [232, 233] AM and subjected to various post process heat treatments.

An effort was undertaken by Sames et al. [234] to circumvent post-processing of IN718 while still achieving peak-aging properties. An *in-situ* heating method was used on a PBF-EB system where the build was consistently held at high temperatures to promote aging. A comparison of the Vickers hardness measured after the *in-situ* heat treatment and under fast and slow cooling is shown in Figure 2.38. Although the measurements showed that optimal hardness values were attainable, further tensile testing revealed significantly lower strength and elongation than control specimens due to the presence elongated cracks. In another study, Schwab et al. [235] used a similar *in-situ* heating method to enhance the properties of Ti-5553 during PBF-L through substrate heating. About a 60% increase in Vickers hardness was achieved and higher compressive strength was measured when comparing the heat treated deposit to the samples with no substrate heating.

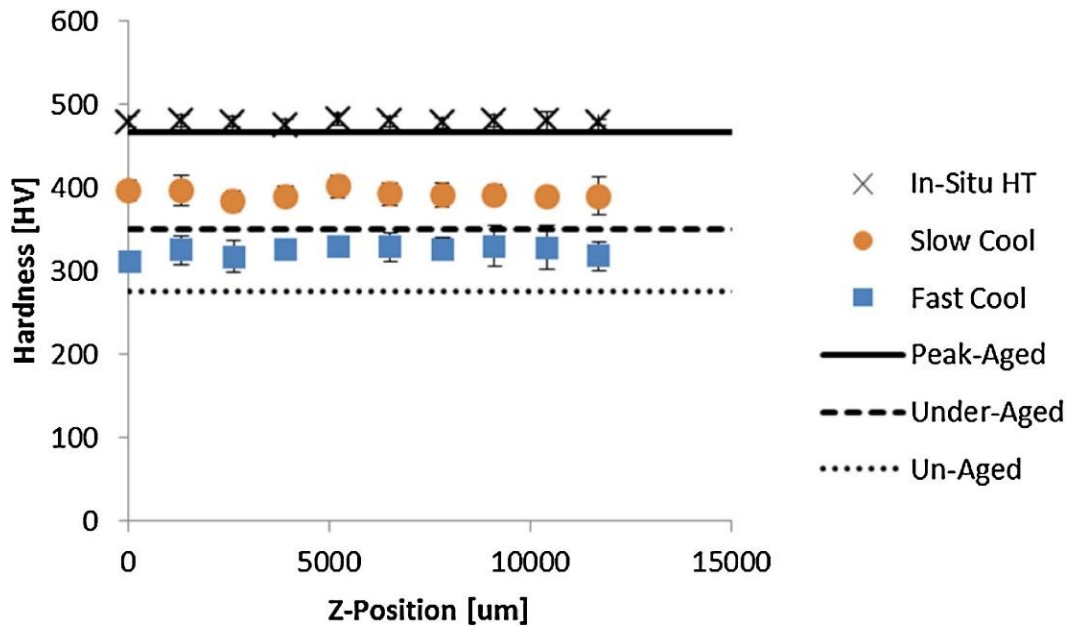


Figure 2.38. Measured Vickers hardness during PBF-EB of IN718 subjected to different cooling cycles and in-situ heat treatment [234].

Khayat and Palmer [218] found for multiple IN625 feedstocks with varying iron contents fabricated by DED-L that HIP resulted in a Vickers hardness roughly 40 HV lower than the as-deposited material. Although the volume fraction of secondary phases increased during post-processing, which normally contribute to increased hardening, it is likely that the observation was outweighed by other factors like decreased dislocation density and elimination of the fine dendritic structure.

#### 2.3.2.4 Titanium alloys

The combination of high strength and low density make titanium alloys an attractive alloy for AM in aerospace applications. The Ti-6Al-4V alloy is the most studied of the titanium alloys. The microstructure of Ti-6Al-4V consists of hexagonal close packed ( $\alpha$ ) and body centered cubic ( $\beta$ ) phases as shown by the phase diagram in Figure 2.39. The addition of Al stabilizes the  $\alpha$  phase while V stabilizes  $\beta$ . Generally, as-deposited microstructures after powder bed fusion (PBF) AM exhibit a fine martensitic ( $\alpha'$ ) structure with acicular laths while the microstructures in directed energy deposition (DED) AM typically have a coarser structure consisting of lamellar  $\alpha$  and small amounts of  $\beta$  [153]. Figure 2.40 (a) and (b) shows representative micrographs of Ti-6Al-4V fabricated by DED and PBF AM.

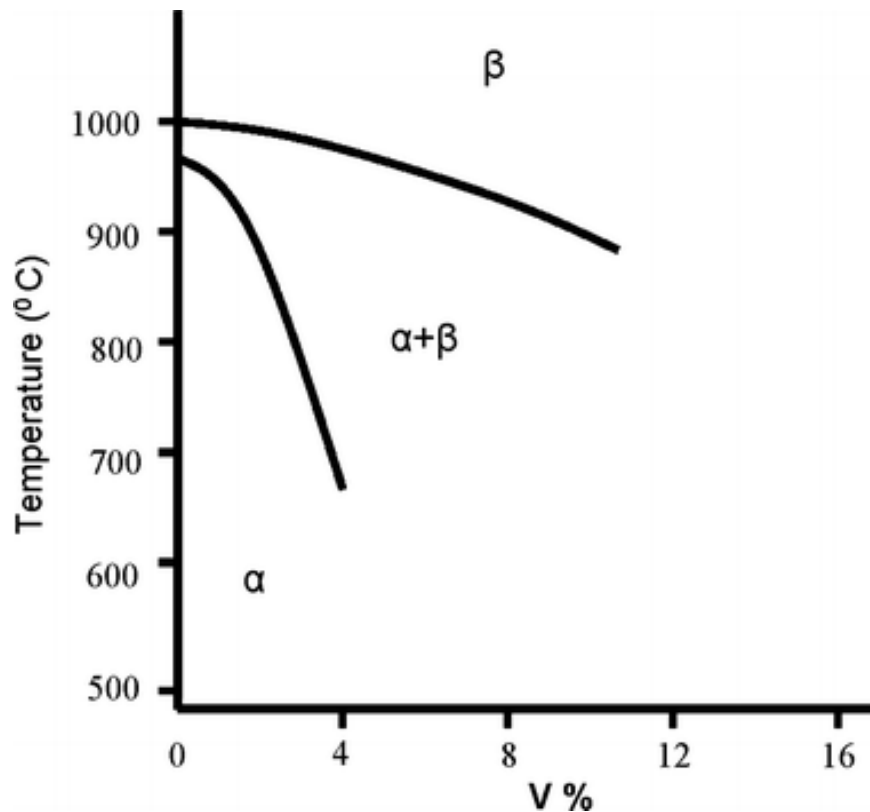


Figure 2.39. A portion of the Ti-Al-V phase diagram [236] for a constant aluminum concentration of 6 wt%.

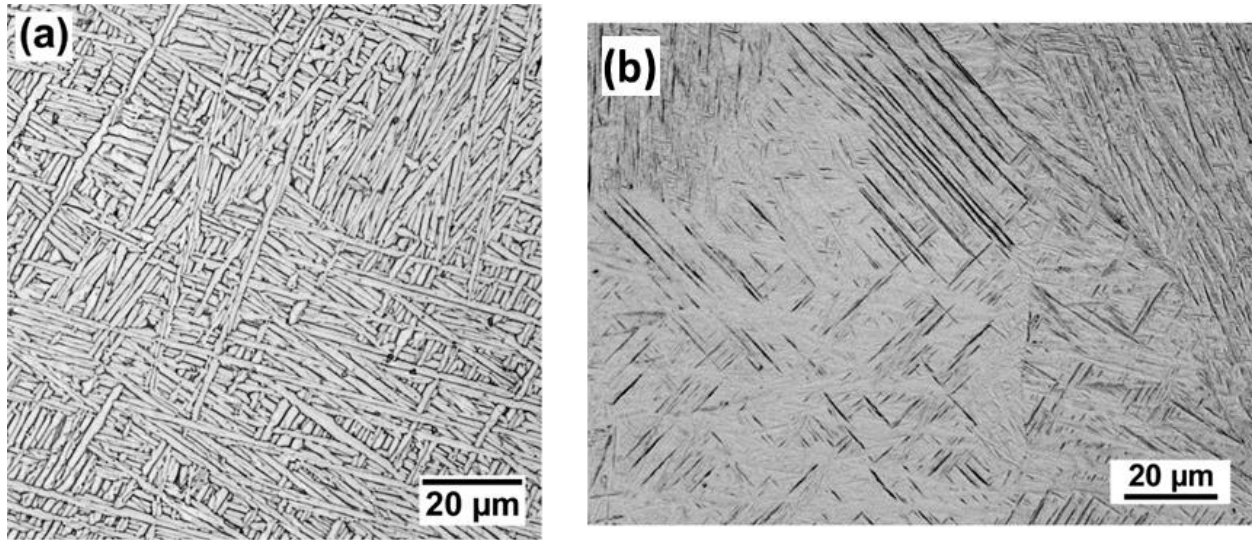


Figure 2.40. Representative micrographs of Ti-6Al-4V fabricated by (a) DED and (b) PBF after stress relieving [153]. Components fabricated by DED typically display coarse lamellar  $\alpha$ -laths with small amounts of  $\beta$  while PBF components have much finer acicular martensite ( $\alpha'$ ).

Ti-6Al-4V undergoes a transformation from the body centered cubic  $\beta$ -phase to a two phase structure consisting primarily hexagonally close-packed  $\alpha$ -phase and small amounts of  $\beta$ -phase at a temperature of approximately 1000°C [237]. The solid-state transformation can lead to quantifiable microstructural features within grains and depending on the cooling rate through transition temperature, the  $\alpha$ -phase can exhibit different morphologies. In many AM builds, needle-like  $\alpha$ -laths are present inside the large, prior  $\beta$  grains. Multiple studies have investigated the quantitative relationship between  $\alpha$ -lath width and mechanical properties like hardness, strength and ductility. A collection of measured data correlating  $\alpha$ -lath width to Vickers hardness is presented in Figure 2.41, which shows a decrease in hardness with the coarsening of the lath for DED-L and PBF-EB.

Heat treatments are used to relieve residual stresses and coarsen  $\alpha$ -phase morphology for increasing ductility and toughness at the expense of strength and hardness in Ti-6Al-4V components fabricated by AM. A similar behavior was observed during the wire fed DED-L of Ti-6Al-4V that was stress relieved at 600°C for 4 hours. The Vickers hardness of multiple samples deposited with different process parameters (~327 HV) was found to increase to approximately 343 HV after stress relieving. It was suggested that a combination of precipitation hardening and solid solution strengthening contributed the increase, as the selected heat treatment temperature

can also be used for aging and energy dispersive spectroscopy showed slightly less segregation compared to the as-deposited condition.

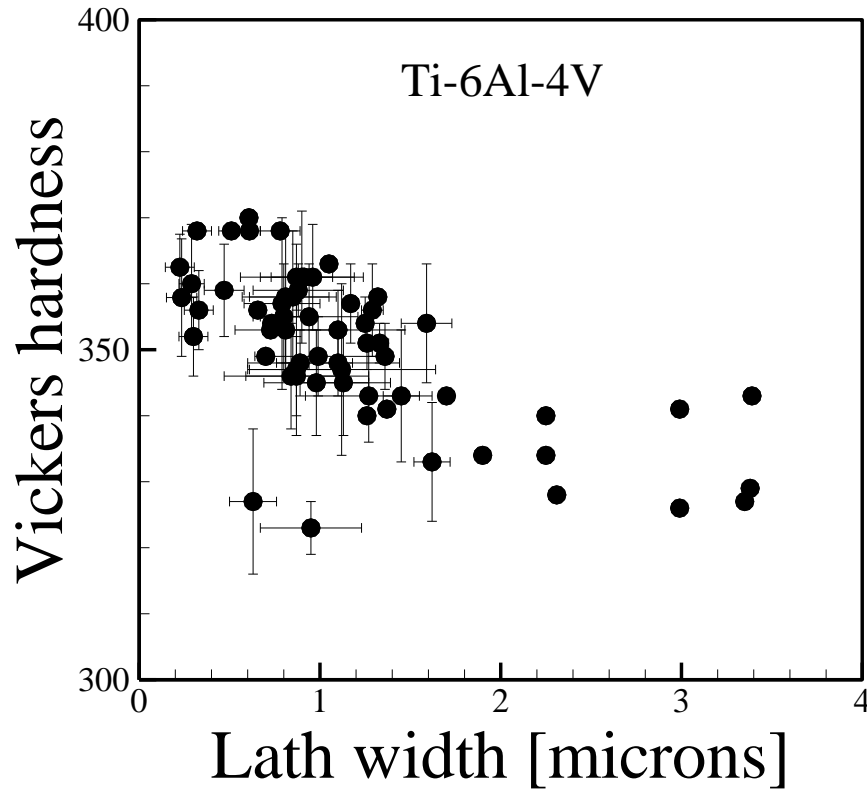


Figure 2.41. Vickers microhardness as a function of alpha lath width for Ti-6Al-4V fabricated by AM from [117, 215, 238-243]. Error bars, where available, represent the standard deviation in measurements.

### 2.3.2.5 Grain size

Grain size refining is known to have a significant impact on the strength and hardness of metals and alloys. The early works of Hall [21] and Petch [22, 244] described the effect of grain size,  $d$ , on yield strength,  $\sigma_y$ , in the well-known Hall-Petch relation,

$$\sigma_y = \sigma_0 + \frac{k_y}{\sqrt{d}} \quad (2.9)$$

where  $\sigma_0$  and  $k_y$  are material constants that represent the yield stress of a grain-free material and the strengthening coefficient, respectively. The expression was formulated to explain the observed phenomenon that fine-grained materials exhibit higher stresses prior to yielding compared to alloys with coarse grains. At grain boundaries where there is a change in crystallographic orientation, dislocations require more energy to move from one grain to another, thereby impeding dislocation

motion. Therefore, higher grain boundary area per unit volume (smaller grain size) effectively strengthens a material by blocking dislocation motion.

The works of Tabor [245] and Cahoon [246] have shown that hardness is directly proportional to yield strength. Recently, Keist and Palmer[153] investigated the strength-hardness relationships for the DED of Ti-6Al-4V using both laser and electron beam heat sources. Their correlation is plotted along with independent experimental data for Ti-6Al-4V components fabricated by PBF and DED processes in Figure 2.42. Similarly, a collection of data for the AM of SS316L is shown in Figure 2.43. While scatter in data from multiple researchers can be expected, both Figure 2.42 and Figure 2.43 clearly show positive correlations between yield strength and hardness for AM alloys fabricated by multiple techniques. Therefore, Equation (2.9) can also be applied to studies involving the relationship between hardness and grain size. When considering the microhardness measurement using a Vickers indenter, the relationship takes a similar form, where yield strength is replaced by Vickers hardness,  $HV$ , and  $HV_0$  is material constant reference hardness value replacing  $\sigma_0$ . As hardness is a measurement of *localized* plastic deformation, a hardness indent may be fully encompassed within a grain depending on the load, dwell time, and size of grains and the effect of strengthening due to dislocation propagation and pileup at grain boundaries may not be captured. Also, significant variability in measurements could result depending on where measurements are taken with respect to grains (center of grain, boundary, triple junction, etc.). Regardless, the acquisition of ample hardness measurements for many AM microstructures provides a simple means for investigating the effect of grain size on hardness.

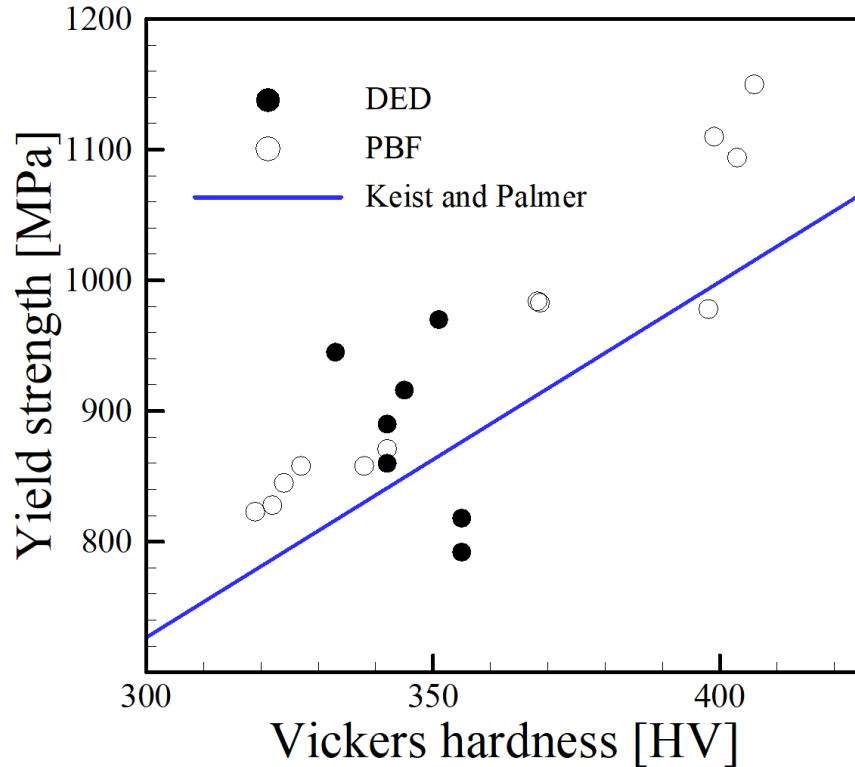


Figure 2.42. Comparison between the correlation developed by Keist and Palmer [153] and independent experimental data [117-121, 247-249] for yield strength and hardness measurements spanning multiple AM processes.

The Hall-Petch relation was originally developed for equiaxed grains and has found good agreement with experimental results in the grain size range on the order of approximately a few to hundreds of microns. Grain sizes in AM alloys typically fall within this range, however many grains have a columnar rather than equiaxed morphology. Also, grain sizes in PBF processes exhibit smaller grain sizes compared to DED processes. In the AM of IN625 for example, Li et al. [250] measured grain sizes  $<40 \mu\text{m}$  after PBF-L while Khayat and Palmer [218] measured sizes in the hundreds of microns for DED-L. Typically, aspect ratios in AM, which are defined as the ratio of grain length to grain width, range between 1 (equiaxed) and 10 (elongated columnar). As-deposited microstructures usually exhibit lower aspect ratios than heat treated samples where significant growth along the length dimension can occur. As relationships between grain size and yield strength are commonly reported in AM literature, it is important for researchers to be specific about the grain dimension used for analysis.

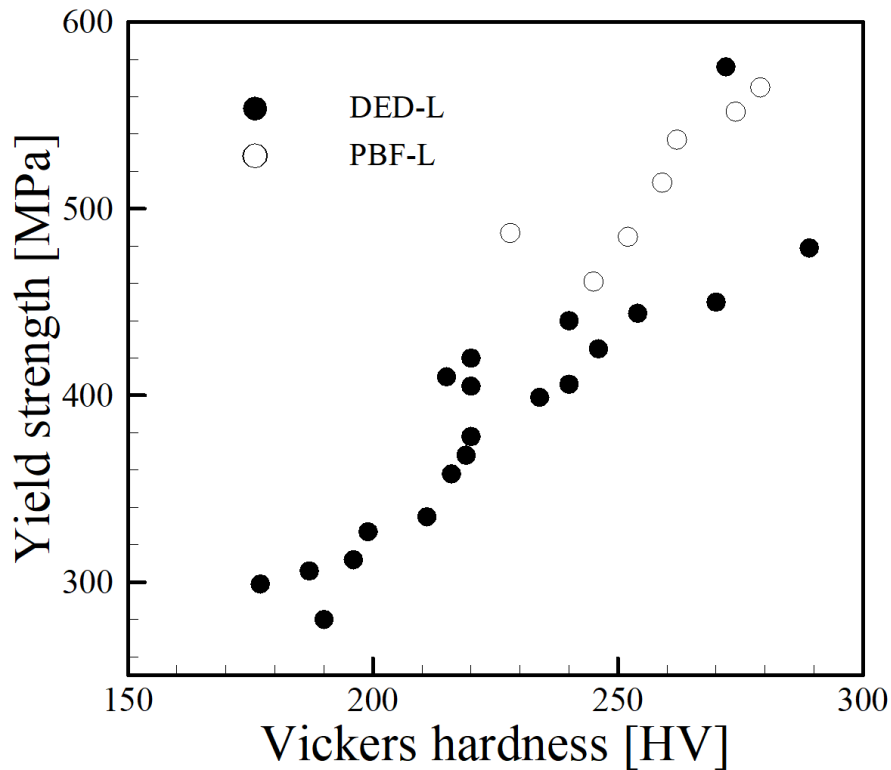


Figure 2.43. A collection of independent experimental data showing a comparison between measured yield strength and Vickers hardness for SS316L fabricated by AM [109, 111, 112, 251, 252].

Since grain coarsening is a thermally activated process, the amount of time that an alloy remains at high temperatures ultimately determines the size of grains. Therefore, high cooling rates such as those encountered in PBF processes tend to yield small grain sizes while low cooling rates in high power DED processes exhibit larger grains. Experimental data [151, 251] relating cooling rate to grain size and Vickers hardness for the AM of SS316L is shown in Figure 2.44. The data includes measurements from both DED-L and PBF-L processes at various combinations of laser power and scanning speed. In each study, the average grain diameter decreased with an increase in cooling rate. Consequently, an inverse relationship was obtained between Vickers hardness and average grain diameter, resulting in the Hall-Petch effect.

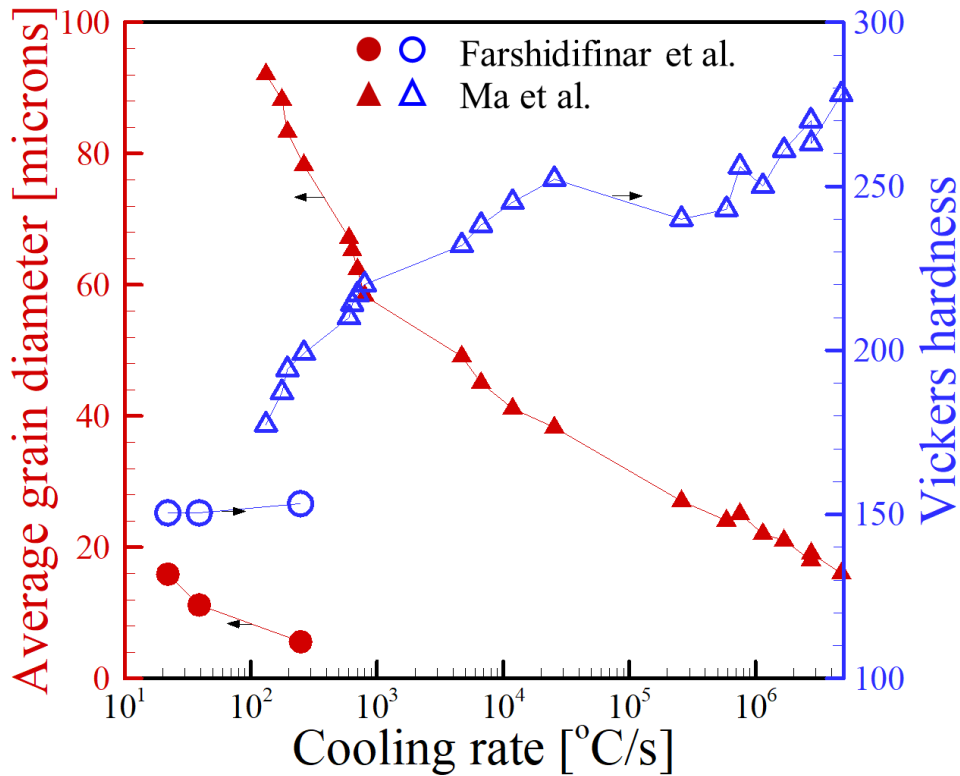


Figure 2.44. The relationship between cooling rate, average grain diameter, and Vickers hardness for the AM of SS316L [151, 251]. The cooling rate on the horizontal axis is plotted with a logarithmic scale and black arrows indicate the y-axis for each data set.

Wang et al. [253] studied the effects of processing conditions and microstructural features on the tensile properties of SS304L during DED-L. In their discussion, the grain dimension was defined as the average measured length of the grain in the direction of loading. It was found that the measured yield strength and grain sizes obeyed the Hall-Petch relation. Interestingly, the yield and tensile strengths measured in the transverse (parallel to the long grain axis) and longitudinal (parallel to the short grain axis) showed no clear anisotropic trends. In fact, a collection of literature data in a recent review [60] showed that although the microstructures of AM alloy components exhibit elongated columnar grains, the amount of anisotropy is negligible when comparing tensile properties in orthogonal directions. This finding is summarized in Figure 2.45 for different alloys and AM processes. Data points near the dotted lines in Figure 2.45 represent little anisotropy while those that stray from the line exhibit more anisotropic behavior.

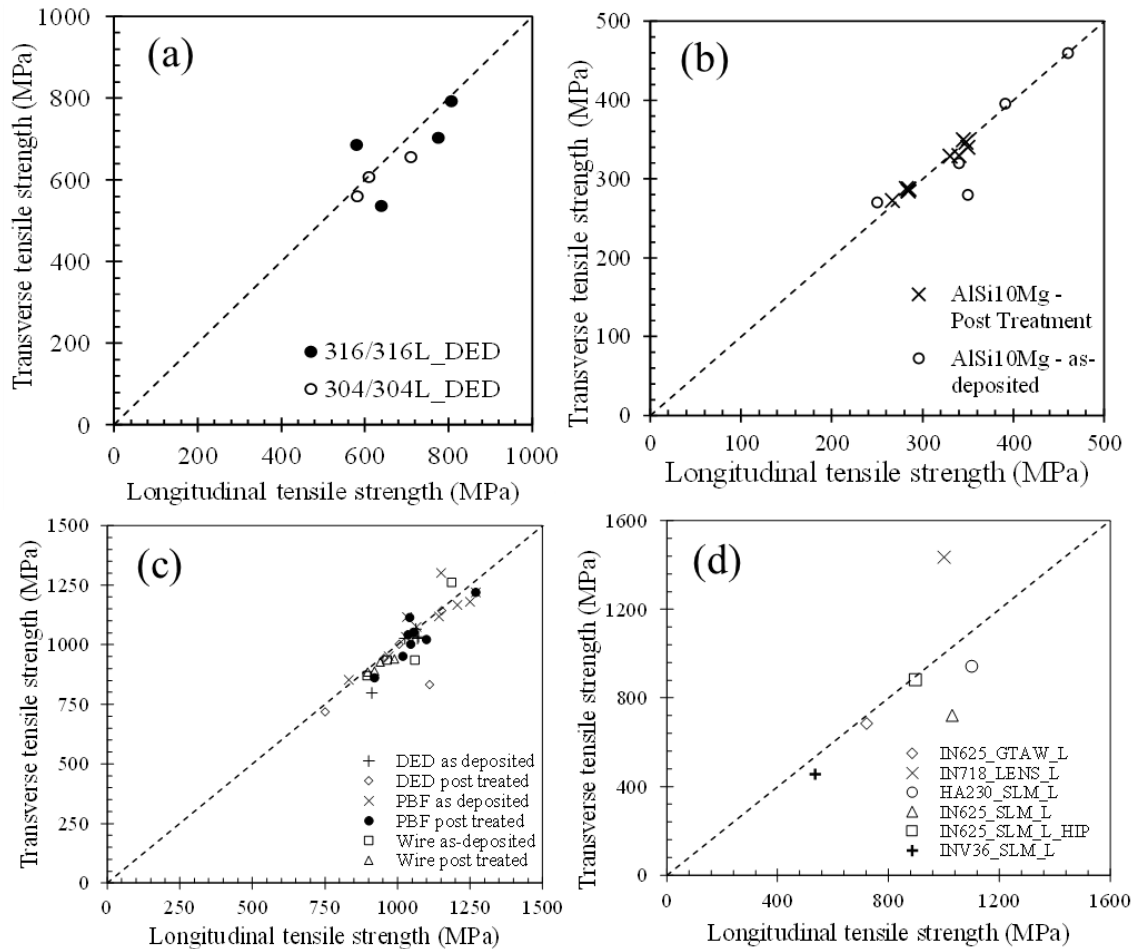
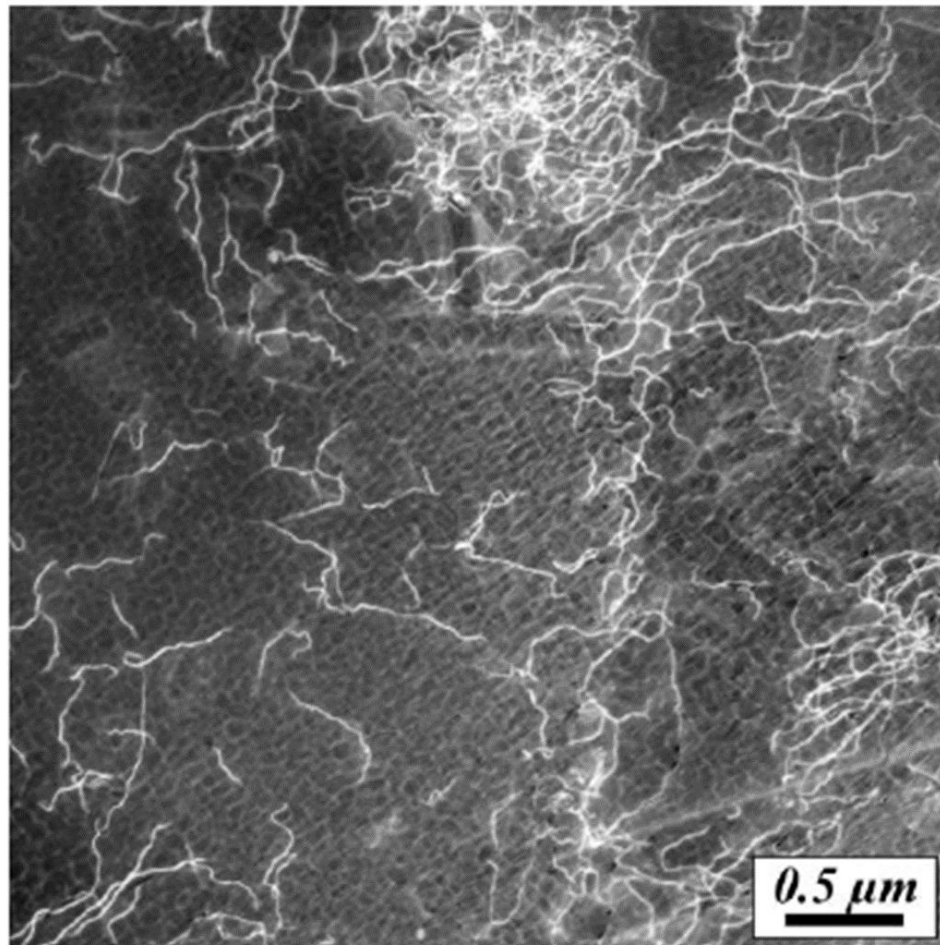


Figure 2.45. An analysis of anisotropic behavior [60] through a comparison between the transverse and longitudinal tensile strengths in additively manufactured (a) stainless steels [108, 109, 111, 253, 254] (b) aluminum alloy AlSi10Mg [168, 169, 255-259] (c) Ti-6Al-4V [62, 69, 117, 119, 260-271] and (d) nickel alloys [272-277]. Data points deviating from the dashed one-to-one line are exhibit more anisotropy compared to those lying close to the line.

### 2.3.2.6 Dislocations in AM materials

Although no investigations have directly examined the impact of dislocation structures on hardness in AM materials, it is important to discuss the role of dislocations on strengthening in general. The scale of dislocations requires experimental observation to be performed by transmission electron microscopy and Figure 2.46 shows an example of dislocations in a single crystal alloy fabricated by PBF-EB. In conventional metals processing, parts are often work hardened to achieve desired properties, which effectively uses plastic deformation to introduce a high density of dislocations. Dislocations can exist in many different forms such as edge, screw or mixed, where each introduces strain in the crystal lattice which affects the movement of neighboring dislocations during plastic deformation. In most introductory materials science and

engineering textbooks, the tradeoff between strength and ductility is formulated in which any increase in strength due to work hardening is accompanied by a loss in ductility. In a recent work by Wang and co-workers [278], a hierarchy of microstructures spanning multiple orders of magnitude was attributed to help overcome the conventional strength-ductility tradeoff for PBF-L of SS316L. Very fine cellular walls with high dislocation densities and elemental segregation were found to pin dislocation motion and promote twinning, which ultimately lead to an increase in both strength and ductility due to a steady work hardening behavior.



*Figure 2.46. TEM micrograph of dislocations in nickel-based superalloy CMSX-4 processed by PBF-EB AM [279].*

In a recent review, Gorsse et al. [280] offered a calculation procedure to determine the upper limit of dislocation density ( $5 \times 10^{15} \text{ m}^{-2}$ ) for steels by assuming that all linear thermal strain is accompanied by dislocations upon cooling after solidification. This rough estimation is in good agreement with reported dislocation densities of AM materials in Table 2.6. Overall, the

dislocation densities are comparable to those determined in wrought materials, which is uncharacteristic for materials that have not been work hardened. Moreover, the dislocations in AM materials are often organized into networks [281], as shown in Figure 2.47(a). As in conventional materials, heat treatment will effectively lead to a reduction in dislocation density as shown in Figure 2.47(b). Future research can take advantage of the unique dislocation structures in AM materials if the macroscopic process can be used to control the sub-micron microstructural features [278].

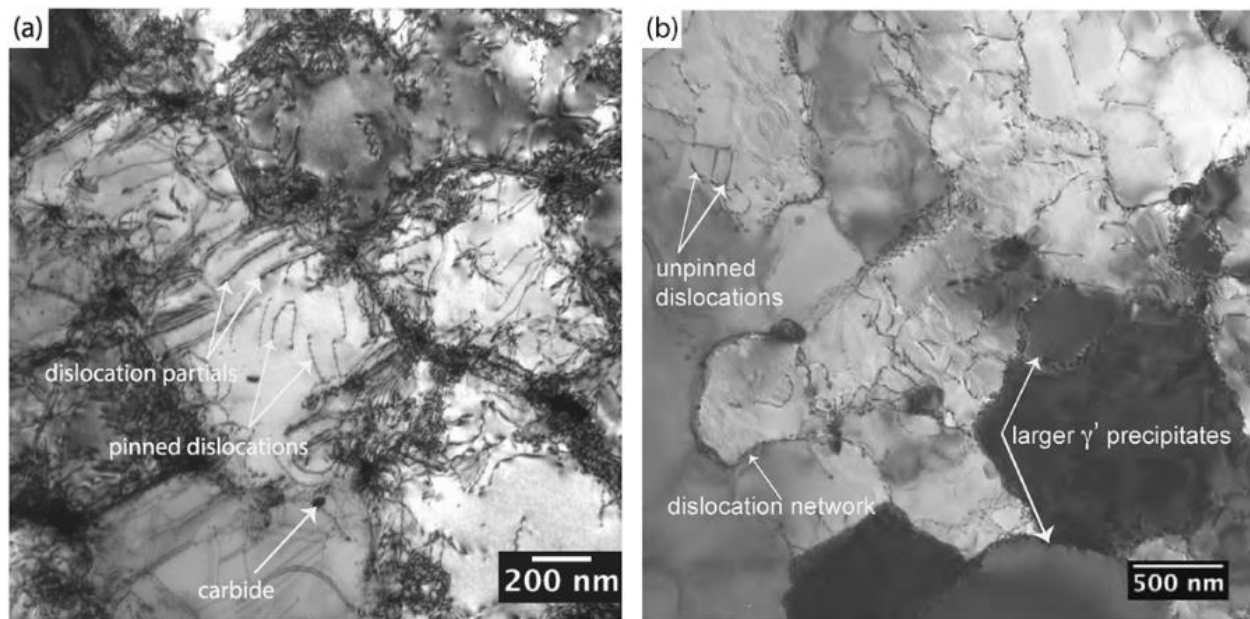


*Figure 2.47. Dislocation structures in nickel-based superalloy CM247LC fabricated by PBF-L [281] showing (a) high dislocation density in the as-deposited condition, especially near cell edges and (b) reduced dislocation density after heat treatment at 1230°C for 2h followed by air cooling.*

Table 2.6. A summary of dislocation densities reported for AM alloys

Alloy	Process	Dislocation density [m <sup>-2</sup> ]	Reference
SS316L	PBF-L	1.5 x 10 <sup>14</sup>	[282]
SS316L	PBF-L + Solutionized	9.7 x 10 <sup>13</sup>	[282]
SS316L	Hot worked + Solutionized	3.5 x 10 <sup>13</sup>	[282]
SS316L	DED-L	2.77 x 10 <sup>14</sup>	[283]
SS304L	DED-L	4.31 to 7.45 x 10 <sup>12</sup>	[283]
SS304L	PBF-EB	2.72 x 10 <sup>14</sup>	[283]
SS304L	Wrought	1.84 x 10 <sup>14</sup>	[283]
CrMnFeCoNi	DED-L	0.89 to 1.19 x 10 <sup>14</sup>	[284]
IN718	PBF-L	2.00 x 10 <sup>13</sup> to 5.62 x 10 <sup>15</sup>	[285]
Nb	PBF-EB	10 <sup>13</sup> to 10 <sup>14</sup>	[286]
Ti-6Al-4V	DED-EB + HIP	10 <sup>11</sup>	[287]
Ti-6Al-4V	DED-EB + Stress relieved	10 <sup>15</sup>	[287]
SS304L	PBF-L	(3.8 ± 1) x 10 <sup>14</sup>	[288]
SS304L	DED-L	(2.5 ± 1) x 10 <sup>14</sup>	[288]
SS304L	Wrought (deformed)	(6.8 ± 1) x 10 <sup>14</sup>	[288]

### 2.3.3 Compositional variables

#### 2.3.3.1 Iron alloys

A particularly useful approach for predicting properties of steels that has been previously used in the welding community is through the carbon equivalent [289]. The carbon equivalent can take on many forms that include various alloying elements to best suit the target application. The HV for various iron-based alloys can be related to composition using the critical weldability ( $P_{cm}$ ), which was originally derived for evaluating crack susceptibility for a wide variety of alloy steels, given as [290]:

$$P_{cm} = C + \frac{Si}{30} + \frac{Mn+Cu+Cr}{20} + \frac{Ni}{60} + \frac{Mo}{15} + \frac{V}{10} + 5B \quad (2.10)$$

All elements in Equation (2.10) are expressed in weight percent. The average HV values from independent experimental data [74, 155-162, 289] were plotted versus the  $P_{cm}$  of the alloy for the

following ranges of alloying elements: 0.02-0.99 wt% C, 0-10.2 wt% Co, 0-13.3 wt% Cr, 0.2-1.62 wt% Mn, 0.06-7.97 wt% Mo, 0.15-18.8 wt% Ni, 0.011-0.025 wt% P, 0.29-1.02 wt% Si, 0-0.88 wt% Ti, 0.03-2.01 wt% V and 0-6.32 wt% W. Since different measurement methods such as the Rockwell C hardness test are used for steels, a conversion between the hardness scales is needed. The following relationship was used to convert from the Rockwell C (HRC) to the HV scale [291]:

$$HV = 111e^{0.0316(HRC)} \quad (2.11)$$

Figure 2.48 shows that a linear fit is achieved between HV and composition for data from AM. It is well-accepted that process variables affect hardness of steels in AM based on many factors that include microstructural features. However, the linearity of Figure 2.48 shows that chemical composition of steels can provide an approximate value of hardness independent of the AM process variables selected.

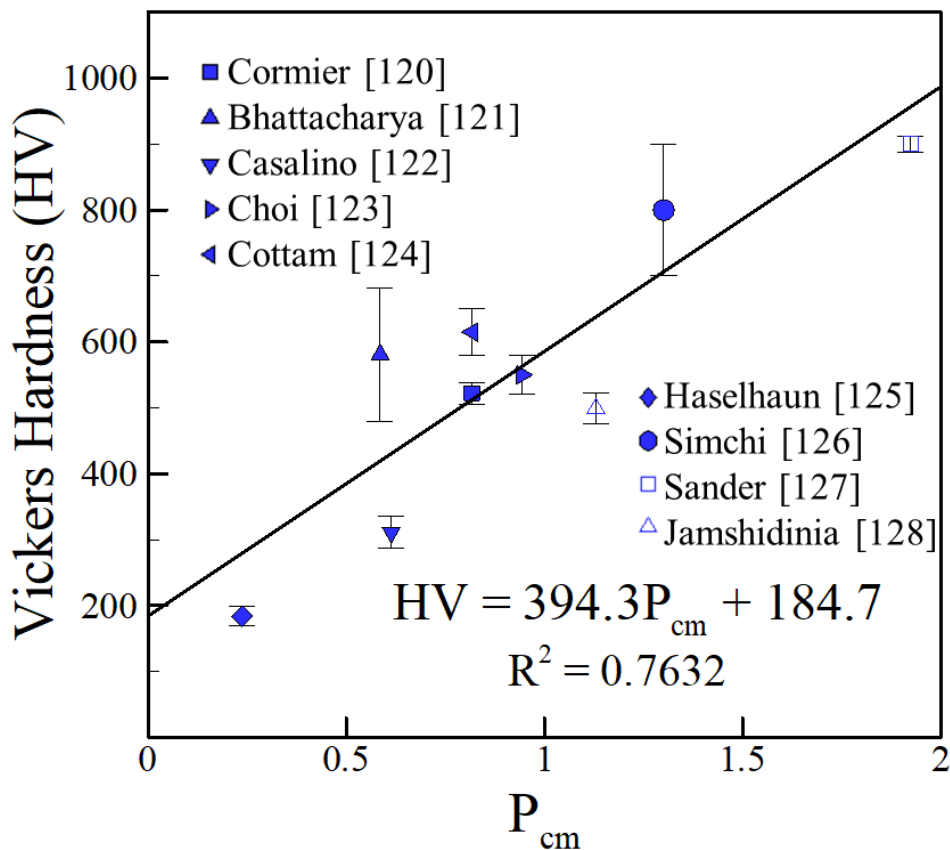


Figure 2.48. Experimentally measured hardness [74, 155-162] vs.  $P_{cm}$  of iron-based alloys for AM.

Table 2.7. Compositions (in wt%),  $P_{cm}$  values and average HV numbers for iron-based alloys

Alloy	C	Co	Cr	Mn	Mo	Ni	Si	Ti	V	W	$P_{cm}$	Average HV	Ref.
H13	0.37	-	4.99	0.2	1.1	-	1.02	-	0.8	-	0.817	‡498.5 ± 15	[155]
4340	0.42	-	0.9	0.74	0.45	2.63	0.29	-	-	-	0.586	580.5 ± 101	[156]
18Ni300 Maraging steel	0.02	10.2	-	-	4.2	18.8	-	0.88	-	-	0.613	‡323.5 ± 22	[157]
H13	0.47	-	5.01	0.2	1.2	-	0.63	-	1.12	-	0.944	550 ± 30	[158]
H13	0.35	-	5	0.35	1.5	-	-	-	1	-	0.818	615 ± 35	[159]
ER70S-6	0.1	-	0.15	1.62	0.15	0.15	1	-	0.03	-	0.237	184 ± 15	[160]
M2 steel	0.86	-	1.25	0.37	5.23	-	0.33	-	-	6.32	1.301	800 ± 100	[161]
FeCrMoVC tool steel	0.99	-	4.02	-	7.97	-	-	-	2.01	-	1.923	900 ± 12	[162]
420 SS	0.42	-	13.3	0.33	0.06	0.37	0.54	-	-	-	1.130	‡478 ± 20	[74]

‡ Converted from HRC to HV using Equation (2.11)

### 2.3.3.2 Aluminum alloys

Aluminum alloys offer great opportunity for producing lightweight parts for aerospace and automotive applications. As pure aluminum is a relatively soft metal, these alloys often rely on alloying elements to achieve higher strength and hardness through solid solution strengthening and work hardening, such as in 5xxx series alloys, or precipitation hardening, as in the 6xxx and 7xxx series.

A constrained multi-variate linear regression analysis is used for determining the dependence of as-deposited hardness on composition for the AM of aluminum alloys. The following relationship between experimentally measured HV values and chemical composition was obtained where each element is in weight percent:

$$\begin{aligned}
 HV = & 37.99 + 19.47Ag + 2.85Cu + 23.36Fe + 24.47Mg \\
 & + 30.00Mn + 5.43Si + 20.86Ti + 19.06Zn
 \end{aligned}
 \tag{2.12}$$

The correlation presented is valid for the following ranges of alloying elements: 0-0.5 wt% Ag, 0-5.3 wt% Cu, 0-0.8 wt% Fe, 0-1.95 wt% Mg, 0-0.55 wt% Mn, 0-12.2 wt% Si, 0-0.064 wt% Ti and 0-0.1 wt% Zn. The data points with alloying elements that were well outside of the valid ranges

mentioned above were omitted. The relationship between the measured hardness and the hardness calculated using Equation (2.12) for AM data [163-171] is shown in Figure 2.49. The solid line in the plot is the one-to-one relationship between measured and calculated values, meaning that a point falling on this line is exactly predicted by Equation (2.12). The chemical compositions are shown in Table 2.8.

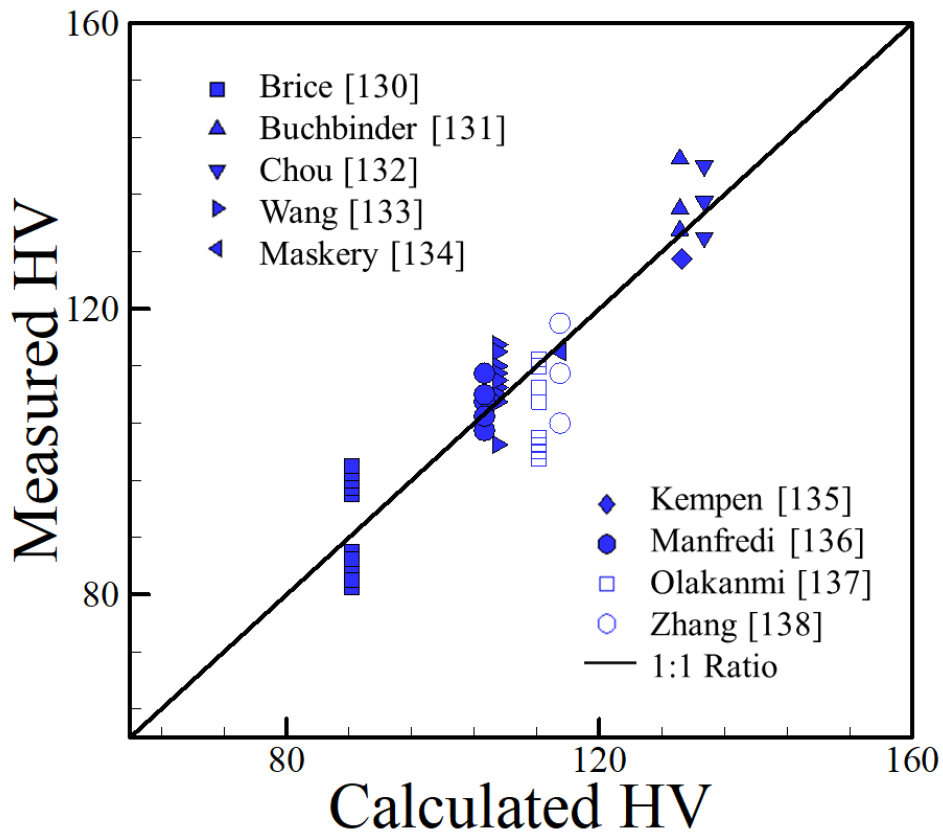


Figure 2.49. Experimentally measured [163-171] and calculated HV of aluminum alloys fabricated by AM using Equation (2.12).

Table 2.8. Compositions (in wt%) and HV ranges used for aluminum-based alloys

Alloy	Ag	Cu	Fe	Mg	Mn	Si	Ti	Zn	HV	Ref.
Al 2139	0.5	5.3	0.08	0.52	0.31	0.051	0.064	-	81-103	[163]
AlSi10Mg	-	-	0.55	0.4	0.45	10	-	0.1	131-141	[164]
Al-12Si	-	0.3	0.8	0.1	0.15	12	-	0.2	130-140	[165]
Al-12Si	-	0.003	0.12	-	-	12.2	-	-	107-115	[166]
AlSi10Mg	-	0.05	0.25	0.4	0.1	10	0.1	0.1	114	[167]
AlSi10Mg	-	0.1	0.55	0.4	0.45	10	-	0.1	127	[168]
AlSi10Mg	-	0.001	0.16	0.35	0.002	10.08	0.01	0.002	103-111	[169]
Al-12Si	-	0.08	0.36	-	-	12.1	-	-	99-113	[170]
Al 2024	-	4.47	-	1.95	0.55	-	-	-	104-118	[171]

### 2.3.3.3 Nickel alloys

Nickel alloys are sought after for their excellent high temperature properties and corrosion resistance. Often, alloying elements can account for nearly 50% of the total weight of the alloy. Many nickel alloys are age-hardenable and under the appropriate heat treatment, they can exhibit numerous equilibrium phases consisting of solid solutions, intermetallic compounds and fine precipitates. However, it is often found that due to the high cooling rates encountered during AM, insufficient time is given for these secondary phases to nucleate and grow and many major alloying elements can remain in solid solution [292].

A form of the nickel equivalent [293] is adopted, which is used as a guide for predicting austenite stability during high cooling rate processes, such as welding. The expression used is given as:

$$Ni_{EQ} = Ni + 0.65Cr + 0.98Mo + 1.05Mn + 0.35Si + 12.6C \quad (2.13)$$

where all elements are given in weight percentage. To include other alloying elements, a linear regression analysis can be applied to the remainder of elements that are not included in the  $Ni_{EQ}$  expression. The final term, which will be denoted as  $\phi$ , can be expressed as:

$$\phi = Ni_{EQ} - 6.36Al + 3.80B + 0.01Co + 0.26Fe + 7.06Hf + 1.20Nb + 4.95Ta + 5.78Ti + 2.88W \quad (2.14)$$

where all elements are given in weight percentage. The expression is valid in the following range of elements: 0-6.5 wt% Al, 0-3.75 wt% B, 0-0.5 wt% C, 0-19.2 wt% Co, 0-21.8 wt% Cr, 0-24.7 wt% Fe, 0-1.5 wt% Hf, 0-0.48 wt% Mn, 0-9.75 wt% Mo, 0-5.1 wt% Nb, 0-4.25 wt% Si, 0-6.35 wt% Ta, 0-4.7 wt% Ti and 0-4.9 wt% W. The compositions and HV values used are shown in Table 2.9. Only elements which either were common to the majority of the alloys considered or contributed to a significant portion of the alloy composition were considered in the analysis as they had negligible effects on the outcome. When independent HV measurements [129, 172-186, 188, 294] are plotted against  $\phi$  for various nickel alloys, the trend is linear as shown in Figure 2.50.

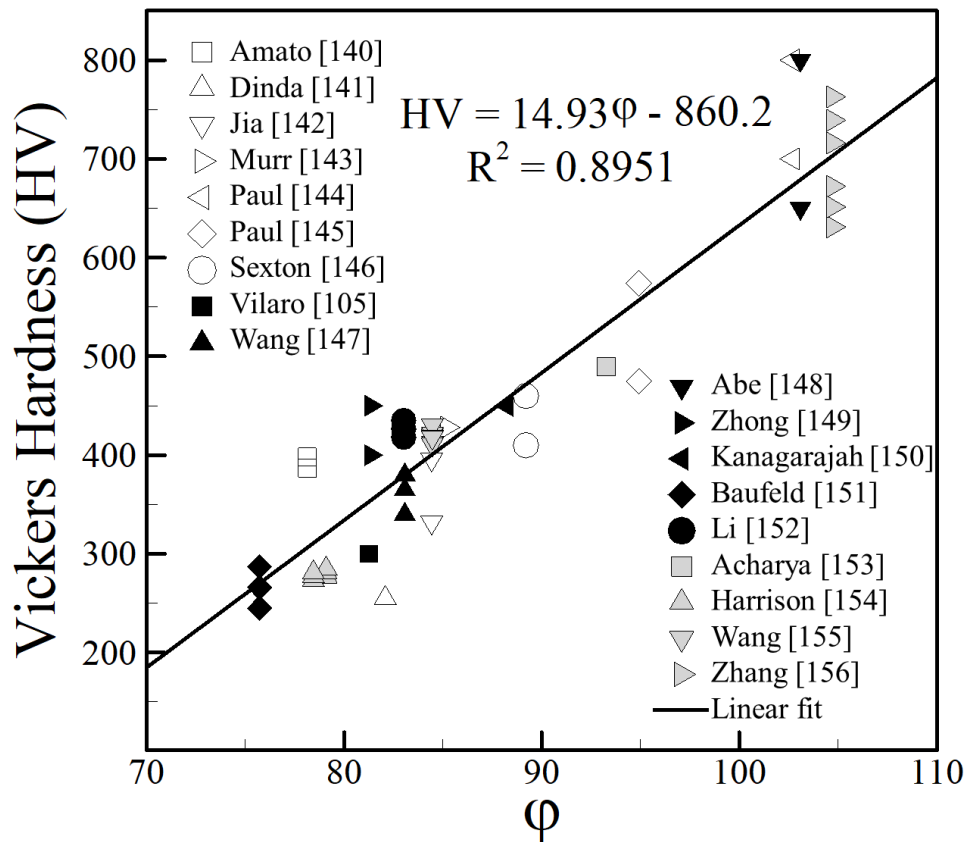


Figure 2.50. As-deposited HV [129, 172-186, 188, 294] as a function of  $\phi$ , which depends on the chemical composition of nickel-based AM alloys.

Table 2.9. Compositions (in wt%) and range of HV numbers for nickel alloys

Alloy	Al	Co	Cr	Fe	Mo	Nb	Si	Ti	C	Other	HV	Ref.
IN718	0.5	1.0	19.0	22.0	3.0	5.0	-	1.0	-	-	387-398	[172]
IN718	0.5	-	19.0	22.0	3.0	5.0	-	1.0	-	-	255	[173]
IN718	0.3	-	18.4	17.7	4.2	5.1	-	0.9	0.08	-	331.9-395.8	[129]
Rene 142	6.15	12.0	6.8	-	1.5	5.1	-	0.9	0.12	0.02B-1.5Hf- 6.35Ta-4.9W	428.1	[174]
Colmonoy 6	-	0.24	13.6	4.75	-	-	4.25	-	0.6	2.5B	700-800	[176]
IN625	0.4	1.0	21.3	5.0	9.2	1.8	0.5	0.4	0.1	1.8Ta	‡474.9-574.1	[175]
Rene 142	3.0	9.5	14.0	0.1	3.8	0.03	0.01	5.0	0.14	0.02B-0.01Hf- 0.01Mn-0.01Ta	410-460	[177]
Nimonic 263	0.5	19.2	19.5	0.5	6.0	-	0.2	2.4	-	-	300	[178]
IN718	0.29	-	18.2	18.9	3.1	5.1	-	0.9	0.03	-	340-380	[179]
Experimental	-	-	9.4	2.0	-	-	2.8	-	0.4	1.8B	650-800	[180]
IN718	0.41	-	15.9	17.1	1.9	2.23	-	1.27	-	0.31W	400-450	[181]
IN939	1.9	19.0	22.4	-	-	1.0	-	3.7	0.15	0.01B-1.4Ta- 2.0W	450	[182]
IN718	-	-	19.0	24.7	3.0	-	0.35	-	0.08	0.35Mn	245-287	[183]
Rene 41	1.6	11.0	19.0	5.0	9.75	-	0.5	3.25	0.09	0.01B-0.5Mn	418.1-435.1	[184]
Rene 80	3.0	9.0	14.0	-	4.0	-	-	4.7	0.16	0.02B-0.8Hf	489.8	[185]
Hastelloy X	-	1.77	21.8	18.6	9.4	-	0.31	-	0.05	0.22Mn-1.05W	276.9-284.9	[186]
Hastelloy X	-	1.04	21.3	19.5	9.0	-	0.32	-	0.06	0.48Mn-0.56W	273.2-281.0	[186]
IN718	-	-	18.3	18.9	2.0	4.6	-	0.83	-	-	410.8-430.2	[187]
Ni60A	-	-	16.5	8.0	-	-	4.25	-	0.75	3.75B	‡631.1-762.9	[188]

‡ Converted from HRC to HV using Equation (2.11)

#### 2.3.3.4 Comparison with other processes

It is often useful to compare microstructures and properties with the cooling rates of various processes. Since AM is a rapidly emerging field and the underlying science is still being understood, it can be beneficial to compare the hardness of AM alloys with measurements from other processes. Let us consider fusion welding, where melting is used for joining, and friction stir welding (FSW), a process where solidification is not involved and joining is performed in solid state. To understand the relative role of manufacturing process variables and the chemical composition of steels, Figure 2.51 combines hardness data for steels from AM, FSW and fusion welding literature. Table 2.7 shows the specific compositions for AM while the compositions and hardness values for FSW and fusion welding can be found elsewhere [289, 295, 296]. To give the reader a sense of the cooling rates, Table 2.10 shows a collection of available data for cooling rates measured in the three processes. There are many orders of magnitude difference between the processes, ranging from reported values of 3 K/s for friction stir welding to  $10^4$  K/s for additive manufacturing.

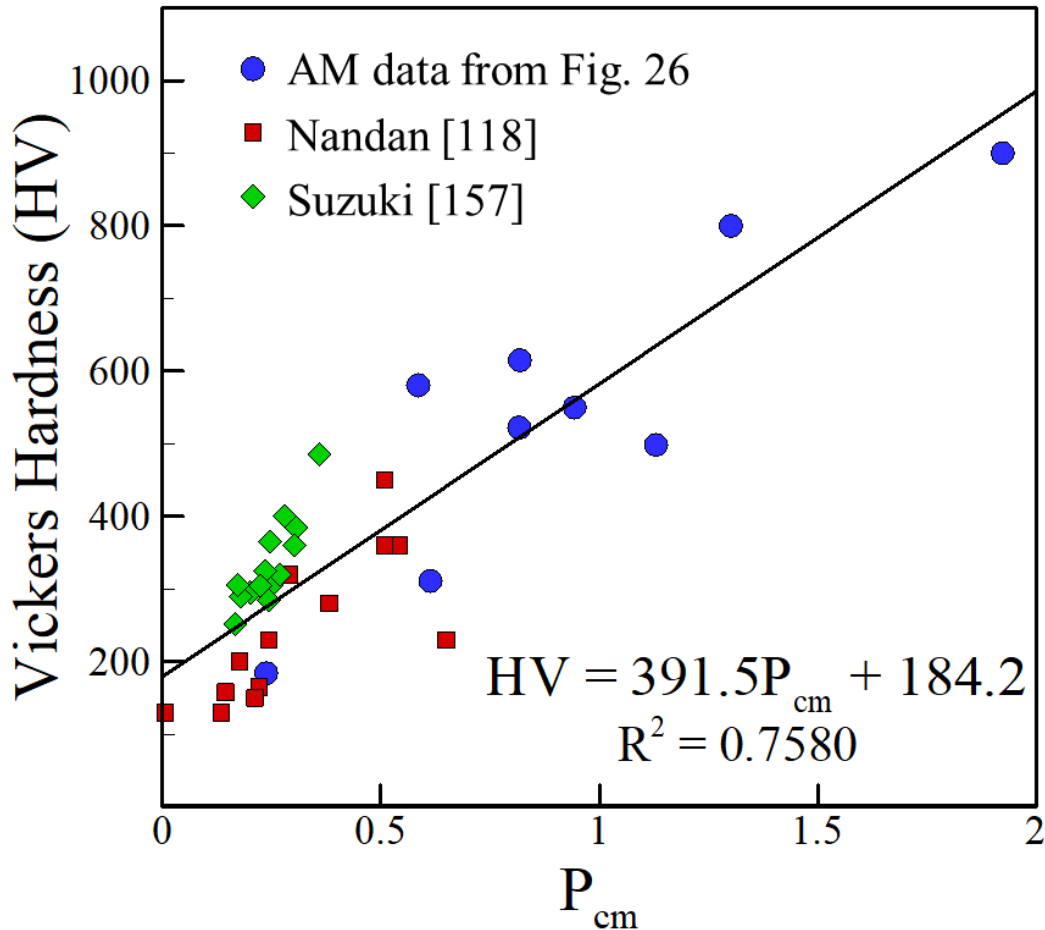


Figure 2.51. Comparison between measured as-deposited hardness values of iron-based alloys in AM, TMAZ hardness values of FSW and as-welded hardness from fusion welding.

Similar analyses for the hardness of steels in the thermo-mechanically affected zone (TMAZ) of FSW and the heat affected zone (HAZ) of fusion welding were presented by Nandan et al. [289] and Suzuki [295]. When comparing their work to Figure 2.51, striking similarities are observed. Combining the data from AM, FSW and fusion welding, the HV of steels is linearly dependent on  $P_{cm}$  with  $R^2=0.7580$ , which is slightly lower than the value of  $R^2 = 0.7632$  obtained for only AM data alone indicating consistency in the relationships. Figure 2.51 shows that when hardness is calculated for the TMAZ of FSW and the HAZ of fusion welding using Equation (2.10), a good correlation with a trend consistent to the AM data is obtained. It is important to note that the data from Ito and Bessyo [296] for which  $P_{cm}$  was originally derived for was clustered around small  $P_{cm}$  values of less than 0.4 that resulted in a large slope of the  $P_{cm}$  vs. HV plot as shown by Suzuki [295]. As this work extends to a much broader range of  $P_{cm}$  values up to almost 2, a smaller slope is obtained. These findings show that the presented approximations can be

applied to three different types of joining processes while still producing consistent results, highlighting the important role of composition for predicting hardness of steels.

*Table 2.10. Reported cooling rates for FSW, fusion welding and AM*

<b>Process</b>	<b>Values/Ranges [K/s]</b>	<b>Reference</b>
FSW	~5	[297]
FSW	~3 to 5	[298]
FSW	~90 to 120	[299]
FSW	~10	[300]
Submerged FSW	~20	[301]
Fusion welding	~5	[302]
Laser welding	$10^0$ to $10^5$	[26]
Fusion welding	$\sim 10^3$	[290]
DED-L	4500	[303]
PBF-L	$10^3$ to $10^4$	[260]
DED-L	$10^4$	[304]
DED-L	$\sim 10^3$ - $10^4$	[152]
PBF-L	$1.0 \times 10^6$ to $4.0 \times 10^7$	[305]

Data for the measured and predicted as-deposited hardness of FSW aluminum alloys is also compared to AM data in Figure 2.52. A similar plot for the hardness of aluminum alloys were presented by Arora et al. [306] for the FSW of aluminum alloys. Figure 2.52 shows that when as-welded hardness is calculated for the TMAZ of FSW using Equation (2.12), a good correlation with a trend consistent to the AM data is obtained. These findings show that Equation (2.12) can be applied to both AM and FSW while ignoring process variables and is still capable of producing approximate hardness values, signifying the importance of chemical composition in determining the hardness of aluminum alloys. For the FSW data, Mg and Zn were important alloying elements for the alloys considered, which is not the case here.

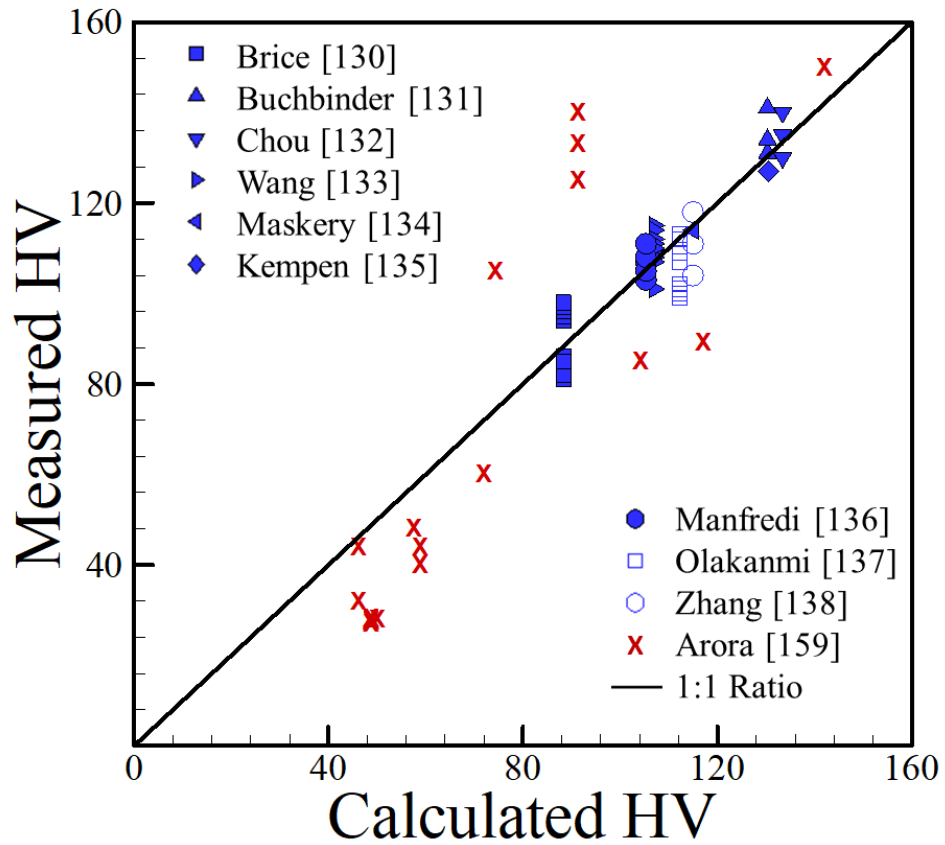


Figure 2.52. Comparison between measured and calculated hardness values using Equation (2.12) for AM and FSW data [306].

#### 2.3.4 Summary

The role of cooling rate, microstructure and alloy composition on the published hardness data of iron, aluminum, titanium and nickel alloy components fabricated by additive manufacturing are examined. When the available data are critically reviewed, the following important conclusions that cannot be made from individual papers become apparent:

- The variations of process parameters and cooling rates change microstructures of AM alloys. However, when the influence of AM process parameters on hardness is evaluated from the reported independent hardness values of fabricated components prior to post-deposition heat treatment, the variation of hardness falls within a narrow band of values for ferrous, aluminum and nickel alloys.
- The range of hardness variation of AM alloys in the as-fabricated state attainable by varying AM process parameters is much lower than the hardness enhancement attainable by subsequent heat treatment or aging. The extent of hardness variation by varying AM process variables is roughly the same as the reported variations of hardness of iron and aluminum alloy weld metals when welding parameters are varied.
- The reported hardness data show approximate linear trends with appropriate compositional variables for iron, aluminum, and nickel alloys over a wide range of AM variables and processes. The scatter in the hardness data for all alloy systems fall within a small band of values that correlates well with the concentration of alloying elements. The correlations developed are approximate and valid for the range of composition indicated, but the findings are consistent over a wide range of processes and process parameters.
- Although AM offers many advantages in fabricating metallic components, a target hardness of components in as fabricated condition is much more easily obtained by alloy selection rather than by changing AM processing variables. In this sense, the AM produced materials behave in a similar manner to other conventional metals processing technologies.

## 2.4 References

- [1] D. Roberts, R. Ryder, R. Viswanathan, Performance of dissimilar welds in service, *J. Press. Vess.*, 107(3) (1985) 247-254.
- [2] C. Lundin, Dissimilar metal welds-transition joints literature review, *Weld. J.*, 61(2) (1982) 58-63.
- [3] J. DuPont, R. Mizia, Review of dissimilar metal welding for the NGNP helical-coil steam generator, Idaho Falls, ID, 2010,
- [4] J. DuPont, Microstructural evolution and high temperature failure of ferritic to austenitic dissimilar welds, *Int. Mater. Rev.*, 57(4) (2012) 208-234.
- [5] M. Sireesha, V. Shankar, S.K. Albert, S. Sundaresan, Microstructural features of dissimilar welds between 316LN austenitic stainless steel and alloy 800, *Mater. Sci. Eng. A*, 292(1) (2000) 74-82.
- [6] C. Jang, J. Lee, J.S. Kim, T.E. Jin, Mechanical property variation within Inconel 82/182 dissimilar metal weld between low alloy steel and 316 stainless steel, *Int. J. Pres. Ves. Pip.*, 85(9) (2008) 635-646.
- [7] L.S. Darken, Diffusion of carbon in austenite with a discontinuity in composition, *Trans. AIME.*, 180 (1949) 430-438.
- [8] C. Wagner, *Thermodynamics of alloys*, Addison-Wesley Press, Cambridge, MA, 1952.
- [9] J.N. DuPont, Microstructural evolution and high temperature failure of ferritic to austenitic dissimilar welds, *Int. Mater. Rev.*, 57(4) (2012) 208-234.
- [10] S. Sridhar, P. Rozzelle, B. Morreale, D. Alman, Materials challenges for advanced combustion and gasification fossil energy systems, *Metall. Mater. Trans. A*, 42(4) (2011) 871-877.
- [11] C. Sudha, A.L.E. Terrance, S.K. Albert, M. Vijayalakshmi, Systematic study of formation of soft and hard zones in the dissimilar weldments of Cr–Mo steels, *J. Nucl. Mater.*, 302(2) (2002) 193-205.
- [12] R. Ryder, C. Li, R. Viswanathan, J. Dimmer, Dissimilar metal weld failures in power plants—Causes and remedies, *Trends in electric utility research*, (1984) 137.
- [13] M. Huang, d.L. Wang, Carbon migration in 5Cr-0.5 Mo/21Cr-12Ni dissimilar metal welds, *Metall. Mater. Trans. A*, 29(12) (1998) 3037-3046.
- [14] F. Mas, C. Tassin, N. Valle, F. Robaut, F. Charlot, M. Yescas, F. Roch, P. Todeschini, Y. Bréchet, Metallurgical characterization of coupled carbon diffusion and precipitation in dissimilar steel welds, *J. Mater. Sci.*, 51(10) (2016) 4864-4879.
- [15] F.C. Liu, T.W. Nelson, S.L. McCracken, Effect of Post-weld Heat Treatment on Microstructure and Mechanical Properties of Dissimilar Metal Weld Used in Power Plants, *Metall. Mater. Trans. A*, 50(6) (2019) 2826-2834.
- [16] Y. Zhao, J. Gong, X. Wang, W. Gao, Q. Li, Carbon diffusion in dissimilar joints between P91 and 12Cr1MoV steels welded by different consumables at high temperature, *Mater. High Temp.*, 32(6) (2015) 557-565.
- [17] T. Helander, J. Ågren, Computer simulation of multicomponent diffusion in joints of dissimilar steels, *Metall. Mater. Trans. A*, 28(2) (1997) 303-308.
- [18] J.P. Galler, J.N. DuPont, S.S. Babu, M. Subramanian, Design of Graded Transition Joints Through Thermodynamic and Kinetic Modeling, *Metall. Mater. Trans. A*, 50(6) (2019) 2765-2783.
- [19] G. Brentrup, B. Snowden, J. DuPont, J. Grenestedt, Design considerations of graded transition joints for welding dissimilar alloys, *Weld. J.*, 91 (2012) 252-59.

- [20] S.A. David, J.A. Siefert, Z. Feng, Welding and weldability of candidate ferritic alloys for future advanced ultrasupercritical fossil power plants, *Sci. Technol. Weld. Joi*, 18(8) (2013) 631-651.
- [21] E. Hall, The deformation and ageing of mild steel: III discussion of results, *Proceedings of the Physical Society of London Section B*, 64(9) (1951) 747-753.
- [22] N.J. Petch, The cleavage strength of polycrystals, *Journal of the Iron and Steel Institute*, 174 (1953) 25-28.
- [23] A.K. Bhaduri, S. Venkadesan, P. Rodriguez, P.G. Mukunda, Transition metal joints for steam generators—An overview, *Int. J. Pres. Ves. Pip.*, 58(3) (1994) 251-265.
- [24] B. Dooley, P.S. Chang, The current state of boiler tube failures in fossil plants, *Power Plant Chemistry*, 2(4) (2000) 197-203.
- [25] A. Elrefaey, Y. Javadi, J.A. Francis, M.D. Callaghan, A.J. Leonard, Evolution of microstructure and toughness in 2.25 Cr-1Mo steel welds, *Int. J. Pres. Ves. Pip.*, (2018).
- [26] T. DebRoy, S.A. David, Physical processes in fusion welding, *Rev. Mod. Phys.*, 67(1) (1995) 85-112.
- [27] S. David, T. DebRoy, Current issues and problems in welding science, *Science*, 257(5069) (1992) 497-502.
- [28] J. Dupont, C. Kusko, Martensite formation in austenitic/ferritic dissimilar alloy welds, *Weld. J.*, 86(2) (2007) 51.
- [29] W.D. Callister, D.G. Rethwisch, *Materials science and engineering: An introduction*, John Wiley & Sons New York, 2007.
- [30] M. Gittos, T. Gooch, The interface below stainless steel and nickel-alloy claddings, *Weld. J.*, 71 (1992) 461s-472s.
- [31] S.-J. Lee, K.-S. Park, Prediction of martensite start temperature in alloy steels with different grain sizes, *Metall. Mater. Trans. A*, 44(8) (2013) 3423-3427.
- [32] G. Ghosh, G. Olson, Computational thermodynamics and the kinetics of martensitic transformation, *J. Phase Equilib.*, 22(3) (2001) 199.
- [33] T. Cool, H.K.D.H. Bhadeshia, Prediction of martensite start temperature of power plant steels, *Mater. Sci. Tech.*, 12(1) (1996) 40-44.
- [34] A. Dalcher, T. Yang, C. Chu, High temperature thermal-elastic analysis of dissimilar metal transition joints, *J. Eng. Mater.*, (1977).
- [35] R. Klueh, J. King, Austenitic stainless steel-ferritic steel weld joint failures, *Weld. J.*, 61(9) (1982) 302-311.
- [36] A. Joseph, S.K. Rai, T. Jayakumar, N. Murugan, Evaluation of residual stresses in dissimilar weld joints, *Int. J. Pres. Ves. Pip.*, 82(9) (2005) 700-705.
- [37] K. Laha, K.B.S. Rao, S. Mannan, Creep behaviour of post-weld heat-treated 2.25 Cr-1Mo ferritic steel base, weld metal and weldments, *Mater. Sci. Eng. A*, 129(2) (1990) 183-195.
- [38] J. Race, H. Bhadeshia, Precipitation sequences during carburisation of Cr–Mo steel, *Mater. Sci. Tech.*, 8(10) (1992) 875-882.
- [39] K. Laha, K. Chandravathi, K.B.S. Rao, S. Mannan, D. Sastry, An assessment of creep deformation and fracture behavior of 2.25 Cr-1Mo similar and dissimilar weld joints, *Metall. Mater. Trans. A*, 32(1) (2001) 115-124.
- [40] K. Laha, K.S. Chandravathi, P. Parameswaran, S. Goyal, M.D. Mathew, A comparison of creep rupture strength of ferritic/austenitic dissimilar weld joints of different grades of Cr-Mo ferritic steels, *Metall. Mater. Trans. A*, 43(4) (2012) 1174-1186.

- [41] Q. Wu, F. Lu, H. Cui, X. Liu, P. Wang, X. Tang, Role of butter layer in low-cycle fatigue behavior of modified 9Cr and CrMoV dissimilar rotor welded joint, *Mater. Des.*, 59 (2014) 165-175.
- [42] Q. Wu, F. Lu, H. Cui, X. Liu, P. Wang, Y. Gao, Soft zone formation by carbon migration and its effect on the high-cycle fatigue in 9% Cr–CrMoV dissimilar welded joint, *Mater. Lett.*, 141 (2015) 242-244.
- [43] Y. Zhao, J. Gong, Y. Jiang, The effect of carbon diffusion on creep behaviours for a dissimilar joint between P91 and 12Cr1MoV steels, ASME 2016 Pressure Vessels and Piping Conference, American Society of Mechanical Engineers, 2016, p. V005T09A024.
- [44] J.W. Kim, K. Lee, J.S. Kim, T.S. Byun, Local mechanical properties of Alloy 82/182 dissimilar weld joint between SA508 Gr.1a and F316 SS at RT and 320°C, *J. Nucl. Mater.*, 384(3) (2009) 212-221.
- [45] M. Subramanian, J. Galler, J. DuPont, B. Kombaiah, X. Yu, Z. Feng, S. Babu, Heterogeneous creep deformation in Dissimilar Metal Welds (DMWs), *Mater. Sci. Eng. A*, 749 (2019) 1-13.
- [46] R.M. Mahamood, E.T. Akinlabi, M. Shukla, S. Pityana, Functionally graded material: an overview, Proceedings of the World Congress on Engineering, London, UK, 2012, pp. 2-6.
- [47] Y. Fu, H. Du, S. Zhang, Functionally graded TiN/TiNi shape memory alloy films, *Mater. Lett.*, 57(20) (2003) 2995-2999.
- [48] M. Domack, J. Baughman, Development of nickel-titanium graded composition components, *Rapid Prototyp. J.*, 11(1) (2005) 41-51.
- [49] S. Tammam-Williams, I. Todd, Design for additive manufacturing with site-specific properties in metals and alloys, *Scripta Mater.*, (2016).
- [50] G.H. Loh, E. Pei, D. Harrison, M.D. Monzón, An overview of functionally graded additive manufacturing, *Addit. Manuf.*, 23 (2018) 34-44.
- [51] C. Zhang, F. Chen, Z. Huang, M. Jia, G. Chen, Y. Ye, Y. Lin, W. Liu, B. Chen, Q. Shen, L. Zhang, E.J. Lavernia, Additive manufacturing of functionally graded materials: A review, *Mater. Sci. Eng. A*, 764 (2019) 138209.
- [52] K. Feng, H. Chen, J. Xiong, Z. Guo, Investigation on diffusion bonding of functionally graded WC–Co/Ni composite and stainless steel, *Mater. Des.*, 46 (2013) 622-626.
- [53] N.W. Ahamad, I. Jauhari, S.A.A. Azis, N.H.A. Aziz, Surface properties and activation energy of superplastically carburized duplex stainless steel, *Mater. Chem. Phys.*, 122(2) (2010) 454-458.
- [54] M. Naebe, K. Shirvanimoghaddam, Functionally graded materials: A review of fabrication and properties, *Applied Materials Today*, 5 (2016) 223-245.
- [55] A.G. Arsha, E. Jayakumar, T.P.D. Rajan, V. Antony, B.C. Pai, Design and fabrication of functionally graded in-situ aluminium composites for automotive pistons, *Mater. Des.*, 88 (2015) 1201-1209.
- [56] S. Stewart, R. Ahmed, T. Itsukaichi, Contact fatigue failure evaluation of post-treated WC–NiCrBSi functionally graded thermal spray coatings, *Wear*, 257(9) (2004) 962-983.
- [57] B. Kieback, A. Neubrand, H. Riedel, Processing techniques for functionally graded materials, *Mater. Sci. Eng. A*, 362(1) (2003) 81-106.
- [58] J. Zhu, Z. Lai, Z. Yin, J. Jeon, S. Lee, Fabrication of ZrO<sub>2</sub>–NiCr functionally graded material by powder metallurgy, *Mater. Chem. Phys.*, 68(1) (2001) 130-135.
- [59] J. Xiong, Y. Lei, H. Chen, G. Zhang, Fabrication of inclined thin-walled parts in multi-layer single-pass GMAW-based additive manufacturing with flat position deposition, *J. Mater. Process. Technol.*, 240 (2017) 397-403.

- [60] T. DebRoy, H. Wei, J. Zuback, T. Mukherjee, J. Elmer, J. Milewski, A. Beese, A. Wilson-Heid, A. De, W. Zhang, Additive manufacturing of metallic components—process, structure and properties, *Prog. Mater. Sci.*, 92 (2018) 112-224.
- [61] M.K. Imran, S.H. Masood, M. Brandt, S. Bhattacharya, J. Mazumder, Direct metal deposition (DMD) of H13 tool steel on copper alloy substrate: Evaluation of mechanical properties, *Mater. Sci. Eng. A*, 528(9) (2011) 3342-3349.
- [62] J.S. Keist, T.A. Palmer, Role of geometry on properties of additively manufactured Ti-6Al-4V structures fabricated using laser based directed energy deposition, *Mater. Des.*, 106 (2016) 482-494.
- [63] M. Ma, Z. Wang, X. Zeng, Effect of energy input on microstructural evolution of direct laser fabricated IN718 alloy, *Mater. Charact.*, 106 (2015) 420-427.
- [64] K. Malukhin, K. Ehmann, Material Characterization of NiTi Based Memory Alloys Fabricated by the Laser Direct Metal Deposition Process, *J. Manuf. Sci. Eng.*, 128(3) (2005) 691-696.
- [65] S.H. Riza, S.H. Masood, C. Wen, D. Ruan, S. Xu, Dynamic behaviour of high strength steel parts developed through laser assisted direct metal deposition, *Mater. Des.*, 64 (2014) 650-659.
- [66] K. Shah, A.J. Pinkerton, A. Salman, L. Li, Effects of Melt Pool Variables and Process Parameters in Laser Direct Metal Deposition of Aerospace Alloys, *Mater. Manuf. Process.*, 25(12) (2010) 1372-1380.
- [67] B. Baufeld, E. Brandl, O. van der Biest, Wire based additive layer manufacturing: Comparison of microstructure and mechanical properties of Ti-6Al-4V components fabricated by laser-beam deposition and shaped metal deposition, *J. Mater. Process. Technol.*, 211(6) (2011) 1146-1158.
- [68] E. Brandl, A. Schoberth, C. Leyens, Morphology, microstructure, and hardness of titanium (Ti-6Al-4V) blocks deposited by wire-feed additive layer manufacturing (ALM), *Mater. Sci. Eng. A*, 532 (2012) 295-307.
- [69] E. Brandl, C. Leyens, F. Palm, Mechanical properties of additive manufactured Ti-6Al-4V using wire and powder based processes, *IOP Conference Series: Materials Science and Engineering*, IOP Publishing, 2011, p. 012004.
- [70] T. Wang, Y.Y. Zhu, S.Q. Zhang, H.B. Tang, H.M. Wang, Grain morphology evolution behavior of titanium alloy components during laser melting deposition additive manufacturing, *J. Alloy. Comp.*, 632 (2015) 505-513.
- [71] D. Ding, Z. Pan, D. Cuiuri, H. Li, Wire-feed additive manufacturing of metal components: technologies, developments and future interests, *The International Journal of Advanced Manufacturing Technology*, 81(1) (2015) 465-481.
- [72] J. Ding, P. Colegrove, J. Mehnert, S. Ganguly, P.M. Sequeira Almeida, F. Wang, S. Williams, Thermo-mechanical analysis of Wire and Arc Additive Layer Manufacturing process on large multi-layer parts, *Comp. Mater. Sci.*, 50(12) (2011) 3315-3322.
- [73] S.W. Williams, F. Martina, A.C. Addison, J. Ding, G. Pardal, P. Colegrove, Wire + Arc Additive Manufacturing, *Mater. Sci. Tech.*, 32(7) (2016) 641-647.
- [74] M. Jamshidinia, A. Sadek, W. Wang, S. Kelly, Additive manufacturing of steel alloys using laser powder-bed fusion, *Adv. Mater. Process.*, 173(1) (2015) 20-24.
- [75] C. Kamath, B. El-dasher, G.F. Gallegos, W.E. King, A. Sisto, Density of additively-manufactured, 316L SS parts using laser powder-bed fusion at powers up to 400 W, *The International Journal of Advanced Manufacturing Technology*, 74(1) (2014) 65-78.

- [76] S.A. Khairallah, A.T. Anderson, A. Rubenchik, W.E. King, Laser powder-bed fusion additive manufacturing: Physics of complex melt flow and formation mechanisms of pores, spatter, and denudation zones, *Acta Mater.*, 108 (2016) 36-45.
- [77] T.M. Mower, M.J. Long, Mechanical behavior of additive manufactured, powder-bed laser-fused materials, *Mater. Sci. Eng. A*, 651 (2016) 198-213.
- [78] G. Brentrup, J. DuPont, Fabrication and characterization of graded transition joints for welding dissimilar alloys, *Weld. J.*, 92 (2013) 72-79.
- [79] B.E. Carroll, R.A. Otis, J.P. Borgonia, J.-o. Suh, R.P. Dillon, A.A. Shapiro, D.C. Hofmann, Z.-K. Liu, A.M. Beese, Functionally graded material of 304L stainless steel and inconel 625 fabricated by directed energy deposition: Characterization and thermodynamic modeling, *Acta Mater.*, 108 (2016) 46-54.
- [80] L. Murr, S. Gaytan, F. Medina, H. Lopez, E. Martinez, B. Machado, D. Hernandez, L. Martinez, M. Lopez, R. Wicker, Next-generation biomedical implants using additive manufacturing of complex, cellular and functional mesh arrays, *Philos. T. Roy. Soc. A*, 368(1917) (2010) 1999-2032.
- [81] R. Dehoff, M. Kirka, W. Sames, H. Bilheux, A. Tremsin, L. Lowe, S. Babu, Site specific control of crystallographic grain orientation through electron beam additive manufacturing, *Mater. Sci. Tech.*, 31(8) (2015) 931-938.
- [82] A. Bandyopadhyay, B. Krishna, W. Xue, S. Bose, Application of laser engineered net shaping (LENS) to manufacture porous and functionally graded structures for load bearing implants, *J. Mater. Sci-mater. M.*, 20 (2009) 29-34.
- [83] J. Parthasarathy, B. Starly, S. Raman, A design for the additive manufacture of functionally graded porous structures with tailored mechanical properties for biomedical applications, *Journal of Manufacturing Processes*, 13(2) (2011) 160-170.
- [84] L.E. Murr, S. Gaytan, F. Medina, H. Lopez, E. Martinez, B. Machado, D. Hernandez, L. Martinez, M. Lopez, R. Wicker, Next-generation biomedical implants using additive manufacturing of complex, cellular and functional mesh arrays, *Philosophical Transactions of the Royal Society A: Mathematical, Physical and Engineering Sciences*, 368(1917) (2010) 1999-2032.
- [85] S.L. Sing, J. An, W.Y. Yeong, F.E. Wiria, Laser and electron-beam powder-bed additive manufacturing of metallic implants: A review on processes, materials and designs, *J. Orthopaed. Res.*, 34(3) (2016) 369-385.
- [86] M. Mehrli, F.S. Shirazi, M. Mehrli, H.S.C. Metselaar, N.A.B. Kadri, N.A.A. Osman, Dental implants from functionally graded materials, *Journal of Biomedical Materials Research Part A*, 101(10) (2013) 3046-3057.
- [87] V.A. Popovich, E.V. Borisov, A.A. Popovich, V.S. Sufiiarov, D.V. Masaylo, L. Alzina, Functionally graded Inconel 718 processed by additive manufacturing: Crystallographic texture, anisotropy of microstructure and mechanical properties, *Mater. Des.*, 114 (2017) 441-449.
- [88] F.S.H.B. Freeman, A. Lincoln, J. Sharp, A. Lambourne, I. Todd, Exploiting thermal strain to achieve an in-situ magnetically graded material, *Mater. Des.*, 161 (2019) 14-21.
- [89] K.B. Hazlehurst, C.J. Wang, M. Stanford, The potential application of a Cobalt Chrome Molybdenum femoral stem with functionally graded orthotropic structures manufactured using Laser Melting technologies, *Med. Hypotheses.*, 81(6) (2013) 1096-1099.
- [90] L.D. Bobbio, R.A. Otis, J.P. Borgonia, R.P. Dillon, A.A. Shapiro, Z.-K. Liu, A.M. Beese, Additive manufacturing of a functionally graded material from Ti-6Al-4V to Invar: Experimental characterization and thermodynamic calculations, *Acta Mater.*, 127 (2017) 133-142.

- [91] L.D. Bobbio, B. Bocklund, R. Otis, J.P. Borgonia, R.P. Dillon, A.A. Shapiro, B. McEnerney, Z.-K. Liu, A.M. Beese, Characterization of a functionally graded material of Ti-6Al-4V to 304L stainless steel with an intermediate V section, *J. Alloy. Comp.*, 742 (2018) 1031-1036.
- [92] L.D. Bobbio, B. Bocklund, R. Otis, J.P. Borgonia, R.P. Dillon, A.A. Shapiro, B. McEnerney, Z.-K. Liu, A.M. Beese, Experimental analysis and thermodynamic calculations of an additively manufactured functionally graded material of V to Invar 36, *J. Mater. Res.*, 33(11) (2018) 1642-1649.
- [93] P. Collins, R. Banerjee, S. Banerjee, H. Fraser, Laser deposition of compositionally graded titanium–vanadium and titanium–molybdenum alloys, *Mater. Sci. Eng. A*, 352(1) (2003) 118-128.
- [94] J.P. Galler, J.N. DuPont, S.S. Babu, M. Subramanian, Microstructural Evolution of Graded Transition Joints, *Metall. Mater. Trans. A*, 50(5) (2019) 2201-2217.
- [95] T. Hwang, Y.Y. Woo, S.W. Han, Y.H. Moon, Functionally graded properties in directed-energy-deposition titanium parts, *Opt. Laser. Technol.*, 105 (2018) 80-88.
- [96] F. Khodabakhshi, M.H. Farshidianfar, S. Bakhshivash, A.P. Gerlich, A. Khajepour, Dissimilar metals deposition by directed energy based on powder-fed laser additive manufacturing, *Journal of Manufacturing Processes*, 43 (2019) 83-97.
- [97] D.-K. Kim, W. Woo, E.-Y. Kim, S.-H. Choi, Microstructure and mechanical characteristics of multi-layered materials composed of 316L stainless steel and ferritic steel produced by direct energy deposition, *J. Alloy. Comp.*, 774 (2019) 896-907.
- [98] W. Li, X. Chen, L. Yan, J. Zhang, X. Zhang, F. Liou, Additive manufacturing of a new Fe-Cr-Ni alloy with gradually changing compositions with elemental powder mixes and thermodynamic calculation, *The International Journal of Advanced Manufacturing Technology*, 95(1) (2018) 1013-1023.
- [99] Y. Liu, C. Liang, W. Liu, Y. Ma, C. Liu, C. Zhang, Dilution of Al and V through laser powder deposition enables a continuously compositionally Ti/Ti6Al4V graded structure, *J. Alloy. Comp.*, 763 (2018) 376-383.
- [100] C. Schneider-Maunoury, L. Weiss, P. Acquier, D. Boisselier, P. Laheurte, Functionally graded Ti6Al4V-Mo alloy manufactured with DED-CLAD® process, *Addit. Manuf.*, 17 (2017) 55-66.
- [101] K. Shah, I.U. Haq, S.A. Shah, F.U. Khan, M.T. Khan, S. Khan, Experimental Study of Direct Laser Deposition of Ti-6Al-4V and Inconel 718 by Using Pulsed Parameters, *The Scientific World Journal*, 2014 (2014) 841945.
- [102] N. Sridharan, E. Cakmak, B. Jordan, D. Leonard, W. Peter, R. Dehoff, D. Gandy, S. Babu, Design, fabrication, and characterization of graded transition joints, *Weld. J.*, 96(8) (2017) 295S-306S.
- [103] D.C. Hofmann, S. Roberts, R. Otis, J. Kolodziejska, R.P. Dillon, J.-o. Suh, A.A. Shapiro, Z.-K. Liu, J.-P. Borgonia, Developing gradient metal alloys through radial deposition additive manufacturing, *Sci. Rep.*, 4 (2014) 5357.
- [104] L.D. Bobbio, B. Bocklund, A. Reichardt, R. Otis, J.P. Borgonia, R.P. Dillon, A.A. Shapiro, B.W. McEnerney, P. Hosemann, Z.-K. Liu, A.M. Beese, Analysis of formation and growth of the  $\sigma$  phase in additively manufactured functionally graded materials, *J. Alloy. Comp.*, (2019) 151729.
- [105] W. Woo, D.-K. Kim, E.J. Kingston, V. Luzin, F. Salvemini, M.R. Hill, Effect of interlayers and scanning strategies on through-thickness residual stress distributions in additive manufactured ferritic-austenitic steel structure, *Mater. Sci. Eng. A*, 744 (2019) 618-629.

- [106] B.K. Foster, A.M. Beese, J.S. Keist, E.T. McHale, T.A. Palmer, Impact of Interlayer Dwell Time on Microstructure and Mechanical Properties of Nickel and Titanium Alloys, *Metall. Mater. Trans. A*, 48(9) (2017) 4411-4422.
- [107] H. Attar, S. Ehtemam-Haghighi, D. Kent, I.V. Okulov, H. Wendrock, M. Bönisch, A.S. Volegov, M. Calin, J. Eckert, M.S. Dargusch, Nanoindentation and wear properties of Ti and Ti-TiB composite materials produced by selective laser melting, *Mater. Sci. Eng. A*, 688 (2017) 20-26.
- [108] K. Zhang, S. Wang, W. Liu, X. Shang, Characterization of stainless steel parts by Laser Metal Deposition Shaping, *Mater. Des.*, 55 (2014) 104-119.
- [109] J. Yu, M. Rombouts, G. Maes, Cracking behavior and mechanical properties of austenitic stainless steel parts produced by laser metal deposition, *Mater. Des.*, 45 (2013) 228-235.
- [110] J. Li, D. Deng, X. Hou, X. Wang, G. Ma, D. Wu, G. Zhang, Microstructure and performance optimisation of stainless steel formed by laser additive manufacturing, *Mater. Sci. Tech.*, 32(12) (2016) 1223-1230.
- [111] M. Ziętała, T. Durejko, M. Polański, I. Kunce, T. Płociński, W. Zieliński, M. Łazińska, W. Stępniewski, T. Czujko, K.J. Kurzydłowski, Z. Bojar, The microstructure, mechanical properties and corrosion resistance of 316L stainless steel fabricated using laser engineered net shaping, *Mater. Sci. Eng. A*, 677 (2016) 1-10.
- [112] M. Ma, Z. Wang, D. Wang, X. Zeng, Control of shape and performance for direct laser fabrication of precision large-scale metal parts with 316L Stainless Steel, *Opt. Laser. Technol.*, 45 (2013) 209-216.
- [113] K. Abd-Elghany, D.L. Bourell, Property evaluation of 304L stainless steel fabricated by selective laser melting, *Rapid Prototyp. J.*, 18(5) (2012) 420-428.
- [114] I. Tolosa, F. Garcandia, F. Zubiri, F. Zapirain, A. Esnaola, Study of mechanical properties of AISI 316 stainless steel processed by "selective laser melting", following different manufacturing strategies, *Int. J. Adv. Manuf. Technol.*, 51(5-8) (2010) 639-647.
- [115] Z. Sun, X. Tan, S.B. Tor, W.Y. Yeong, Selective laser melting of stainless steel 316L with low porosity and high build rates, *Mater. Des.*, 104 (2016) 197-204.
- [116] G.L. Knapp, T. Mukherjee, J.S. Zuback, H.L. Wei, T.A. Palmer, A. De, T. DebRoy, Building blocks for a digital twin of additive manufacturing, *Acta Mater.*, 135 (2017) 390-399.
- [117] H. Galarraga, D.A. Lados, R.R. Dehoff, M.M. Kirka, P. Nandwana, Effects of the microstructure and porosity on properties of Ti-6Al-4V ELI alloy fabricated by electron beam melting (EBM), *Addit. Manuf.*, 10 (2016) 47-57.
- [118] E. Brandl, B. Baufeld, C. Leyens, R. Gault, Additive manufactured Ti-6Al-4V using welding wire: comparison of laser and arc beam deposition and evaluation with respect to aerospace material specifications, *Phys. Procedia*, 5 (2010) 595-606.
- [119] B.E. Carroll, T.A. Palmer, A.M. Beese, Anisotropic tensile behavior of Ti-6Al-4V components fabricated with directed energy deposition additive manufacturing, *Acta Mater.*, 87 (2015) 309-320.
- [120] Y. Zhu, J. Li, X. Tian, H. Wang, D. Liu, Microstructure and mechanical properties of hybrid fabricated Ti-6.5 Al-3.5 Mo-1.5 Zr-0.3 Si titanium alloy by laser additive manufacturing, *Mater. Sci. Eng. A*, 607 (2014) 427-434.
- [121] B. Vrancken, L. Thijs, J.P. Kruth, J. Van Humbeeck, Microstructure and mechanical properties of a novel  $\beta$  titanium metallic composite by selective laser melting, *Acta Mater.*, 68 (2014) 150-158.

- [122] B. Baufeld, O. Van der Biest, Mechanical properties of Ti-6Al-4V specimens produced by shaped metal deposition, *Sci. Technol. Adv. Mat.*, 10(1) (2009) 015008.
- [123] F. Abe, K. Osakada, Y. Kitamura, M. Matsumoto, M. Shiomi, Manufacturing of titanium parts for medical purposes by selective laser melting, *Proc. 8th Int. Conf. Rapid Prototyping*, Tokyo, Japan, 2000, pp. 288-293.
- [124] N. Hrabec, T. Quinn, Effects of processing on microstructure and mechanical properties of a titanium alloy (Ti-6Al-4V) fabricated using electron beam melting (EBM), Part 2: Energy input, orientation, and location, *Materials Science and Engineering a-Structural Materials Properties Microstructure and Processing*, 573 (2013) 271-277.
- [125] H. Attar, M. Calin, L.C. Zhang, S. Scudino, J. Eckert, Manufacture by selective laser melting and mechanical behavior of commercially pure titanium, *Mater. Sci. Eng. A*, 593 (2014) 170-177.
- [126] L.E. Murr, S.M. Gaytan, A. Ceylan, E. Martinez, J.L. Martinez, D.H. Hernandez, B.I. Machado, D.A. Ramirez, F. Medina, S. Collins, R.B. Wicker, Characterization of titanium aluminide alloy components fabricated by additive manufacturing using electron beam melting, *Acta Mater.*, 58(5) (2010) 1887-1894.
- [127] H. Schwab, K. Prashanth, L. Löber, U. Kühn, J. Eckert, Selective Laser Melting of Ti-45Nb Alloy, *Metals*, 5(2) (2015) 686.
- [128] J.A. Cherry, H.M. Davies, S. Mehmood, N.P. Lavery, S.G.R. Brown, J. Sienz, Investigation into the effect of process parameters on microstructural and physical properties of 316L stainless steel parts by selective laser melting, *The International Journal of Advanced Manufacturing Technology*, 76(5) (2015) 869-879.
- [129] Q. Jia, D. Gu, Selective laser melting additive manufacturing of Inconel 718 superalloy parts: Densification, microstructure and properties, *J. Alloy. Comp.*, 585 (2014) 713-721.
- [130] L. Thijs, F. Verhaeghe, T. Craeghs, J. Van Humbeeck, J.-P. Kruth, A study of the microstructural evolution during selective laser melting of Ti-6Al-4V, *Acta Mater.*, 58(9) (2010) 3303-3312.
- [131] T. Mukherjee, V. Manvatkar, A. De, T. DebRoy, Dimensionless numbers in additive manufacturing, *J. Appl. Phys.*, 121(6) (2017) 064904.
- [132] T. Amine, J.W. Newkirk, F. Liou, Investigation of effect of process parameters on multilayer builds by direct metal deposition, *Appl. Therm. Eng.*, 73(1) (2014) 500-511.
- [133] A. Bardelcik, C.P. Salisbury, S. Winkler, M.A. Wells, M.J. Worswick, Effect of cooling rate on the high strain rate properties of boron steel, *Int. J. Impact. Eng.*, 37(6) (2010) 694-702.
- [134] T. Nishibata, N. Kojima, Effect of quenching rate on hardness and microstructure of hot-stamped steel, *J. Alloy. Comp.*, 577 (2013) S549-S554.
- [135] M. Olasolo, P. Uranga, J. Rodriguez-Ibabe, B. López, Effect of austenite microstructure and cooling rate on transformation characteristics in a low carbon Nb-V microalloyed steel, *Mater. Sci. Eng. A*, 528(6) (2011) 2559-2569.
- [136] S. Thompson, D.V. Col, G. Krauss, Continuous cooling transformations and microstructures in a low-carbon, high-strength low-alloy plate steel, *Metall. Trans. A*, 21(6) (1990) 1493-1507.
- [137] S. Thompson, D. Colvin, G. Krauss, Austenite decomposition during continuous cooling of an HSLA-80 plate steel, *Metall. Mater. Trans. A*, 27(6) (1996) 1557-1571.
- [138] Z. Qiao, Y. Liu, L. Yu, Z. Gao, Effect of cooling rate on microstructural formation and hardness of 30CrNi3Mo steel, *Appl. Phys. A-Mater.*, 95(3) (2009) 917-922.
- [139] Y. Birol, Optimization of homogenization for a low alloyed AlMgSi alloy, *Mater. Charact.*, 80 (2013) 69-75.

- [140] C. Brito, T.A. Costa, T.A. Vida, F. Bertelli, N. Cheung, J.E. Spinelli, A. Garcia, Characterization of Dendritic Microstructure, Intermetallic Phases, and Hardness of Directionally Solidified Al-Mg and Al-Mg-Si Alloys, *Metall. Mater. Trans. A*, 46(8) (2015) 3342-3355.
- [141] E. Çadırlı, Effect of solidification parameters on mechanical properties of directionally solidified Al-Rich Al-Cu alloys, *Met. Mater-Int.*, 19(3) (2013) 411-422.
- [142] J.L. Cavazos, R. Colás, Precipitation in a heat-treatable aluminum alloy cooled at different rates, *Mater. Charact.*, 47(3-4) (2001) 175-179.
- [143] L. Zhang, Y. Jiang, Z. Ma, S. Shan, Y. Jia, C. Fan, W. Wang, Effect of cooling rate on solidified microstructure and mechanical properties of aluminium-A356 alloy, *J. Mater. Process. Technol.*, 207(1) (2008) 107-111.
- [144] S. Milenkovic, I. Sabirov, J. Llorca, Effect of the cooling rate on microstructure and hardness of MAR-M247 Ni-based superalloy, *Mater. Lett.*, 73 (2012) 216-219.
- [145] R. Mitchell, M. Preuss, S. Tin, M. Hardy, The influence of cooling rate from temperatures above the  $\gamma'$  solvus on morphology, mismatch and hardness in advanced polycrystalline nickel-base superalloys, *Mater. Sci. Eng. A*, 473(1) (2008) 158-165.
- [146] L. Geng, Y.-S. Na, N.-K. Park, Continuous cooling transformation behavior of alloy 718, *Mater. Lett.*, 30(5-6) (1997) 401-405.
- [147] M. Rahimian, S. Milenkovic, I. Sabirov, Microstructure and hardness evolution in MAR-M247 Ni-based superalloy processed by controlled cooling and double heat treatment, *J. Alloy. Comp.*, 550 (2013) 339-344.
- [148] E. Karaköse, M. Keskin, Effect of microstructural evolution and elevated temperature on the mechanical properties of Ni-Cr-Mo alloys, *J. Alloy. Comp.*, 619 (2015) 82-90.
- [149] W.D. Callister, D.G. Rethwisch, *Materials science and engineering*, John Wiley & Sons, Hoboken, NJ, 2011.
- [150] V. Manvatkar, A. De, T. DebRoy, Spatial variation of melt pool geometry, peak temperature and solidification parameters during laser assisted additive manufacturing process, *Mater. Sci. Tech.*, 31(8) (2015) 924-930.
- [151] M.H. Farshidianfar, A. Khajepour, A.P. Gerlich, Effect of real-time cooling rate on microstructure in laser additive manufacturing, *J. Mater. Process. Technol.*, 231 (2016) 468-478.
- [152] V. Manvatkar, A. De, T. DebRoy, Heat transfer and material flow during laser assisted multi-layer additive manufacturing, *J. Appl. Phys.*, 116(12) (2014) 124905.
- [153] J.S. Keist, T.A. Palmer, Development of strength-hardness relationships in additively manufactured titanium alloys, *Mater. Sci. Eng. A*, 693 (2017) 214-224.
- [154] Y. Tian, D. McAllister, H. Colijn, M. Mills, D. Farson, M. Nordin, S. Babu, Rationalization of Microstructure Heterogeneity in INCONEL 718 Builds Made by the Direct Laser Additive Manufacturing Process, *Metall. Mater. Trans. A*, 45(10) (2014) 4470-4483.
- [155] D. Cormier, A. Harrysson, H. West, Characterization of H13 steel produced via electron beam melting, *Rapid Prototyp. J.*, 10(1) (2004) 35-41.
- [156] S. Bhattacharya, G.P. Dinda, A.K. Dasgupta, J. Mazumder, Microstructural evolution of AISI 4340 steel during Direct Metal Deposition process, *Mater. Sci. Eng. A*, 528(6) (2011) 2309-2318.
- [157] G. Casalino, S.L. Campanelli, N. Contuzzi, A.D. Ludovico, Experimental investigation and statistical optimisation of the selective laser melting process of a maraging steel, *Opt. Laser. Technol.*, 65 (2015) 151-158.
- [158] J. Choi, Y. Chang, Characteristics of laser aided direct metal/material deposition process for tool steel, *International Journal of Machine Tools and Manufacture*, 45(4-5) (2005) 597-607.

- [159] R. Cottam, J. Wang, V. Luzin, Characterization of microstructure and residual stress in a 3D H13 tool steel component produced by additive manufacturing, *J. Mater. Res.*, 29(17) (2014) 1978-1986.
- [160] A.S. Haselhuhn, B. Wijnen, G.C. Anzalone, P.G. Sanders, J.M. Pearce, In situ formation of substrate release mechanisms for gas metal arc weld metal 3-D printing, *J. Mater. Process. Technol.*, 226 (2015) 50-59.
- [161] A. Simchi, H. Asgharzadeh, Densification and microstructural evaluation during laser sintering of M2 high speed steel powder, *Mater. Sci. Tech.*, 20(11) (2004) 1462-1468.
- [162] J. Sander, J. Hufenbach, L. Giebeler, H. Wendrock, U. Kuhn, J. Eckert, Microstructure and properties of FeCrMoVC tool steel produced by selective laser melting, *Mater. Des.*, 89 (2016) 335-341.
- [163] C. Brice, R. Shenoy, M. Kral, K. Buchannan, Precipitation behavior of aluminum alloy 2139 fabricated using additive manufacturing, *Mater. Sci. Eng. A*, 648 (2015) 9-14.
- [164] D. Buchbinder, W. Meiners, N. Pirch, K. Wissenbach, J. Schrage, Investigation on reducing distortion by preheating during manufacture of aluminum components using selective laser melting, *J. Laser Appl.*, 26(1) (2014) 012004.
- [165] R. Chou, J. Milligan, M. Paliwal, M. Brochu, Additive Manufacturing of Al-12Si Alloy Via Pulsed Selective Laser Melting, *JOM*, 67(3) (2015) 590-596.
- [166] X.J. Wang, L.C. Zhang, M.H. Fang, T.B. Sercombe, The effect of atmosphere on the structure and properties of a selective laser melted Al-12Si alloy, *Mater. Sci. Eng. A*, 597 (2014) 370-375.
- [167] I. Maskery, N.T. Aboulkhair, M.R. Corfield, C. Tuck, A.T. Clare, R.K. Leach, R.D. Wildman, I.A. Ashcroft, R.J.M. Hague, Quantification and characterisation of porosity in selectively laser melted Al-Si10-Mg using X-ray computed tomography, *Mater. Charact.*, 111 (2016) 193-204.
- [168] K. Kempen, L. Thijs, J. Van Humbeeck, J.-P. Kruth, Mechanical properties of AlSi10Mg produced by selective laser melting, *Phys. Procedia*, 39 (2012) 439-446.
- [169] D. Manfredi, F. Calignano, M. Krishnan, R. Canali, E.P. Ambrosio, E. Atzeni, From powders to dense metal parts: Characterization of a commercial AlSiMg alloy processed through direct metal laser sintering, *Materials*, 6(3) (2013) 856-869.
- [170] E.O. Olakanmi, R.F. Cochrane, K.W. Dalgarno, Densification mechanism and microstructural evolution in selective laser sintering of Al-12Si powders, *J. Mater. Process. Technol.*, 211(1) (2011) 113-121.
- [171] H. Zhang, H.H. Zhu, T. Qi, Z.H. Hu, X.Y. Zeng, Selective laser melting of high strength Al-Cu-Mg alloys: Processing, microstructure and mechanical properties, *Mater. Sci. Eng. A*, 656 (2016) 47-54.
- [172] K.N. Amato, S.M. Gaytan, L.E. Murr, E. Martinez, P.W. Shindo, J. Hernandez, S. Collins, F. Medina, Microstructures and mechanical behavior of Inconel 718 fabricated by selective laser melting, *Acta Mater.*, 60(5) (2012) 2229-2239.
- [173] G.P. Dinda, A.K. Dasgupta, J. Mazumder, Texture control during laser deposition of nickel-based superalloy, *Scripta Mater.*, 67(5) (2012) 503-506.
- [174] L.E. Murr, E. Martinez, X.M. Pan, S.M. Gaytan, J.A. Castro, C.A. Terrazas, F. Medina, R.B. Wicker, D.H. Abbott, Microstructures of Rene 142 nickel-based superalloy fabricated by electron beam melting, *Acta Mater.*, 61(11) (2013) 4289-4296.
- [175] C.P. Paul, P. Ganesh, S.K. Mishra, P. Bhargava, J. Negi, A.K. Nath, Investigating laser rapid manufacturing for Inconel-625 components, *Opt. Laser. Technol.*, 39(4) (2007) 800-805.

- [176] C.P. Paul, A. Jain, P. Ganesh, J. Negi, A.K. Nath, Laser rapid manufacturing of Colmonoy-6 components, *Opt. Laser. Eng.*, 44(10) (2006) 1096-1109.
- [177] L. Sexton, S. Lavin, G. Byrne, A. Kennedy, Laser cladding of aerospace materials, *J. Mater. Process. Technol.*, 122(1) (2002) 63-68.
- [178] T. Vilaro, C. Colin, J.D. Bartout, L. Nazé, M. Sennour, Microstructural and mechanical approaches of the selective laser melting process applied to a nickel-base superalloy, *Mater. Sci. Eng. A*, 534 (2012) 446-451.
- [179] Z. Wang, K. Guan, M. Gao, X. Li, X. Chen, X. Zeng, The microstructure and mechanical properties of deposited-IN718 by selective laser melting, *J. Alloy. Comp.*, 513 (2012) 518-523.
- [180] F. Abe, K. Osakada, M. Shiomi, K. Uematsu, M. Matsumoto, The manufacturing of hard tools from metallic powders by selective laser melting, *J. Mater. Process. Technol.*, 111(1) (2001) 210-213.
- [181] M. Zhong, L. Yang, W. Liu, T. Huang, J. He, Laser rapid manufacturing of special pattern Inco 718 nickel-based alloy component, *Photonics Asia 2004*, International Society for Optics and Photonics, 2005, pp. 59-66.
- [182] P. Kanagarajah, F. Brenne, T. Niendorf, H.J. Maier, Inconel 939 processed by selective laser melting: Effect of microstructure and temperature on the mechanical properties under static and cyclic loading, *Mater. Sci. Eng. A*, 588 (2013) 188-195.
- [183] B. Baufeld, Mechanical Properties of INCONEL 718 Parts Manufactured by Shaped Metal Deposition (SMD), *J. Mater. Eng. Perform.*, 21(7) (2012) 1416-1421.
- [184] J. Li, H.M. Wang, H.B. Tang, Effect of heat treatment on microstructure and mechanical properties of laser melting deposited Ni-base superalloy Rene'41, *Mater. Sci. Eng. A*, 550 (2012) 97-102.
- [185] R. Acharya, R. Bansal, J.J. Gambone, M.A. Kaplan, G.E. Fuchs, N.G. Rudawski, S. Das, Additive Manufacturing and Characterization of René 80 Superalloy Processed Through Scanning Laser Epitaxy for Turbine Engine Hot-Section Component Repair, *Adv. Eng. Mater.*, 17(7) (2015) 942-950.
- [186] N.J. Harrison, I. Todd, K. Mumtaz, Reduction of micro-cracking in nickel superalloys processed by Selective Laser Melting: A fundamental alloy design approach, *Acta Mater.*, 94 (2015) 59-68.
- [187] X. Wang, Y.K. Chou, A method to estimate residual stress in metal parts made by Selective Laser Melting, *ASME 2015 International Mechanical Engineering Congress and Exposition*, American Society of Mechanical Engineers, 2015, pp. V02AT02A015-V02AT02A015.
- [188] K. Zhang, W.J. Liu, X.F. Shang, Characteristics of Laser Aided Direct Metal Powder Deposition Process for Nickel-Based Superalloy, *Mater. Sci. Forum.*, 534-536 (2007) 457-460.
- [189] N. Sridharan, M.W. Noakes, A. Nycz, L.J. Love, R.R. Dehoff, S.S. Babu, On the toughness scatter in low alloy C-Mn steel samples fabricated using wire arc additive manufacturing, *Mater. Sci. Eng. A*, 713 (2018) 18-27.
- [190] J.S. Zuback, T.A. Palmer, T. DebRoy, Additive manufacturing of functionally graded transition joints between ferritic and austenitic alloys, *J. Alloy. Comp.*, 770 (2019) 995-1003.
- [191] A.J. Pinkerton, L. Li, Direct additive laser manufacturing using gas-and water-atomised H13 tool steel powders, *The International Journal of Advanced Manufacturing Technology*, 25(5-6) (2005) 471-479.
- [192] O. Hentschel, C. Scheitler, A. Fedorov, D. Junker, A. Gorunov, A. Haimerl, M. Merklein, M. Schmidt, Experimental investigations of processing the high carbon cold-work tool steel 1.2358

- by laser metal deposition for the additive manufacturing of cold forging tools, *J. Laser Appl.*, 29(2) (2017) 022307.
- [193] M. Mazur, P. Brincat, M. Leary, M. Brandt, Numerical and experimental evaluation of a conformally cooled H13 steel injection mould manufactured with selective laser melting, *The International Journal of Advanced Manufacturing Technology*, 93(1-4) (2017) 881-900.
- [194] M. Zhang, C. Chen, L. Qin, K. Yan, G. Cheng, H. Jing, T. Zou, Laser additive manufacturing of M2 high-speed steel, *Mater. Sci. Tech.*, 34(1) (2018) 69-78.
- [195] H. Chen, D. Gu, D. Dai, C. Ma, M. Xia, Microstructure and composition homogeneity, tensile property, and underlying thermal physical mechanism of selective laser melting tool steel parts, *Mater. Sci. Eng. A*, 682 (2017) 279-289.
- [196] J. Sander, J. Hufenbach, L. Giebeler, M. Bleckmann, J. Eckert, U. Kühn, Microstructure, mechanical behavior, and wear properties of FeCrMoVC steel prepared by selective laser melting and casting, *Scripta Mater.*, 126(1) (2017) 41-44.
- [197] H. Fayazfar, M. Salarian, A. Rogalsky, D. Sarker, P. Russo, V. Paserin, E. Toyserkani, A critical review of powder-based additive manufacturing of ferrous alloys: Process parameters, microstructure and mechanical properties, *Mater. Des.*, 144 (2018) 98-128.
- [198] S. David, J. Vitek, R. Reed, T. Hebble, Effect of rapid solidification on stainless steel weld metal microstructures and its implications on the Schaeffler diagram, TN, USA, 1987, 10.2172/5957599.
- [199] T. Amine, J.W. Newkirk, F. Liou, An investigation of the effect of direct metal deposition parameters on the characteristics of the deposited layers, *Case Studies in Thermal Engineering*, 3 (2014) 21-34.
- [200] K. Shah, I. ul Haq, A. Khan, S.A. Shah, M. Khan, A.J. Pinkerton, Parametric study of development of Inconel-steel functionally graded materials by laser direct metal deposition, *Mater. Des.*, 54 (2014) 531-538.
- [201] H.K. Rafi, D. Pal, N. Patil, T.L. Starr, B.E. Stucker, Microstructure and Mechanical Behavior of 17-4 Precipitation Hardenable Steel Processed by Selective Laser Melting, *J. Mater. Eng. Perform.*, 23(12) (2014) 4421-4428.
- [202] L.E. Murr, E. Martinez, J. Hernandez, S. Collins, K.N. Amato, S.M. Gaytan, P.W. Shindo, Microstructures and Properties of 17-4 PH Stainless Steel Fabricated by Selective Laser Melting, *J. Mater. Res. Technol.*, 1(3) (2012) 167-177.
- [203] S. Cheruvathur, E.A. Lass, C.E. Campbell, Additive manufacturing of 17-4 PH stainless steel: post-processing heat treatment to achieve uniform reproducible microstructure, *JOM*, 68(3) (2016) 930-942.
- [204] L. Thijs, K. Kempen, J.P. Kruth, J. Van Humbeeck, Fine-structured aluminium products with controllable texture by selective laser melting of pre-alloyed AlSi10Mg powder, *Acta Mater.*, 61(5) (2013) 1809-1819.
- [205] G.P. Dinda, A.K. Dasgupta, S. Bhattacharya, H. Natu, B. Dutta, J. Mazumder, Microstructural Characterization of Laser-Deposited Al 4047 Alloy, *Metall. Mater. Trans. A*, 44(5) (2012) 2233-2242.
- [206] H. Kaya, E. Çadırılı, U. Büyük, N. Maraşlı, Variation of microindentation hardness with solidification and microstructure parameters in the Al based alloys, *Appl. Surf. Sci.*, 255(5) (2008) 3071-3078.
- [207] N.T. Aboulkhair, C. Tuck, I. Ashcroft, I. Maskery, N.M. Everitt, On the precipitation hardening of selective laser melted AlSi10Mg, *Metall. Mater. Trans. A*, 46(8) (2015) 3337-3341.

- [208] W. Li, S. Li, J. Liu, A. Zhang, Y. Zhou, Q. Wei, C. Yan, Y. Shi, Effect of heat treatment on AlSi10Mg alloy fabricated by selective laser melting: Microstructure evolution, mechanical properties and fracture mechanism, *Mater. Sci. Eng. A*, 663 (2016) 116-125.
- [209] K. Kempen, L. Thijs, J. Van Humbeeck, J.-P. Kruth, Processing AlSi10Mg by selective laser melting: parameter optimisation and material characterisation, *Mater. Sci. Tech.*, 31(8) (2015) 917-923.
- [210] M. Javidani, J. Arreguin-Zavala, J. Danovitch, Y. Tian, M. Brochu, Additive manufacturing of AlSi10Mg alloy using direct energy deposition: Microstructure and hardness characterization, *J. Therm. Spray. Techn.*, 26(4) (2017) 587-597.
- [211] C. Yan, L. Hao, A. Hussein, P. Young, J. Huang, W. Zhu, Microstructure and mechanical properties of aluminium alloy cellular lattice structures manufactured by direct metal laser sintering, *Mater. Sci. Eng. A*, 628 (2015) 238-246.
- [212] I. Rosenthal, R. Shneck, A. Stern, Heat treatment effect on the mechanical properties and fracture mechanism in AlSi10Mg fabricated by additive manufacturing selective laser melting process, *Mater. Sci. Eng. A*, 729 (2018) 310-322.
- [213] U. Tradowsky, J. White, R. Ward, N. Read, W. Reimers, M. Attallah, Selective laser melting of AlSi10Mg: influence of post-processing on the microstructural and tensile properties development, *Mater. Des.*, 105 (2016) 212-222.
- [214] K. Feng, Y. Chen, P. Deng, Y. Li, H. Zhao, F. Lu, R. Li, J. Huang, Z. Li, Improved high-temperature hardness and wear resistance of Inconel 625 coatings fabricated by laser cladding, *J. Mater. Process. Technol.*, 243 (2017) 82-91.
- [215] B. Foster, A. Beese, J. Keist, E. McHale, T. Palmer, Impact of interlayer dwell time on microstructure and mechanical properties of nickel and titanium alloys, *Metall. Mater. Trans. A*, 48(9) (2017) 4411-4422.
- [216] N. Hussein, J. Segal, D. McCartney, I. Pashby, Microstructure formation in Waspaloy multilayer builds following direct metal deposition with laser and wire, *Mater. Sci. Eng. A*, 497(1-2) (2008) 260-269.
- [217] J. Jones, M. Whittaker, R. Buckingham, R. Johnston, M. Bache, D. Clark, Microstructural characterisation of a nickel alloy processed via blown powder direct laser deposition (DLD), *Mater. Des.*, 117 (2017) 47-57.
- [218] Z. Khayat, T. Palmer, Impact of iron composition on the properties of an additively manufactured solid solution strengthened nickel base alloy, *Mater. Sci. Eng., A*, 718 (2018) 123-134.
- [219] F. Zhang, L.E. Levine, A.J. Allen, M.R. Stoudt, G. Lindwall, E.A. Lass, M.E. Williams, Y. Idell, C.E. Campbell, Effect of heat treatment on the microstructural evolution of a nickel-based superalloy additive-manufactured by laser powder bed fusion, *Acta Mater.*, 152 (2018) 200-214.
- [220] S. Floreen, G.E. Fuchs, W.J. Yang, The metallurgy of alloy 625, *Superalloys*, 718(625) (1994) 13-37.
- [221] X. Zhao, J. Chen, X. Lin, W. Huang, Study on microstructure and mechanical properties of laser rapid forming Inconel 718, *Mater. Sci. Eng. A*, 478(1-2) (2008) 119-124.
- [222] C. Zhong, A. Gasser, J. Kittel, K. Wissenbach, R. Poprawe, Improvement of material performance of Inconel 718 formed by high deposition-rate laser metal deposition, *Mater. Des.*, 98 (2016) 128-134.
- [223] E.L. Stevens, J. Toman, A.C. To, M. Chmielus, Variation of hardness, microstructure, and Laves phase distribution in direct laser deposited alloy 718 cuboids, *Mater. Des.*, 119 (2017) 188-198.

- [224] I. Taberero, A. Lamikiz, S. Martínez, E. Ukar, J. Figueras, Evaluation of the mechanical properties of Inconel 718 components built by laser cladding, *Int. J. Mach. Tool. Manu*, 51(6) (2011) 465-470.
- [225] W.M. Tucho, P. Cu villier, A. Sjolyst-Kverneland, V. Hansen, Microstructure and hardness studies of Inconel 718 manufactured by selective laser melting before and after solution heat treatment, *Mater. Sci. Eng. A*, 689 (2017) 220-232.
- [226] D. Zhang, W. Niu, X. Cao, Z. Liu, Effect of standard heat treatment on the microstructure and mechanical properties of selective laser melting manufactured Inconel 718 superalloy, *Mater. Sci. Eng. A*, 644 (2015) 32-40.
- [227] W. Tillmann, C. Schaak, J. Nellesen, M. Schaper, M. Aydinöz, K.-P. Hoyer, Hot isostatic pressing of IN718 components manufactured by selective laser melting, *Addit. Manuf.*, 13 (2017) 93-102.
- [228] M. Aydinöz, F. Brenne, M. Schaper, C. Schaak, W. Tillmann, J. Nellesen, T. Niendorf, On the microstructural and mechanical properties of post-treated additively manufactured Inconel 718 superalloy under quasi-static and cyclic loading, *Mater. Sci. Eng. A*, 669 (2016) 246-258.
- [229] V. Popovich, E. Borisov, A. Popovich, V.S. Sufiiarov, D. Masaylo, L. Alzina, Impact of heat treatment on mechanical behaviour of Inconel 718 processed with tailored microstructure by selective laser melting, *Mater. Des.*, 131 (2017) 12-22.
- [230] E. Chlebus, K. Gruber, B. Kuznicka, J. Kurzac, T. Kurzynowski, Effect of heat treatment on the microstructure and mechanical properties of Inconel 718 processed by selective laser melting, *Materials Science and Engineering a-Structural Materials Properties Microstructure and Processing*, 639 (2015) 647-655.
- [231] D. Deng, R.L. Peng, H. Brodin, J. Moverare, Microstructure and mechanical properties of Inconel 718 produced by selective laser melting: sample orientation dependence and effects of post heat treatments, *Mater. Sci. Eng. A*, (2017).
- [232] D. Deng, J. Moverare, R.L. Peng, H. Söderberg, Microstructure and anisotropic mechanical properties of EBM manufactured Inconel 718 and effects of post heat treatments, *Mater. Sci. Eng. A*, 693 (2017) 151-163.
- [233] D. Deng, J. Saarimäki, H. Söderberg, R. Peng, H. Brodin, J. Moverare, Microstructural characterization of as-manufactured and heat treated electron beam melted Inconel 718, *Mater. Sci. Tech., Materials Science & Technology*, Salt Lake City, UT, 2016, pp. 105-112.
- [234] W.J. Sames, K.A. Unocic, G.W. Helmreich, M.M. Kirka, F. Medina, R.R. Dehoff, S.S. Babu, Feasibility of in situ controlled heat treatment (ISHT) of Inconel 718 during electron beam melting additive manufacturing, *Addit. Manuf.*, 13 (2017) 156-165.
- [235] H. Schwab, M. Bönisch, L. Giebeler, T. Gustmann, J. Eckert, U. Kuehn, Processing of Ti-5553 with improved mechanical properties via an in-situ heat treatment combining selective laser melting and substrate plate heating, *Mater. Des.*, 130 (2017) 83-89.
- [236] G. Dinda, L. Song, J. Mazumder, Fabrication of Ti-6Al-4V scaffolds by direct metal deposition, *Metall. Mater. Trans. A*, 39(12) (2008) 2914-2922.
- [237] A.M. Beese, B.E. Carroll, Review of Mechanical Properties of Ti-6Al-4V Made by Laser-Based Additive Manufacturing Using Powder Feedstock, *JOM*, 68(3) (2016) 724-734.
- [238] S. Kelly, S. Kampe, Microstructural evolution in laser-deposited multilayer Ti-6Al-4V builds: Part I. Microstructural characterization, *Metall. Mater. Trans. A*, 35(6) (2004) 1861-1867.
- [239] N. Hrabec, T. Quinn, Effects of processing on microstructure and mechanical properties of a titanium alloy (Ti-6Al-4V) fabricated using electron beam melting (EBM), part 1: Distance from build plate and part size, *Mater. Sci. Eng. A*, 573 (2013) 264-270.

- [240] H. Galarraga, R.J. Warren, D.A. Lados, R.R. Dehoff, M.M. Kirka, P. Nandwana, Effects of heat treatments on microstructure and properties of Ti-6Al-4V ELI alloy fabricated by electron beam melting (EBM), *Mater. Sci. Eng. A*, 685 (2017) 417-428.
- [241] A.R. Nassar, J.S. Keist, E.W. Reutzel, T.J. Spurgeon, Intra-layer closed-loop control of build plan during directed energy additive manufacturing of Ti-6Al-4V, *Addit. Manuf.*, 6 (2015) 39-52.
- [242] P. Wang, X. Tan, M.L.S. Nai, S.B. Tor, J. Wei, Spatial and geometrical-based characterization of microstructure and microhardness for an electron beam melted Ti-6Al-4V component, *Mater. Des.*, 95 (2016) 287-295.
- [243] M. Jamshidinia, M.M. Atabaki, M. Zahiri, S. Kelly, A. Sadek, R. Kovacevic, Microstructural modification of Ti-6Al-4V by using an in-situ printed heat sink in electron beam melting (EBM), *J. Mater. Process. Technol.*, 226 (2015) 264-271.
- [244] N. Petch, The fracture of metals, *Prog. Metal Phys.*, 5 (1954) 1-52.
- [245] D. Tabor, The hardness of metals, Oxford University Press Inc., New York, 2000.
- [246] J. Cahoon, W. Broughton, A. Kutzak, The determination of yield strength from hardness measurements, *Metall. Trans.*, 2(7) (1971) 1979-1983.
- [247] X. Tan, Y. Kok, Y.J. Tan, M. Descoins, D. Mangelinck, S.B. Tor, K.F. Leong, C.K. Chua, Graded microstructure and mechanical properties of additive manufactured Ti-6Al-4V via electron beam melting, *Acta Mater.*, 97 (2015) 1-16.
- [248] P. Åkerfeldt, M.-L. Antti, R. Pederson, Influence of microstructure on mechanical properties of laser metal wire-deposited Ti-6Al-4V, *Mater. Sci. Eng. A*, 674 (2016) 428-437.
- [249] S. Palanivel, A. Dutt, E. Faierson, R. Mishra, Spatially dependent properties in a laser additive manufactured Ti-6Al-4V component, *Mater. Sci. Eng. A*, 654 (2016) 39-52.
- [250] C. Li, Y. Guo, J. Zhao, Interfacial phenomena and characteristics between the deposited material and substrate in selective laser melting Inconel 625, *J. Mater. Process. Technol.*, 243 (2017) 269-281.
- [251] M. Ma, Z. Wang, X. Zeng, A comparison on metallurgical behaviors of 316L stainless steel by selective laser melting and laser cladding deposition, *Mater. Sci. Eng. A*, 685 (2017) 265-273.
- [252] Y. Zhong, L. Liu, S. Wikman, D. Cui, Z. Shen, Intragranular cellular segregation network structure strengthening 316L stainless steel prepared by selective laser melting, *J. Nucl. Mater.*, 470 (2016) 170-178.
- [253] Z. Wang, T.A. Palmer, A.M. Beese, Effect of processing parameters on microstructure and tensile properties of austenitic stainless steel 304L made by directed energy deposition additive manufacturing, *Acta Mater.*, 110 (2016) 226-235.
- [254] M.L. Griffith, M.T. Ensz, J.D. Puskar, C.V. Robino, J.A. Brooks, J.A. Philliber, J.E. Smugeresky, W. Hofmeister, Understanding the microstructure and properties of components fabricated by laser engineered net shaping (LENS), *MRS Proc.*, 625 (2000) 9 doi:10.1557/PROC-625-9.
- [255] D. Manfredi, E. Ambrosio, F. Calignano, M. Krishnan, R. Canali, S. Biamino, M. Pavese, E. Atzeni, L. Iuliano, P. Fino, Direct metal laser sintering: an additive manufacturing technology ready to produce lightweight structural parts for robotic applications, *Metall. Ital.*, (10) (2013) 15-24.
- [256] N. Read, W. Wang, K. Essa, M.M. Attallah, Selective laser melting of AlSi10Mg alloy: Process optimisation and mechanical properties development, *Mater. Des.*, 65 (2015) 417-424.
- [257] I. Rosenthal, A. Stern, N. Frage, Strain rate sensitivity and fracture mechanism of AlSi10Mg parts produced by Selective Laser Melting, *Mater. Sci. Eng. A*, 682 (2017) 509-517.

- [258] I. Rosenthal, A. Stern, N. Frage, Microstructure and mechanical properties of AlSi10Mg parts produced by the laser beam additive manufacturing (AM) technology, *Metall. Microstruct. Anal.*, 3(6) (2014) 448-453.
- [259] M. Tang, P.C. Pistorius, Oxides, porosity and fatigue performance of AlSi10Mg parts produced by selective laser melting, *Int. J. Fatigue.*, 94 (2017) 192-201.
- [260] T. Vilaro, C. Colin, J.D. Bartout, As-Fabricated and Heat-Treated Microstructures of the Ti-6Al-4V Alloy Processed by Selective Laser Melting, *Metall. Mater. Trans. A*, 42A(10) (2011) 3190-3199.
- [261] M. Simonelli, Y.Y. Tse, C. Tuck, Effect of the build orientation on the mechanical properties and fracture modes of SLM Ti-6Al-4V, *Materials Science and Engineering a-Structural Materials Properties Microstructure and Processing*, 616 (2014) 1-11.
- [262] X. Zhao, S. Li, M. Zhang, Y. Liu, T.B. Sercombe, S. Wang, Y. Hao, R. Yang, L.E. Murr, Comparison of the microstructures and mechanical properties of Ti-6Al-4V fabricated by selective laser melting and electron beam melting, *Mater. Des.*, 95 (2016) 21-31.
- [263] P. Edwards, A. O'Conner, M. Ramulu, Electron Beam Additive Manufacturing of Titanium Components: Properties and Performance, *J. Manuf. Sci. E-t. Asme*, 135(6) (2013) 7.
- [264] Y. Zhai, H. Galarraga, D.A. Lados, Microstructure evolution, tensile properties, and fatigue damage mechanisms in Ti-6Al-4V alloys fabricated by two additive manufacturing techniques, *Procedia Eng.*, 114 (2015) 658-666.
- [265] C. Qiu, G. Ravi, C. Dance, A. Ranson, S. Dilworth, M.M. Attallah, Fabrication of large Ti-6Al-4V structures by direct laser deposition, *J. Alloy. Comp.*, 629 (2015) 351-361.
- [266] J. Alcisto, A. Enriquez, H. Garcia, S. Hinkson, T. Steelman, E. Silverman, P. Valdovino, H. Gigerenzer, J. Foyos, J. Ogren, Tensile properties and microstructures of laser-formed Ti-6Al-4V, *J. Mater. Eng. Perform.*, 20(2) (2011) 203-212.
- [267] C. Qiu, N.J. Adkins, M.M. Attallah, Microstructure and tensile properties of selectively laser-melted and of HIPed laser-melted Ti-6Al-4V, *Mater. Sci. Eng. A*, 578 (2013) 230-239.
- [268] H. Rafi, N. Karthik, H. Gong, T.L. Starr, B.E. Stucker, Microstructures and mechanical properties of Ti6Al4V parts fabricated by selective laser melting and electron beam melting, *J. Mater. Eng. Perform.*, 22(12) (2013) 3872-3883.
- [269] P. Kobryn, S. Semiatin, Mechanical properties of laser-deposited Ti-6Al-4V, *Solid Freeform Fabrication Proceedings*, Austin, 2001, pp. 6-8.
- [270] E. Amsterdam, G. Kool, High cycle fatigue of laser beam deposited Ti-6Al-4V and Inconel 718, *ICAF 2009, Bridging the Gap between Theory and Operational Practice*, Springer, 2009, pp. 1261-1274.
- [271] B. Yao, X.-L. Ma, F. Lin, W.-J. Ge, Microstructure and mechanical properties of Ti-6Al-4V components fabricated by laser micro cladding deposition, *Rare Metals*, 34(7) (2015) 445-451.
- [272] J. Wang, Q. Sun, H. Wang, J. Liu, J. Feng, Effect of location on microstructure and mechanical properties of additive layer manufactured Inconel 625 using gas tungsten arc welding, *Mater. Sci. Eng. A*, 676 (2016) 395-405.
- [273] K. Amato, J. Hernandez, L. Murr, E. Martinez, S. Gaytan, P. Shindo, S. Collins, Comparison of microstructures and properties for a Ni-base superalloy (alloy 625) fabricated by electron beam melting, *J. Mater. Sci. Res.*, 1(2) (2012) 3.
- [274] C. Qiu, N.J. Adkins, M.M. Attallah, Selective laser melting of Invar 36: microstructure and properties, *Acta Mater.*, 103 (2016) 382-395.
- [275] T. Bauer, K. Dawson, A. Spierings, K. Wegener, Microstructure and mechanical characterisation of SLM processed Haynes® 230®, *Solid Freeform Symposium*, 2015.

- [276] I. Yadroitsev, P. Bertrand, I. Smurov, Parametric analysis of the selective laser melting process, *Appl. Surf. Sci.*, 253(19) (2007) 8064-8069.
- [277] P. Blackwell, The mechanical and microstructural characteristics of laser-deposited IN718, *J. Mater. Process. Technol.*, 170(1-2) (2005) 240-246.
- [278] Y.M. Wang, T. Voisin, J.T. McKeown, J. Ye, N.P. Calta, Z. Li, Z. Zeng, Y. Zhang, W. Chen, T.T. Roehling, Additively manufactured hierarchical stainless steels with high strength and ductility, *Nat. Mater.*, 17(1) (2018) 63-70.
- [279] A.B. Parsa, M. Ramsperger, A. Kostka, C. Somsen, C. Körner, G. Eggeler, Transmission electron microscopy of a CMSX-4 Ni-base superalloy produced by selective electron beam melting, *Metals*, 6(11) (2016) 258.
- [280] S. Gorsse, C. Hutchinson, M. Gouné, R. Banerjee, Additive manufacturing of metals: a brief review of the characteristic microstructures and properties of steels, Ti-6Al-4V and high-entropy alloys, *Sci. Technol. Adv. Mat.*, 18(1) (2017) 584-610.
- [281] V. Divya, R. Muñoz-Moreno, O. Messé, J. Barnard, S. Baker, T. Illston, H.J. Stone, Microstructure of selective laser melted CM247LC nickel-based superalloy and its evolution through heat treatment, *Mater. Charact.*, 114 (2016) 62-74.
- [282] K. Akino, K. Takechi, Strengths and microstructure of SUS316L fabricated by selective laser melting, *Mater. Trans.*, 59(3) (2018) 482-487.
- [283] B.M. Morrow, T.J. Lienert, C.M. Knapp, J.O. Sutton, M.J. Brand, R.M. Pacheco, V. Livescu, J.S. Carpenter, G.T. Gray, Impact of defects in powder feedstock materials on microstructure of 304L and 316L stainless steel produced by additive manufacturing, *Metall. Mater. Trans. A*, 49(8) (2018) 3637-3650.
- [284] Z. Qiu, C. Yao, K. Feng, Z. Li, P.K. Chu, Cryogenic deformation mechanism of CrMnFeCoNi high-entropy alloy fabricated by laser additive manufacturing process, *Int. J. Light. Mater. Manuf.*, 1(1) (2018) 33-39.
- [285] Y.S.J. Yoo, T.A. Book, M.D. Sangid, J. Kacher, Identifying strain localization and dislocation processes in fatigued Inconel 718 manufactured from selective laser melting, *Mater. Sci. Eng. A*, 724 (2018) 444-451.
- [286] E. Martinez, L.E. Murr, J. Hernandez, X. Pan, K. Amato, P. Frigola, C. Terrazas, S. Gaytan, E. Rodriguez, F. Medina, Microstructures of niobium components fabricated by electron beam melting, *Metall. Microstruct. Anal.*, 2(3) (2013) 183-189.
- [287] B.J. Hayes, B.W. Martin, B. Welk, S.J. Kuhr, T.K. Ales, D.A. Brice, I. Ghamarian, A.H. Baker, C.V. Haden, D.G. Harlow, Predicting tensile properties of Ti-6Al-4V produced via directed energy deposition, *Acta Mater.*, 133 (2017) 120-133.
- [288] R. Pokharel, L. Balogh, D. Brown, B. Clausen, G. Gray, V. Livescu, S. Vogel, S. Takajo, Signatures of the unique microstructure of additively manufactured steel observed via diffraction, *Scripta Mater.*, 155 (2018) 16-20.
- [289] R. Nandan, T. DebRoy, H.K.D.H. Bhadeshia, Recent advances in friction-stir welding - Process, weldment structure and properties, *Prog. Mater. Sci.*, 53(6) (2008) 980-1023.
- [290] J.F. Lancaster, *Metallurgy of welding*, 6th ed., Elsevier, Cambridge, London, 1999.
- [291] ASM handbook, *Welding fundamentals and processes*, ASM International, Materials Park, OH, 2011.
- [292] E.A. Jägle, Z. Sheng, L. Wu, L. Lu, J. Risse, A. Weisheit, D. Raabe, Precipitation Reactions in Age-Hardenable Alloys During Laser Additive Manufacturing, *JOM*, 68(3) (2016) 943-949.

- [293] L. Zhang, M. Wen, M. Imade, S. Fukuyama, K. Yokogawa, Effect of nickel equivalent on hydrogen gas embrittlement of austenitic stainless steels based on type 316 at low temperatures, *Acta Mater.*, 56(14) (2008) 3414-3421.
- [294] L. Wang, N. Wang, W.J. Yao, Y.P. Zheng, Effect of substrate orientation on the columnar-to-equiaxed transition in laser surface remelted single crystal superalloys, *Acta Mater.*, 88 (2015) 283-292.
- [295] H. Suzuki, Carbon equivalent and maximum hardness, *Transactions of the Japan Welding Society*, 15(1) (1984) 25-33.
- [296] Y. Ito, K. Bessyo, Weldability formula of high strength steels: Related to heat-affected zone cracking, *IIW*, (1968) 416-428.
- [297] T. Lienert, W. Stellwag Jr, B. Grimmert, R. Warke, Friction stir welding studies on mild steel, *Weld. J.*, 82(1) (2003) 1-9.
- [298] R. Nandan, G. Roy, T. Lienert, T. Debroy, Three-dimensional heat and material flow during friction stir welding of mild steel, *Acta Mater.*, 55(3) (2007) 883-895.
- [299] L. Cui, H. Fujii, N. Tsuji, K. Nogi, Friction stir welding of a high carbon steel, *Scripta Mater.*, 56(7) (2007) 637-640.
- [300] M. Khandkar, J.A. Khan, A.P. Reynolds, Prediction of temperature distribution and thermal history during friction stir welding: input torque based model, *Sci. Technol. Weld. Joi*, 8(3) (2003) 165-174.
- [301] D.C. Hofmann, K.S. Vecchio, Thermal history analysis of friction stir processed and submerged friction stir processed aluminum, *Mater. Sci. Eng. A*, 465(1-2) (2007) 165-175.
- [302] T. Kasuya, N. Yurioka, Prediction of welding thermal history by a comprehensive solution, *Weld. J.*, 72 (1993) 107-115.
- [303] C. Kenel, D. Grolimund, X. Li, E. Panepucci, V.A. Samson, D.F. Sanchez, F. Marone, C. Leinenbach, In situ investigation of phase transformations in Ti-6Al-4V under additive manufacturing conditions combining laser melting and high-speed micro-X-ray diffraction, *Sci. Rep.*, 7(1) (2017) 16358.
- [304] B. Zheng, Y. Zhou, J.E. Smugeresky, J.M. Schoenung, E.J. Lavernia, Thermal Behavior and Microstructural Evolution during Laser Deposition with Laser-Engineered Net Shaping: Part I. Numerical Calculations, *Metall. Mater. Trans. A*, 39(9) (2008) 2228-2236.
- [305] P.A. Hooper, Melt pool temperature and cooling rates in laser powder bed fusion, *Addit. Manuf.*, 22 (2018) 548-559.
- [306] A. Arora, T. DebRoy, H. Bhadeshia, Back-of-the-envelope calculations in friction stir welding—velocities, peak temperature, torque, and hardness, *Acta Mater.*, 59(5) (2011) 2020-2028.

## Chapter 3

### USING FUNCTIONALLY GRADED MATERIALS TO LIMIT CARBON DIFFUSION BETWEEN FERRITIC AND AUSTENITIC ALLOYS

#### 3.1 The problem of carbon diffusion in dissimilar welds

The interstitial carbon concentration in iron is arguably one of the most important factors that determine the properties of steels and other ferrous alloys. Desirable properties in commercial steels can be achieved by tailoring the carbon concentration to produce an acceptable balance between strength and ductility. Slight changes in carbon concentration affect nearly all mechanical properties, such as hardness [1], strength [2], ductility [3], fracture toughness [4], creep [5], and fatigue [6]. For example, variations in Rockwell hardness (HRC) are observed in Jominy end-quench experiments for 8600 series steel alloys with carbon concentrations ranging from 0.20 to 0.60 wt% C, as shown in Figure 3.1. Therefore, special attention needs to be given to the local variations of carbon concentration when designing dissimilar alloy components.

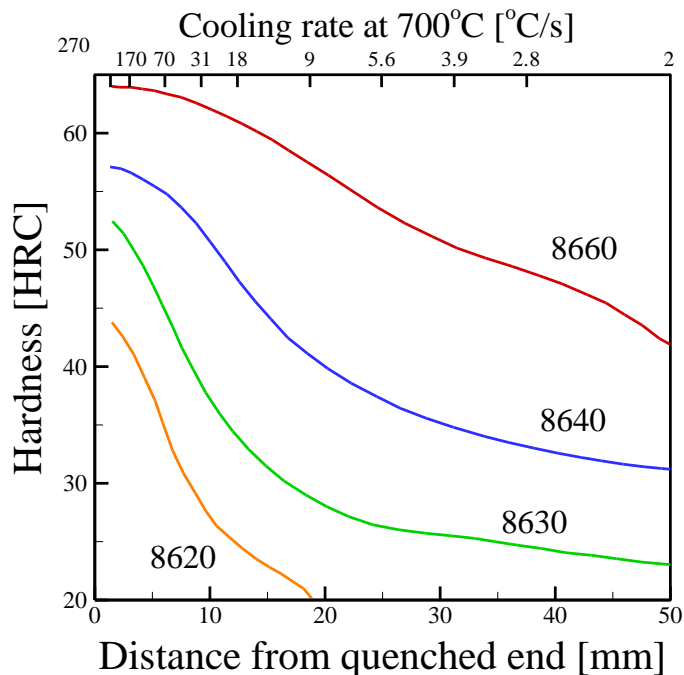


Figure 3.1. Hardenability curves for Jominy end-quench experiments on 8600 series steels (0.55Ni, 0.50Cr, 0.20Mo) with carbon concentrations of 0.20, 0.30, 0.40, and 0.60 wt% C [1, 4]. For any given distance from the quenched end, i.e. positions having similar cooling rates, a stark increase in hardness is measured as the carbon concentration increases.

Carbon migration after years of service at elevated temperatures is a major detriment to the integrity of dissimilar metal welds (DMWs) between ferritic and austenitic alloys [7-9]. Carbon generally diffuses from the ferritic steel towards the austenitic alloy or filler metal [10, 11], causing a carbon-depleted zone near the weld interface [12]. The carbon-depleted region is often much weaker than the surrounding material, resulting in a discontinuity in the local strain distribution along the weld interface [13, 14]. This region also contains few stable carbides, which are often beneficial for improving creep strength [9]. Most damage in DMWs between ferritic and austenitic alloys occur in or near this carbon-depleted zone, and carbon migration consequently has been identified as a major factor leading to premature failure [7, 8].

The problem of diffusive carbon loss from ferritic steels in DMWs has been studied extensively [10, 15-18]. The flux of carbon atoms, or the amount of carbon diffusing through a unit area per unit time, depends on both thermodynamic and kinetic factors [8, 19]. Although the spatial distribution of carbon is roughly uniform in the as-welded condition, abrupt changes in the chemical composition of other alloying elements produce a substantial carbon chemical potential gradient [20], which is the driving force for diffusion. Since these DMWs are exposed to temperatures of approximately 400-600°C, carbon diffusivity is relatively low, taking years before noticeable changes in the carbon concentration profile are observed [16]. Attempts have been made to adjust the chemical composition of the filler metal in DMWs to lower the carbon chemical potential difference and diffusivity [21]. However, the problem of carbon diffusion stills exists due to the large thermodynamic driving force. A gradual change in chemical composition extending over a larger distance would effectively lower the driving force for carbon diffusion and limit the flux of carbon away from the ferritic steel [22].

In this chapter<sup>2</sup>, functionally graded materials (FGMs) are employed to limit carbon diffusion between a ferritic steel (2.25Cr-1Mo steel) and an austenitic alloy (Alloy 800H) by lowering the thermodynamic driving force. Thermodynamic calculations are used to reduce the spatial gradient in carbon chemical potential by tailoring the concentration profiles of alloying elements. The diffusion of carbon is simulated in both a DMW and the FGM for temperatures and times relevant to service conditions. A laser-based directed energy deposition additive

---

<sup>2</sup> Portions of this chapter are reproduced from J.S. Zuback, T.A. Palmer, T. DebRoy, 'Additive manufacturing of functionally graded transition joints between ferritic and austenitic alloys', *J. Alloy Comp.*, 770 (2019) 995-1003.

manufacturing process is used to fabricate the FGM with the desired composition profiles using custom-blended powder mixtures. Accelerated heat treatments are then used to experimentally test the effectiveness of the compositional grading in limiting carbon diffusion compared to a DMWs.

### 3.2 Thermodynamic and kinetic modeling of carbon diffusion

#### 3.2.1 Model background and calculation setup

Carbon diffusion between 2.25Cr-1Mo steel and Alloy 800H DMWs and graded transition joints are investigated using thermodynamic and kinetic simulations. The problem is similar to that studied by Helander and Ågren [18] in which an interstitial element diffuses across a dissimilar alloy steel interface. The total amount of a diffusing element through an area per unit time depends both on the chemical composition of the alloy and the ability of that element to move through the phase in question. In multicomponent diffusion, as shown in Figure 3.2, the flux of a species,  $k$ , perpendicular to an axis,  $z$ , is given by [23]

$$J_k = - \sum_{i=1}^n L_{ki} \frac{\partial \mu_i}{\partial z} \quad (3.1)$$

where  $L_{ki}$  is a mobility factor and  $\mu_i$  is the chemical potential of species  $i$ . The mobility factor,  $L_{ki}$ , is related to the interdiffusion coefficients,  $D_{kj}$ , for each element of interest as

$$D_{kj} = - \sum_{i=1}^n L_{ki} \frac{\partial \mu_i}{\partial c_j} \quad (3.2)$$

where  $c_j$  is the concentration of element  $j$ . The time evolution of the concentration profile of species  $k$  is obtained by solving

$$\frac{\partial c_k}{\partial t} = - \frac{\partial}{\partial z} (J_k) \quad (3.3)$$

in which  $t$  is time. In equation (3.1), the driving force for diffusion is the spatial gradient of chemical potential,  $\partial \mu / \partial z$ , which is a function of both temperature and chemical composition at a constant pressure. Hence, a reduction in the carbon chemical potential gradient will effectively reduce the amount of carbon diffusion.

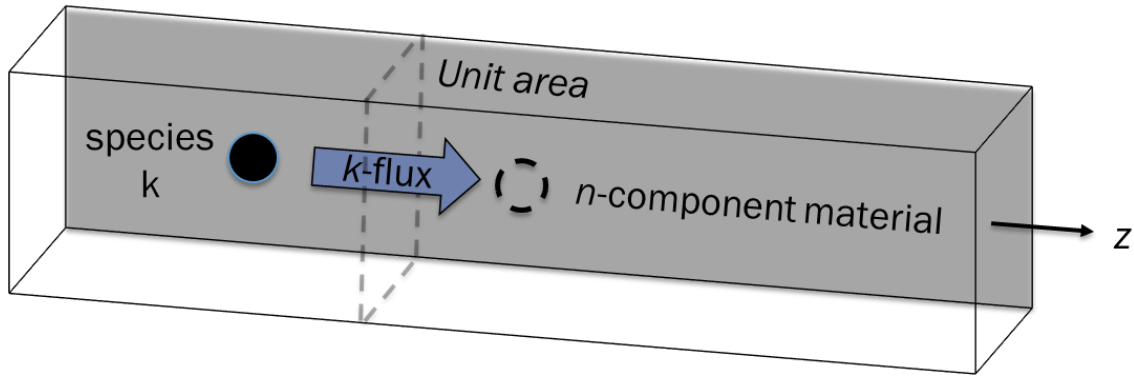


Figure 3.2. A visual representation of the one-dimensional diffusion flux of a species,  $k$ , in a multicomponent material along an axis,  $z$ .

To assess the functionality of different composition profiles for reducing carbon diffusion, ThermoCalc® and DICTRA® (Thermocalc Software AB, Stockholm, Sweden) are used. The programs are coupled during diffusion simulations to allow for simultaneous thermodynamic and kinetic calculations at each time step. The 1-D calculations allow each grid point to have a specific chemical composition to evaluate the effect of various composition gradients on carbon diffusion during extended times at elevated temperatures. The simulated carbon profiles as functions of both distance and time serve as a first step in the design for the functionality graded transition joints.

A model system is used to compare carbon diffusion between 2.25Cr-1Mo steel and Alloy 800H in a DMW with a sharp concentration change and across a diffuse compositional gradient with a linear variation in alloy concentration. The major alloying elements in the material system are Fe, Ni, Cr, Mo, and C. A temperature of 773 K (500°C), which falls within the range of common service conditions, is used for simulations. Ferrite, austenite, sigma, and  $M_{23}C_6$  phases are considered. The rule of mixtures homogenization function is employed for the estimation of local kinetic data, and a simulation time of  $6.3072 \times 10^8$  s (20 years) was used in both cases to replicate expected service lifetimes.

In current applications, 2.25Cr-1Mo steel is often fusion welded to Alloy 800H using a Ni-base filler metal (Inconel 82/182), which contains high amounts of Cr, to alleviate the coefficient of thermal expansion mismatch [24, 25]. A schematic diagram of the calculation domain for the DMW is also shown in Figure 3.3(a). The simulation contains a total region domain of 500  $\mu\text{m}$  which only includes the interface between the ferritic steel and austenitic filler metal where carbon depletion occurs [26]. To account for dilution, a 40  $\mu\text{m}$  region is defined in which an approximate

linear change in chemical composition occurs from 2.25Cr-1Mo (Fe-2.25Cr-1Mo-0.1C) to IN82 (Fe-77Ni-20Cr-0.1C) centered in the middle of the region, as shown in Figure 3.3(a). A double geometric grid system is used to provide more grid points around the dilution region of the weld with values of 0.85 and 1.15 for the lower and upper parts of the region, respectively.

Similarly, a 10 mm region was chosen for a hypothetical FGM, as shown in Figure 3.3(b). The entire region contains 2.25Cr-1Mo steel (Fe-2.25Cr-1Mo-0.1C) connected to Alloy 800H (Fe-34Ni-21Cr-0.1C) by a linear composition gradient. The chemical composition for all elements varied linearly from 2.25Cr-1Mo to Alloy 800H over a distance of approximately 6.75 mm centered in the middle of the region as shown in Figure 3.3(b). A linear grid spacing was used for the composition gradient simulation.

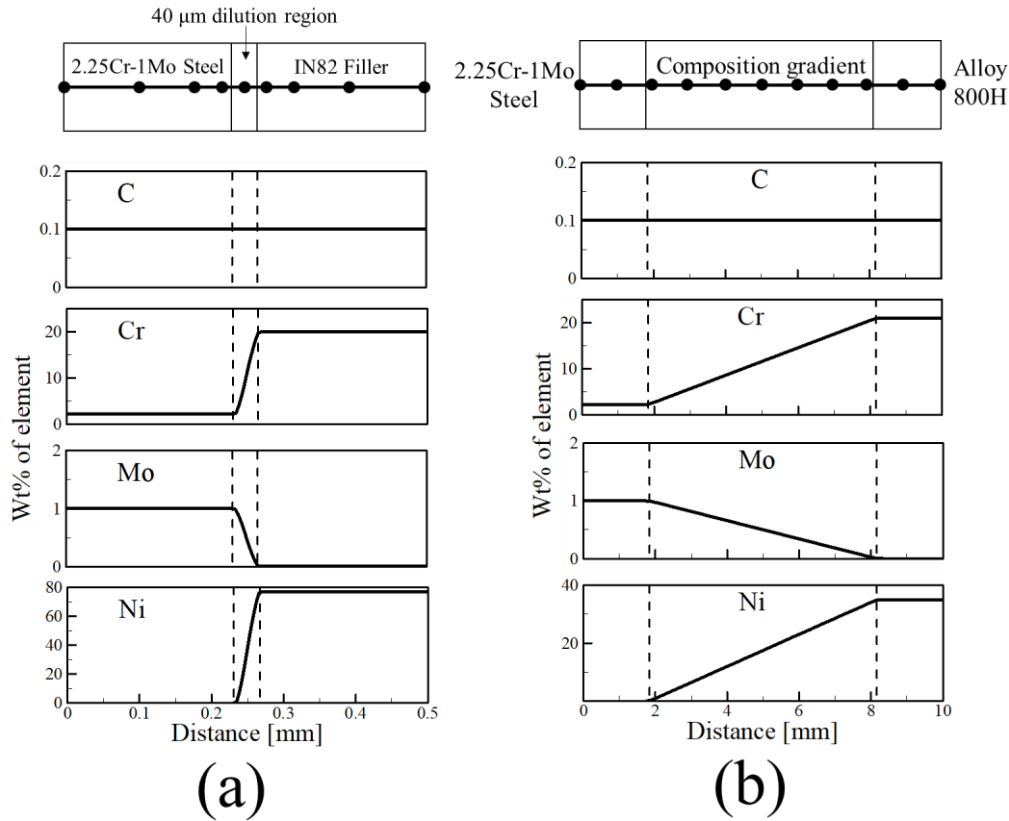


Figure 3.3. Schematic diagram of the calculation region for carbon diffusion calculations and initial composition profiles for C, Cr, Mo and Ni in (a) a dissimilar metal weld and (b) a functionally graded material between 2.25Cr-1Mo steel and Alloy 800H. The (a) double geometric and (b) linear grid spacings are shown by the solid black dots.

### 3.2.2 Influence of chemical composition on thermodynamic driving force

In order to address the reduction of carbon migration through the use of FGMs, simulations were used to compare carbon diffusion across the DMW and FGM between 2.25Cr-1Mo steel and Alloy 800H. The carbon chemical potential as a function of distance at the beginning of the simulation for the DMW and FGM are shown in Figure 3.4 (a) and (b), respectively. A large drop in chemical potential is observed in the DMW in Figure 3.4(a) over a relatively short distance, resulting in a large driving force for diffusion. The sudden decrease can be attributed to both the increase of chromium, a strong carbide forming element, and the change in microstructure from ferrite to austenite. Since austenite has a higher solubility of carbon, an additional driving force for carbon diffusion is introduced. In contrast, Figure 3.4(b) shows that the driving force is significantly lowered as the change in carbon chemical potential occurs gradually over a much longer distance.

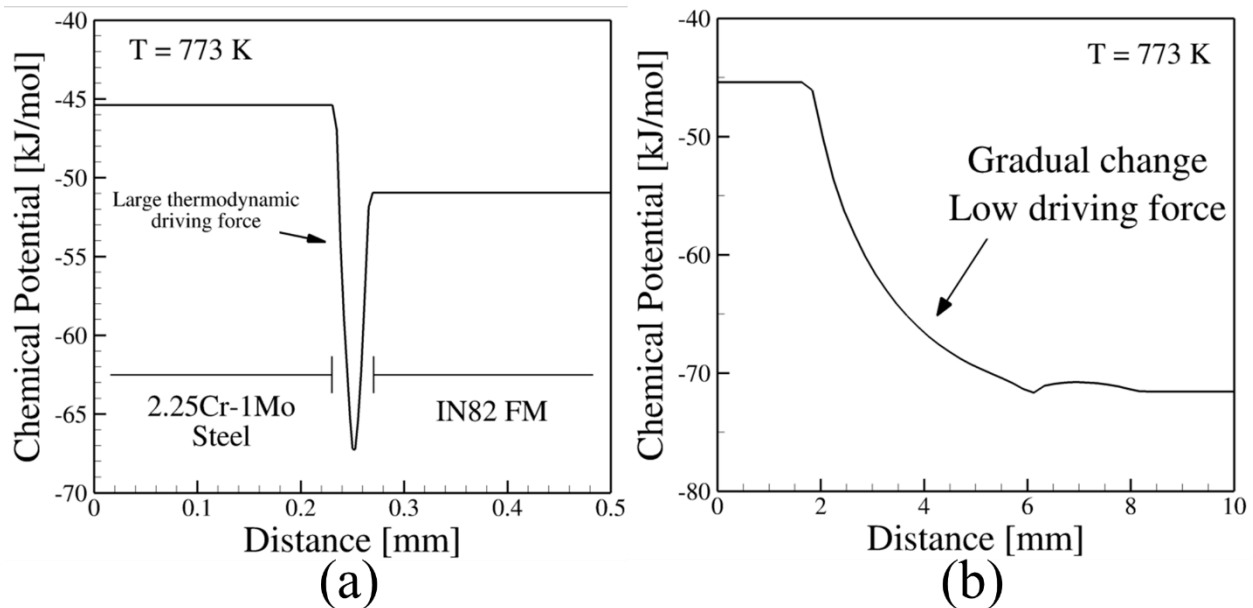


Figure 3.4. The abrupt change of the carbon chemical potential in (a) dissimilar metal welds results in a much larger thermodynamic driving force for carbon diffusion than the gradual change in (b) functionally graded materials.

### 3.2.3 Predicting carbon diffusion during service

Using these calculated carbon chemical potential gradients, the simulated carbon profiles as a function of time and distance are shown in Figure 3.5(a) and (b) for the weld and FGM, respectively. In the DMW (Figure 3.5 (a)), a large amount of carbon migrates from the ferritic steel towards the austenitic filler metal. A peak carbon concentration of 0.446 wt% is reached at

approximately the midpoint of the weld, while the carbon content in the ferritic steel is constantly lowered as time increases. The overall trends in the plot are consistent with experimental observations of carbon diffusion in DMWs [10, 15, 27]. The peak carbon concentration and widths of the enriched and depleted zones are highly dependent on the different experimental conditions, such as materials, heat treatment and measurement techniques. In contrast to the DMW, the carbon migration in the compositionally graded joint is drastically hindered, as shown in Figure 3.5 (b). The maximum and minimum carbon concentrations reached in the gradient after a simulated time of 20 years at 773 K are 0.106 and 0.090 wt% C, respectively. These results show that the linear composition gradient of the FGM is effective for significantly slowing carbon diffusion compared to its DMW counterpart.

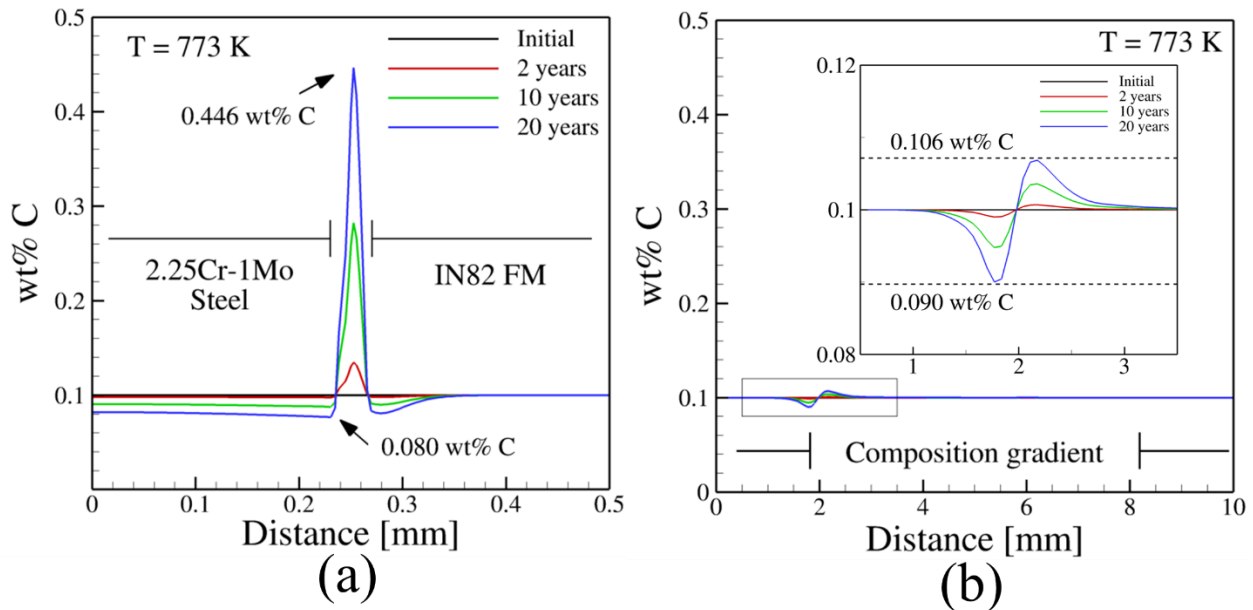


Figure 3.5. Changes in the carbon concentration profile as a function of time for (a) a dissimilar metal weld and (b) a functionally graded material between 2.25Cr-1Mo steel and Alloy 800H.

### 3.2.4 Testing model with literature data

To date, experimentally measured carbon concentration profiles across DMWs between 2.25Cr-1Mo steel and Alloy 800H using IN82 filler metal are not available. Therefore, carbon diffusion is simulated and compared with experimental data [10] between ferritic 5.0Cr-0.5Mo and austenitic 21Cr-12Ni steels to validate the coupled thermodynamic and kinetic model. The measured carbon concentrations in the as-welded condition were directly entered into the simulation at the beginning of the heat treatment (773 K for 500 h). The effects of dilution were accounted for by considering a linear change in chemical composition from the ferritic to austenitic

steel over approximately 20  $\mu\text{m}$ . The ferrite, austenite and  $\text{M}_{23}\text{C}_6$  phases were considered in the calculations and the system was simplified to contain only Fe, Ni, Cr, Mo and C. Although the  $\text{M}_6\text{C}$  carbide was observed experimentally [10], only small amounts were reported, and the effects of excluding this phase in the calculations is assumed to be negligible.

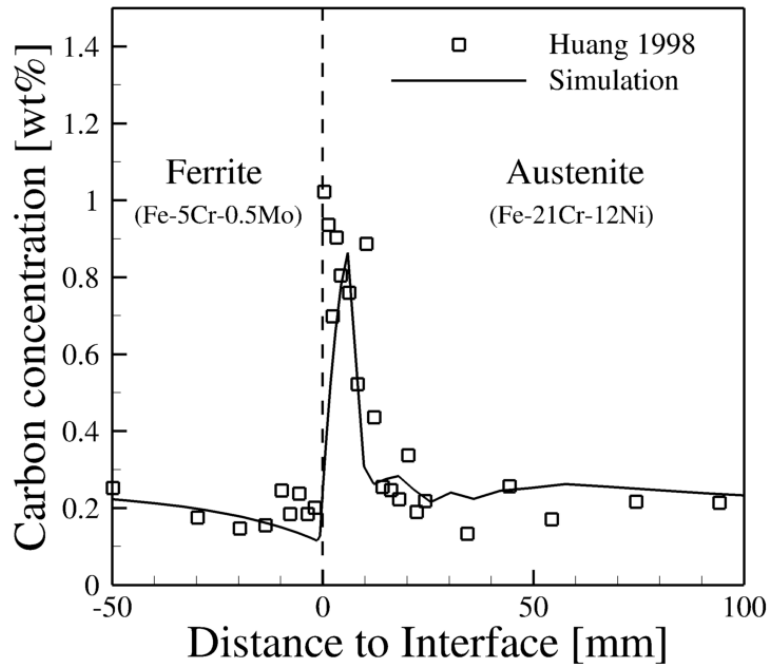


Figure 3.6. Comparison of simulated carbon diffusion profiles with experimental measurements between a 5Cr-0.5Mo/21Cr-12Ni weld heat treated at 773 K for 500 h.

Figure 3.6 shows good agreement between the measured and simulated profiles. Non-destructive profile measurements for low carbon concentrations are notoriously difficult and measurements with two different techniques on the same material can show different results [15]. However, it is worthwhile to note the trends that the model was able to accurately predict. The maximum peak was located beside the original weld interface just inside the austenitic side of the weld. Furthermore, the width of the carbon enriched zone is approximately 10 to 20  $\mu\text{m}$ . On the ferritic side of the interface, a slight depletion of carbon is observed. In failed DMWs, this region is often the location of failure [7]. The agreement between the predicted and measured values allows for the simulations to be used for the design of FGMs in this study.

### 3.3 Experimental methods and materials

#### 3.3.1 Powder feedstock and compositional grading

The powder feedstock used during deposition consisted of pre-alloyed Pyromet® 800 (Carpenter Powder Products, Inc.) and commercially pure iron and chromium (Atlantic Equipment Engineers, Micron Metals, Inc.). All powders had a size range from 45 to 145 µm in diameter, and compositions of the substrate and powders are shown in Table 3.1. Since the DED system is equipped with only one powder feeder, compositional grading was performed by blending Pyromet® 800 (800H) and the custom blended Fe-Cr mixture (Fe-2.25Cr) to produce the desired composition prior to deposition at each height of the gradient. A schematic illustration of the steps in powder blending is shown in Figure 3.7.

*Table 3.1. Composition (in wt%) of materials used in the DED-L process. Single values in the baseplate composition represent the maximum allowable concentration.*

Material*	Al	Cr	Mn	Ni	Si	Ti	C	O	S	Other
Baseplate	-	2.0-2.5	0.3-0.6	-	0.50	-	0.05-0.15	0.035	0.035	0.035P, 0.90-1.1Mo
Pyromet® 800	0.38	21.0	0.88	34.0	0.62	0.41	0.095	0.015	0.006	0.003P, 0.003N
Fe Powder	0.002	0.002	-	0.03	-	-	0.003	0.01	-	0.007Co
Cr Powder	0.02	Bal.	-	-	0.01	-	0.02	0.02	0.01	0.02Fe

\* All material compositions have Fe balance, except for Cr powder.

A total of 9 different mixtures from 10% to 90% 800H were blended in increments of 10% 800H using a twin-screw mixing method. The compositions, in terms of percent 800H and the corresponding layers, are identified in the schematic diagram shown in Figure 3.8. The laser beam remained off for approximately 5 minutes each time a new powder mixture was introduced. While this method added to the overall machine time, discontinuous processes have been shown to be beneficial for reducing residual stresses and distortion [28]. A total of 34 layers were deposited using 5 passes per layer. All passes within a layer were scanned in the same direction, and successive layers were scanned in the opposite direction to produce an alternating layer build path plan.

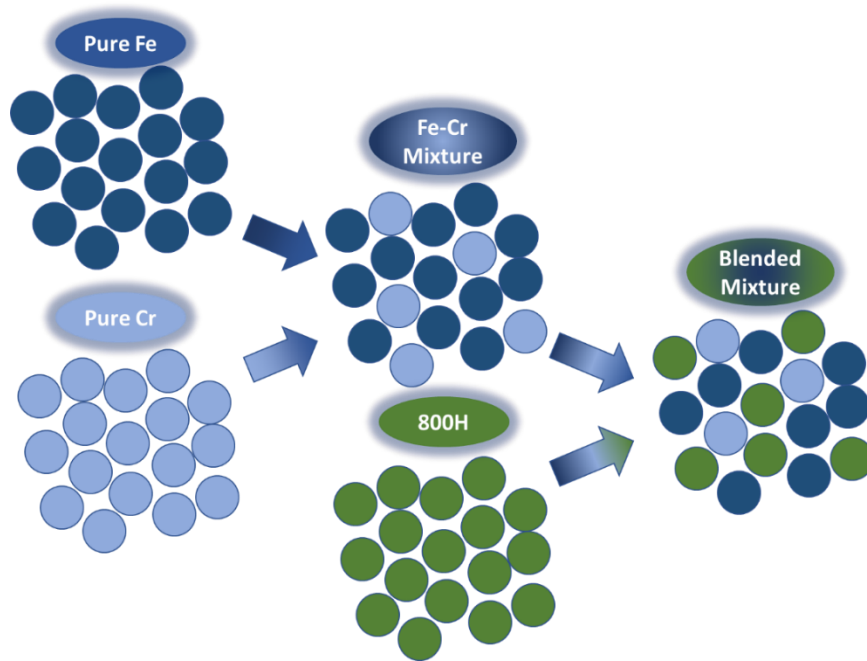


Figure 3.7. Illustration showing the steps for achieving blended mixtures using a combination of elemental (Fe, Cr) and pre-alloyed powder (800H)

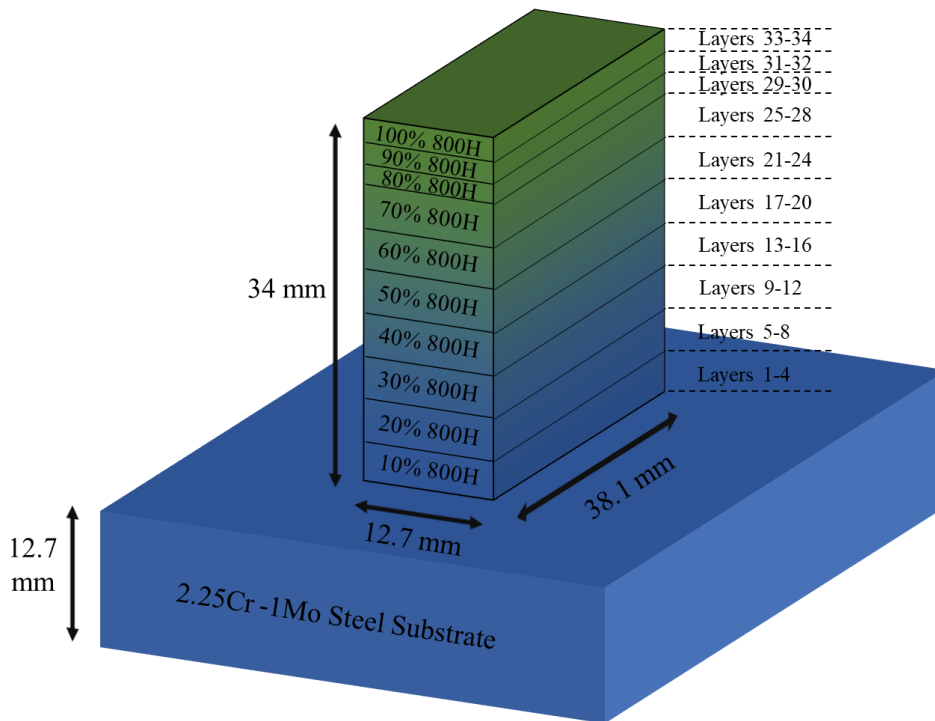


Figure 3.8. Schematic diagram of the build dimensions in the functionally graded material between 2.25Cr-1Mo steel and Alloy 800H.

### 3.3.2 Specimen fabrication and preparation

A laser-based DED process designed to operate at high laser powers was used to fabricate a series of compositionally graded joints on a normalized and tempered 150 mm x 150 mm x 12.7 mm thick SAE387 Grade 22 steel substrate. During processing, the build chamber was purged with high purity argon, and the oxygen content, as measured by an oxygen meter, was held between 300 and 500 ppm to reduce the potential for oxidation of the deposited material. A ytterbium fiber laser (IPG Photonics® YLR-12000-L) with a wavelength ranging from 1070-1080 nm was used at a power of 2000 W and a travel speed of 10.6 mm/s, giving a linear heat input of 189 J/mm. Powder was delivered through four nozzles with 1.6 mm diameter orifices at a total flow rate of approximately 0.25 g/s. Each nozzle was angled to converge the powder streams coaxially with the laser to a spot 10 mm below the point of exit, which corresponds to a laser beam radius of approximately 2 mm. Additional shielding was supplied by argon gas flowing coaxially with the laser beam.

A DMW between 2.25Cr-1Mo steel and Alloy 800H was fabricated using a multi-pass gas metal arc welding process with IN82 filler metal with a 1.14 mm diameter. The plates were beveled to an angle of 30° from the vertical plane and a root spacing of 10 mm was used. The welding sequence consisted of 4 layers with one pass in the 1<sup>st</sup> layer, two passes in the 2<sup>nd</sup> layer, two passes in the 3<sup>rd</sup> layer, and three passes in the 4<sup>th</sup> layer. Using a preheat temperature of 280°C, the plates were joined using a voltage of 21 V, current of 210 A, wire feed speed of 127 mm/s and travel speed of 4.23 mm/s. The shielding gas consisted of a mixture of CO<sub>2</sub> and Ar.

After deposition, a thin slice was extracted near the middle of the functionally graded deposit using electrical discharge machining to reveal the transverse cross section. A small sample was sectioned around the 2.25Cr-1Mo steel/IN82 filler metal interface of the DMW using an abrasive saw. The samples were mounted and ground with a series of silicon carbide papers up to P2000 ISO grit size, polished with 3 μm and 1 μm polycrystalline diamond suspension, and finished with 0.05 μm colloidal silica.

### 3.3.3 Chemical composition profile measurements

For quantitative, high resolution chemistry measurements, chemical composition along the grading direction was measured by electron probe microanalysis (EPMA) using a CAMECA SXFive. EPMA measurements allow for non-destructive characterization with accurate spatial

resolution. The instrument was operated at a voltage of 20 keV and current of 30 nA. The EPMA trace spanned vertically along the build direction in increments of 1 mm and the main alloying elements (Fe, Ni and Cr) in the graded joint were analyzed.

Measurements of the spatial distribution of carbon in both the DMW and FGM were made following the procedure outlined by Poelt and Fian [29] using EPMA. The instrument was operated at a 15kV accelerating voltage and 200 nA beam current. A liquid nitrogen cooling trap kept at approximately -190°C was used to limit contamination. A total of three line scans measuring 300  $\mu\text{m}$  each were centered on the interface of interest in 1  $\mu\text{m}$  steps using a 5 s counting time at each location and the number of counts per second were recorded in each sample. Measurements were taken at the 2.25Cr-1Mo steel/IN82 filler metal interface in the DMW and at the 2.25Cr-1Mo steel/10% 800H interface in the FGM. The number of counts per second were converted to wt% C by calibrating the known carbon concentrations of NIST (National Institute of Standards and Technology) standard reference materials containing 0.016 wt% C (SRM2159), 0.1143 wt% C (SRM36b) and 0.082 wt% C (SRM866) through linear interpolation.

### **3.4 Testing the effectiveness of FGM**

#### *3.4.1 Calibrating carbon measurements*

The accuracy of EPMA measurements for light elements such as carbon is highly dependent on the standards used for calibration. Reference materials were selected to represent the range of elements and concentrations expected in the test specimens. The low alloy steel (SRM2159) contained only carbon and a small amount of sulfur. The Cr-Mo steel (SRM36b) and Incoloy 800 (SRM866) reference materials were selected since their chemical compositions are similar to the parent alloys of 2.25Cr-1Mo steel and Alloy 800H. Line scans were performed on each reference material and the number of counts per second for all data points were averaged. The results of the line scans are shown in Figure 3.9 (a)-(c). Larger standard deviations were recorder in the Cr-Mo steel and Incoloy 800 materials, which is likely due to the presence of small carbides. Both the Cr-Mo steel and Incoloy 800 materials contain strong carbide forming elements, such as Cr, Mo, and Ti.

Poelt and Fian [29] used EPMA measurements on steel grades with various chemical compositions to show that there exists an almost perfectly linear trend between the intensity of carbon x-rays and wt% C. More importantly, the linear trend was largely unaffected by differences

in chemical composition, which allows for a simple way to measure carbon concentration profiles in steels using calibration curves from standard reference materials. Following this procedure, a linear fit was applied to the averaged counts per second for each reference material as a function of the known carbon content. The linear fit, for which an  $R^2$  value of 0.861 was obtained, is shown in Figure 3.9(d). Using the linear fit, the number of counts per second can be converted to wt% C to measure carbon concentration profiles in the DMW and FGM.

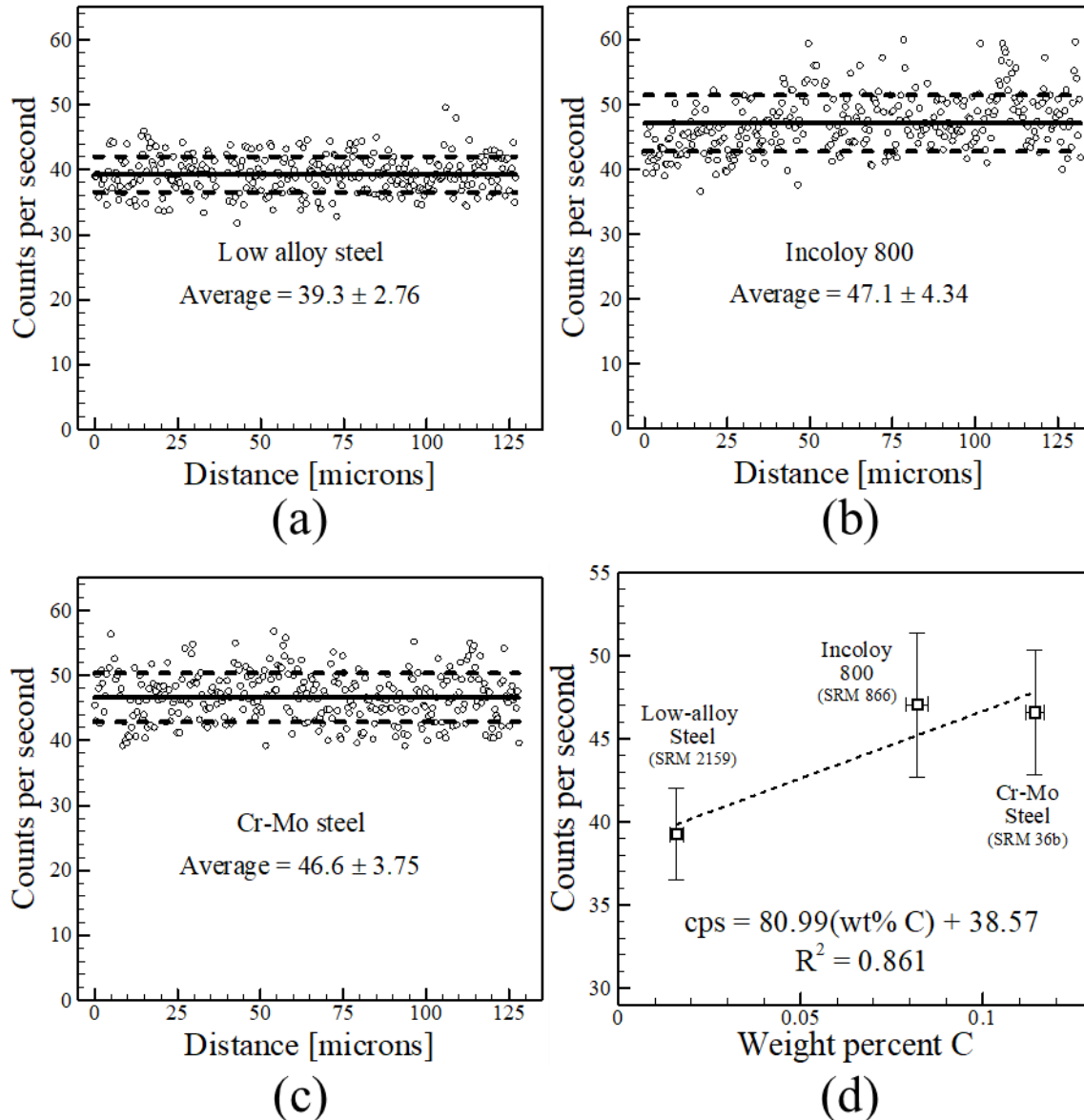


Figure 3.9. For quantitative carbon concentration measurements, carbon counts per second were recorded during line scans on standard reference materials of (a) low alloy steel, (b) Incoloy 800, and (c) Cr-Mo steel with known carbon concentrations. (d) A linear interpolation between data points was then used to determine the carbon concentration of unknown samples.

### 3.4.2 Initial chemical concentration profiles

It is evident from Figure 3.4 and Figure 3.5 that control of the variation of chemical composition within the FGM is important to reduce the driving force for carbon diffusion compared to a DMW. The concentrations of the main alloying elements, Fe, Ni and Cr, at various locations along the length of the AM build measured using EPMA are shown in Figure 3.10. The expected compositions are overlaid by solid lines on the measured values for comparison. The expected chemical composition variations were calculated using the rule of mixtures from the known compositions of the powder feedstock and the respective weight fractions of each powder in the mixture. Overall, the measured compositions closely follow the expected step-wise trend of the chemical compositions. Small deviations, particularly in the Fe concentration, occurred in regions corresponding to the interface between two layers of different compositions, which is likely due to dilution resulting from the remelting of the previously deposited layers.

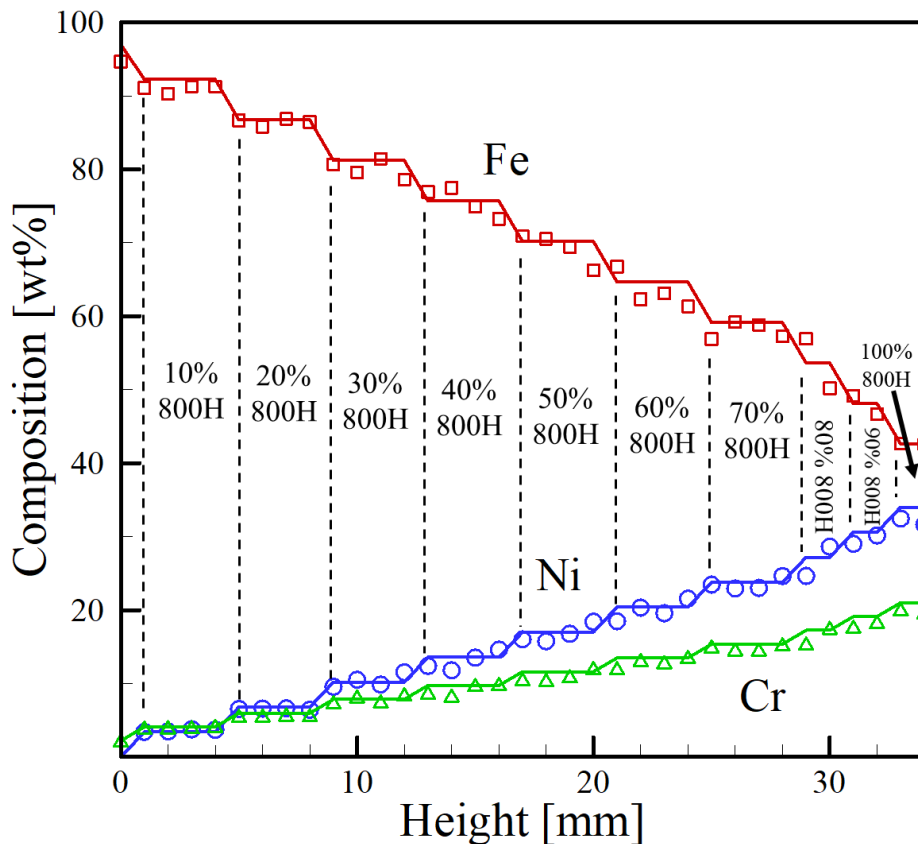


Figure 3.10. The measured concentrations of Fe, Ni, and Cr show that a gradual, stepwise change in chemical composition was achieved in the functionally graded material close to the expected variations calculated using a simple rule of mixtures.

The spatial variation of the carbon chemical potential can be calculated using computational thermodynamics at any given temperature using the measured chemical compositions. It is worthwhile to note that the absolute values of chemical potential depend on the experimental data used when the CALPHAD database was developed or the reference state chosen for each element. Therefore, these values can vary from program to program. However, the calculated values of chemical potential can be considered arbitrary, and the difference between two data points are of more interest. The chemical potential of carbon as a function of distance along the length of the FGM was calculated using the General Steel database of JMatPro® V8. A typical service temperature of 773 K (500°C) was selected for the calculations. Clearly, the change in the carbon chemical potential in the FGM is gradual and no abrupt changes in chemical potential occurs. Thus, the driving force for carbon diffusion from the ferritic steel to the austenitic alloy is significantly reduced.

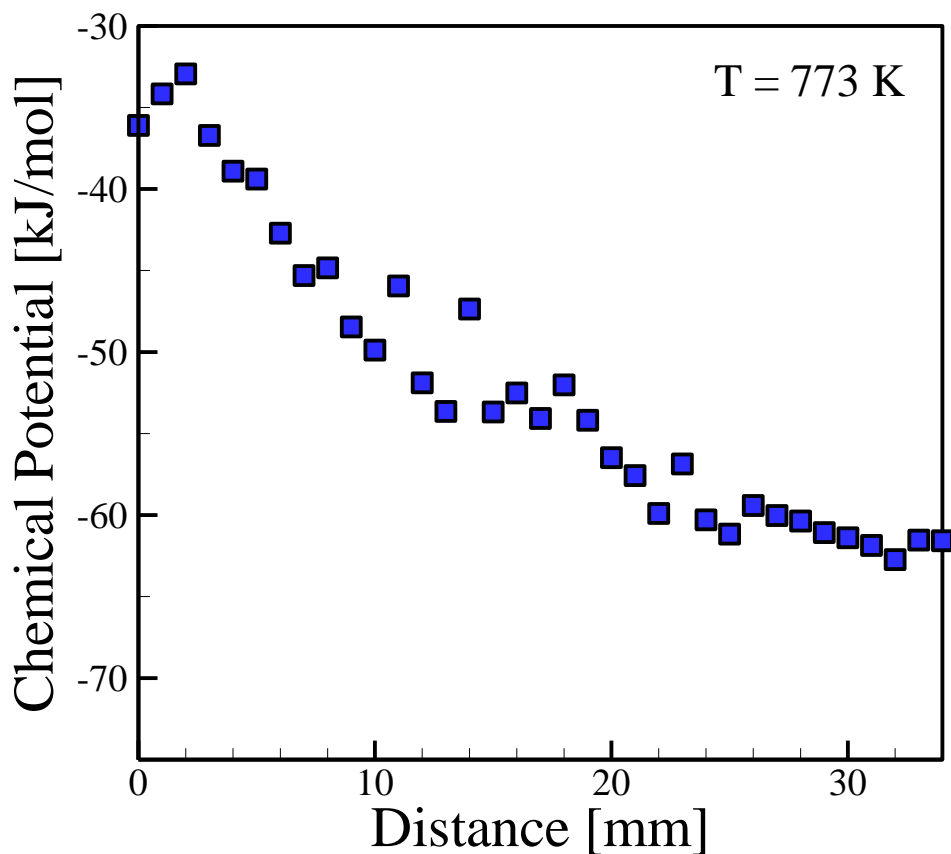


Figure 3.11. The calculated variation in carbon chemical potential at 773 K (500°C) as a function of distance using the measured chemical compositions in Figure 3.10 shows a gradual change in the thermodynamic driving force for carbon diffusion.

The carbon concentration profiles were also measured using EPMA via three line scans across the interface adjacent to the 2.25Cr-1Mo steel baseplate for each sample. The points for each location correspond to the average values of the three line scans and the error bars represent the standard deviation. In the weld, the IN82 filler metal was immediately adjacent to the steel baseplate, whereas the 10% 800H region is the beginning of the FGM. In the as-welded condition, an approximately downward linear trend is observed in Figure 3.12(a) near the interface moving from the ferritic steel towards the austenitic filler metal, indicating dilution during welding. Nominally, the ferritic steel contains slightly more carbon than the filler metal, as was measured by EPMA. The carbon concentration in Figure 3.12(b) was roughly uniform across the interface between the baseplate and the first layer of the FGM. Although the baseplate ( $\sim 0.1$  wt% C) contains more carbon than the blended powders of the first layer ( $\sim 0.01$  wt% C), the uniform carbon concentration in Fig. 8a indicates significant dilution and mixing of the molten pool.

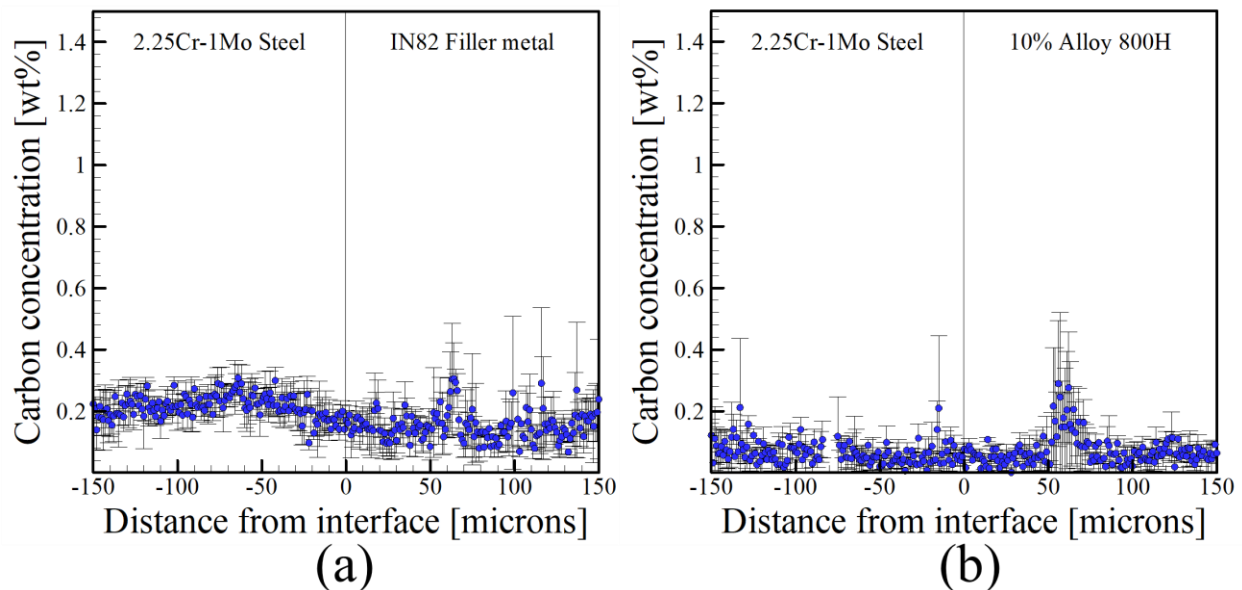


Figure 3.12. The smooth changes in the initial carbon concentrations of the (a) dissimilar weld and (b) functionally graded material in the as-welded and as-deposited conditions, respectively, indicate that both samples experienced dilution during processing.

### 3.4.3 Selecting an effective heat treatment

The DMWs in power generation plants are deployed in service at about 773 K (500°C) for several decades before their performance is compromised due to metallurgical degradation resulting from carbon migration away from the ferritic side of the joint. These long durations are not feasible for laboratory experiments. To examine the effectiveness of the FGM to overcome this problem, the FGM and a DMW need to be subjected to an accelerated heat treatment to investigate carbon diffusion from the ferritic side of the joint. However, there is currently no available tool for selecting effective accelerated heat treatments

Decades of typical service conditions were simulated by selecting a temperature of heat treatment that was much higher than the typical service temperature of 773K. The selection of time and temperature was based on the application of the Larson-Miller parameter,

$$LMP = T(C + \log(t)) \quad (3.4)$$

where  $T$  is temperature in K,  $C$  is a material constant, and  $t$  is the time in hours. The Larson-Miller parameter [30] is frequently used for extrapolating experimentally measured creep data for homogeneous materials to prolonged times at which laboratory experiments are not feasible. The results of two experimental data appoints are said to be comparable when they have equivalent  $LMP$  values.

In equation (3.4), a reduction in time must be accompanied by a corresponding increase in temperature to maintain a constant Larson-Miller parameter, which allows for laboratory experiments to be performed in a timely manner. The variation of LMP with time and temperature is shown in Figure 3.13, where a value of  $C=20$  was chosen, corresponding to commonly used values for applications involving 2.25Cr-1Mo steel [31]. The red circles in Figure 3.13, which have equivalent  $LMP$ , for example, demonstrate that an accelerated heat treatment at 973 K (700°C) for 3 h can be used to simulate an experiment at 823 K (550°C) lasting 20,000 h, or approximately 2.3 years. Using this procedure, the DMW and FGM were held at 998 K (725°C) for 235 h (~10 days). From equation (3.4), this treatment has an equivalent  $LMP$  to conditions of 773 K and approximately  $7.6 \times 10^8$  h, conditions much more severe than typical service conditions.

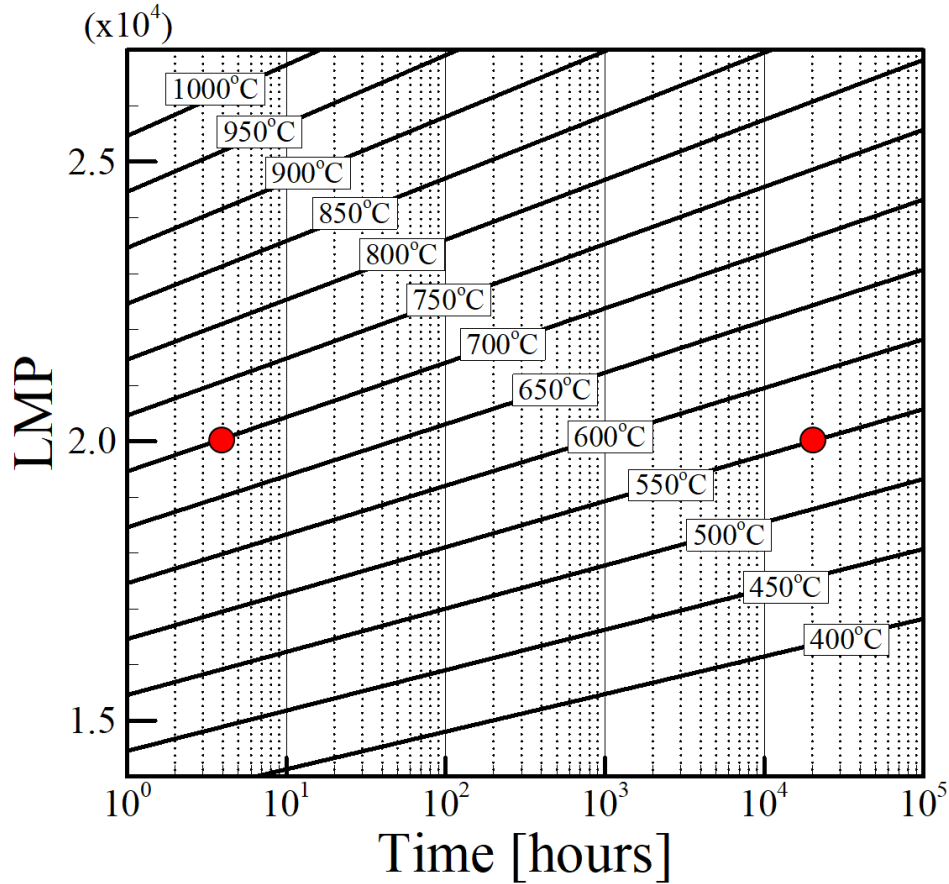


Figure 3.13. The variation of the Larson-Miller parameter with time and temperature calculated from equation (3.4) ( $C=20$ ) with two equivalent LMP values at different times and temperatures shown by the red circles.

#### 3.4.4 Carbon concentration profiles after heat treatment

Following the heat treatment, the DMW and FGM were ground and polished with the standard reference materials so that all surfaces were prepared similarly. A total of three EPMA line scans were performed at the interface of interest and the average carbon concentration was calculated at each distance from the interface. Carbon diffusion simulations for the accelerated heat treatment of both the DMW and FGM were performed using the initial measured carbon concentration profiles and the heat treatment time and temperature as inputs. Identical numerical schemes consisting of 100 grid points in a 2 mm wide region centered on the interface were used for calculations.

High carbon concentrations in the DMW are observed on the austenitic side of the interface while the average carbon concentration on the ferritic side is slightly depleted, as shown in Figure 3.14(a). The measured concentration profiles shown good agreement with the predicted profile.

The peak carbon concentration ( $\sim 1$  wt% C) in the weld was about an order of magnitude higher than the initial carbon concentration at the weld interface ( $\sim 0.1$  wt% C). The measurements indicate that a significant amount of carbon diffuses from the ferritic steel and the austenitic filler metal becomes enriched. The large standard deviations in the austenitic filler metal adjacent to the weld interface are due to the precipitation of carbides, which are commonly observed after high temperature exposure [7].

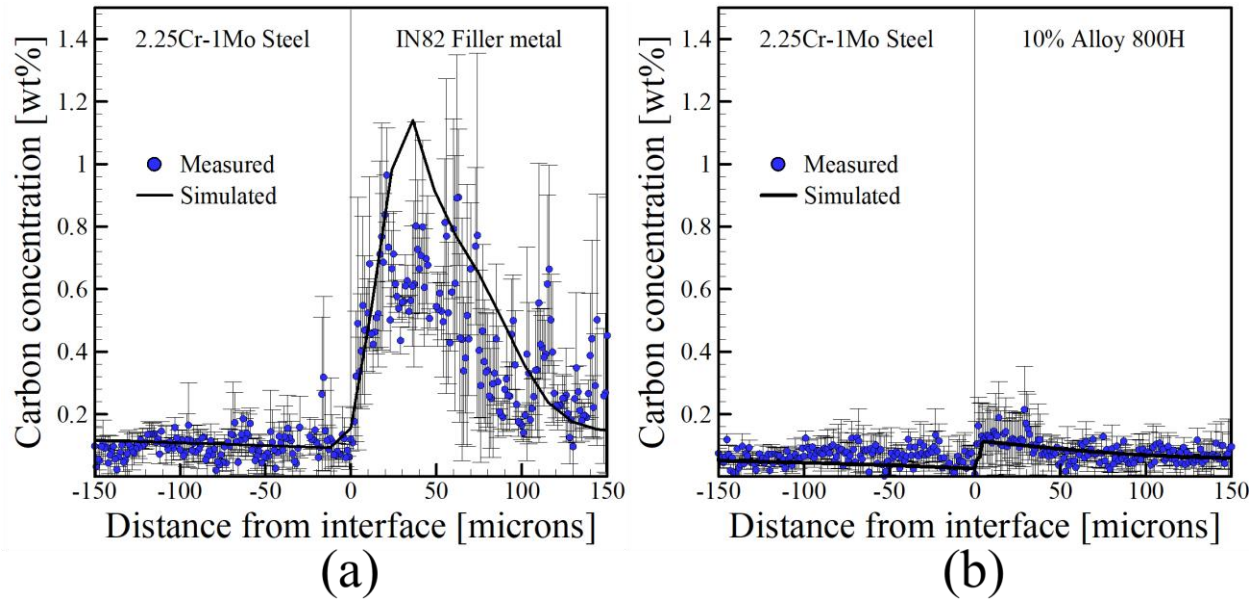


Figure 3.14. A comparison of the carbon concentration profiles in the (a) DMW and (b) FGM after an accelerated heat treatment at 998 K (725°C) for 235 h demonstrate that carbon diffusion is significantly suppressed in the FGM compared to the DMW.

In contrast to the weld, the FGM shows very little changes in the carbon concentration profile after heat treatment in Figure 3.14(b). The predicted carbon concentration profile shows only a minute amount of depletion in the baseplate and resulting accumulation in the first deposited layer. However, these fluctuations are much too subtle to be resolved by EPMA due to the experimental error in measurements. Regardless, carbon diffusion from the ferritic steel is undoubtedly suppressed in the presence of the chemical composition gradient of the FGM even under conditions more extreme than typical service conditions.

The use of composition gradients instead of dissimilar metal weld have long been proposed as a viable solution to limit carbon diffusion during service. However, there has been no experimental evidence to directly support this claim and most studies have been purely theoretical. The accelerated heat treatment and the subsequent carbon concentration profile measurements by

EPMA experimentally show, for the first time, that compositionally graded joints prevent the diffusive carbon loss from the ferritic side of the joint. These results prove that a linear composition gradient fabricated by AM has the potential to mitigate some long-standing metallurgical issues associated with dissimilar metal joints in nuclear and fossil power generation applications.

### **3.5 Minimizing the driving force for carbon diffusion**

The use of a linear change in chemical composition between 2.25Cr-1Mo steel and Alloy 800H has theoretically and experimentally been shown to reduce carbon diffusion during high temperature heat treatments when compared to a dissimilar weld. The choice of a linear change is convenient because it requires only a simple mixture of various elemental and pre-alloyed powders in predefined weight fractions for specimen fabrication. However, a linear variation in chemical composition does not necessarily lead to an optimal solution in terms of minimizing diffusive carbon loss because a linear change in chemical composition does not result in a linear variation in the carbon chemical potential, as shown in Figure 3.4(b). The minimum thermodynamic driving force for carbon diffusion occurs when the carbon chemical potential as a function of position is linear. A method is provided in this section which tailors the chemical composition profile in a FGM by optimizing the variation in chromium to minimize the driving force for carbon diffusion. Computational thermodynamic calculations are coupled with a genetic search algorithm to provide a solution that minimizes the carbon chemical potential gradient.

It is known that the amount of chromium significantly affects the carbon chemical potential. Brentrup et al. [16] demonstrated that a lowering the chromium concentration in a compositionally graded transition joint between 2.25Cr-1Mo steel and Alloy 800H can reduce the carbon chemical potential gradient. A thermodynamic calculation was made for a linear variation in chemical composition, but assuming Alloy 800H hypothetically contained 10 wt% Cr instead of the nominal 21 wt% Cr. Therefore, it is assumed for simplicity that all compositions will vary linearly, and chromium can be adjusted to manipulate the carbon chemical potential. In this methodology, the chromium concentration profile which minimizes the carbon potential gradient at different locations across the transition joint is determined. For simplicity, four equally spaced locations across the FGM which has an arbitrary overall length are considered. The nominal compositions of 2.25Cr-1Mo steel (Position 0), Alloy 800H (Position 5), and Positions 1 to 4 are shown below in Table 3.2.

Table 3.2. Chemical compositions at various positions along a hypothetical functionally graded material, where the chromium concentration is to be determined at each location and all other elements vary linearly between 2.25Cr-1Mo steel and Alloy 800H.

Position	Fe	Cr	Mo	Mn	Ni	Si	C	Cu	Ti	Al
0	Bal.	2.25	1	0.5	0.045	0.5	0.1	-	-	-
1	Bal	?	0.8	0.7	7.03	0.6	0.1	0.15	0.12	0.12
2	Bal	?	0.6	0.9	14.01	0.7	0.1	0.3	0.24	0.24
3	61.94	?	0.3	1.2	Bal	0.8	0.1	0.45	0.36	0.36
4	50.72	?	0.2	1.3	Bal	0.9	0.1	0.6	0.48	0.48
5	39.5	21	-	1.5	Bal.	1	0.1	0.75	0.6	0.6

In this example, the FGM is assumed to be in service at a temperature of 500°C, which is included in the typical service range. Using the thermodynamic database JMatPro® V8, the carbon chemical potential for any alloy concentration can be calculated. To start, the compositions of the two end member alloys are entered, and the carbon chemical potential is calculated. A generic linear equation in the form of  $y=mx+b$  is calculated where  $y$  is chemical potential,  $m$  is the slope,  $x$  is the position and  $b$  is the chemical potential at the 0 position. A linear interpolation is chosen since the minimum thermodynamic driving force for carbon diffusion occurs when carbon chemical potential as a function of position is linear. Using the linear equation, the optimal chemical potential at each location can be obtained.

Using JMatPro® V8, the carbon chemical potential is calculated as a function of the concentration of any alloying element. Each of the compositions in Table 2 above is entered and the chemical potential of carbon as a function of chromium concentration is calculated for each composition. The data can then be fitted to a 4<sup>th</sup> order polynomial equation, resulting in four different equations corresponding to the locations along the FGM that relate carbon chemical potential to chromium concentration.

At this point, there is now an optimized linear relation between carbon chemical potential and position and 4 polynomial equations relating carbon chemical potential to chromium concentration. Next, a genetic search algorithm is applied to the 4 polynomial equations. The genetic algorithm will create a random population of chromium concentrations and test each value

to finally determine the chromium concentration at the 4 positions along the joint which minimize the carbon potential gradient.

The genetic search algorithm used in this problem has been well documented and details can be found elsewhere [32-34]. In the input file, the user defines the number of variables, population members, number of generations in the first line, a weighting factor, and crossover ratio. Last, the range of values for each variable for the genetic algorithm to operate in are specified, which can be useful to decrease the amount of computing time. An example of the input file is shown below:

```
4,50,800      !# of variables, population members, generations
0.8, 0.5      !weighting factor, crossover ratio
0 21.0        !lower and upper bounds of the first variable
0 21.0        !lower and upper bounds of the second variable
0 21.0        !lower and upper bounds of the third variable
0 21.0        !lower and upper bounds of the fourth variable
```

The source code then performs the genetic algorithm by first generating an initial random population based on user inputs. The fitness of individual in the population is then tested. The variables correspond to a chromium concentration at the selected positions along the transition joint. For example, the first variable is the chromium concentration at position 1, the second variable is the chromium concentration at position 2 and so on. The parameter ‘*value*’ is the objective function. Each objective function contains the polynomial equation for the 4 different locations along the joint, as described above. The lines take the form

$$value = \left( 1 + \frac{ax^4 + bx^3 + cx^2 + dx + e}{const} \right)^2 \quad (2)$$

The polynomials in each function correspond to the variables. The term ‘*const*’ in each line is the absolute value of the optimized carbon chemical potential found using the linear relation described above. The polynomial will give a negative value, since we are simulating in a range of chromium

concentrations that can only give negative chemical potentials. Ideally, the objective function will approach zero by the end of the simulation, however, an acceptable fitness value is set at which point the simulation will end. The results from the simulation are written in output file, where a table is created showing the initial population and also the values for each of the variables with their corresponding fitness value.

A comparison between the optimized carbon chemical potential gradient as described above and that calculated in Figure 3.4(b) for a linear change in chemical composition is shown in Figure 3.15 as a function of arbitrary distance units. A linear variation in all alloying elements from the high carbon chemical potential in 2.25Cr-1Mo steel to the low potential Alloy 800H significantly deviates from the optimal solution. Clearly, a linear composition change is not the optimal solution for limiting carbon migration from the ferritic steel.

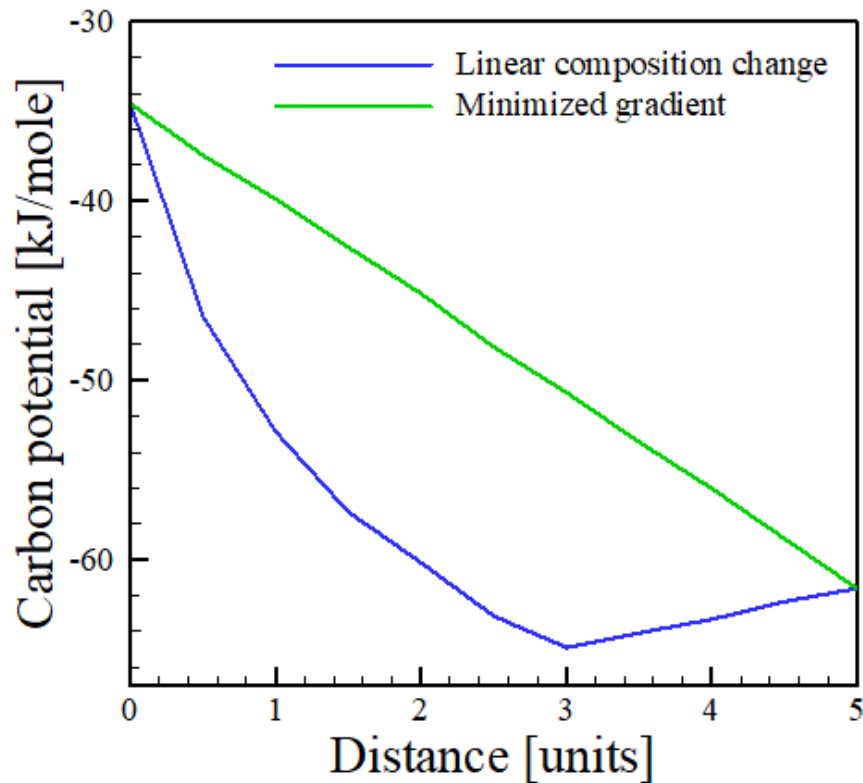


Figure 3.15. Carbon potential as a function of distance at 500°C for a linear composition change (blue) and a composition change modeled to minimize carbon potential gradient (green) from 2.25Cr-1Mo steel ( $x=0$ ) to Alloy 800H ( $x=5$ ).

By controlling the concentration of chromium at various locations while all other elements vary linearly, the optimal solution can be obtained. The results from the genetic search algorithm

are shown in Figure 3.16. Compared to the case where chromium is varied linearly, chromium needs to be significantly lowered to minimize the driving force for carbon diffusion at all locations across the graded alloy. Since chromium has a negative first-order interaction coefficient with carbon in solution, the addition of chromium effectively lowers the Gibbs free energy, and also the chemical potential, of carbon. Hence, to increase the chemical potential, some chromium needs to be removed from solution to achieve the linear variation in carbon chemical potential gradient.

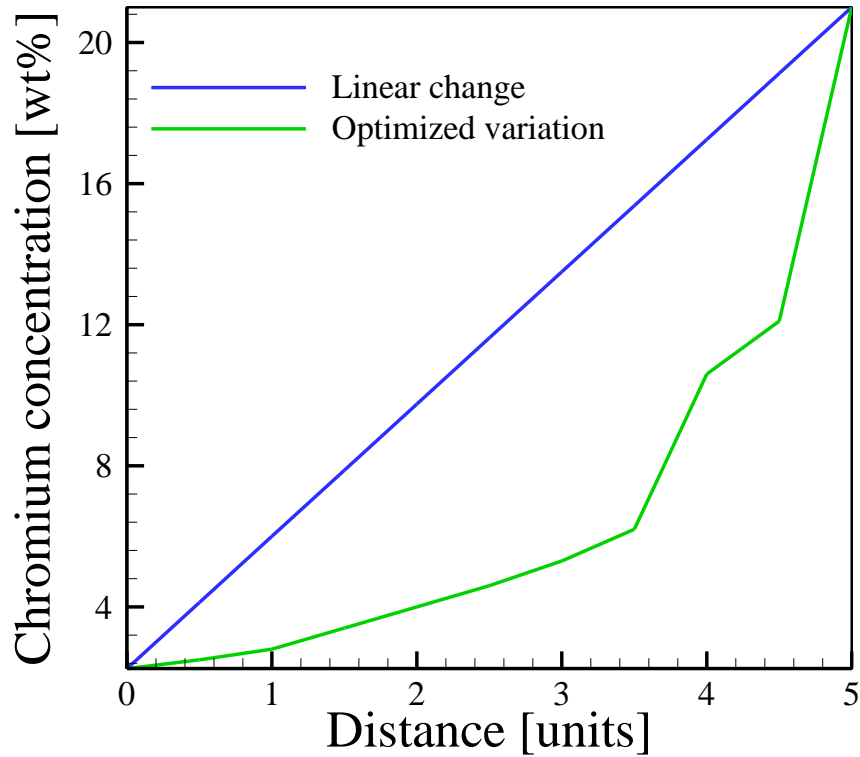


Figure 3.16. Chromium concentration as a function of distance at 500°C for a linear composition change (blue) and a composition change modeled to minimize carbon potential gradient (green) from 2.25Cr-1Mo steel (position=0) to Alloy 800H (position=5).

In the calculations, the distance was chosen as arbitrary because the optimal solution is a linear carbon chemical potential gradient regardless of the length. To investigate the dependence on the transition joint length on the minimization of the carbon chemical potential gradient, it assumed that the composition has been chosen such that a linear change in chemical potential results. The carbon potential gradient is calculated as a function of the length of the transition joint and the results are shown in Figure 3.17. For all temperatures, a FGM as small as five centimeters in length is adequate in further reducing the carbon chemical potential gradient and benefits in compositional grading beyond this point are marginal. Such results are beneficial for experimental

fabrication because shorter lengths will save materials, labor, and equipment costs, reduce fabrication time, and limit the potential for introducing process-related defects, such as lack of fusion voids, residual stresses and distortion, or delamination.

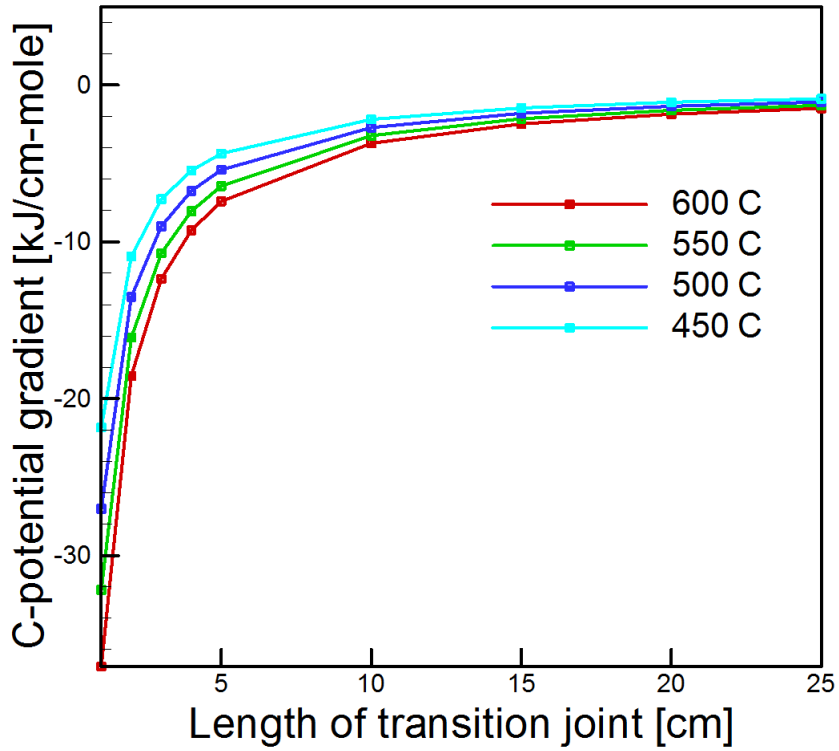


Figure 3.17. Carbon potential gradient as a function of length of transition joint at four different temperatures within the typical service range.

### 3.6 Summary and conclusions

The diffusion of carbon away from ferritic steels in dissimilar ferritic-to-austenitic welds is a major detriment to structural materials in nuclear and fossil power generation facilities. Functionally graded materials have the potential to improve the properties and performance of ferritic/austenitic joints compared to dissimilar welds by reducing carbon migration. A solution to the problem involves the reduction of the thermodynamic driving force for diffusion through tailoring the chemical composition profiles. In this chapter, the spatial variation of the carbon chemical potential through compositional grading between a ferritic steel and an austenitic alloy was investigated experimentally and theoretically. Functionally graded transition joints were fabricated using additive manufacturing and characterized to understand carbon loss by diffusion. A method was then developed to minimize the carbon chemical potential gradient using a genetic search algorithm coupled with computational thermodynamic simulations. The major findings in can be summarized in the following conclusions:

- The abrupt change in chemical composition over a relatively small distance in dissimilar metal welds causes a rapid drop in the carbon chemical potential gradient. Consequently, a large thermodynamic driving force (carbon potential gradient) for carbon diffusion exists. On the other hand, a functionally graded material with a gradual change in chemical composition extended over approximately 6 mm significantly lowers the carbon chemical potential gradient and reduces the driving force for carbon diffusion.
- Due to the large driving force for diffusion, the initial uniform carbon concentration profile of a 2.25Cr-1Mo steel/Alloy 800H weld changes significantly as a function of time during a simulated heat treatment at 773 K (550°C). The ferritic steel becomes depleted in carbon and a peak carbon concentration approximately four times higher than the initial concentration accumulates in the austenitic filler metal after a 20 year diffusion time. In contrast, the initial carbon concentration profile in the functionally graded material shows negligible variations during the same heat treatment and remains virtually unchanged. The diminished carbon diffusion in the functionally graded material compared to the dissimilar weld is a result of the significantly lowered thermodynamic driving force.
- Experimentally measured carbon concentration profiles after accelerated heat treatment show that a functionally graded material between 2.25Cr-1Mo steel and Alloy 800H is highly effective in reducing carbon diffusion compared to a dissimilar weld. While

depletion in the ferritic steel and accumulation in the filler metal were observed in the dissimilar weld, negligible changes in the carbon concentration profile were observed in the functionally graded material before and after heat treatment.

- A method is described that utilizes a combination of computational thermodynamic software and a genetic search algorithm to minimize the driving force for carbon diffusion. By isolating specific alloying elements, the concentration can be adjusted to tailor carbon chemical potential gradient. In the example given, the concentration profile of chromium was varied to provide the optimal solution. When all other elements vary linearly, a significant reduction in the chromium concentration at any point along the functionally graded material is needed to minimize the carbon chemical potential gradient.
- Functionally graded materials with overall lengths as small as 5 cm can be effective for reducing the carbon chemical potential gradient. For an optimized material, benefits from increasing length beyond this point are marginal because the driving force for carbon diffusion is not significantly reduced.

### 3.7 References

- [1] J.S. Zuback, T. DebRoy, The hardness of additively manufactured alloys, *Materials*, 11(11) (2018) 2070.
- [2] E. Keehan, L. Karlsson, H.O. Andrén, H.K.D.H. Bhadeshia, Influence of carbon, manganese and nickel on microstructure and properties of strong steel weld metals: Part 3 – Increased strength resulting from carbon additions, *Sci. Technol. Weld. Joi*, 11(1) (2006) 19-24.
- [3] P.J. Wray, Effect of carbon content on the plastic flow of plain carbon steels at elevated temperatures, *Metall. Trans. A*, 13(1) (1982) 125-134.
- [4] W.D. Callister, D.G. Rethwisch, *Materials science and engineering: An introduction*, John Wiley & Sons New York, 2007.
- [5] R.L. Klueh, The effect of carbon on 2.25 Cr-1 Mo steel: (II). Creep—rupture properties, *J. Nucl. Mater.*, 54(1) (1974) 55-63.
- [6] M. Tayanç, A. Aytaç, A. Bayram, The effect of carbon content on fatigue strength of dual-phase steels, *Mater. Des.*, 28(6) (2007) 1827-1835.
- [7] J.N. DuPont, Microstructural evolution and high temperature failure of ferritic to austenitic dissimilar welds, *Int. Mater. Rev.*, 57(4) (2012) 208-234.
- [8] C. Lundin, Dissimilar metal welds-transition joints literature review, *Weld. J.*, 61(2) (1982) 58-63.
- [9] J. Race, H. Bhadeshia, Precipitation sequences during carburisation of Cr–Mo steel, *Mater. Sci. Tech.*, 8(10) (1992) 875-882.
- [10] M. Huang, d.L. Wang, Carbon migration in 5Cr-0.5 Mo/21Cr-12Ni dissimilar metal welds, *Metall. Mater. Trans. A*, 29(12) (1998) 3037-3046.
- [11] J. Clark, D. McCartney, H. Saghafifar, P. Shipway, Modelling chemical and microstructural evolution across dissimilar interfaces in power plants, ASME 2014 Power Conference, Citeseer, 2014, pp. V001T07A004-V001T07A004.
- [12] C. Sudha, A.L.E. Terrance, S.K. Albert, M. Vijayalakshmi, Systematic study of formation of soft and hard zones in the dissimilar weldments of Cr–Mo steels, *J. Nucl. Mater.*, 302(2) (2002) 193-205.
- [13] M. Subramanian, J. Galler, J. DuPont, B. Kombaiah, X. Yu, Z. Feng, S. Babu, Heterogeneous creep deformation in Dissimilar Metal Welds (DMWs), *Mater. Sci. Eng. A*, 749 (2019) 1-13.
- [14] F. Mas, G. Martin, P. Lhuissier, Y. Bréchet, C. Tassin, F. Roch, P. Todeschini, A. Simar, Heterogeneities in local plastic flow behavior in a dissimilar weld between low-alloy steel and stainless steel, *Mater. Sci. Eng. A*, 667 (2016) 156-170.
- [15] F. Mas, C. Tassin, N. Valle, F. Robaut, F. Charlot, M. Yescas, F. Roch, P. Todeschini, Y. Bréchet, Metallurgical characterization of coupled carbon diffusion and precipitation in dissimilar steel welds, *J. Mater. Sci.*, 51(10) (2016) 4864-4879.
- [16] G. Brentrup, B. Snowden, J. DuPont, J. Grenestedt, Design considerations of graded transition joints for welding dissimilar alloys, *Weld. J.*, 91 (2012) 252-59.
- [17] J.P. Galler, J.N. DuPont, S.S. Babu, M. Subramanian, Design of Graded Transition Joints Through Thermodynamic and Kinetic Modeling, *Metall. Mater. Trans. A*, 50(6) (2019) 2765-2783.
- [18] T. Helander, J. Ågren, Computer simulation of multicomponent diffusion in joints of dissimilar steels, *Metall. Mater. Trans. A*, 28(2) (1997) 303-308.
- [19] H. Larsson, L. Höglund, Multiphase diffusion simulations in 1D using the DICTRA homogenization model, *CALPHAD: Comput. Coupling Phase DiagramsThermochem.*, 33(3) (2009) 495-501.

- [20] L.S. Darken, Diffusion of carbon in austenite with a discontinuity in composition, *Trans. AIME.*, 180 (1949) 430-438.
- [21] Q. Wu, F. Lu, H. Cui, X. Liu, P. Wang, X. Tang, Role of butter layer in low-cycle fatigue behavior of modified 9Cr and CrMoV dissimilar rotor welded joint, *Mater. Des.*, 59 (2014) 165-175.
- [22] J.S. Zuback, T.A. Palmer, T. DebRoy, Additive manufacturing of functionally graded transition joints between ferritic and austenitic alloys, *J. Alloy. Comp.*, 770 (2019) 995-1003.
- [23] A. Borgenstam, L. Höglund, J. Ågren, A. Engström, DICTRA, a tool for simulation of diffusional transformations in alloys, *J. Phase Equilib.*, 21(3) (2000) 269.
- [24] J. DuPont, R. Mizia, Review of dissimilar metal welding for the NGNP helical-coil steam generator, Idaho Falls, ID, 2010,
- [25] A.K. Bhaduri, S. Venkadesan, P. Rodriguez, P.G. Mukunda, Transition metal joints for steam generators—An overview, *Int. J. Pres. Ves. Pip.*, 58(3) (1994) 251-265.
- [26] K. Laha, K.B.S. Rao, S. Mannan, Creep behaviour of post-weld heat-treated 2.25 Cr-1Mo ferritic steel base, weld metal and weldments, *Mater. Sci. Eng. A*, 129(2) (1990) 183-195.
- [27] R. Ryder, C. Li, R. Viswanathan, J. Dimmer, Dissimilar metal weld failures in power plants—Causes and remedies, *Trends in electric utility research*, (1984) 137.
- [28] E.R. Denlinger, J.C. Heigel, P. Michaleris, T. Palmer, Effect of inter-layer dwell time on distortion and residual stress in additive manufacturing of titanium and nickel alloys, *J. Mater. Process. Technol.*, 215 (2015) 123-131.
- [29] P. Poelt, A. Fian, Steels, Carbon Concentration, and Microhardness, *Modern Developments and Applications in Microbeam Analysis*, Springer, 1998, pp. 201-205.
- [30] F. Larson, J. Miller, Time-temperature relationship for rupture and creep stresses, *Transactions of ASME*, 74 (1952) 765-771.
- [31] R. Klueh, A. Nelson, Ferritic/martensitic steels for next-generation reactors, *J. Nucl. Mater.*, 371(1) (2007) 37-52.
- [32] A. Kumar, T. DebRoy, Guaranteed fillet weld geometry from heat transfer model and multivariable optimization, *Int. J. Heat Mass. Tran.*, 47(26) (2004) 5793-5806.
- [33] R. Rai, T. DebRoy, Tailoring weld geometry during keyhole mode laser welding using a genetic algorithm and a heat transfer model, *J. Phys. D. Appl. Phys.*, 39(6) (2006) 1257-1266.
- [34] S. Mishra, T. DebRoy, A computational procedure for finding multiple solutions of convective heat transfer equations, *J. Phys. D. Appl. Phys.*, 38(16) (2005) 2977-2985.

## Chapter 4

# MICROSTRUCTURAL EVOLUTION IN A FUNCTIONALLY GRADED 2.25CR-1MO STEEL AND ALLOY 800H SYSTEM

### 4.1 Chapter overview

Phase transformations in steels have been widely studied over the past century. For many steels, the microstructure and properties can be manipulated through tight control of chemical composition and thermal processing to provide a range of properties for specific applications. Unlike other commonly used AM materials, like aluminum, nickel, and copper alloys, many ferrous alloys undergo important solid-state transformations during cooling that significantly impact mechanical properties. When steels are used in FGMs, these transformations are impacted by changes in chemical composition, so an understanding of the physical metallurgy is crucial.

Consequently, the overall performance of FGMs between ferritic and austenitic alloys depend on the spatial variation of microstructure and properties. During compositional grading of alloys of different crystal structures, it can be expected that changes in microstructure will occur. However, the ability to predict the spatial distribution of phase compositions and transformation temperatures are largely in question. In FGMs fabricated by AM, unexpected metastable phases, abrupt changes in properties, and remnants of solidification products are often observed.

In this chapter<sup>3</sup>, the FGM between 2.25Cr-1Mo steel and Alloy 800H was characterized to investigate microstructural changes along the composition gradient. Additional single-alloy components were fabricated to characterize the phase transformation behavior. Where applicable, the results of microstructural characterization were coupled with theoretical calculations to explain experimental observations. The problem of carbon diffusion was also revisited to identify tradeoffs between desirable microstructures and design functionality of the FGM.

---

<sup>3</sup> Portions of this chapter are reproduced from J.S. Zuback, T.A. Palmer, T. DebRoy, 'Additive manufacturing of functionally graded transition joints between ferritic and austenitic alloys', *J. Alloy Comp.*, 770 (2019) 995-1003.

## 4.2 Experimental methods and theoretical calculations

### 4.2.1 Sample fabrication and preparation

The FGM between 2.25Cr-1Mo steel and Alloy 800H fabricated in Chapter 3 was used for characterization. Additional single composition builds ranging from 10 to 70% 800H were fabricated with the same specimen geometry and process parameters as the FGM. Electrical discharge machining was used to extract 3 to 4 mm thick specimens of the transverse cross section of each material for metallurgical characterization. Samples were mounted in epoxy, ground with a series of SiC papers, and polished with 1 and 3  $\mu\text{m}$  diamond suspensions. A final mirror finish was obtained by polishing with 0.05 colloidal silica for approximately 10 minutes. For dilatometry experiments, 10 mm long samples with a 4 x 4 mm square cross section were extracted from the single composition builds using a low-speed abrasive saw.

### 4.2.2 Characterization techniques

Micro-hardness measurements were taken using a LECO M-400-G1 microhardness tester with a Vickers indenter. A 300 g load with a dwell time of 5 s was used for all indentations. Hardness traces were recorded at 1 mm intervals along the build direction starting at the fusion line between the base metal and the first layer of the deposition. This spacing was chosen to coincide with the approximate layer height of 1 mm and to avoid interactions between individual hardness indents. A total of 5 hardness measurements were taken per layer at each height and the standard deviation is reported.

Scanning electron microscopy (SEM) using a FEI Quanta 200 was used to view microstructures along the composition gradient. A 20 kV accelerating voltage and 4 mm spot size were used for both secondary electron and backscatter electron images. The SEM is equipped for use with energy dispersive spectroscopy (EDS), which can provide the spatial intensity of multiple elements simultaneously. EDS composition maps were used to show segregation of important carbide forming elements (Cr, Ti) near dendritic boundaries.

Laboratory X-ray diffraction (XRD) measurements were used to determine the relative ferrite and austenite phase fractions in the as-deposited single alloy specimens. Measurements were performed on a Malvern Panalytical Empyrean (3<sup>rd</sup> gen.) using a  $\theta/\theta$  configured Bragg-Bretano HD with a Co-K $\alpha$  source ( $\lambda = 1.78899 \text{ \AA}$ ) and a programable anti-scatter slit Xcelerator detector. A  $2\theta$  range of 45-126°, a step size of approximately 0.02°, and a spot size of 10 mm were

used for all measurements. A total of three XRD scans were measured for each sample to provide statistical data. The two prominent peaks for ferrite and austenite, which are (110) and (111), respectively, were used to determine the lattice spacing from Bragg's Law. It was assumed that the lattice parameters of the BCT martensite phase and BCC ferrite phase were equivalent [1]. The proportional parameter,  $R_i^{hkl}$  was determined for each  $hkl$  peak using tabulated values of the multiplicity factor, atomic scattering factor, temperature factor, and structure factor for each phase [2]. The volume fraction of austenite ( $V_\gamma$ ) was then calculated using the direct comparison method [3], and is expressed as,

$$V_\gamma = \frac{\left(\frac{1}{q} \sum_{j=1}^q \frac{I_{\gamma j}}{R_{\gamma j}}\right)}{\left(\frac{1}{p} \sum_{i=1}^p \frac{I_{\alpha i}}{R_{\alpha i}}\right) + \left(\frac{1}{q} \sum_{j=1}^q \frac{I_{\gamma j}}{R_{\gamma j}}\right)} \quad (4.1)$$

$\alpha$  and  $\gamma$  represent ferrite and austenite, respectively,  $I$  is integrated intensity,  $R$  is the proportional parameter,  $p$  corresponds to the four ferrite peaks, and  $q$  corresponds to the five austenite peaks.

Dilatometric measurements were performed using a horizontal TA Instruments DIL805A quenching dilatometer. The instrument uses inductive heating by passing alternating current through a copper coil to precisely control temperature and measures dimensional changes based on displacement of pushrods. The sample was placed between alumina pushrods and temperature was monitored by a type S thermocouple spot welded to the center of each sample. All samples were heated in vacuum to 900°C at a rate of 5°C/min, held for 3 hours, and cooled to room temperature at a cooling rate of 5°C/min using argon gas flow. The measured strain was calibrated by subjecting a platinum specimen with known thermal expansion characteristics to an identical heat treatment.

#### 4.2.3 Predictions of microstructure and phase transformations

During AM of alloys, rapid solidification and heat transfer to surrounding material leads to high cooling rates both upon solidification and through important solid-state transformation temperature ranges [4-6]. As a result, the observed phases can often deviate from equilibrium due to rapid temperature changes, limiting the use of equilibrium thermodynamic calculations for phase predictions. JMatPro® V8 (Sente Software LTD, United Kingdom), which also uses the CALPHAD approach and minimization of the Gibbs energy method, is equipped with modules

developed for specific material processing calculations. Unlike ThermoCalc®, these material-specific modules solve for important phase transformations to account for non-equilibrium phases and microconstituents. Equilibrium phase predictions, martensite formation temperatures, continuous cooling transformation diagrams, and Scheil solidification calculations are performed using the General Steel and NiFe Superalloy databases in JMatPro® for microstructure predictions. Inputs for calculations include chemical composition and temperature ranges of interest, with the expected chemical composition of each powder blend serving as input. The benefit of including non-equilibrium phase considerations in the design of functionally graded materials is the ability to predict the likelihood of forming undesired phases.

In Fe-based alloys, the consideration of non-equilibrium phases becomes increasingly important due to the formation of martensite and bainite microconstituents. The formation of metastable martensite must be considered in the steel rich regions of the composition gradient. For the same chemical composition, martensite can have significantly different mechanical properties than other microconstituents or phases, like bainite, ferrite, or pearlite, which form during relatively slower cooling rates. The martensite start ( $M_s$ ), 50% completion ( $M_{50}$ ), and 90% completion ( $M_f$ ) temperatures are calculated in JMatPro® based on chemical compositions similar to the methods by Ghosh and Olson [7] and Lee and Park [8]. These methods calculate the temperature as a function of alloying elements to determine the critical chemical free energy change required for martensite nucleation. The  $M_s$  is often represented as  $M_s = \sum_i k_i w_i$  where  $k_i$  is a constant coefficient and  $w_i$  is weight percent of element  $i$ , but the effects of prior austenite grain size are neglected.

Continuous cooling transformation (CCT) calculations are used to determine critical cooling rates needed for the formation of pearlite and bainite in the steel-rich region of the composition gradient. The CCT diagrams are calculated by first developing transformation diagrams under isothermal conditions and transforming data to continuous cooling conditions based on well-established additivity rules [9, 10]. All transformation related data is presented in a semi-quantitative manner, since the time-temperature data was not experimentally measured during DED.

Since the presence of carbides is important for creep strength of the FGM, the consideration of carbide formation is necessary for the design process. Carbides formed upon solidification that

remain stable at the service temperature can significantly alter carbon migration. Here, the goal is to identify and establish the ability to predict carbides in the as-deposited condition. Scheil-Gulliver calculations [11] are used to demonstrate the effect of elemental segregation during solidification. Scheil solidification follows the basic assumption that perfect mixing occurs in the liquid and no diffusion occurs in the solid. The solidification path is approximated through small discrete temperature intervals at which local equilibrium at the interface between liquid and solid is reached. The calculations can provide mass fractions and compositions of phases during solidification. Due to these basic assumptions, results from simulations should be viewed as upper limits for secondary phase fractions and compositions as less segregation is expected during the actual experiments [12].

### 4.3 As-deposited microstructure in FGM

Although it was shown in Chapter 3 that control over chemical composition during DED is achievable, the overall design of FGMs also requires consideration of the deposited microstructure. To relate chemical composition to microstructure, the Schaeffler constitution diagram, which is commonly used for determining the main microstructural phases formed during fusion welding of alloy steels, stainless steels, and DMWs [13], is utilized. The measured compositions at each location were converted to nickel and chromium equivalents, as defined in Equations (4.2) and (4.3) (in wt%), and plotted onto the Schaeffler diagram, as shown in Figure 4.1.

$$Ni_{EQ} = \%Ni + 30 * \%C + 0.5 * \%Mn \quad (4.2)$$

$$Cr_{EQ} = \%Cr + \%Mo + 1.5 * \%Si + 0.5 * \%Nb \quad (4.3)$$

Due to the relatively low amounts of carbon in the as-received powder, the impact of estimating carbon content in the  $Ni_{EQ}$  and  $Cr_{EQ}$  values is assumed to be minimal. The expected microstructure is martensitic up to a height of 12 mm (low  $Ni_{EQ}$  and  $Cr_{EQ}$ ) above which there is a transition to austenite at heights from 12 to 18 mm above the base plate. These changes in  $Ni_{EQ}$  and  $Cr_{EQ}$  values as well as microstructure correspond to an increase in the amount of Alloy 800H added to the graded build. Previous work using arc-based AM processes with a similar alloy system showed microstructural observations consistent with these predictions [14].

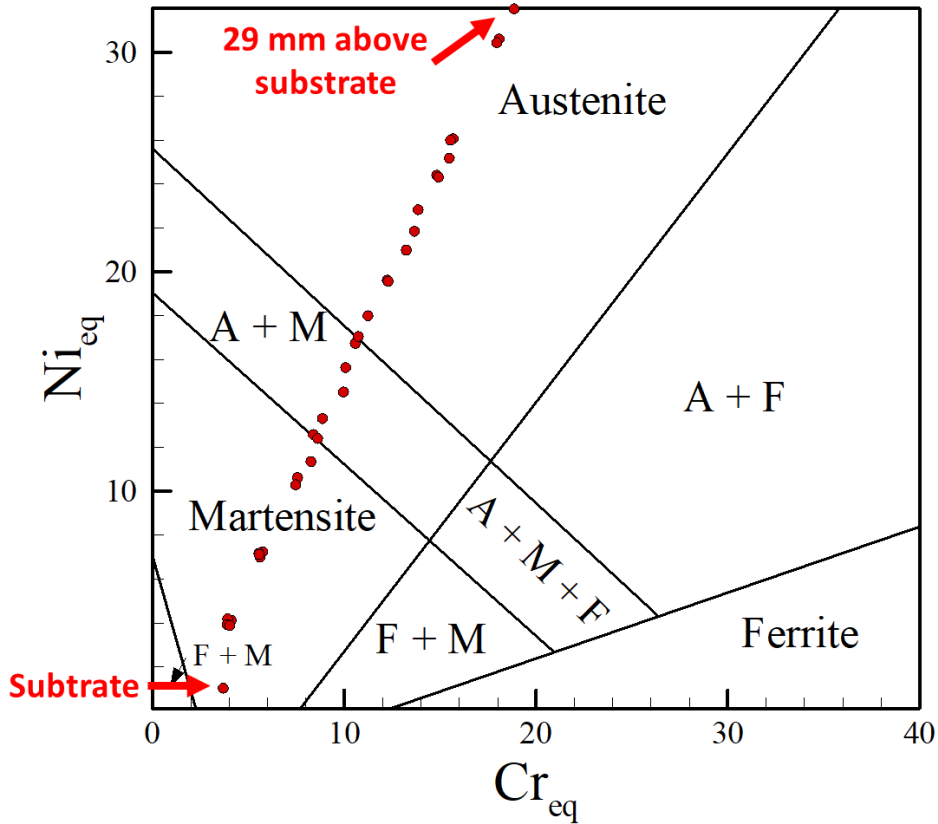


Figure 4.1. EPMA data were converted to nickel and chromium equivalents and plotted on the Schaeffler constitution diagram to determine the main microstructural phases across the gradient.

To assess the validity of the Schaeffler diagram predictions, the microstructures in the as-deposited condition were examined. Due to the significantly different mechanical properties of austenite and martensite, an approximate indication of microstructure can be obtained through microhardness measurements. Figure 4.2 shows Vickers hardness traces taken along the height of the build. Regions of martensite and austenite, as predicted by the Schaeffler diagram, are shown by the dotted lines. Significant differences in Vickers hardness are observed as a function of build height. The highest hardness values fall within the fully martensitic region, and large amounts of scatter in the hardness measurements are observed in the region predicted to contain a combination of martensite and austenite. The lowest Vickers hardness measurements are recorded in the fully austenitic regions.

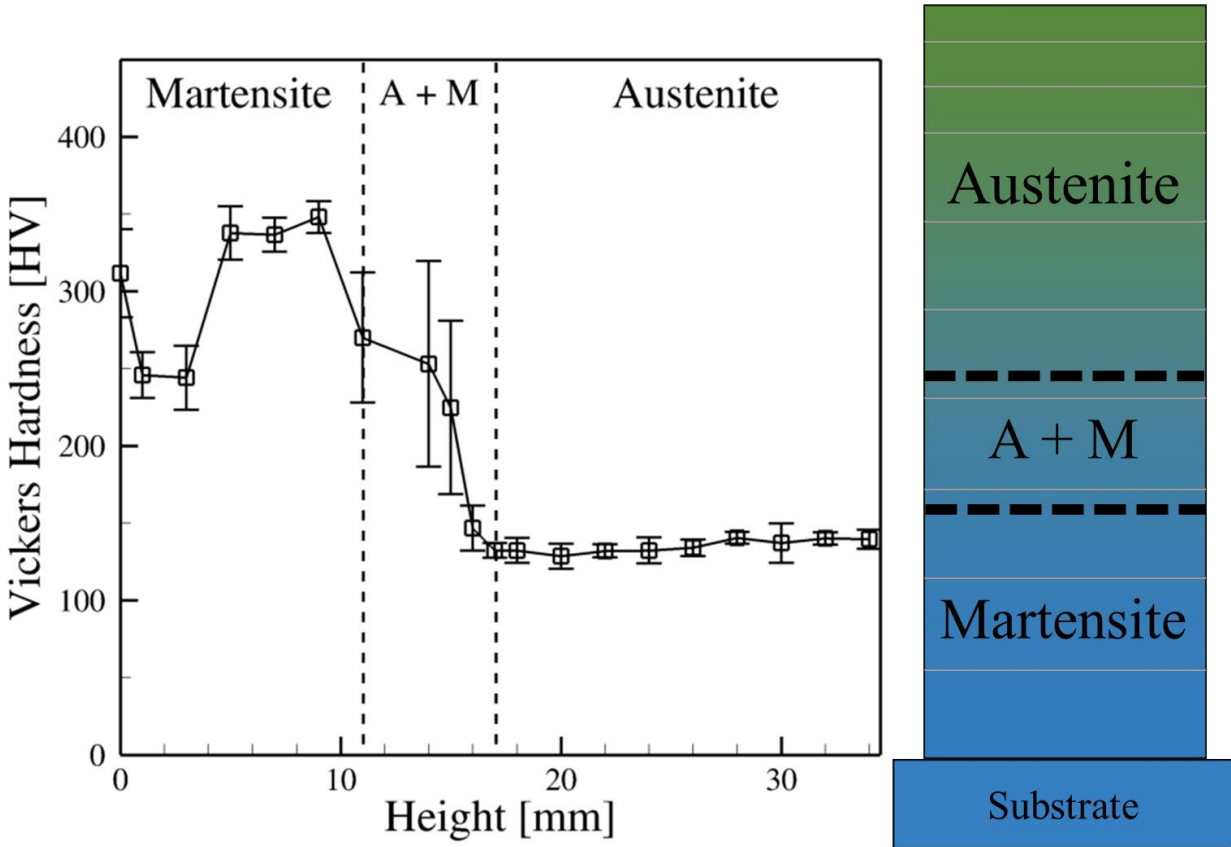
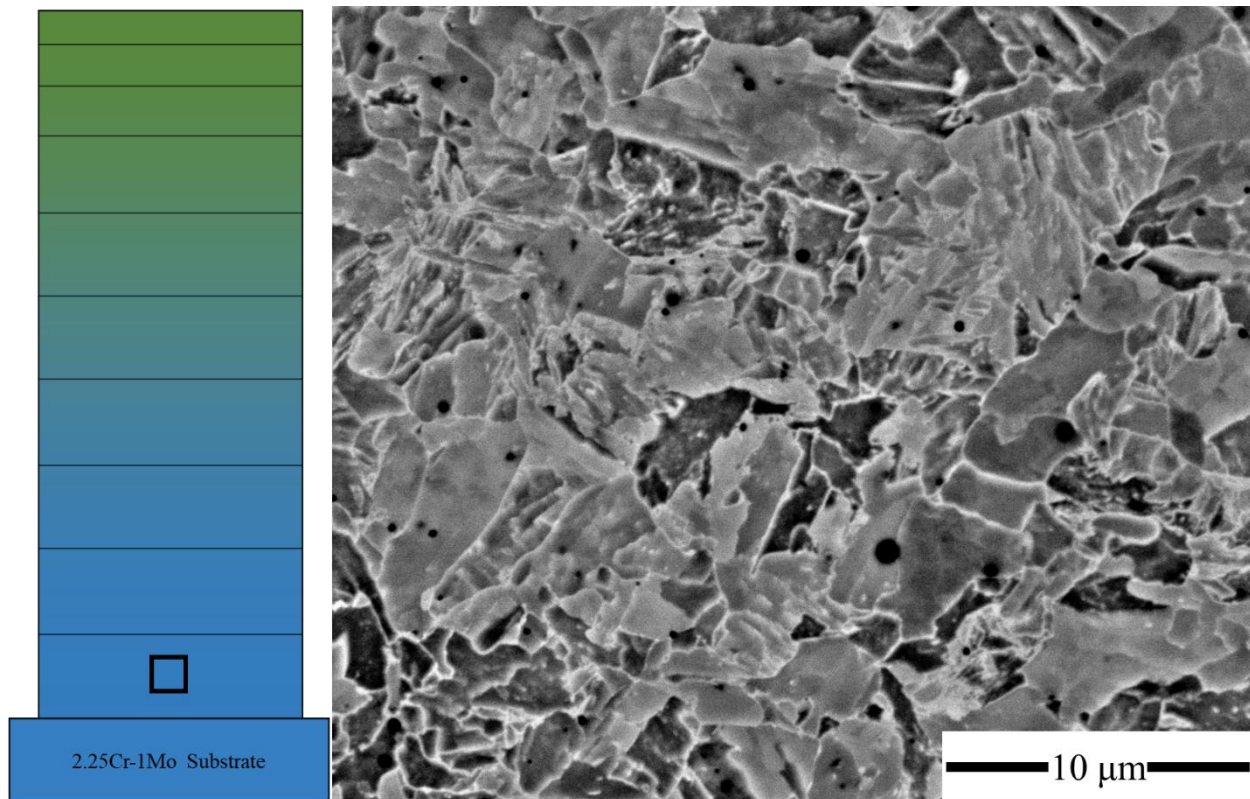


Figure 4.2. Vickers hardness measurements along the compositionally graded sample. Regions of martensite, austenite and a mixture of austenite and martensite predicted by the Schaeffler diagram are separated by dotted lines.

Within the first 4 mm of the build height, however, the hardness drops to a level of approximately  $245 \pm 15$  HV, which is much lower than the base material hardness of  $312 \pm 25$  HV. The composition in this region corresponds to a powder blend representing 10% 800H and  $\text{Ni}_{\text{EQ}}$  and  $\text{Cr}_{\text{EQ}}$  both approximately equal to 4, which is predicted by the Schaeffler diagram to be martensitic. Figure 4.3 shows a micrograph in the region approximately 3 mm above the baseplate. While no observable grain boundaries were revealed after etching, small, plate-like structures with sharp edges were present throughout the region.



*Figure 4.3. SEM micrograph taken approximately 3 mm from the baseplate in the build direction, corresponding to the 3<sup>rd</sup> deposited layer and a composition of 10% 800H.*

To provide insight into this observation, a continuous cooling diagram was calculated for the composition range of interest. Figure 4.4 shows the calculated bainite and pearlite curves for the compositions corresponding to 10 and 20% 800H regions of the composition gradient. The bainite peak for the 10% 800H region extends much further into the higher cooling rate region than other peaks, indicating that bainite, rather than martensite, is likely to form during cooling. While no time-temperature data are available, the presence of bainite in the 10% 800H region would explain the unusually low hardness values.

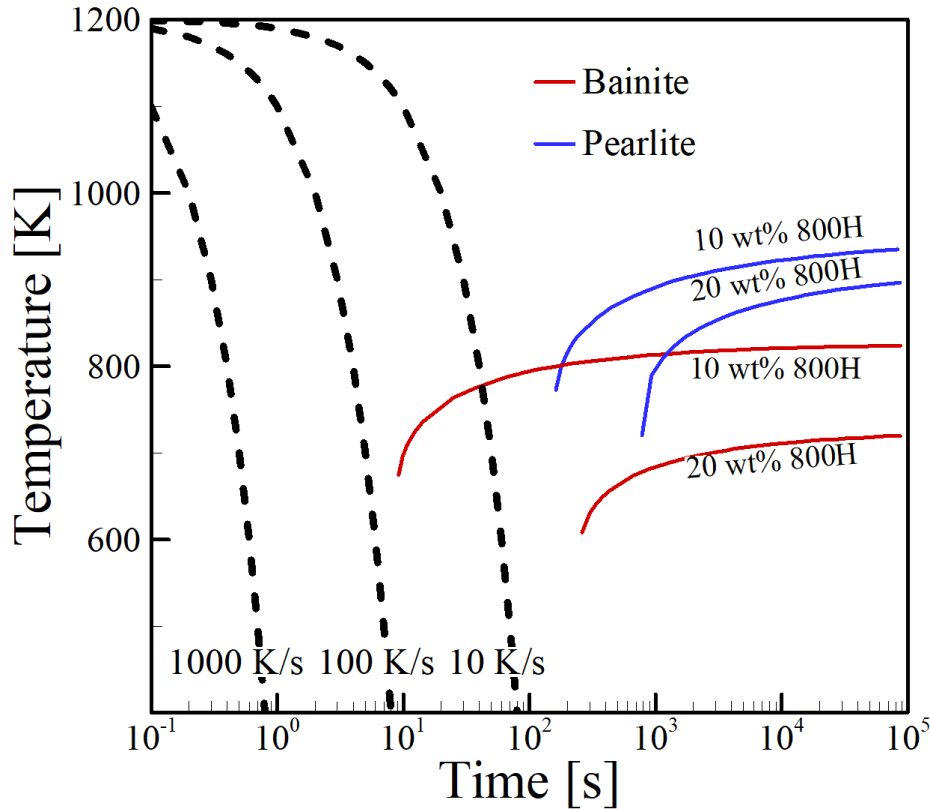


Figure 4.4. Continuous cooling diagram for the austenite transformation of steel-rich compositions (10 and 20% 800H) within the FGM calculated from JMatPro®.

A sudden increase in hardness to about 345 HV is observed as the build height increases, representing composition blends ranging from 20 to 30% 800H. As displayed in Figure 4.4, the maximum cooling rate required for the formation of bainite is nearly an order of magnitude lower for 20% 800H compared to 10% 800H. Therefore, even for a cooling rate as slow as 10 K/s, no bainite is likely to form in the 20% 800H region, and the microstructure is expected to be martensitic. Figure 4.5(a) shows the microstructure present at a location 7 mm above the baseplate corresponding to a composition of 20% 800H. The solidification sub-grain structure of dendrite boundaries is easily observable, as further shown in Figure 4.5(b), and displays large amounts of lath martensite. Smaller regions of austenite appear, as indicated by the white arrows.

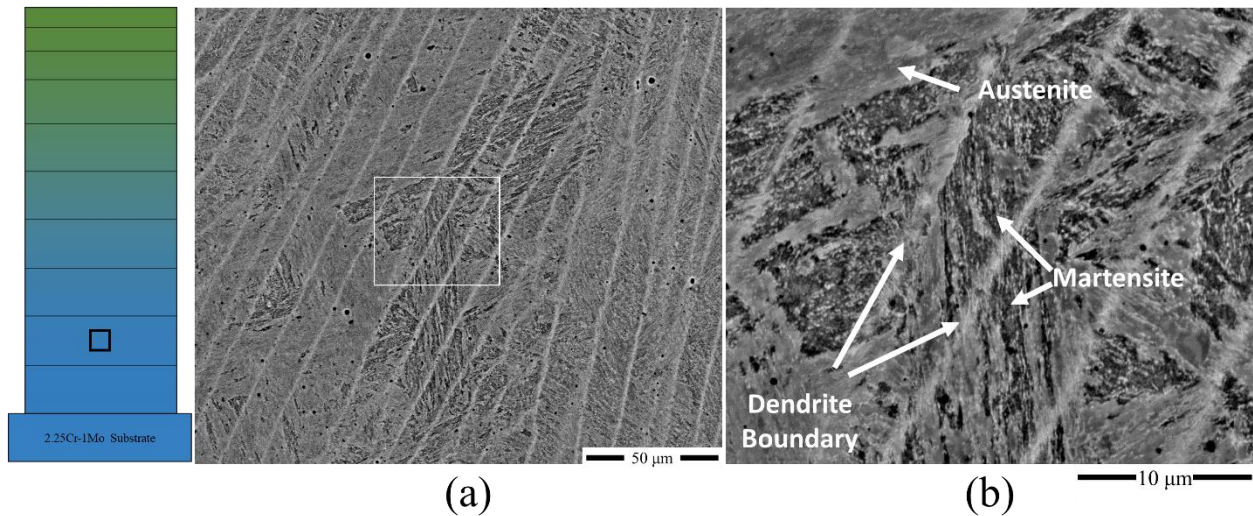


Figure 4.5. (a) SEM micrograph approximately 7 mm from the baseplate in the build direction, corresponding to the 7<sup>th</sup> deposited layer and a composition of 20% 800H and (b) a higher magnification image outlined by the white box in (a) showing martensite and austenite.

With increasing height from 11 to 16 mm (30 to 40% 800H), the hardness gradually decreased, on average, but also displayed a large amount of scatter. The large standard deviations indicate microstructural inhomogeneities consisting of hard regions dispersed in a softer matrix. Figure 4.6 (a) and (b) show representative micrographs for regions which correspond to compositions of 30 and 40% 800H graded regions, respectively. Sharp martensitic laths and larger austenitic blocks are present at each location. However, the amount of austenite gradually increased with build height as more austenite forms on the boundaries between cells and dendrites, while the cores remain martensitic.

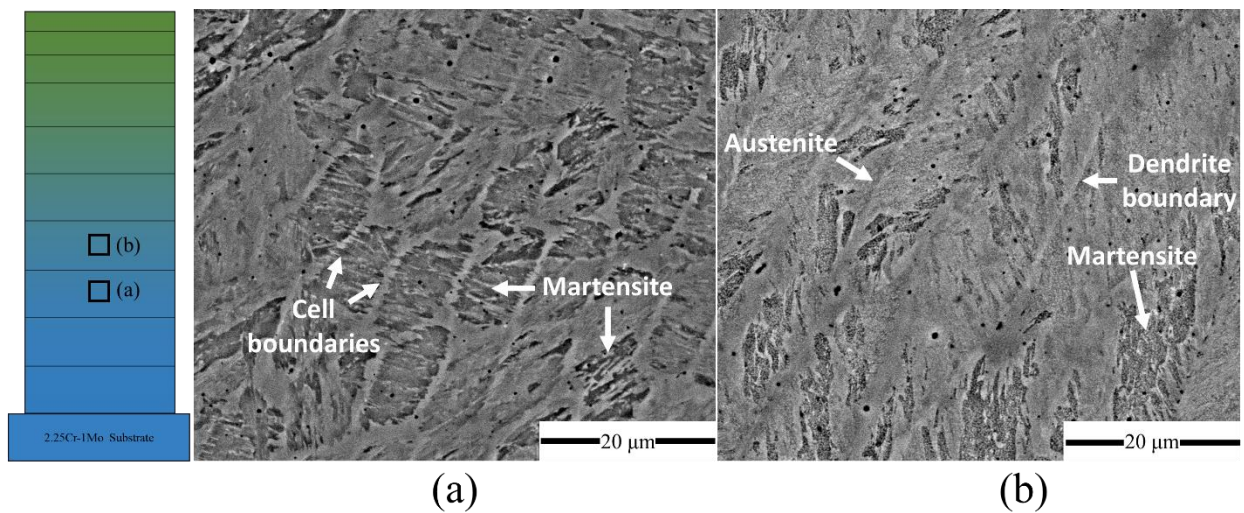


Figure 4.6. SEM micrographs taken approximately (a) 11 mm and (b) 15 mm from the baseplate in the build direction. The microstructures correspond to the 11<sup>th</sup> and 15<sup>th</sup> deposited layers and compositions of 30 and 40% 800H, respectively.

As the percentage of 800H is increased, less martensite is expected, as was observed experimentally. To explain the varying amounts of austenite and martensite with increasing additions of 800H to the graded structure, it is worthwhile to investigate the martensite transformation temperatures. Figure 4.7 shows calculations of  $M_s$ ,  $M_{50}$ , and  $M_f$  as a function of 800H additions. At additions up to 30% 800H, both  $M_s$  and  $M_f$  are above room temperature, meaning that the martensitic transformation is likely to reach completion. At a composition of 40% 800H,  $M_f$  drops below room temperature, indicating that although the transformation has started, it does not reach completion upon cooling to room temperature. After 40% 800H, the calculations show that the  $M_s$  values drops below room temperature, prohibiting the martensitic transformation from ever initiating, leading to high amounts of retained austenite.

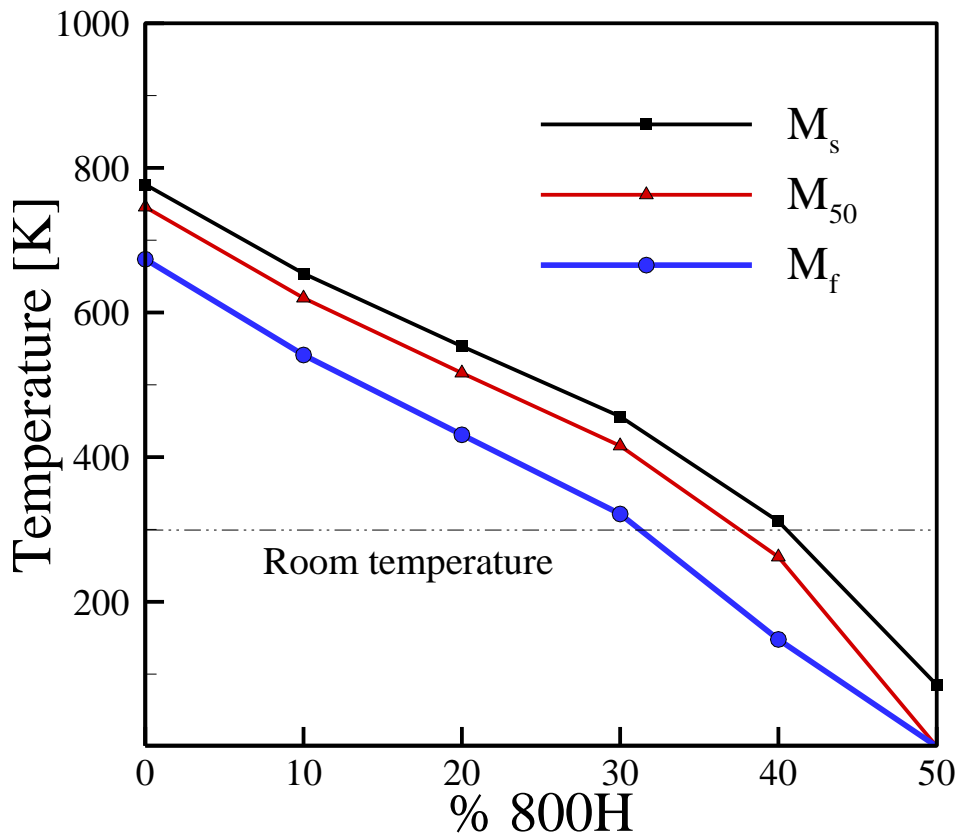


Figure 4.7. Changes in the martensite start ( $M_s$ ), 50% completion ( $M_{50}$ ) and finish ( $M_f$ ) temperatures for the martensite transformation as a function of composition in terms of percent 800H.

Above a build height of 16 mm, the compositions correspond to powder blends from 40 to 100% 800H with approximate  $Cr_{EQ}$  values ranging from 8.4 to 21 and  $Ni_{EQ}$  values ranging from 12.6 to 35. A plateau in Vickers hardness was reached and measurements showed a consistent value slightly below 150 HV and a dendritic microstructure was present, as displayed in Figure 4.8 (a) and (b). No fine features like lath martensite were observed, and the microstructure displayed large, elongated grains with a dendritic sub-structure. However, small particles were present along the grain boundaries and interdendritic regions of the austenitic microstructure, indicating secondary phase formation.

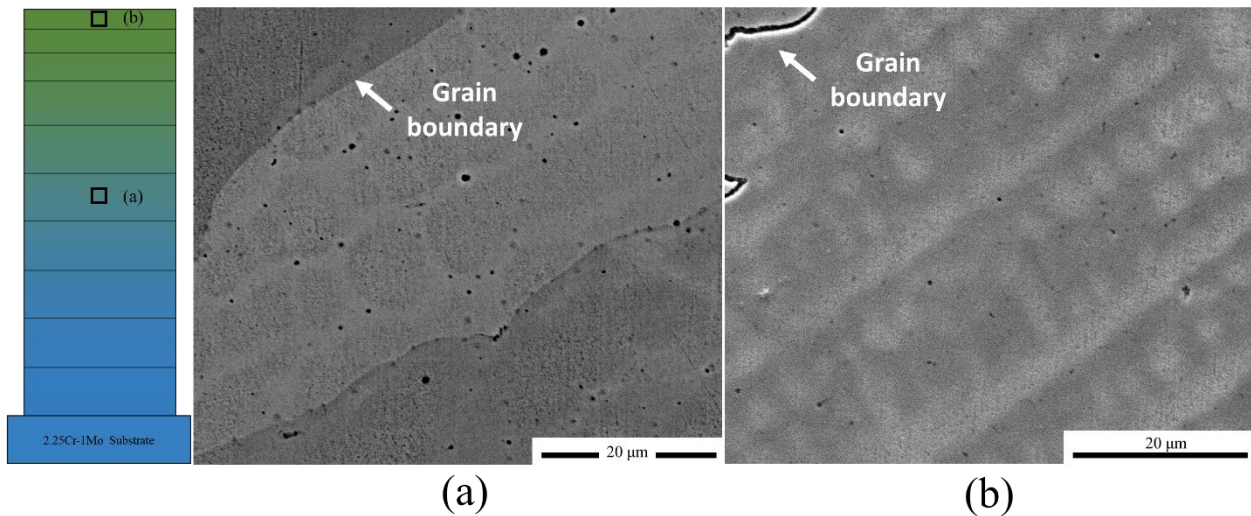


Figure 4.8. SEM micrographs approximately (a) 19 mm and (b) 34 mm from the baseplate in the build direction. The microstructures correspond to the 19<sup>th</sup> and 34<sup>th</sup> deposited layer, and compositions of 50 and 100% 800H, respectively.

Significant elemental segregation during AM can lead to the formation of both desirable and unwanted phases. The identification of alloying elements in a small particle is a simple, quick way to provide information about secondary phases. A secondary electron image accompanied by elemental distribution maps near a grain boundary in the 90% 800H region of the gradient is shown in Figure 4.9. The region along the grain boundary and between dendrite arms showed a significant depletion in iron and accumulation of titanium, while all other elements show no clear segregation. Moreover, the bright spots of titanium in the elemental map correspond to dark, spherical particles on the secondary electron image, indicating carbide formation.

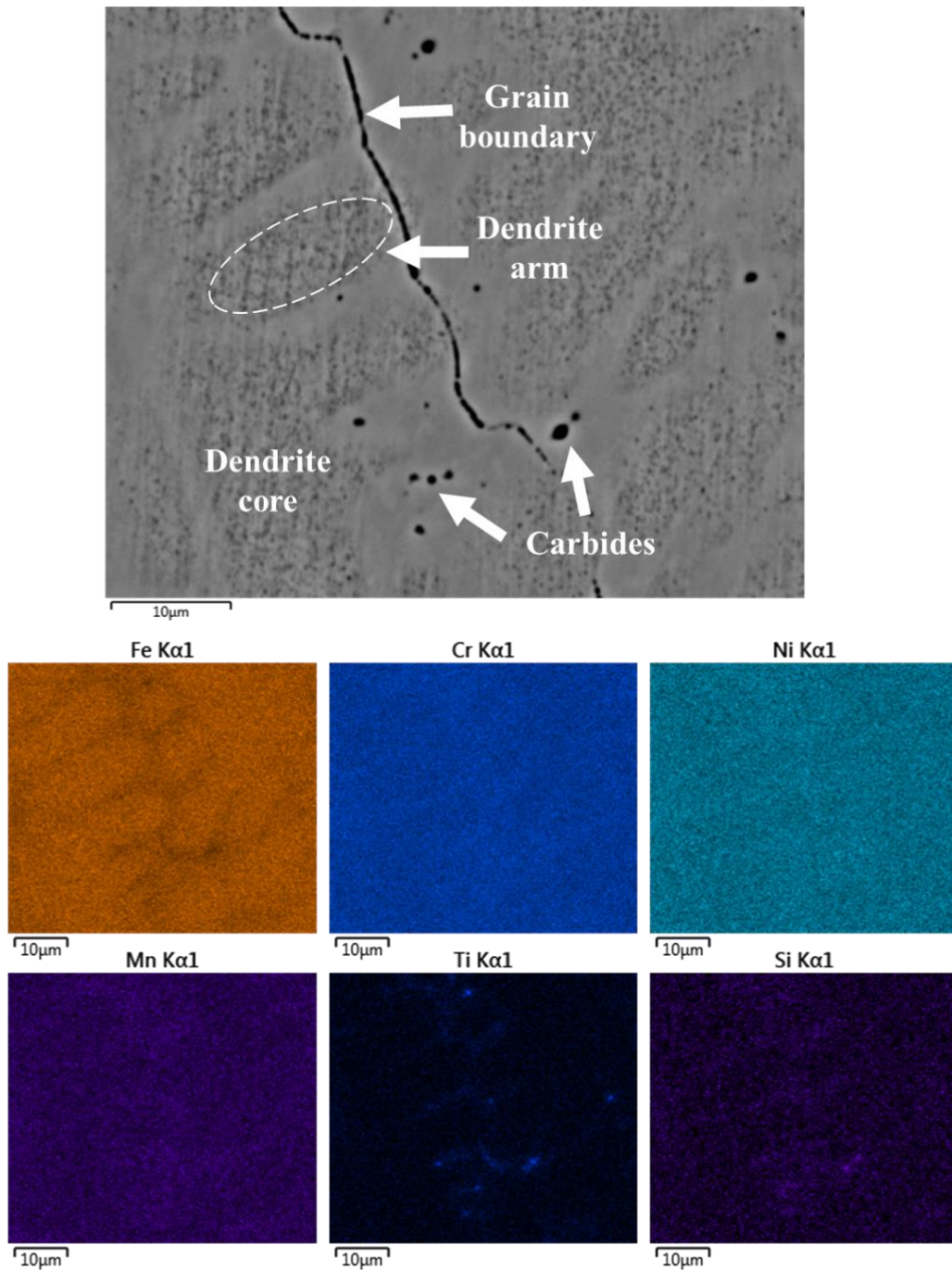


Figure 4.9. EDS map showing elemental segregation along the grain boundaries and interdendritic regions in the 90% 800H region of the composition gradient.

The two carbides existing in the 90% 800H region in equilibrium calculations are of the MC (Ti-rich) and  $M_{23}C_6$  type (Cr-rich), as shown in Figure 4.10(a). In the typical service temperature range of approximately 673-873K (400-600°C), the  $M_{23}C_6$  carbide is dominant, while the MC carbide is more stable at higher temperatures. Both  $M_{23}C_6$  and MC are predicted to exist

at an equilibrium mass percent of less than 1%. The Scheil-Gulliver model of JMatPro® was used to calculate mass fractions and phase compositions during idealized solidification. In Figure 4.10(b), only MC and austenite form upon solidification, with the Ti-rich MC phase constituting less than 1% of the overall mass. Based on the thermodynamic calculations and experimental observations, it can be concluded that the observed Ti-rich particles are carbides are of the MC type. No Cr-rich carbides were observed in the as-deposited condition.

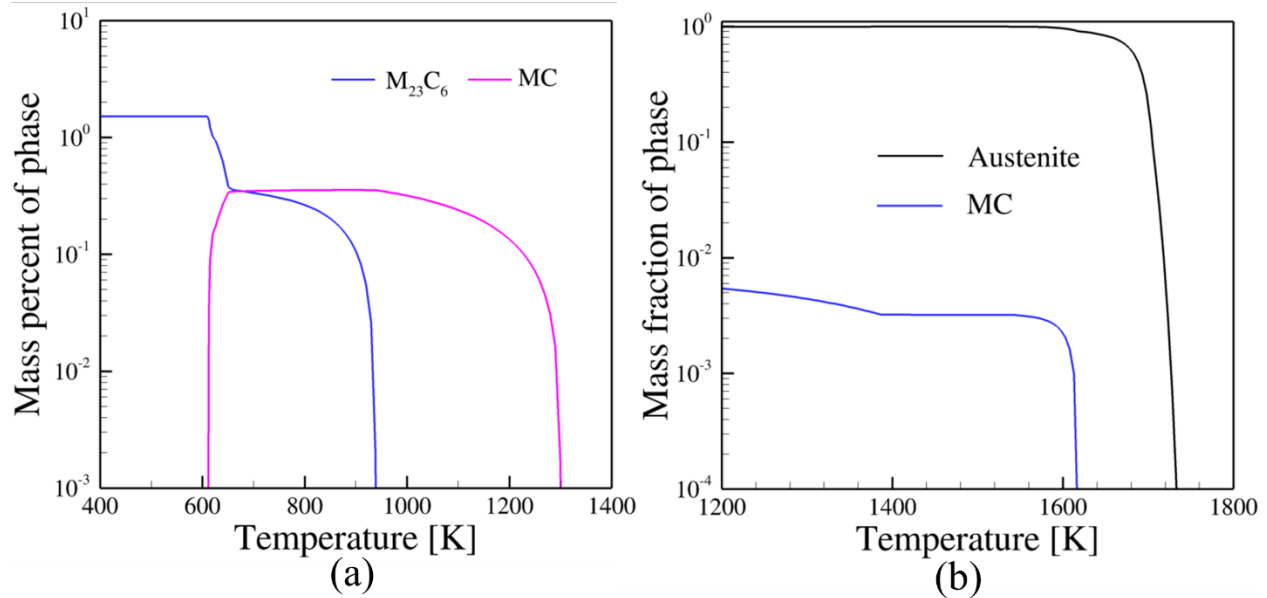


Figure 4.10. Thermodynamic calculations in the 90% 800H region showing (a) stable carbides as a function of temperature and (b) mass fractions of solidified phases from Scheil simulation

The presence of carbides in dissimilar ferritic/austenitic joints can impact creep performance. Many studies have investigated the precipitation and dissolution sequences of carbides in 2.25Cr-1Mo steel and dissimilar weldments [15, 16]. A common finding is that systems tend towards the formation of Cr-rich  $M_{23}C_6$  and Mo-rich  $M_6C$  carbides when approaching equilibrium, at the expense of  $M_2C$ ,  $M_7C_3$  and cementite dissolution [15-17]. Table 4.1 shows equilibrium thermodynamic calculations for carbides at different compositions throughout the FGM in this work. Due to the low carbon concentration of the powder and the absence of Mo in the custom blended mixture, the variety of different carbides likely to form through the composition gradient is limited. Furthermore, the formation of the Ti-rich MC carbide during solidification can significantly alter carbon migration through the joint because MC is also stable at service temperatures for many compositions.

Table 4.1. Carbides in equilibrium for different alloy compositions at 773 K.

Composition (% 800H)	Stable carbides	Equilibrium mass percent
10	M <sub>23</sub> C <sub>6</sub>	0.16
20	M <sub>23</sub> C <sub>6</sub>	0.15
30	MC + M <sub>23</sub> C <sub>6</sub>	0.10 + 0.14
40	MC + M <sub>23</sub> C <sub>6</sub>	0.15 + 0.13
50	MC + M <sub>23</sub> C <sub>6</sub>	0.24 + 0.069
60	MC + M <sub>23</sub> C <sub>6</sub>	0.29 + 0.077
70	M <sub>23</sub> C <sub>6</sub>	1.20
80	M <sub>23</sub> C <sub>6</sub>	1.36
90	M <sub>23</sub> C <sub>6</sub>	1.52
100	M <sub>23</sub> C <sub>6</sub>	1.68

#### 4.4 Phase transformations in single alloy samples

The experimental investigation of phase transformation in FGMs using tradition characterization techniques can be difficult due to inhomogeneities in both chemical composition and microstructure. Consequently, sophisticated techniques are needed to locally observe microstructural transformations. To overcome this hurdle, separate AM specimens were fabricated with chemical compositions corresponding to distinct regions of the FGM, providing macroscopically homogeneous materials that can be characterized with conventional techniques. The alloy compositions ranged from 10 to 70% 800H, which encompass the full microstructural transition from a ferritic to austenitic microstructure.

The relative phase fractions of ferrite and austenite for each alloy composition were determined from laboratory XRD measurements. The measured intensities of diffraction spectra are shown in Figure 4.11 for a  $2\theta$  range from 45-126°. For the 10 and 20% 800H compositions the microstructure is entirely BCC. In the 30 and 40% 800H regions, FCC peaks emerge, resulting in

a mixture of BCC and FCC phases. The larger FCC peaks in the 40% 800H indicate more austenite present in the alloy. At alloy compositions of 50% 800H and higher, the microstructure becomes fully austenitic. Using the direct comparison method, the volume fractions of austenite was quantified for the dual phase microstructure, which were determined to be (in %)  $0.97 \pm 0.17$  and  $67.71 \pm 0.42$  for the 30 and 40% 800H regions, respectively

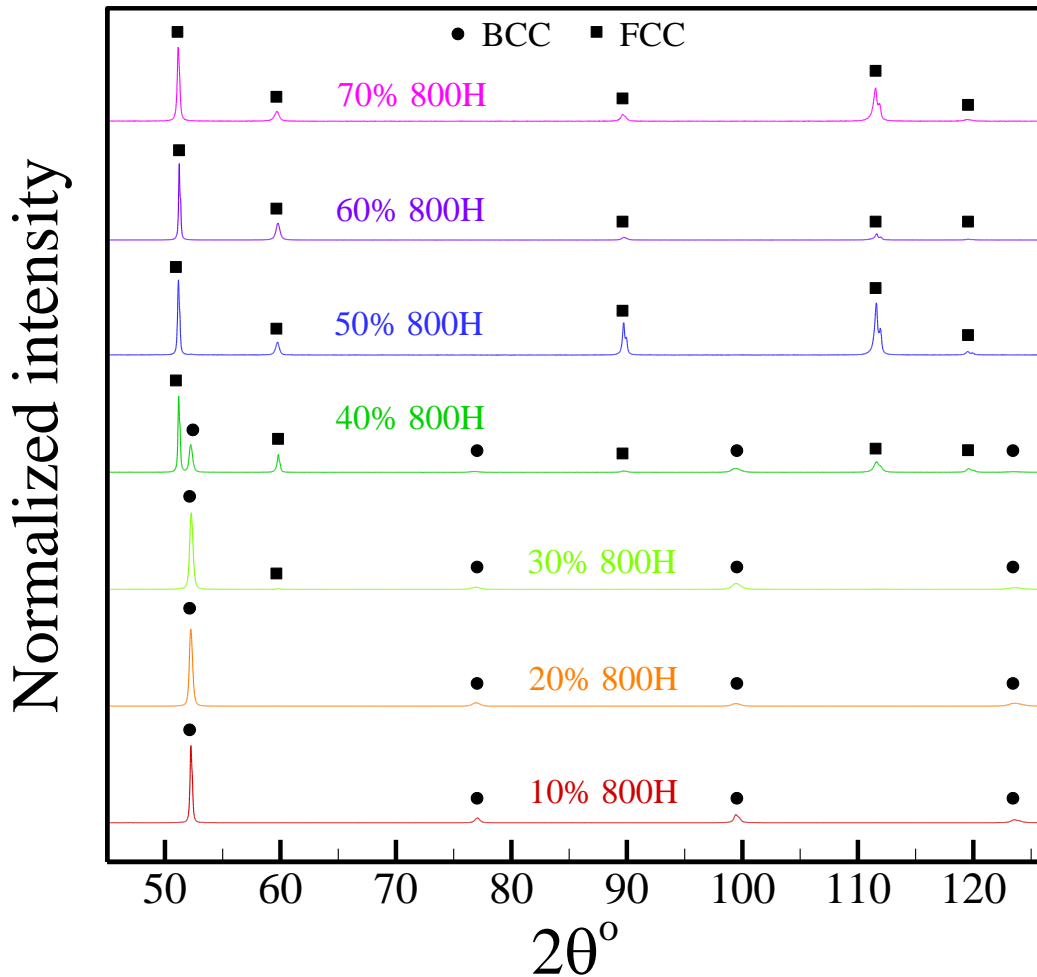


Figure 4.11. The measured XRD patterns show the change from a fully BCC to a fully FCC microstructure for alloy compositions ranging from 10 to 70% 800H. The circle and square symbols correspond to BCC and FCC peaks, respectively.

The  $2\theta$  angles of the prominent diffraction peaks were used to determine the lattice parameters of ferrite and austenite for each of the alloy compositions. The calculated lattice parameters are shown in Figure 4.12, where the error bars represent the standard deviation from multiple measurements. It is important to note that although martensite has a body centered tetragonal (BCT) crystal structure, the expansion along the c-axis of the unit cell is too small to be resolved by laboratory

XRD. Therefore, the lattice parameters of ferrite and martensite are assumed to be equivalent. Overall, the lattice parameters of each phase remain roughly constant (within experimental error) for each of the alloy compositions. This finding indicates that changes in chemical composition have a negligible effect on the unit cell volume along the composition gradient.

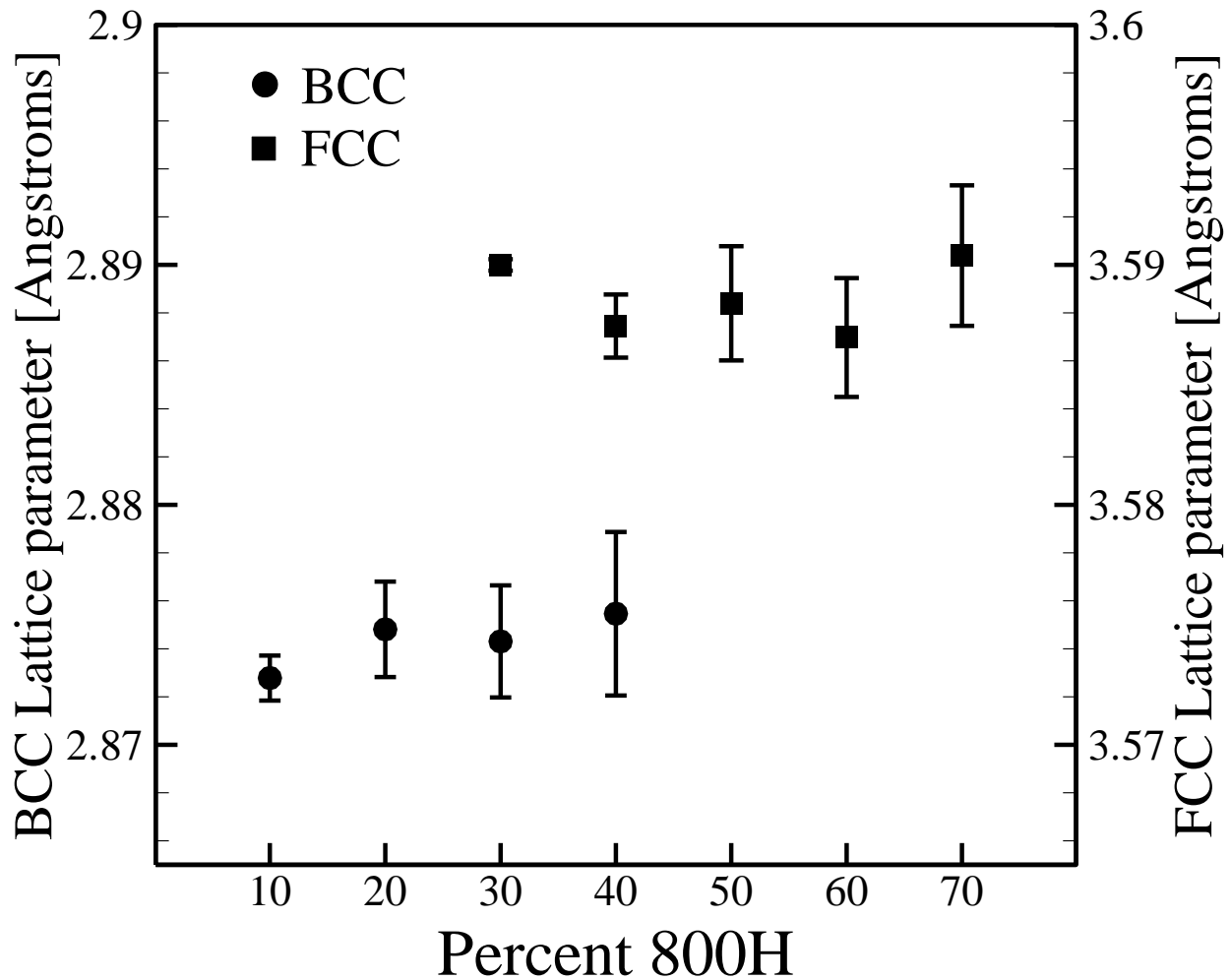


Figure 4.12. Calculated lattice parameters for the BCC and FCC phases as a function of alloy composition show that the unit cell of each phase is largely unaffected by changes in chemical composition.

To study the effects of temperature on phase transformations for different alloy compositions, a pushrod dilatometer was used. In these experiments, changes in length are measured as a function of temperature, where abrupt changes in dilation indicate a phase transformation. The results of a dilatometric experiment for a sample extracted from the baseplate material are shown in Figure 4.13(a), where the relative length change (*RLC*) is calculated by,

$$RLC(\%) = \frac{\Delta l}{l_0} \times 100 \quad (4.4)$$

where  $\Delta l$  is the change in length, and  $l_0$  is the initial length of the specimen. An initial length of approximately 10 mm was used for all samples. Important phase transformations are observed in Figure 4.13(b). During heating, the ferritic microstructure begins to transform to austenite at approximately 752°C, and this temperature is referred to as  $A_{c1}$ . The end of the transformation occurs at a temperature called  $A_{c3}$ , which is approximately 856°C in this material. Upon cooling, the fully austenitic material can transform to a variety of microconstituents, including ferrite, pearlite, cementite, bainite, and martensite, depending mainly on the chemical composition of the alloy and the cooling rate. In Figure 4.13(b), the austenite first transforms to ferrite around 796°C, and the remaining austenite transforms to pearlite at a temperature of 756°C.

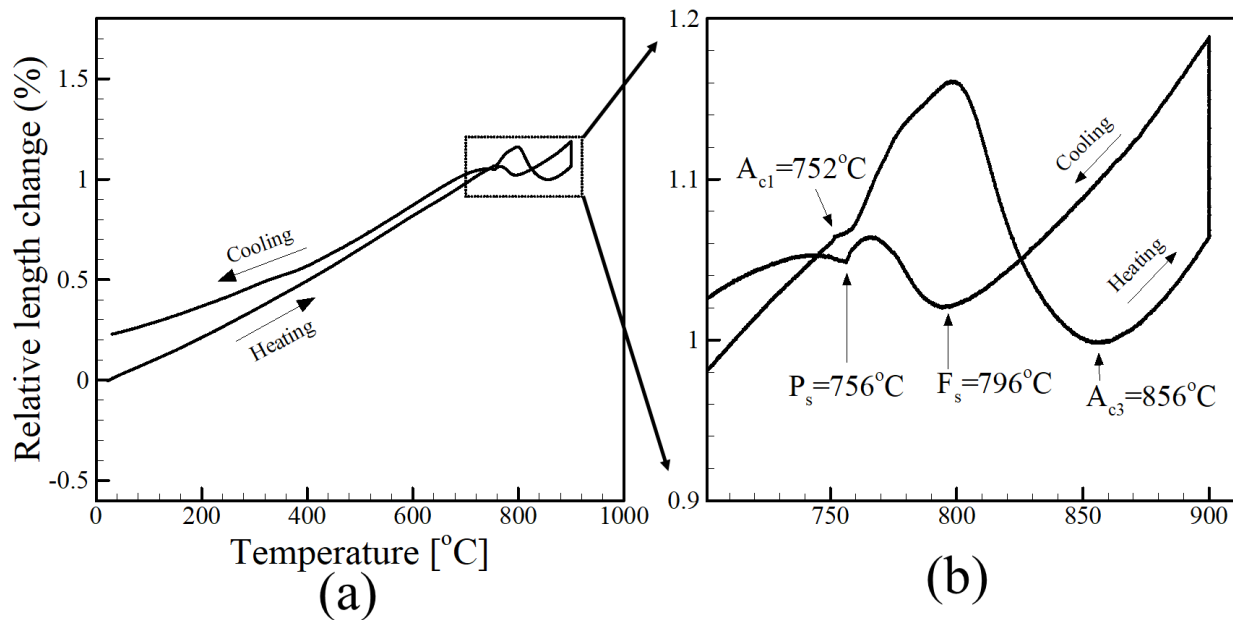


Figure 4.13. (a) The relative length change as a function of temperature for a sample extracted from the SAE387 Gr. 22 steel baseplate with a magnified view of the phase transformations shown in (b).

Using a similar procedure, dilatometric analysis was performed on the single alloy compositions ranging from 10 to 70% 800H. Since the 50, 60, and 70% 800H were fully austenitic throughout the duration of the heat treatment, the remaining discussion will focus on the regions between 10 to 40% 800H. The relative length change is plotted as a function of temperature for these alloy compositions in Figure 4.14. In all alloys, the transformation from ferrite to austenite

on heating occurred in the temperature range of approximately 500-800°C. In general, the  $A_{c1}$  and  $A_{c3}$  temperatures decreased with increasing additions of 800H to the alloy.

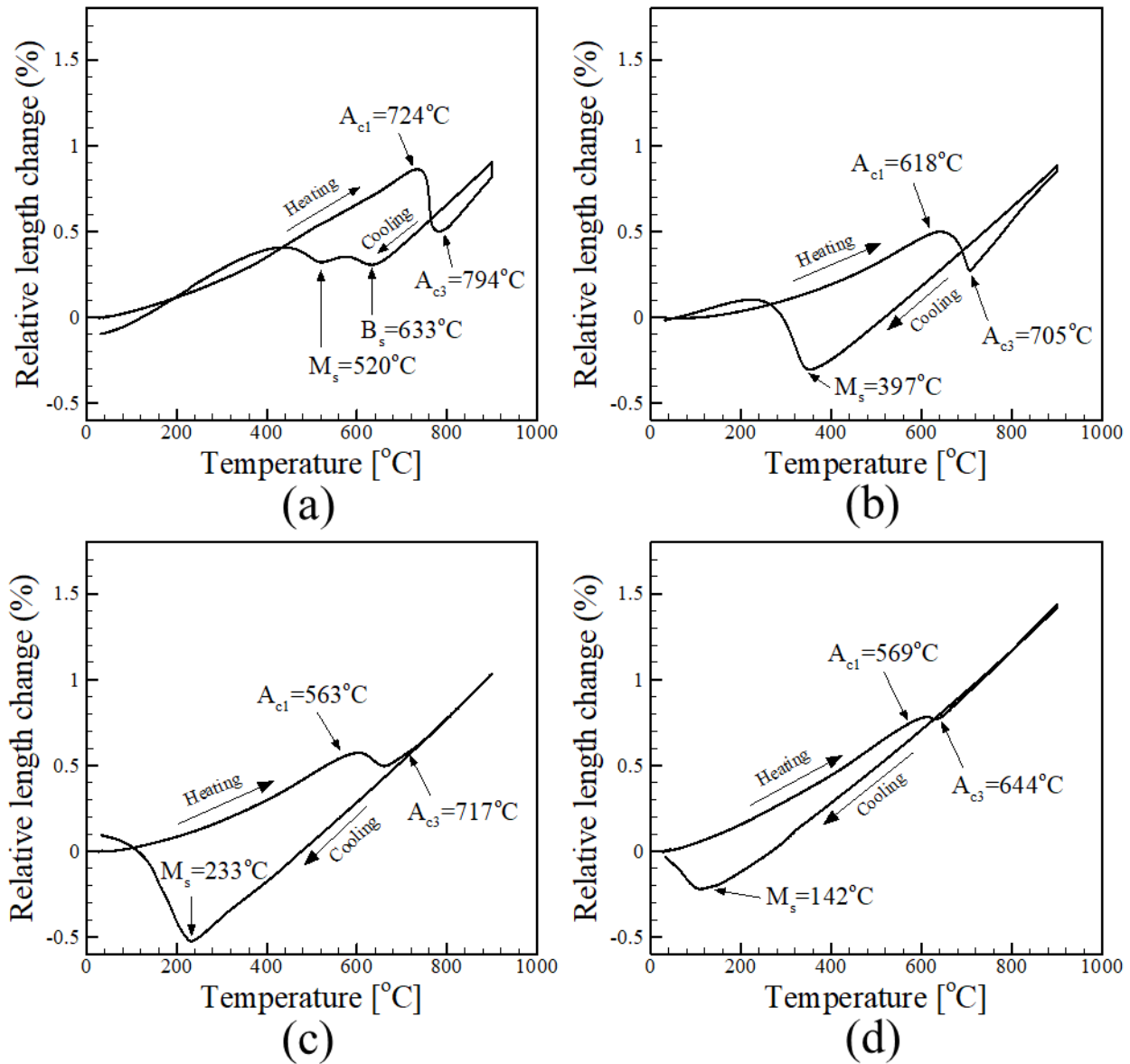


Figure 4.14. The changes in dilation as a function of temperature for the (a) 10%, (b) 20%, (c) 30%, and (d) 40% 800H alloy compositions, where a constant heating and cooling rates of 5°C/min were used.

At a cooling rate of 5°C/min, the 10% 800H alloy undergoes two solid-state transformations in Figure 4.14(a). Austenite begins to transform to bainite around 633°C, and this reaction continues until about 520°C, at which point the martensitic transformation occurs. For the 20 to 40% 800H alloys, austenite transforms to only martensite upon cooling, and the martensite

start temperature decreases with increasing amounts of 800H. In Figure 4.14(b), the slope of the curve reaches a roughly constant values near 200°C, which indicates the 20% 800H alloy completely transform to martensite. In contrast, the 30 and 40% 800H in Figure 4.14 (c) and (d), respectively, do not complete the martensitic transformation before reaching room temperature and some amounts of austenite are retained in the microstructure. Furthermore, the differences in relative length change between the martensite start and room temperature reveal that the 30% 800H alloy (Figure 4.14(c)) approached the end of the martensitic transformation, while the 40% 800H alloy (Figure 4.14(d)) was only in the beginning stages of the transformation. Although both alloys contain a mixture of martensite and austenite, the 40% 800H alloy retains more austenite than the 30% 800H alloy. This finding is consistent with microhardness and SEM micrographs in the FGM, as well as the quantitative XRD measurements in the single alloy composition builds.

A comparison between the calculated and measured transformation temperatures for the 10 to 40% 800H alloy compositions is shown in Figure 4.15. Overall, both the calculated and measured transformation temperatures follow the qualitative trends as a function of alloy composition. Alloy 800H is a source of many austenite stabilizing elements, such as carbon, manganese, and nickel, so an increase in the fraction of 800H added to the alloy increases the stability of austenite. In Figure 4.15, this is captured by the downward trends of  $A_{c1}$  and  $A_{c3}$  as a function of alloy composition. Furthermore, the addition alloying elements increases the hardenability of the alloy, or the relative ease of forming martensite.

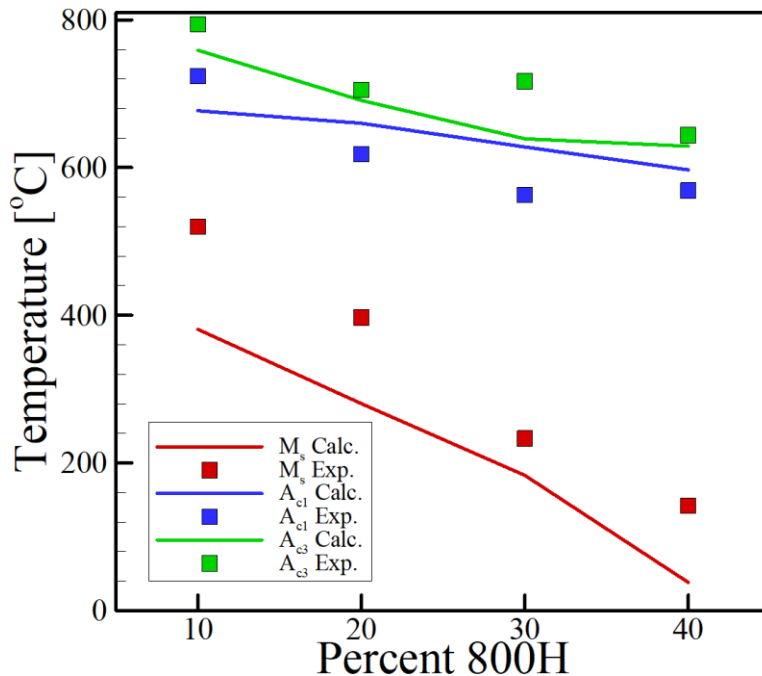


Figure 4.15. Calculated and measured transformation temperatures for the 10 to 40% 800H alloy compositions, including  $A_{c1}$  and  $A_{c3}$  upon heating, and  $M_s$  upon cooling.

#### 4.5 Revisiting the carbon diffusion problem

Since most design processes are inherently iterative, it is worthwhile to search for areas of improvement. The primary function of compositional grading in this work is to reduce the driving force for carbon diffusion. In the model system of the graded transition in Figure 4.16(a), the carbon chemical potential gradient is shown to reach a nearly constant value, as shown in Figure 4.16(c), after a distance of approximately 6 mm. At this location, the corresponding composition in the model system is 15 wt% Cr, 0.31 wt% Mo, 24 wt% Ni and 0.1 wt% C. Compositional grading beyond this composition has little effect on the driving force for carbon diffusion.

To demonstrate this assertion, a hypothetical case of a partial composition gradient with the same numerical setup described in Figure 4.16(a) is considered. The composition profiles are shown in Figure 4.16(b) where the compositional grading ends at Fe-15Cr-0.31Mo-24Ni-0.1C and the remainder of the joint has the composition of 800H (Fe-34Ni-21Cr-0.1C). The carbon chemical potential and diffusion profiles are shown in Figure 4.16 (c)-(e). The dotted line in Figure 4.16(d) represents the carbon potential profile when a full composition gradient is used (Figure 4.16(c)). Since both Figure 4.16 (c) and (d) have similar driving forces for carbon diffusion, nearly identical

diffusion results are produced with the shorter graded structure, as shown in Figure 4.16 (e) and (f).

Additionally, from Equations (4.1) and (4.2), the end of the partial compositional grading would give a  $Ni_{EQ}$  value of 27 and a  $Cr_{EQ}$  value of 15.3. Based on the chemical compositions plotted on the Schaeffler diagram in Figure 4.1, this approximately corresponds to the 60 to 70% 800H region of the graded transition joint in which an austenitic microstructure was observed. As the diagram in Figure 4.1 has shown good agreement with experimental observations, it can be assumed that a fully austenitic microstructure would be obtained at the end of the partial composition gradient. It can thus be concluded that no additional benefits are achieved in compositional grading after 70% 800H because the material is no longer effective at serving its designed function and no changes in microstructure would result.

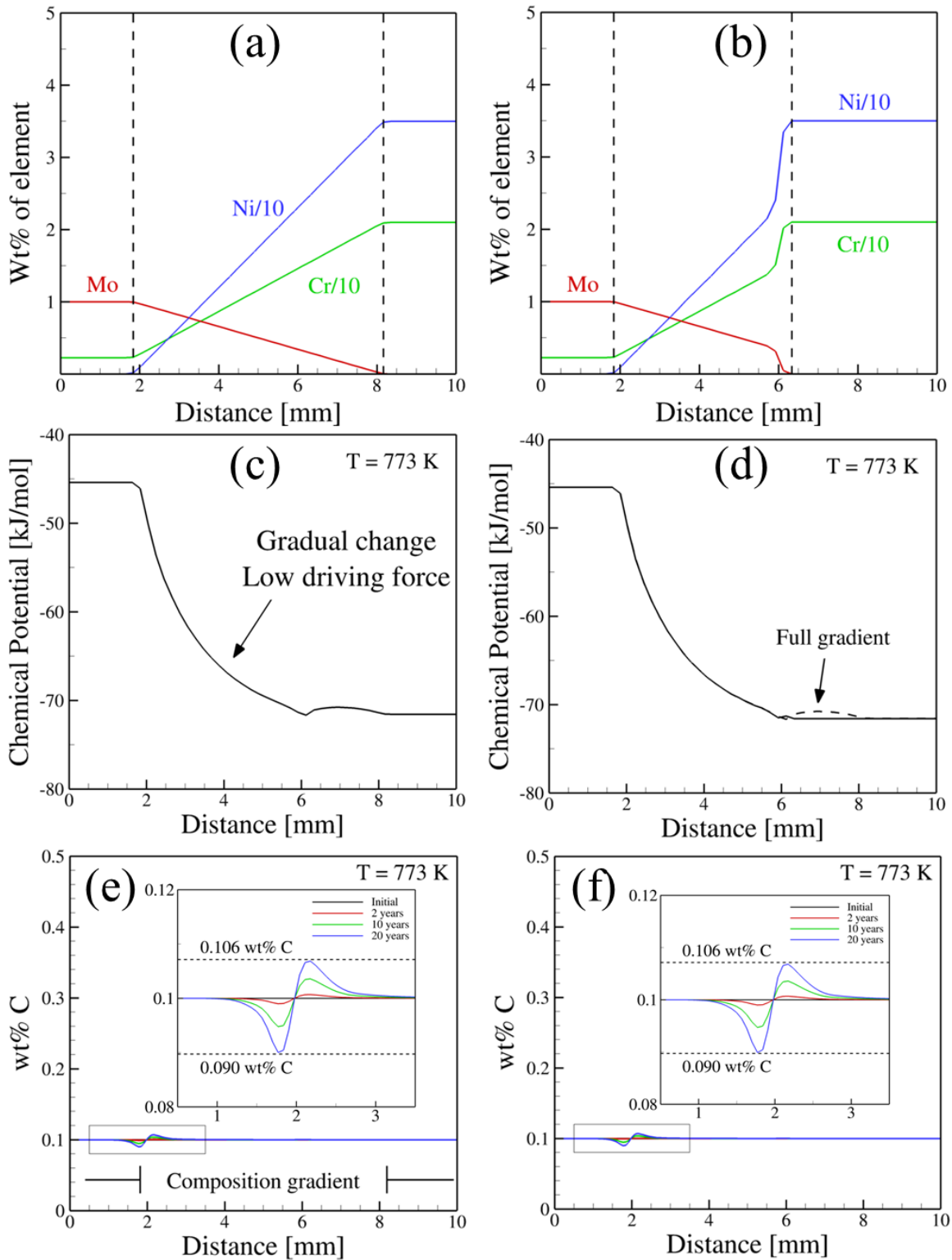


Figure 4.16. The corresponding (a-b) compositional variations (c-d) carbon chemical potential and (e-f) carbon diffusion profiles where only a partial composition gradient from 10% to 70% 800H (b, d, f) is used between 2.25Cr-1Mo steel and Alloy 800H compared to a full composition gradient (a, c, e).

Furthermore, it is desirable to exclude the soft region (245 HV) of the experimental FGM to eliminate abruptness in future builds. By removing the 10% 800H composition from the FGM and starting the grading with 20% 800H, one would effectively eliminate the discontinuity in hardness. However, in order for the removal of the 10% 800H region of the joint to be acceptable for future designs, it must not negatively impact the overall function of the FGM. To investigate the effect of removing 10% 800H from the composition gradient on carbon diffusion, the model system is revisited.

Figure 4.17(b) shows a schematic of the calculation setup similar to that in Figure 4.17(a) with the 10% 800H region removed and the composition gradient starting at 20% 800H and ending with 70% 800H. All other simulation parameters, including time, temperature, domain size, and grid spacing are identical. The carbon chemical potential profiles as a function of distance for both cases are shown in Figure 4.17 (c) and (d), in which the dotted line represents the carbon chemical potential of the original profile. Calculations show that a steeper gradient is obtained when the 10% 800H region is removed, indicating a larger thermodynamic driving force for carbon diffusion. The carbon diffusion results in Figure 4.17(f) show that by not including the 10% 800H region in the FGM, more carbon migrates from the ferritic steel towards the austenitic alloy compared to that in Figure 4.17(e). This situation indicates that a tradeoff between function and desired microstructure exists in the design of FGMs between ferritic and austenitic alloys.

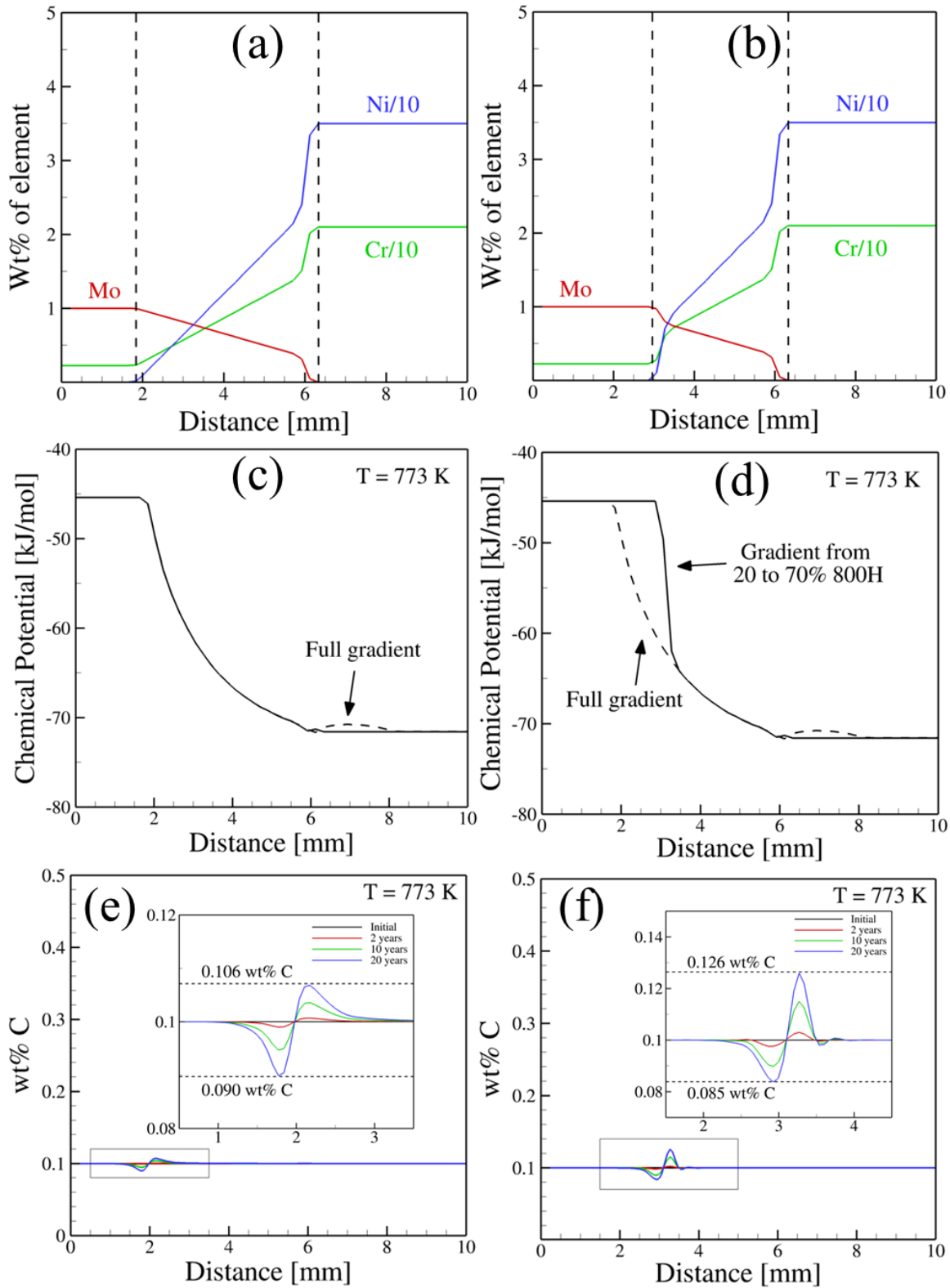
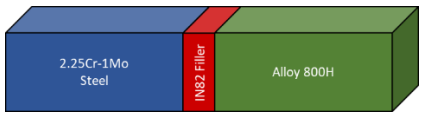
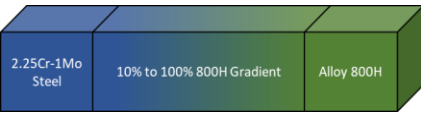


Figure 4.17. The corresponding (a-b) compositional variations (c-d) carbon chemical potential and (e-f) carbon diffusion profiles when a partial composition gradient up to 70% 800H starts from 20% 800H (b, d, f) compared to 10% 800H (a, c, e).

The carbon diffusion flux is a measure of the amount of carbon migrating through a unit area per unit time and is dependent on both location and time. To summarize the different types of joints through which carbon diffusion was simulated in this work, Table 4.2 provides the carbon diffusion fluxes at the location where maximum diffusion occurs after different service times. Since the carbon chemical potential decreases with time, the diffusion flux gradually decreases over time. In other words, the calculations consider the change in driving force with time as the system moves towards equilibrium. A positive value of the diffusion flux indicates carbon migration in the direction away from the ferritic steel towards the austenitic material. In all cases, a FGM shows a lower flux of carbon throughout the expected service life compared to a DMW and is an order of magnitude smaller after 20 years. The corresponding carbon depletion in the ferritic steel for each case after 20 years is approximately 20% for a DMW, 1.2% when grading from 10 to 70 or 100% 800H and 1.6% when grading from 20 to 70% 800H. For each type of joint, the highest flux occurs in the austenitic material along the steel/austenitic material interface. Also, the difference between fluxes of a DMW and FGM increases with time, highlighting the importance of the time scale over which carbon diffusion occurs.

In the case of the different types of FGMs, the tradeoffs between intended function and desired microstructures are clear in Table 4.2. No differences in maximum diffusion flux occur when comparing a full compositional grading to an FGM graded from 10 to 70% 800H. In terms of microstructure, no advantages can be gained in slowing carbon diffusion once the microstructure becomes fully austenitic, allowing a shorter joint to suffice. However, such a joint would include a lower strength bainitic region surrounded by stronger martensitic regions that could lead to different types of failure unrelated to carbon diffusion. Compensating by removal of the bainitic region in the FGM leads to an increase in the carbon diffusion flux. Therefore, a FGM from 10 to 70% 800H is the most effective for limiting carbon diffusion and provides a shorter joint design compared to a full composition gradient. All types of FGMs investigated are effective in slowing carbon diffusion compared to a DMW, as demonstrated by the final column in Table 3. The FGMs from 10 to 70 or 100% 800H require approximately 100 years of service to reach the same carbon depletion as a DMW in 5 years. Although a gradient from 20 to 70% 800H also outperforms a DMW, it is not as effective in reducing carbon diffusion as its other FGM counterparts.

Table 4.2. Comparison of computed diffusion fluxes ( $\text{mol/m}^2\text{-s}$ ) and carbon depletion at 773 K after different service times in dissimilar joints between 2.25Cr-1Mo steel and Alloy 800H.

Type of joint		5 years	20 years	50 years	100 years
	Avg. Flux	$4.94 \times 10^{-13}$	$1.96 \times 10^{-12}$	$1.52 \times 10^{-12}$	$7.85 \times 10^{-13}$
	Depletion	5.0%	20%	23%	29%
	Avg. Flux	$3.92 \times 10^{-14}$	$1.57 \times 10^{-13}$	$3.92 \times 10^{-13}$	$7.85 \times 10^{-13}$
	Depletion	0.3%	1.2%	3.1%	5.0%
	Avg. Flux	$3.92 \times 10^{-14}$	$1.57 \times 10^{-13}$	$3.92 \times 10^{-13}$	$7.85 \times 10^{-13}$
	Depletion	0.3%	1.2%	3.1%	5.0%
	Avg. Flux	$6.16 \times 10^{-14}$	$2.47 \times 10^{-13}$	$6.16 \times 10^{-13}$	$8.48 \times 10^{-13}$
	Depletion	0.4%	1.6%	4.0%	7.3%

#### 4.6 Summary and conclusions

Compositional gradients were fabricated by laser-based directed energy deposition and the spatial variations of microstructure, chemical composition, and hardness were characterized. Additionally, single alloy specimens representing discrete regions of the functionally graded material were also fabricated to investigate phase composition and transformations. The following are the main findings.

- The fabricated compositional profile was expected to produce a martensitic to austenitic transition over the first 20 mm. However, in the 10% 800H region an abrupt decrease in microhardness was observed followed by a sharp return to high hardness in the 20% 800H region. As more of the austenitic alloy was added to the joint, a gradual change from a martensitic to a fully austenitic structure was observed. Taking these microstructural changes into account for an improved joint design led to the finding that a shorter joint can be used to achieve the same intended function.
- No benefits are gained in compositional grading after 70% 800H, where the microstructure is fully austenitic. Further changes in composition cause no appreciable changes in the driving force for carbon diffusion and simulations show nearly identical carbon profiles. Therefore, the functionality of the FGM can be achieved by joining 2.25Cr-1Mo steel to Alloy 800H with a composition gradient ranging from 10 to only 70% 800H.
- A relatively soft bainitic microstructure was found to exist in the 10% 800H region of the joint, causing an abrupt decrease in microhardness which was followed by a rapid return to high hardness levels in the martensitic 20% 800H region. However, if the 10% 800H region of the graded joint is excluded to avoid bainite formation, an increase in the driving force for carbon migration results, leading to higher amounts of carbon diffusion.

## 4.7 Reference

- [1] S.D. Meredith, J.S. Zuback, J.S. Keist, T.A. Palmer, Impact of composition on the heat treatment response of additively manufactured 17–4 PH grade stainless steel, *Mater. Sci. Eng. A*, 738 (2018) 44-56.
- [2] B.D. Cullity, S.R. Stock, *Elements of X-ray Diffraction*, Prentice Hall, New York, 2001.
- [3] ASTM, Standard Practice for X-Ray Determination of Retained Austenite in Steel with Near Random Crystallographic Orientation, 2013, <http://dx.doi.org/10.1520/E0975-13>.
- [4] V. Manvatkar, A. De, T. DebRoy, Heat transfer and material flow during laser assisted multi-layer additive manufacturing, *J. Appl. Phys.*, 116(12) (2014) 124905.
- [5] G.L. Knapp, T. Mukherjee, J.S. Zuback, H.L. Wei, T.A. Palmer, A. De, T. DebRoy, Building blocks for a digital twin of additive manufacturing, *Acta Mater.*, 135 (2017) 390-399.
- [6] A. Raghavan, H. Wei, T. Palmer, T. DebRoy, Heat transfer and fluid flow in additive manufacturing, *J. Laser Appl.*, 25(5) (2013) 052006.
- [7] G. Ghosh, G. Olson, Computational thermodynamics and the kinetics of martensitic transformation, *J. Phase Equilib.*, 22(3) (2001) 199.
- [8] S.-J. Lee, K.-S. Park, Prediction of martensite start temperature in alloy steels with different grain sizes, *Metall. Mater. Trans. A*, 44(8) (2013) 3423-3427.
- [9] N. Saunders, Z. Guo, X. Li, A. Miodownik, J.P. Schillé, The calculation of TTT and CCT diagrams for general steels, *JMatPro Software Literature*, (2004).
- [10] J. Kirkaldy, Diffusion-controlled phase transformations in steels. Theory and applications, *Scand. J. Metall.*, 20(1) (1991) 50-61.
- [11] E. Scheil, Bemerkungen zur schichtkristallbildung, *Z. Metallkd.*, 34(3) (1942) 70-72.
- [12] T. Keller, G. Lindwall, S. Ghosh, L. Ma, B.M. Lane, F. Zhang, U.R. Kattner, E.A. Lass, J.C. Heigel, Y. Idell, Application of finite element, phase-field, and calphad-based methods to additive manufacturing of Ni-based superalloys, *Acta Mater.*, In Press (2017).
- [13] A. Schaeffler, Constitution diagram for stainless steel weld metal, *Metal Prog.*, 56(11) (1949) 680.
- [14] G. Brentrup, J. DuPont, Fabrication and characterization of graded transition joints for welding dissimilar alloys, *Weld. J.*, 92 (2013) 72-79.
- [15] R. Baker, J. Nutting, The tempering of 2.25 Cr%–1% Mo steel after quenching and normalizing, *J. Iron Steel Inst.*, 202 (1959) 257-68.
- [16] J. Race, H. Bhadeshia, Precipitation sequences during carburisation of Cr–Mo steel, *Mater. Sci. Tech.*, 8(10) (1992) 875-882.
- [17] J. Yang, C. Huang, C. Yang, J. Horng, Microstructural examination of 2.25 Cr 1Mo Steel Steam pipes after extended service, *Mater. Charact.*, 30(2) (1993) 75-88.

## Chapter 5

# DEFECT FORMATION DURING THE FABRICATION OF FUNCTIONALLY GRADED ALLOYS

### 5.1 Introduction

The presence of process-related defects remains a major roadblock to the certification, qualification, and implementation of additively manufactured metallic components into safety-critical applications [1]. Commonly encountered defects in AM parts include porosity, lack of fusion voids, solidification cracking, residual stresses and distortion [2]; all of which form while the material is in a fully or semi-liquid state. These defects often negatively impact mechanical properties such as strength [3], ductility [4], and fatigue [5, 6]. The seemingly stochastic origins of defect formation make identify the underlying causative factors a major challenge. Consequently, many efforts to overcome these challenges during AM have relied on trial-and-error experimental techniques that tend to ignore scientific principles with the goal of obtaining a set of process conditions that produce acceptable parts.

In FGMs, the presence of defects can negate the designed functionality of the material. Many defects with different origins have plagued FGMs fabricated by AM, with a few examples shown in Figure 5.1. Bobbio et al. [7] found that a large crack originated in a region of a FGM between Ti-6Al-4V and Invar when a large amount of intermetallic phases formed. Similarly, intermetallic compounds were found near a crack formed during the grading from Ti-6Al-4V to SS304L with an intermediate vanadium section [8]. In another study [9], altering the chemical composition change along the grading direction was needed to avoid solidification cracking in a FGM between a low alloy steel and stainless steel 316L.

The brute-force experimental optimization procedure of FGMs is typically not feasible without proper guidance because, along with adjustable AM machine parameters like laser power and scanning speed, variables spanning composition space must also be explored. Consider a simple parameter optimization experiment of a single alloy with two adjustable variables and three levels each. A set of 9 experimental deposits are needed to span parameter space to formulate process-quality relations. For a FGM with 10 discrete steps in composition, for example, a total of 90 deposits are now needed for the same analysis. Besides being expensive, time consuming, and burdensome, there is no guarantee that an optimal solution will be obtained.

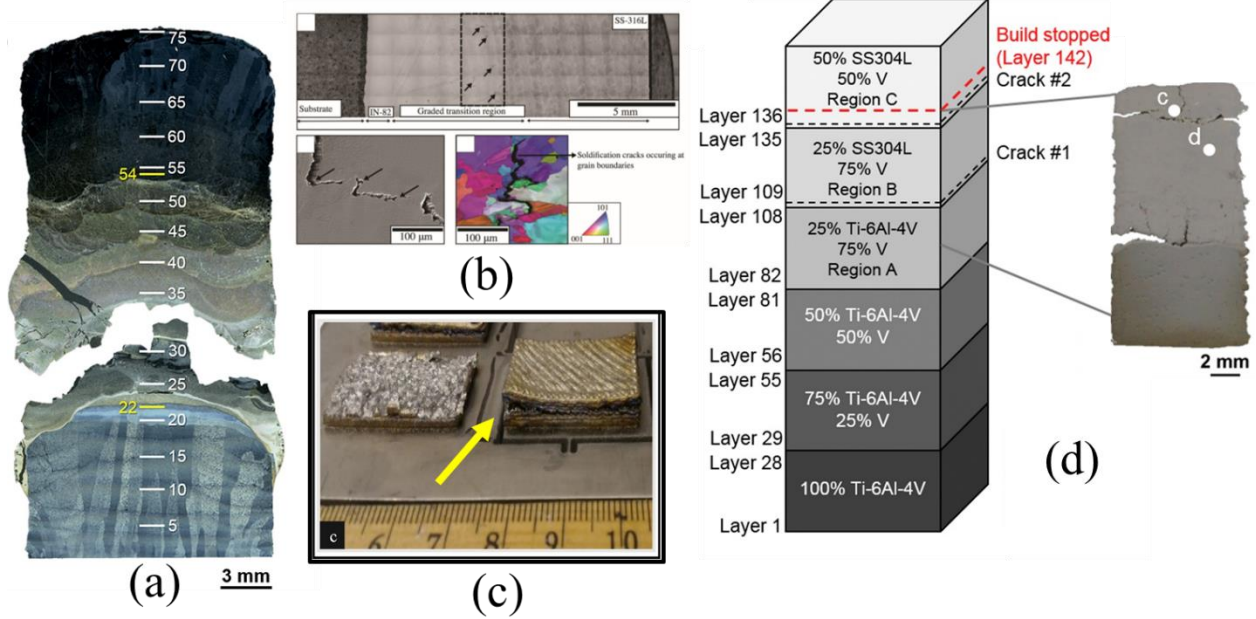


Figure 5.1. Cracks are often observed in a variety of FGM systems fabricated by AM, such as (a) Ti-6Al-4V to Invar 36 [7], (b) Inconel® 82 to SS316L [9], (c) Ti-6Al-4V to Inconel® 718 [10], and (d) Ti-6Al-4V to SS304L [8]. Reprinted with permission from Elsevier.

A combined theoretical and experimental approach is utilized in this chapter to identify the underlying origin of defect formation in a FGM between a ferritic steel and an austenitic alloy. The microstructure of the FGM fabricated in Chapter 3 was further characterized to identify process-related defects. The periodic spacing of lack of fusion defects in discrete composition regions indicated significant variations of molten pool geometry as a function of chemistry. Single pass, single layer deposits with different alloy compositions were deposited with different laser powers to study the effects of processing and chemical composition on molten pool geometry. Calculations of the thermodynamic activity of surface-active elements are coupled with a theoretical description of surface tension and heat transfer and fluid flow simulations to elucidate the effects of chemical composition on convective flow. Ultimately, it is found that the changes in minor alloying element concentrations dictate the liquid metal flow, which cause variations in molten pool geometry. For a constant hatch spacing and set of processing parameters, the differences in geometry lead to the formation of lack of fusion defects.

## 5.2 Theoretical modeling and experimental procedures

### 5.2.1 Surface tension calculations

Several theoretical descriptions of the surface tension of a molten alloy with surface-active elements are available. Belton [11] combined two descriptions of solute adsorption behavior, the Langmuir and Gibbs isotherms, to calculate the surface tension for a binary alloy,

$$\sigma^P - \sigma = RT\Gamma_i^0 \ln(1 + K_i a_i) \quad (5.1)$$

The surface tension of the pure metal is  $\sigma^P$  and  $\sigma$  is the surface tension of a binary mixture of the pure metal with element  $i$ , both at temperature  $T$ . The activity of element  $i$  in the mixture is  $a_i$  and the surface segregation (i.e., adsorption) at full coverage is given by  $\Gamma_i^0$ .  $K_i$  is the equilibrium coefficient and  $R$  is the universal gas constant.

Sahoo et al. [12] noted that Equation (5.1) can be made temperature-dependent by expanding the definition of the equilibrium coefficient to include its relevant components, given by,

$$K_i = k_i \exp(-\Delta H_i^\circ / RT) \quad (5.2)$$

where the adsorption coefficient is defined in terms of two temperature-independent parameters;  $k_i$ , a constant related to the enthalpy of segregation, and  $\Delta H_i^\circ$ , the enthalpy of segregation.

Assuming the interaction between surface active elements is weak allows for effects of multiple surface elements to be additive. Li et al. [13] demonstrated that this approach agreed well with experimental data for oxygen and sulfur in an Fe-Cr alloy. The surface tension can therefore be written as a summation of the right-side of Equation (5.1) for  $N$  surface-active elements in the alloy,

$$\sigma^P - \sigma = \sum_i^N RT\Gamma_i^0 \ln(1 + K_i a_i) \quad (5.3)$$

Differentiating Equation (5.3) with respect to  $T$  gives the temperature coefficient of surface tension,

$$\frac{\partial \sigma}{\partial T} = \frac{\partial \sigma^P}{\partial T} - \sum_i^N \left[ R\Gamma_i^0 \ln(1 + K_i a_i) + \frac{K_i a_i}{(K_i a_i + 1)} \frac{\Delta H_i^\circ \Gamma_i^0}{T} \right] \quad (5.4)$$

which is one of the main factors that determines the magnitude and direction of fluid flow during DED-L [2]. With Equations (5.3) and (5.4), the surface tension and surface tension temperature coefficients can be obtained for a binary alloy mixture of a pure metal and a surface-active element. However, binary alloys are rarely used in practice, and several adjustments and assumptions need to be made when considering a system with commercial alloys:

1. The surface tension of the pure metal,  $\sigma^P$ , is taken as the surface tension of the alloy with no surface-active elements. These values are included in the estimated physical properties of the thermodynamic software package.
2. If the electronegativity difference on the Pauling's scale between the major alloying elements and a surface-active element is greater than 0.5, then  $\Delta H_i^\circ$  has been shown empirically to be constant [12]. In these cases,  $\Delta H_i^\circ$  for the surface-active element and the main alloying elements can be taken as a representative value in the absence of more detailed data. For example, the value of  $\Delta H_O^\circ$  in Fe-O binary alloy is assumed to be similar to  $\Delta H_O^\circ$  in an Fe-Cr-Ni-O alloy. The same assumption applies to  $k_i$ , since  $k_i$  is a constant related to  $\Delta H_i^\circ$ .
3. The magnitude of  $\Gamma_i^0$  is assumed to be similar for a binary alloy (e.g., Fe-O) and a multicomponent alloy (e.g., Fe-Cr-Ni-O), because the surface structure of the liquid is assumed to not change significantly.

With the above considerations, the values of  $\Delta H_i^\circ$ ,  $k_i$  and  $\Gamma_i^0$  for Fe-S and Fe-O binary alloys can be used as representative values for the calculation of surface tension of both Fe-Ni-Cr alloys containing O and S. The values compiled by Sahoo et al. [12] were used in this work and are summarized in Table 5.1.

*Table 5.1. Values for the enthalpy of segregation ( $\Delta H_i^\circ$ ), entropy of segregation factor ( $k_i$ ), and surface excess at saturation ( $\Gamma_i^0$ ) of element  $i$  for binary Fe-O and Fe-S alloys [12].*

Binary alloy	$\Delta H_i^\circ$ [J mol <sup>-1</sup> ]	$k_i$	$\Gamma_i^0$ [mol m <sup>-2</sup> ]
Fe-O	-1.463×10 <sup>5</sup>	1.38×10 <sup>-2</sup>	2.03×10 <sup>-5</sup>
Fe-S	-1.662×10 <sup>5</sup>	3.18×10 <sup>-3</sup>	1.30×10 <sup>-5</sup>

### 5.2.2 Thermodynamic calculations

The use of equilibrium thermodynamic calculations in this chapter are twofold. First, the chemical activities of surface-active elements are calculated to investigate the effects of chemical composition on the surface-tension driven flow of liquid metal during AM. Second, the equilibrium phase fractions as a function of temperature are used to predict important thermophysical properties for different alloy chemistries to be used in numerical heat transfer and fluid flow calculations. The software JMatPro® V8 was used in conjunction with the General Steel database for all thermodynamic calculations.

In a multi-component alloy, interactions between alloying elements generally cause the activity of an element to deviate from the elemental composition. Additionally, some reactive elements may form compounds (oxides, sulfides, carbides, etc.) in the liquid melt that reduce the available amount of the element in solution. The activity of an element,  $i$ , in a multicomponent alloy is expressed as,

$$a_i = \exp\left(\frac{\mu_i - G_i^0}{RT}\right) \quad (5.5)$$

where  $\mu_i$  is the chemical potential,  $G_i^0$  is the reference state of element  $i$ ,  $R$  is the gas constant, and  $T$  is temperature. Here, the reference state is arbitrary, and is usually taken to be that of the pure element at standard pressure and temperature. However, the activity values used for solving Equations (5.3) and (5.4) for the surface tension and surface tension gradient were derived for an infinitely dilute solution, where the activity is equal to unity when the concentration of  $i$  is equal to 1 wt%. Therefore, a change of reference state is needed to convert the activity calculated from JMatPro® to values with a 1 wt% reference basis. The calculated activity was multiplied by a proportionality factor,  $F$ , which is the ratio of the activity values from the two different reference states,

$$F = \frac{a_i}{a'_i} = \frac{1}{a'_i} \quad (5.6)$$

where  $a_i$  is the activity at  $i = 1$  wt% in the 1 wt% reference state, and  $a'_i$  is the activity when  $i = 1$  wt% in the standard reference state [14].

The modeling of thermophysical properties using involves sequential steps. First, the equilibrium distribution of phases is determined through the minimization of the total Gibbs energy method using thermodynamic excess functions to account for the mixing of elements [15]. The property,  $P$ , of interest for each phase is expressed as [16],

$$P = \sum_i x_i P_i^0 + \sum_i \sum_{j>i} x_i x_j \sum_v \Omega_{ij}^v (x_i - x_j)^v \quad (5.7)$$

where  $P_i^0$  is the property of the phase in the pure element,  $\Omega_{ij}^v$  is a binary interaction parameter between elements  $i$  and  $j$  dependent on the integer  $v$ , and  $x_i$  and  $x_j$  are the mole fractions of  $i$  and  $j$  in the phase, respectively. The effects of temperature on the property of a phase are accounted for through both  $P_i^0$  and  $\Omega_{ij}^v$ , which are temperature-dependent. The total property of the alloy is then determined from the phase fractions and properties of each phase using the general law of mixtures [17]. The use of this type of model allows for the approximation of thermophysical properties as functions of composition and temperature and accounts for effects of multi-phase microstructures.

### 5.2.3 Heat transfer and fluid flow model

A transient heat transfer and fluid flow model is coupled with a surface energy minimization model to calculate deposit geometry. The heat transfer and fluid flow model solves the governing equations of continuity, momentum conservation and energy conservation and are given by, respectively,

$$\frac{\partial \rho}{\partial t} + \frac{\partial(\rho u_i)}{\partial x_i} = 0 \quad (5.8)$$

$$\rho \frac{\partial u_i}{\partial t} + \sum_{j=1}^3 \frac{\partial v_i}{\partial x_j} = -\frac{\partial p}{\partial x_i} + \sum_{j=1}^3 \frac{\partial}{\partial x_j} \left( \mu \frac{\partial u_i}{\partial x_j} \right) + S_i \quad (5.9)$$

$$\rho \frac{\partial h}{\partial t} + \frac{\partial(\rho u_i h)}{\partial x_i} = \frac{\partial}{\partial x_i} \left( \frac{k}{C_p} \frac{\partial h}{\partial x_i} \right) - \rho \frac{\partial(f_l \Delta H)}{\partial t} - \rho \frac{\partial(u_i f_l \Delta H)}{\partial x_i} + S \quad (5.10)$$

where  $\rho$  is density,  $\mu$  is the dynamic viscosity,  $h$  is the sensible heat,  $C_p$  is the specific heat,  $f_l$  is the liquid fraction,  $\Delta H$  is the latent heat of fusion,  $p$  is pressure,  $u_i$  is the velocity component in the  $i$ -direction, and  $x_i$  is the spatial component in the  $i$ -direction, where  $i = 1, 2, 3$  corresponds to  $x, y$ , and  $z$  directions, respectively, in a three-dimensional Cartesian coordinate system. The variables

$S_i$  and  $S$  are source terms for Equations (5.9) and (5.10), respectively. The equations are discretized using the finite difference method and solved using a Fortran implementation of the semi-implicit method for pressure-linked equations [18]. An iterative procedure was used to find the solution for the three-dimensional velocity components, sensible heat, and pressure at each time step.

Between each time step, a surface energy minimization technique was applied to calculate the shape of the molten pool surface. Surface deformation occurs due to the addition of material, constrained by energy required to move the surface due to capillary pressure, gravity, powder feedstock impacting the molten pool, vaporization recoil pressure, and surface tension. This is defined by the equation [19, 20],

$$\sigma \left\{ \frac{(1 + \Phi_y^2)\Phi_{xx} - 2\Phi_x\Phi_y\Phi_{xy} + (1 + \Phi_x^2)\Phi_{yy}}{(1 + \Phi_x^2 + \Phi_y^2)^{3/2}} \right\} = \rho g\Phi + P_i + P_c + P_v + \lambda \quad (5.11)$$

where  $\sigma$  is surface tension,  $\rho$  is the density of the material,  $P_i$  is the pressure due to the impact of powder particles,  $P_c$  is the capillary pressure,  $P_v$  is the vapor recoil pressure, and  $\lambda$  is the Lagrangian parameter.  $\Phi$  is the surface deformation normal to the surface,  $\Phi_x$  is  $\partial\Phi/\partial x$ ,  $\Phi_{xx}$  is  $\partial^2\Phi/\partial x^2$ , and so on. The Gauss-Seidel point-by-point method [18] was used to solve Equation (5.11) across the entire domain for an initial guess of the Lagrangian parameter. Error based on the initial guess is given by integrating the added volume to the molten pool and comparing it to the specified mass addition,

$$\int_A \Phi dA - \dot{V} = \epsilon \quad (5.12)$$

where  $\epsilon$  is the error,  $A$  is the area, and  $\dot{V}$  is the volume flow rate of powder into the molten pool. An iterative method is used to determine  $\lambda$  by minimizing the error in Equation (5.12). The calculated surface shape was then used to specify material properties and the fluid flow domain in the next time-step. Since a rectilinear grid was used, the exact surface interface was mapped to the nearest control volumes. The exact location of the surface interface was saved between time steps and was used for subsequent free surface calculations to avoid accumulated error in surface location.

The solution domain consisted of the deposited alloy and the surrounding gaseous phase. Heat transfer was solved across the entire domain, while the fluid flow domain only considered a

sub-region in the alloy material where the temperature was greater than solidus temperature. Boundary conditions for heat transfer were specified on all sides of the rectangular domain as heat fluxes based on natural convection heat transfer coefficients of  $8 \text{ Wm}^{-2}\text{K}^{-1}$  with an ambient temperature of 298 K. Volumetric source terms for the energy equation were applied at the gas/alloy interface to account for heat loss due to radiation, forced convection due to shielding gas and vaporization, as well as the heat input due to the laser heat source. A forced convection coefficient of  $80 \text{ Wm}^{-2}\text{K}^{-1}$  was taken within the powder stream-radius based on previous work [21].

Heat input was calculated considering the interaction of a Gaussian-distributed laser with the powder flow from the four, concentric nozzles. The analytical model proposed by Tabernero et al. [22] was used to calculate the attenuation of the laser beam by the powder flow. Part of the attenuated laser heats the powder particles based on the optical absorptivity of the individual particles, which is assumed to be the same as base material and this heat is considered if the powder is captured into the molten pool. Based on experimental calibrations, the laser was taken to have a  $3\sigma$  radius of 2 mm and the powder flow was taken to be uniformly distributed over a 2.75 mm radius circle centered on the laser beam axis.

Volume capture for Equation (5.12) was calculated based on the assumption that if powder particles hit the molten pool then they have a chance of being absorbed and if the powder hits a solid surface then it ricochets away. As has been shown in high-speed video of the molten pool surface [23], powder particles do not melt immediately upon hitting the surface of the molten pool and during that residence time on the surface they can repel other incoming particles. The residence time was measured experimentally to be on the order of  $10^{-4}$  to  $10^{-3}$  s, depending on powder diameter. Since experimental measurements were not available for these experimental conditions, residence time was estimated as,

$$\tau(x, y) = \frac{m_p}{P(x, y)A_p} \left( \int_{T_{amb}}^{T_L} c_p(T) dT + L \right) \quad (5.13)$$

The residence time at a particular location  $(x, y)$  is given by  $\tau(x, y)$ , which is based on the mass of the powder particle  $m_p$ , the projected area of the particle  $A_p$ , the local power intensity  $P(x, y)$ , and the total amount of energy required to melt the material. The total amount of energy to melt the material is given by integrating the temperature-dependent specific heat  $c_p(T)$  from

ambient to liquidus temperature and adding the latent heat,  $L$ . This approach yields reasonable values of approximately 1 – 10 ms for 100  $\mu\text{m}$  diameter particles for a laser power of 2000 W with a Gaussian energy density distribution. Details for translating residence time to the probability of a powder being absorbed into the molten pool are given by Haley et al. [23]. The probability of capturing a single powder particle into a region on the molten pool is,

$$\eta_m(x, y) = \frac{L(x, y)}{\tau(x, y)F(x, y)} = \frac{F(x, y)B\tau(x, y)A(x, y)}{(\tau(x, y)F(x, y)A_p + BA(x, y))\tau(x, y)F(x, y)} \quad (5.14)$$

In Equation (5.14),  $\eta_m(x, y)$  is the local powder capture efficiency,  $L(x, y)$  is the number of powder particles loaded on the local surface,  $F(x, y)$  is the local powder feedrate in powder particles per seconds,  $A(x, y)$  is the local surface area and  $B$  is geometrically allowable powder packing on the local surface. Integrating  $\eta_m(x, y)$  over the entire surface of the molten pool allows for the total mass capture efficiency to be determined, which can trivially be transformed to volume capture rate by dividing the mass capture rate by material density.

#### 5.2.4 Specimen fabrication and characterization

The desired chemical compositions were achieved by mechanical mixing of multiple alloy powders. Since 2.25Cr-1Mo steel is not commonly available in powder form, a mixture of commercially pure Fe and Cr powders (Atlantic Equipment Engineers, Micron Metals, Inc.) were blended to the approximate nominal composition of Fe-2.25 wt% Cr. The Fe and Cr powders, as determined from the supplier, had mesh ranges of -100/+325 and -100, respectively. Pre-alloyed Micro-Melt® Pyromet 800 powder (Carpenter Powder Products, Bridgeville, PA) was used to represent the chemical composition of Alloy 800H and had a particle size range of -120/+325. Since all powders have similar densities, alloy blends were mixed by weight in 10% increments using the Fe-2.25Cr mixture and Pyromet 800 powders up to a mixture of 60% 800H. Compositional grading beyond 60% 800H was previously deemed unnecessary to the functionality of the FGM. The chemical compositions of materials used are listed in Table 3.1 in Chapter 3.

Single tracks for compositions ranging from 10-60% 800H powder mixtures were deposited onto a 150 mm x 150 mm x 12.7 mm normalized and tempered SAE387 Grade 22 steel substrate (American Alloy Steel, Rome, NY) using a laser-based DED process. All tracks were made using a travel speed of 10.6 mm/s, laser beam diameter of 4 mm, and powder flow rate of

approximately 0.25 g/s. Heat input was varied for each composition using laser powers of 2000, 2500, and 3000 W. All deposits were approximately 30 mm long and were spaced at least 4 mm apart on the substrate. The steel substrate was ground to remove the oxide scale and cleaned with acetone prior to the experiment.

Metallographic cross sections were extracted perpendicular to the scanning direction to observe the deposit geometry. Samples were mounted in epoxy, ground using a series of SiC papers, and polished with 3 and 1  $\mu\text{m}$  polycrystalline diamond suspensions. A final polishing step with 0.05  $\mu\text{m}$  colloidal silica was used to achieve a mirror finish. Micrographs of the deposit geometry were obtained using an optical microscope and optical profilometry measurements were made using a Keyence VHX-2000 digital optical microscope to obtain the relative height of deposits above the substrate. All measurements and image analysis of metallurgical cross-sections were performed using the ImageJ software.

Figure 5.2 shows a schematic illustration of a metallurgical cross section with labeled parameters that were used to quantify the deposit geometries. The dilution depth,  $d$ , is defined as the maximum penetration into the substrate measured from the original location of the top of the substrate. The deposit width,  $w$ , represents the length between the two contact points of the bead on the substrate surface. The melted area below the substrate,  $A_d$ , and the area of the deposited bead material,  $A_b$ , are used to define the percentage of dilution as,

$$D = \frac{A_d}{A_b + A_d} \times 100 \quad (5.15)$$

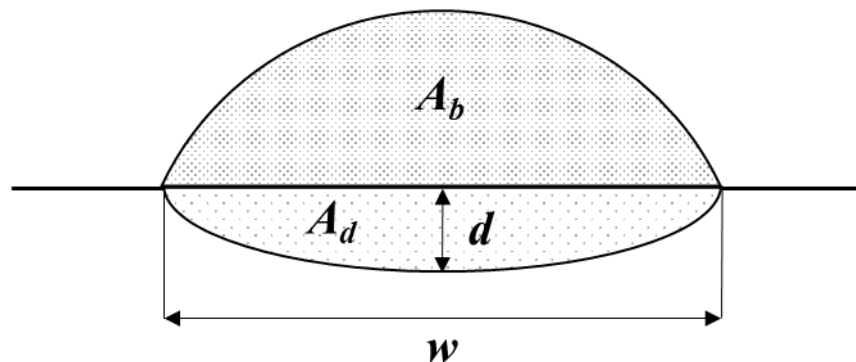


Figure 5.2. Schematic diagram of metallurgical cross section with the quantified parameters labeled.

### 5.3 Lack of fusion defects in functionally graded material

Upon further microstructural investigation, the fabricated FGM between 2.25Cr-1Mo steel and Alloy 800H contained multiple lack of fusion defects in specific locations along the build height. A light optical micrograph of the first half of the FGM (10 to 50% 800H) is shown in Figure 5.3(a), with lack of fusion defects indicated by the red arrows. The defects were vertically aligned along the build direction at a spacing of approximately 2 mm apart, corresponding to two deposited layers. The voids were only observed in the 10 to 30% 800H regions of the FGM, which are distinguished by the different etching regions in Figure 5.3(a). Furthermore, the horizontal spacing between two voids in the same layer was approximately 2.5 mm, corresponding to the hatch spacing used for deposition.

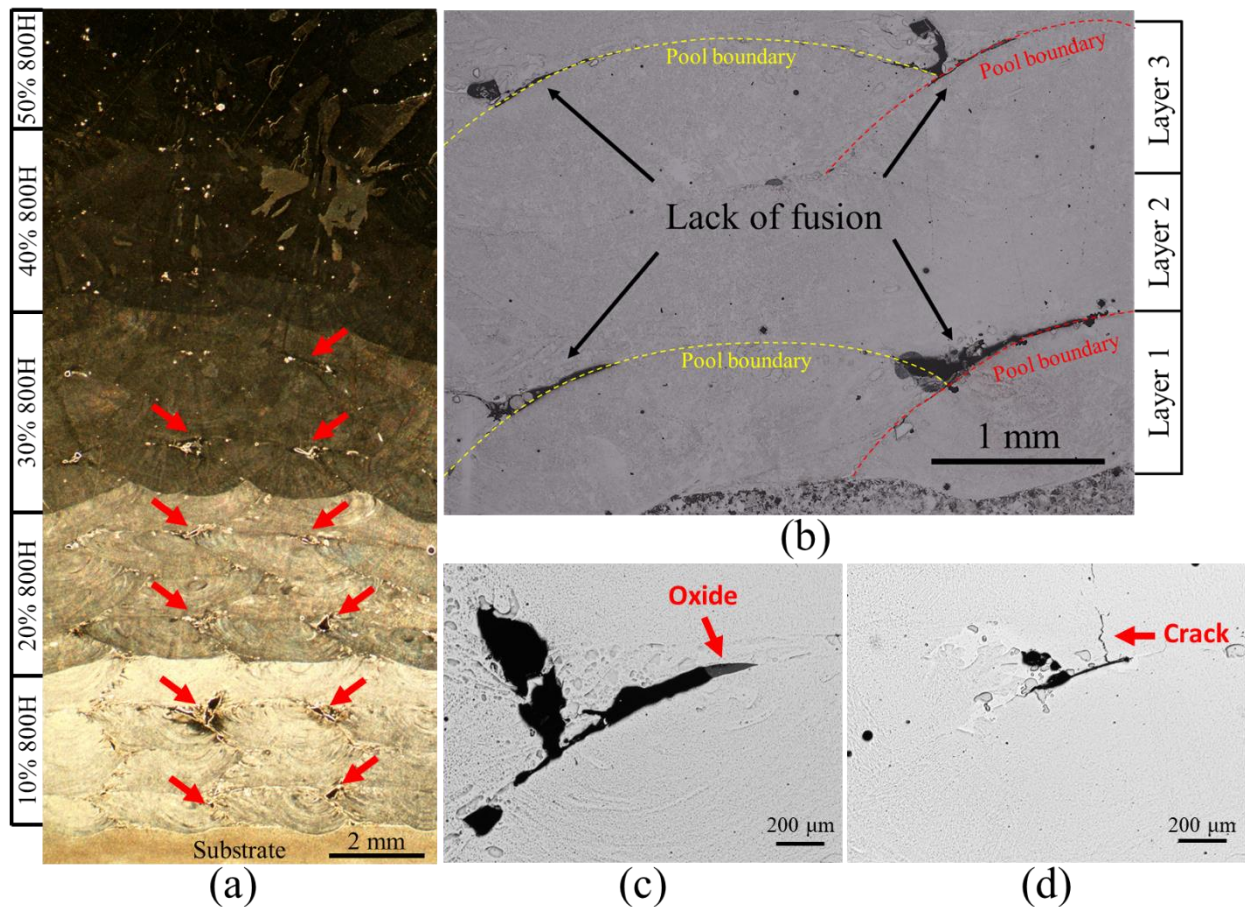


Figure 5.3. (a) Low magnification light optical micrograph of the periodic vertical alignment of lack of fusion defects, indicated by the red arrows. The defects were found at the junctions between subsequent passes and layers, indicated by the light optical micrograph with the approximate pool boundaries indicated in (b). Higher magnification images show the consequences of lack of fusion defects, such as (c) oxide filling and (d) cracking.

Higher magnification micrographs of the 10% 800H region of the FGM in Figure 5.3(b) show that the lack of fusion defects coincide with the deposit boundaries from individual passes within layers. These defects can lead detrimental consequences such as oxide filling and crack initiation, as shown in Figure 5.3 (c) and (d), both of which can impact the properties and performance of the FGM [24, 25]. Upon visual inspection of the defects, noticeable size differences were observed in the different regions of the FGM. Using the ImageJ software, the area of each void within an area spanning three passes and 12 layers of the FGM was measured. This representative area corresponds to two vertically aligned columns of lack of fusion defects. Figure 5.4 shows that both the average individual void size and total void area decrease with increasing amounts of 800H in the FGM, indicating that specific regions of the FGM are more susceptible to the formation of lack of fusion defects than others.

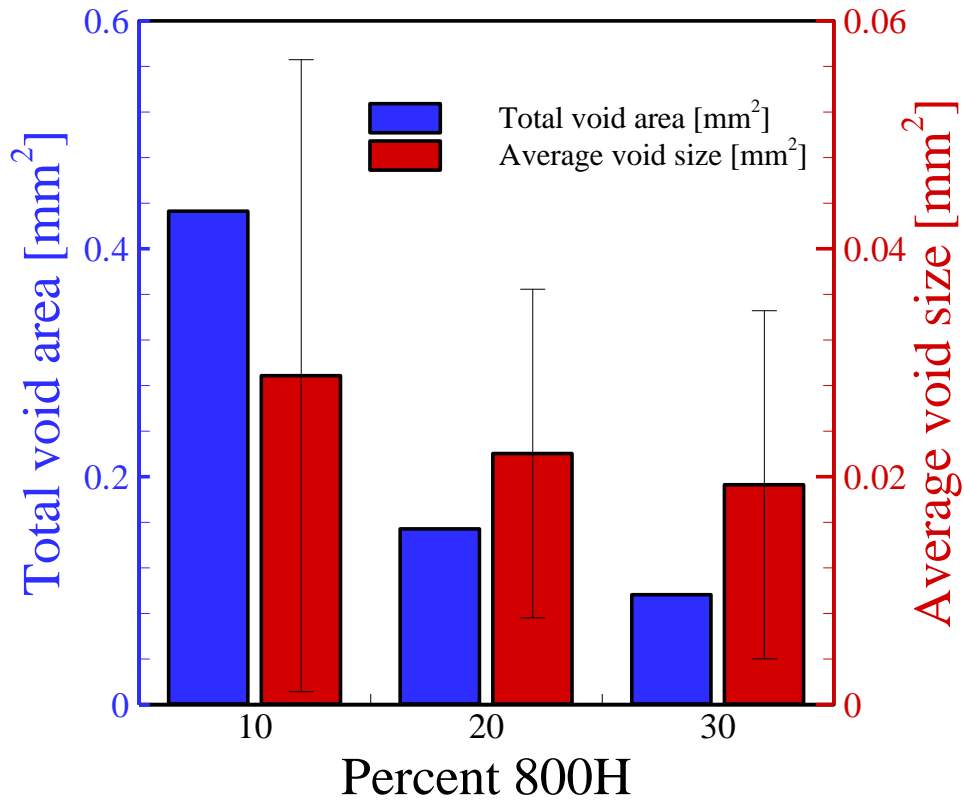


Figure 5.4. Image analysis measurements indicate that both the average individual lack of void size and total void area decrease as more 800H alloy is added to the FGM.

The important findings of the defect characterization are summarized as follows:

- Lack of fusion defects were located at the junctions between passes and layers.
- Defects were periodically spaced in both the vertical and horizontal directions.
- Only the 10 to 30% 800H regions of the FGM contained lack of fusion voids.
- With increasing 800H additions, the individual size and area fraction of voids decreased.

All the above indicate significant changes in molten pool geometry associated with compositional grading during fabrication. Since a constant hatch spacing was used for the FGM, changes in molten pool geometry owing to variations in thermophysical properties of the alloy can lead to improper bonding between subsequent hatches and layers. The larger void size in the 10% 800H regions indicate a relatively small molten pool, and the molten pool size is believed to increase with the addition of Alloy 800H to the alloy.

#### **5.4 Characterization of single bead deposits**

To investigate the impact of compositional changes on molten pool geometry, single track, single layer beads were deposited, and the geometric features were characterized. Optical micrographs of the transverse cross-sections of the as-deposited beads are shown in Figure 5.5, where noticeable changes in deposit geometry occur both as a function of composition and laser power. The bottom edge of the fusion zone that penetrates the substrate varies in shape as the 800H alloy content increases. In general, alloy compositions corresponding to low percentages of 800H exhibit a deep, hemispherical shape in the dilution region penetrating the substrate. As more 800H is added to the alloy, the bottom edge of the fusion zone becomes flatter and penetrates less into the substrate. Qualitatively, alloys with low 800H levels tend to have a narrow, deep molten pool, whereas high levels of 800H lead to wide and shallow deposits.

Based on the measurements of total melted area ( $A_b + A_d$ ), dilution depth, and percent dilution shown in Figure 5.6 (a), (b), and (c), respectively, increasing laser power causes an increase in the overall deposit dimensions for nearly all chemical compositions. In general, the total melted area remains roughly constant as more 800H is added to the alloy, as indicated by the nearly horizontal slopes of the linear fits. The upward trend in the Figure 5.6(a) for the 2500 W laser power is largely due to the outlying data point for the 60% 800H alloy. This finding indicates

that changes in chemical composition from 10 to 60% 800H have marginal effects on the total volume of the molten pool when laser power is constant.

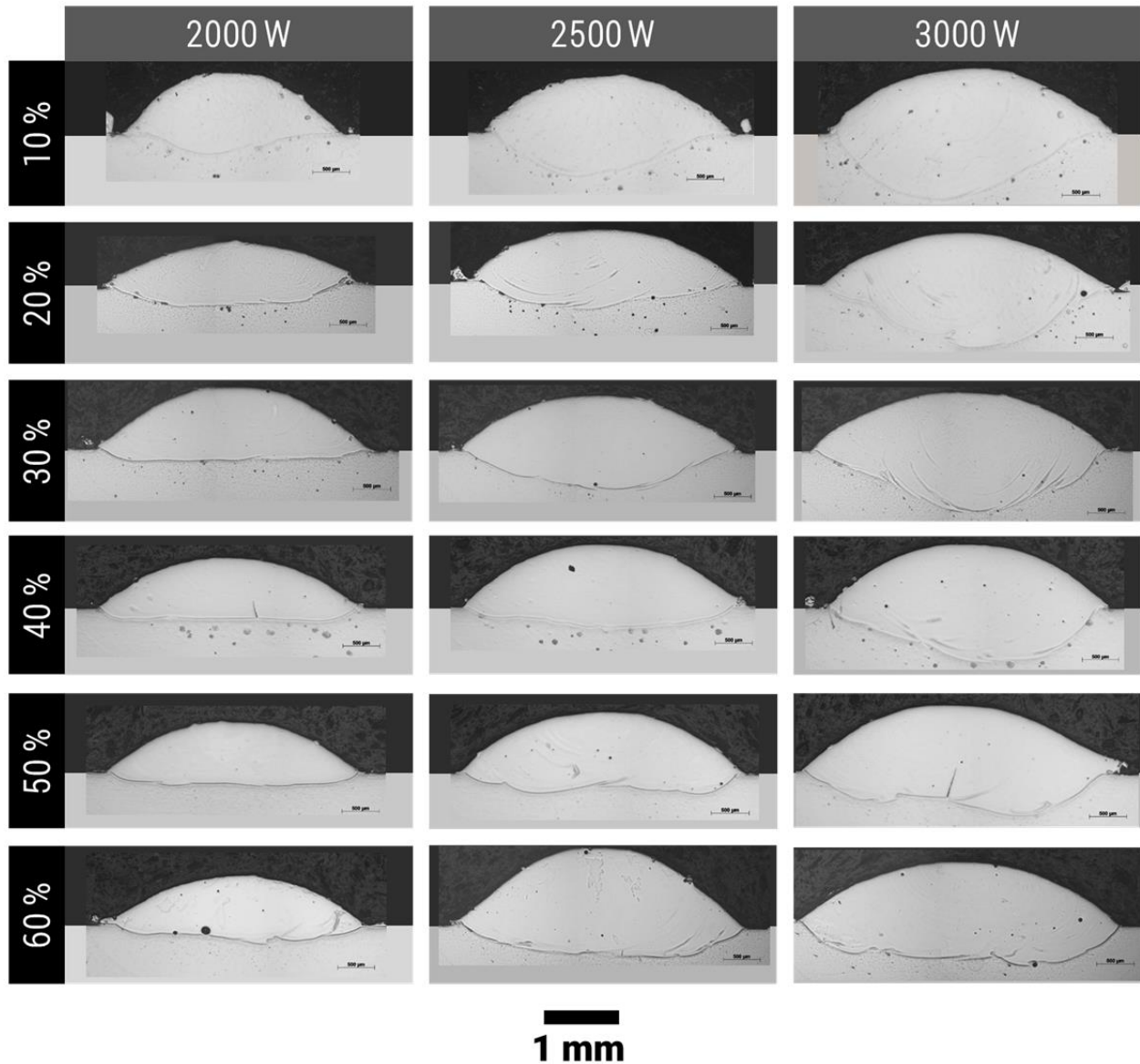


*Figure 5.5. Bead geometry changes as a function of alloy composition and laser power as seen in the optical micrographs of transverse cross-sections of the single bead deposits. The percentages along the left axis represent the amount of 800H added to the alloy.*

While the total volume of melted material is approximately uniform, stark differences were observed in the melting of the substrate and powder blends as a function of alloy composition. For all laser powers, the maximum dilution depth decreases with increasing additions of 800H to the powder blend, as shown in Figure 5.6(b). Similarly, the percent dilution also decreases with higher amounts of 800H additions for the 2500 and 3000 W laser powers shown in Figure 5.6(c), while

the large amounts of scatter for the 2000 W power cause the linear fit to trend slightly upwards. The data in Figure 5.6 (b) and (c) indicate that more energy is used for melting powder particles rather than the substrate as the amount of 800H powder in the alloy increases. Consequently, a higher fraction of the deposit consists of added material from powder flow as more 800H powder is added.

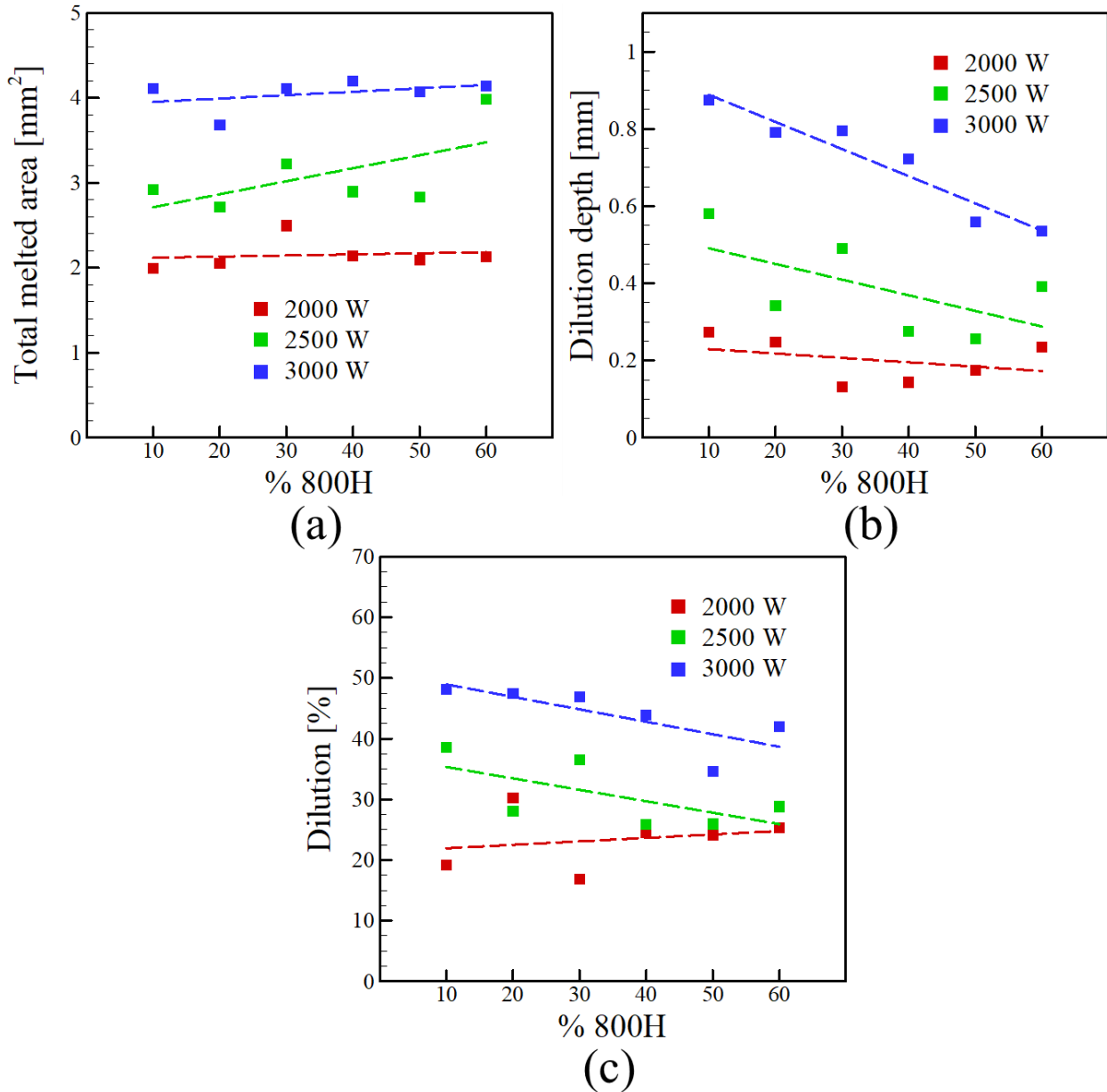


Figure 5.6. The effects of alloy composition and laser power on (a) the total melted area of the deposit, (b) the maximum dilution depth, and (c) the percent dilution calculated from Equation (5.15).

Important data on the deposit surface geometry, namely the deposit height and width, were obtained by optical profilometry measurements. Large deviations in bead height as a function of alloy composition are observed in Figure 5.7(a) for the deposits deposited with the 2000 W laser power, and no trends can be inferred. On the other hand, a sudden decrease followed by a steady increase in bead height were measured as a function of composition for the 2500 and 3000 W laser powers. The deposit width exhibits a general upward trend with increasing Alloy 800H additions for all laser powers, as shown in Figure 5.7(b). For all compositions, an increase in laser power effectively results in a wider bead deposit.

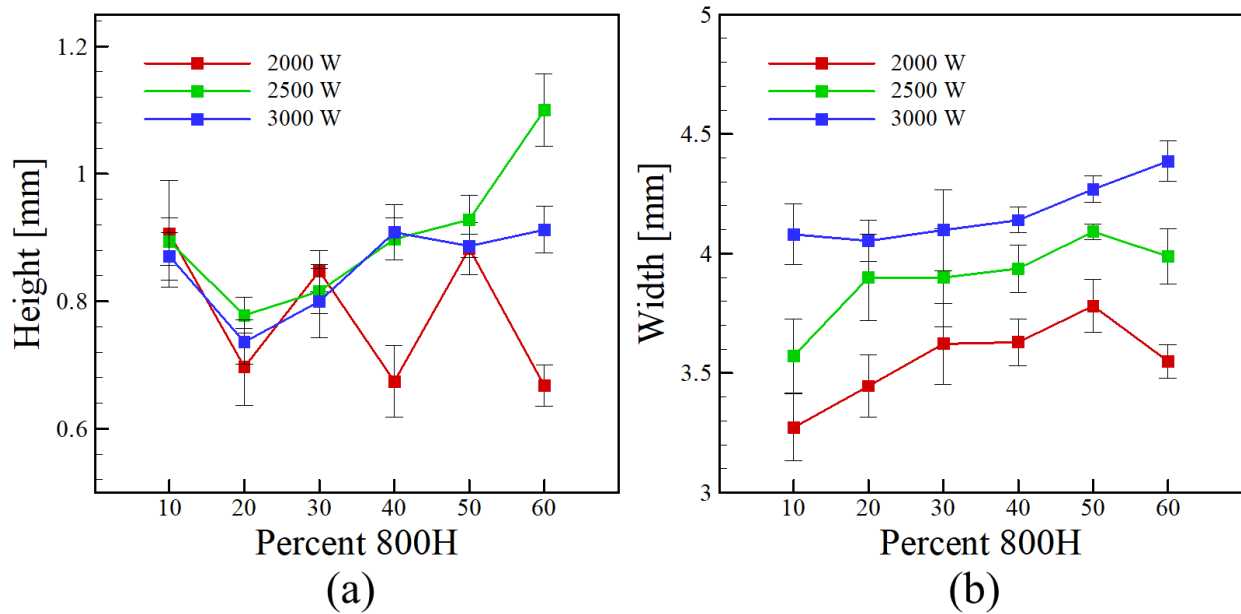


Figure 5.7. The chemical composition and laser power have significant effects on the experimentally measured deposit (a) height and (b) width.

The interpretation of data in Figure 5.6 and Figure 5.7 can be summarized as follows:

- For a given laser power, the total amount of melted material (powder and substrate) remains roughly constant as a function of alloy composition.
- With increasing Alloy 800H additions, the molten pool penetrates less into the substrate and more powder is deposited.
- The fusion zone boundary in the substrate changes from a deep, hemispherical to a shallow, flat shape with increases of 800H in the alloy.
- The deposit width widens as more Alloy 800H is added to the alloy.

## 5.5 Effect of chemical composition on surface tension

The lack of fusion defects in the additively manufactured FGM are believed to originate from changes in molten pool geometry. Significant variations in single-bead deposit geometry have been observed, owing to changes in chemical composition. It is well-known that surface-active elements, such as oxygen and sulfur, influence the molten pool shape due to changing the temperature-dependent surface tension ( $\sigma$ ) and the Marangoni flow in welding [26, 27], and the same concepts apply to AM. Gan et al. [28] showed that flow in the molten pool can change from inwards to outwards as sulfur concentration increases for a Co-based alloy in DED-L. For pure alloys near the melting temperature, the surface tension temperature coefficient ( $d\sigma/dT$ ) is typically negative, and becomes more positive as sulfur content increases [11].

It is apparent from Equation (5.3) that the surface tension of an alloy is dependent on the chemical activity of surface active elements, which can be calculated from Equation (5.5) at any given temperature and reference state. The activity of an element,  $a_i$ , in multicomponent systems is derived from the chemical potential,  $\mu_i$ , sometimes referred to as the partial molar Gibbs free energy, which can be expressed as,

$$\mu_i = \left( \frac{\partial G_m}{\partial x_i} \right) \quad (5.16)$$

at constant temperature and pressure, where  $G_m$  is the molar Gibbs free energy and  $x_i$  is the mole fraction of element  $i$ . The molar Gibbs free energy for multicomponent random solutions is written as

$$G_m = \sum x_i G_i^0 + G_m^I + G_m^E = \sum x_i G_i^0 + RT \sum x_i \ln x_i + G_m^E \quad (5.17)$$

In Equation (5.17), the first term represents contributions from pure elements, the second represents energy contributions from ideal mixing, and the third is the excess mixing energy from non-ideal mixing. The excess mixing energy can be described in terms of the Redlich-Kister polynomial [15],

$$G_m^E = \sum_i \sum_j x_i x_j L_{ij} + \sum_i \sum_j \sum_k x_i x_j x_k L_{ijk} \quad (5.18)$$

where  $L_{ij}$  and  $L_{ijk}$  represent binary and ternary interaction coefficients, respectively. These coefficients can be either positive or negative, and the magnitude indicates the strength of an interaction between elements in a solution. Therefore, higher amounts of alloying elements that interact strongly with oxygen and sulfur will tend to lower the chemical activity of those elements.

The activities of oxygen and sulfur were calculated using JMatPro® for the different alloy compositions at 1600°C as a function of oxygen and sulfur concentration, and the results are shown in Figure 5.8. The results in Figure 5.8(a) indicate that increasing the amount of Alloy 800H in the alloy composition reduces the activity of oxygen for any given concentration of oxygen in the alloy. Furthermore, the oxygen activity is highly sensitive changes in the oxygen concentration for low levels of 800H and becomes less sensitive with increasing amounts of 800H. In contrast, the amount of 800H in the alloy has a negligible impact on the sulfur activity. All alloy compositions exhibit nearly identical behavior in sulfur activity when the amount of sulfur in the alloy changes.

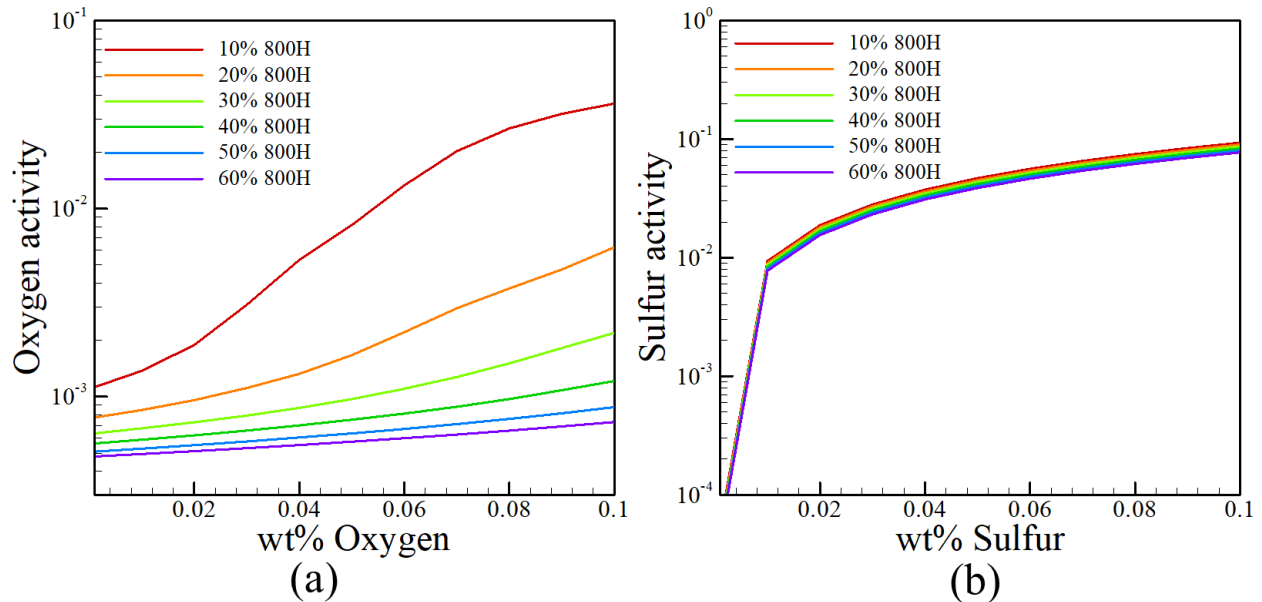


Figure 5.8. The calculated activity as a function of composition for (a) oxygen and (b) sulfur for different alloy compositions at 1600°C.

Although the interaction coefficients used in JMatPro® calculations are proprietary information, the results in Figure 5.8 can be qualitatively assessed using literature data [14, 29]. Experimentally determined binary interaction coefficients for oxygen and sulfur are given in Table 5.2. Clearly, oxygen interacts strongly with multiple alloying elements, including Al, Si, Ti, whereas the relative magnitudes of interaction coefficients between sulfur and these same elements

are much lower. In steelmaking literature, these elements are often referred to as deoxidizing elements because they draw oxygen out of solution to improve properties [30]. Since all solute elements (Al, Cr, Mn, Ni, Si, Ti) increase with Alloy 800H additions, it can be expected that the oxygen activity will be reduced while the activity of sulfur is much less affected.

Table 5.2. First order binary interaction coefficients between surface-active and other alloying elements in liquid iron at 1600°C [14, 29].

Element	Al	Cr	Mn	Ni	Si	Ti
O	-390	-4	-2.1	0.6	-13.1	-60
S	3.5	-1.1	-2.6	0	6.3	-7.2

From the calculated activities in Figure 5.8 at the nominal concentrations of oxygen and sulfur, the surface tension and temperature coefficient of surface tension can be calculated from Equations (5.3) and (5.4), respectively, as functions of temperature. The surface tension calculations in Figure 5.9(a) show the largest deviations for the 10 and 20% 800H alloys, while the plots for the 30 to 60% 800H alloy compositions nearly overlap. These calculations are directly related to the trends in oxygen activity in Figure 5.8(a), where the largest deviations occur at low 800H levels.

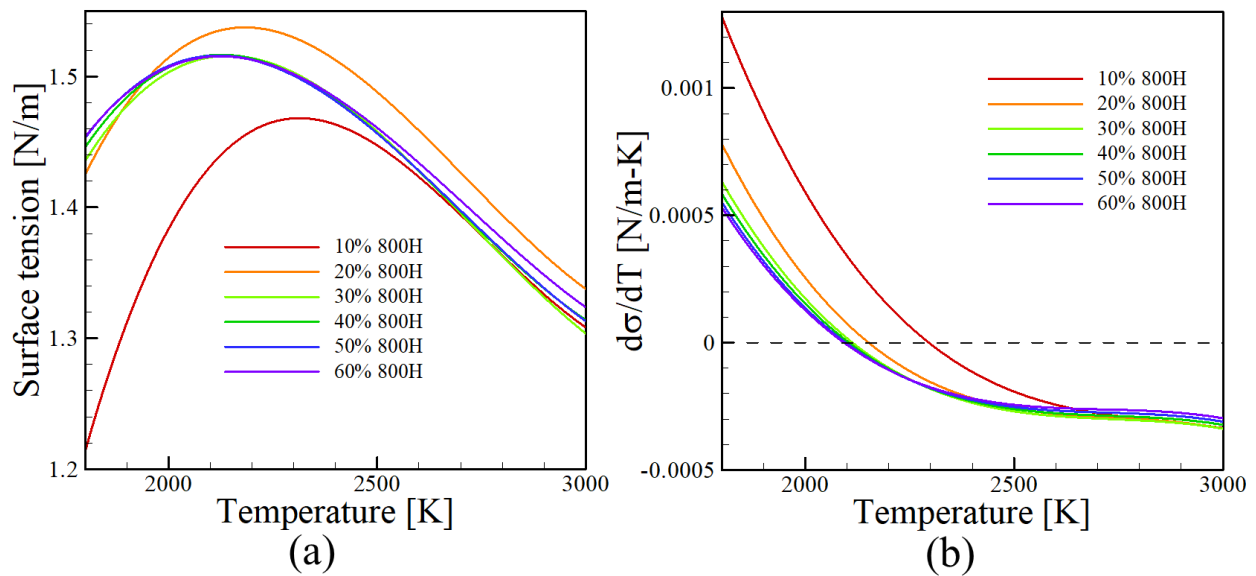


Figure 5.9. Changes in the (a) surface tension and (b) temperature coefficient of surface tension ( $d\sigma/dT$ ) as a function of temperature for different alloy compositions.

The slope of the curves in Figure 5.9(a) represent the temperature coefficient of surface tension ( $d\sigma/dT$ ), which is plotted in Figure 5.9(b) as a function of temperature. At relatively low temperature,  $d\sigma/dT$  for the 10% 800H becomes highly positive, and  $d\sigma/dT$  steadily decreases with increasing Alloy 800H additions. All alloy compositions experience a transition from positive to negative  $d\sigma/dT$  within the temperature range of approximately 2300-2600°C (2027-2327 K). This transition temperature where  $d\sigma/dT = 0$ , coined as the critical temperature ( $T_{crit}$ ), is plotted in Figure 5.10 for each alloy composition. The highest critical temperatures occur at low levels of 800H and decrease as more 800H is added to the alloy.

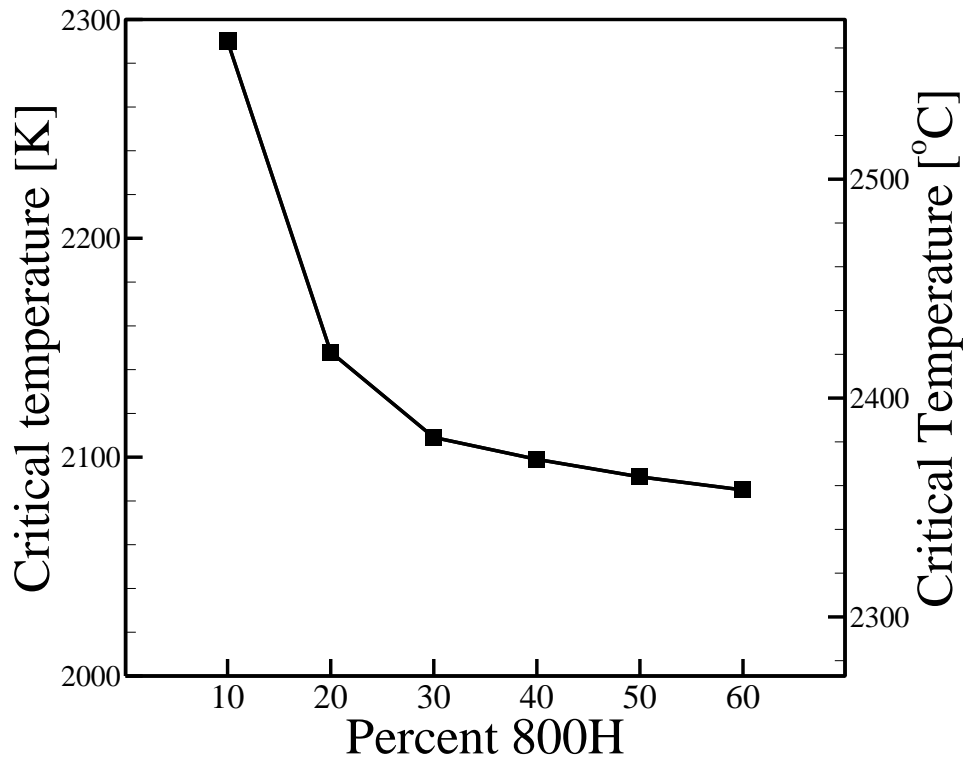


Figure 5.10. The critical temperature, defined as the temperature at which the temperature coefficient of surface tension ( $d\sigma/dT$ ) changes from positive to negative, changes significantly with alloy composition.

### 5.6 Simulated bead shape in single pass deposits

For numerical heat transfer and fluid flow simulations, a full description of thermophysical properties of all alloys is needed as input. The thermophysical properties listed in Table 5.3 were calculated using JMatPro® using the procedure discussed in Section 5.2.2. The absorption coefficient,  $\eta$ , was calculated by approximating each composition as a binary Fe-Ni alloy with

different ratios of elements and using a rule of mixtures between absorption coefficients of the pure elements. The emissivity values were assumed to be constant for all alloy.

During AM, the pickup of gaseous elements, such as oxygen, can cause the chemical composition to deviate from the measured values in the initial powder feedstock. For this reason, a constant value of 0.05 wt% oxygen was arbitrarily chosen as the total amount of oxygen in all deposits, which represents the initial amount of oxygen in the powder as well as a reasonable approximation of oxygen contamination based on the work by Elmer and Gibbs [31]. Since sulfur is typically not present in gaseous form, the chemical composition of sulfur was assumed to be equal to that of the powder feedstock.

Heat transfer and fluid flow simulations of the AM process were performed for the 10 and 60% 800H compositions, which represent the extrema of the composition gradient, to demonstrate the effects of chemical composition on the deposit geometry for the 2000 W laser power. The simulation results with and without surface-active elements considered are shown in Figure 5.11. Figure 5.11 (a) and (c) represent the bead geometries for the 10 and 60% 800H compositions, respectively, ignoring the effects of surface-active elements. Similarly, Figure 5.11 (b) and (d) represent the bead geometries for the 10 and 60% 800H compositions, respectively, when the effects of surface-active elements are considered. The red regions represent temperatures above the liquidus temperature, orange regions represent the solid-liquid two phase region, white is the surrounding gas, and light brown corresponds to all temperatures below the solidus temperature. Experimentally measured deposit geometries are shown by the dotted black lines for comparison.

For both alloy compositions, considering the effects of surface-active elements has a noticeable effect on the deposit geometry in terms of width, height, and penetration depth. However, due to the lower activity of O in the 60 % 800H alloy, the changes in deposit shape are less dramatic when considering the addition of surface-active elements compared to the 10% 800H alloy. The 10% 800H deposit had a width reduction of 23 % when surface-active elements were considered, while the 60 % 800H deposit only had a width reduction of 14 % . Similarly, the height of the deposit shape, when considering surface-active elements, increased by 15 % for the 10% 800H case but only by 9 % for the 60 % 800H case. Changes in penetration depth were more drastic, with the 10 % 800H case having an increase of 115 % and the 60 % 800H case having an increase of only 25 %.

Table 5.3. Calculated thermophysical properties of alloy compositions ranging from 10 to 60% 800H.

Property	Units	Substrate	Material					
			10% 800H	20% 800H	30% 800H	40% 800H	50% 800H	60% 800H
Solidus temperature, $T_s$	K	1739	1746	1736	1707	1689	1671	1650
Liquidus temperature, $T_l$	K	1787	1770	1759	1747	1737	1727	1714
Specific heat of solid, $c_{p,s}$	$J kg^{-1} K^{-1}$	420+0.167T	420+0.167T	420+0.167T	331+0.251T	331+0.251T	331+0.251T	331+0.251T
Specific heat of liquid, $c_{p,l}$	$J kg^{-1} K^{-1}$	810	800	800	790	790	790	780
Thermal conductivity of solid, $k_s$	$W m^{-1} K^{-1}$	13.6+0.0126T	12.3+0.0126T	11.2+0.0126T	10.2+0.0126T	9.54+0.0126T	9.04+0.0126T	8.66+0.0126T
Thermal conductivity of liquid, $k_l$	$W m^{-1} K^{-1}$	32.7	32.33	32.1	31.7	31.5	31.2	30.86
Density, $\rho$	$kg m^{-3}$	7830	7840	7890	7940	7970	7940	7920
Surface tension at $T_l$ , $\sigma$	$N m^{-1}$	1.838	1.805	1.785	1.751	1.738	1.727	1.719
Temperature-coefficient of surface tension, $d\sigma/dT$	$N m^{-1} K^{-1}$	-4.44x10 <sup>-4</sup>	-3.84x10 <sup>-4</sup>	-3.52x10 <sup>-4</sup>	-3.50x10 <sup>-4</sup>	-3.33x10 <sup>-4</sup>	-3.17x10 <sup>-4</sup>	-3.03x10 <sup>-4</sup>
Latent heat of fusion, $\Delta H$	$J kg^{-1}$	2.62x10 <sup>5</sup>	2.58x10 <sup>5</sup>	2.51x10 <sup>5</sup>	2.56x10 <sup>5</sup>	2.57x10 <sup>5</sup>	2.56x10 <sup>5</sup>	2.59x10 <sup>5</sup>
Liquid viscosity, $\mu$	$kg m^{-1} s^{-1}$	6.67x10 <sup>-3</sup>	6.81x10 <sup>-3</sup>	6.89x10 <sup>-3</sup>	6.97x10 <sup>-3</sup>	7.03x10 <sup>-3</sup>	7.09x10 <sup>-3</sup>	7.21x10 <sup>-3</sup>
Thermal expansion coefficient, $\alpha$	$K^{-1}$	1.78x10 <sup>-6</sup>	1.78x10 <sup>-6</sup>	1.96x10 <sup>-6</sup>	2.16x10 <sup>-6</sup>	2.31x10 <sup>-6</sup>	2.26x10 <sup>-6</sup>	2.22x10 <sup>-6</sup>
Absorption coefficient, $\eta$	-	0.351	0.344	0.337	0.329	0.322	0.315	0.308
Emissivity, $\varepsilon$	-	0.3	0.3	0.3	0.3	0.3	0.3	0.3

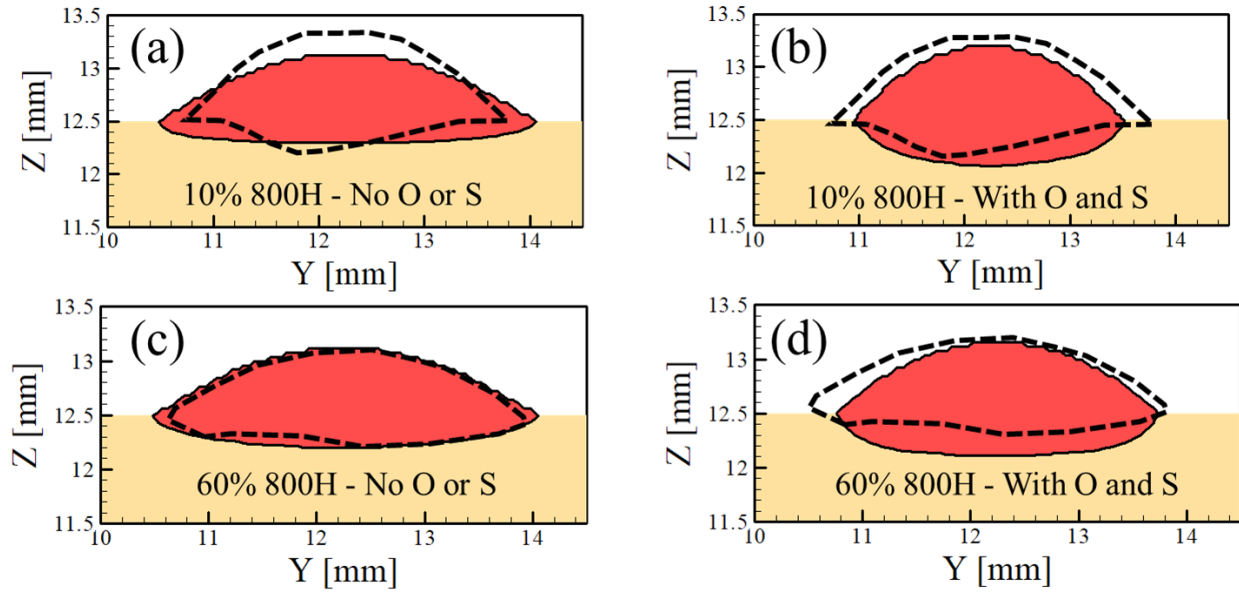


Figure 5.11. The calculated deposit geometries for the 10% 800H alloy compositions (a) ignoring surface-active elements and (b) considering the effects of oxygen and sulfur show considerable differences in shape. In contrast, the changes in deposit geometries for the 60% 800H alloy compositions (c) ignoring surface-active elements and (d) considering the effects of oxygen and sulfur are much less sensitive. Experimentally measured deposit geometries are shown by the dotted black lines.

Three-dimensional views of the simulations considering surface-active elements are shown in Figure 5.12. The local material velocities, shown by the vectors, can be seen to be inwards below the critical temperature ( $T_{crit}$ ), which is the temperature at which the surface tension temperature coefficient changes from positive to negative shown in Figure 5.10. Comparing the two alloy compositions, the 10 % 800H has a higher critical temperature, resulting in a larger region of inward fluid flow, and higher magnitudes of inward velocity. These fluid flow effects limit the amount of heat transfer by the fluid to the edge of the pool, which had the effect of reducing the width of the bead and increasing the depth. Similarly, the strong inward velocities promote heat transfer down through the substrate, resulting in an increase in the penetration depth.



From the simulation results, several trends are displayed that are consistent with conventional understanding of the role of surface tension in determining the shape of the fusion zone. The negative value of the temperature coefficient for the pure alloys indicates that fluid flow will be from the center of the pool (high temperature, low surface tension) to the edge of the pool (low temperature, high surface tension). These conditions lead to a wide and shallow molten pool due to enhanced radial heat transfer by fluid flow. When surface-active elements are present, the temperature coefficient is positive up to  $T_{crit}$ , meaning fluid flow will be from the outer edges of the pool towards the middle of the pool. The calculated values of  $T_{crit}$  can be seen to decrease as a function of alloy composition in Figure 5.10. As the value of  $T_{crit}$  increases, the area of the molten pool surface that experiences inward fluid flow becomes larger. Inward liquid metal flow leads to a relatively narrow deposit and a deeper fusion zone.

To investigate the sensitivity of bead geometry to oxygen content, further calculations were performed for the different alloy compositions with varying amounts of oxygen ranging from 0 to 0.1 wt%. The deposit width, dilution depth, and height were extracted from these calculations, and the results are shown in Figure 5.13 (a), (b), and (c), respectively. The oxygen concentration has the largest effects of alloy compositions up to 30% 800H. Above this composition, the bead dimensions converge as a function of oxygen concentration and the differences become small. Increasing oxygen content does not significantly affect the oxygen activity for alloy compositions from 30 to 60% 800H due to the presence of respectable amounts of deoxidizing elements. Additionally, the simulated deposit dimensions remain roughly constant for the simulations with 0.0 wt% O, indicating that changes in thermophysical have a negligible effect on bead geometry. Accordingly, the differences in deposit geometry are mainly governed by the effects of surface-active elements on surface tension. Furthermore, since the activity of sulfur, the only other surface active element present, was similar in both alloys, variations in oxygen activity are likely responsible for the observed variations in deposit shape.

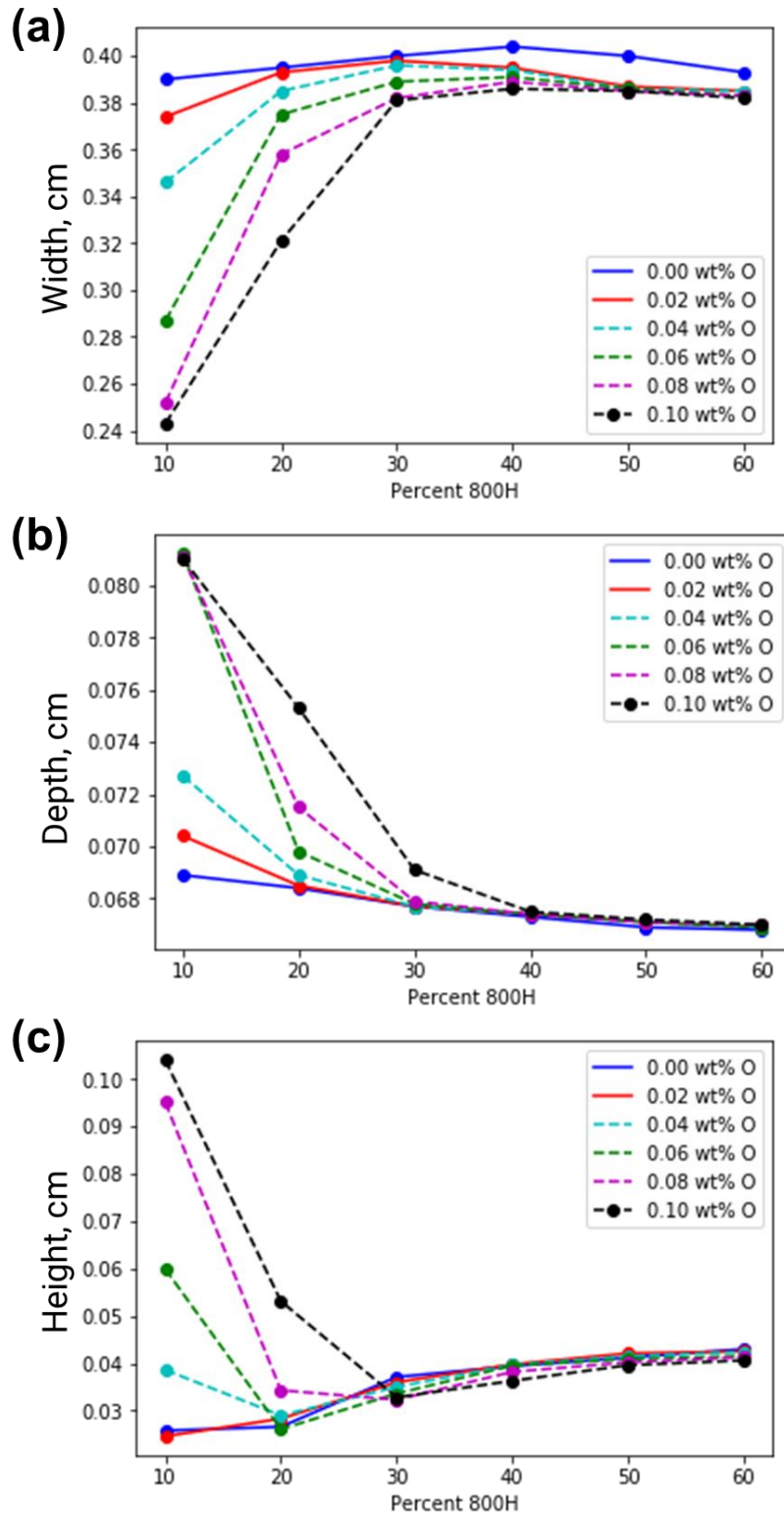


Figure 5.13. The calculated deposit (a) width, (b) depth, and (c) height as a function of alloy composition and oxygen concentration for a 2000 W laser power. All other parameters used in the simulations were the same as experimental conditions.

## 5.7 Summary and conclusions

Variations in molten pool geometry caused by changes in chemical composition were believed to cause lack of fusion defects during the additive manufacturing of functionally graded materials. A combined experimental and theoretical approach was used to understand these changes in molten pool behavior for alloy compositions relevant to a transition from 2.25Cr-1Mo steel to Alloy 800H. Single track beads were deposited using different powder blends and quantitative measurements were made to characterize the deposit geometry. Thermodynamic calculations coupled with a numerical heat transfer and fluid flow model were then used to explain the experimentally observed variations in deposit geometry. The following are the main conclusions:

- Changes in major alloying elements, which largely determine thermophysical properties, have negligible effects on the shape and size of the molten pool for the alloy compositions investigated. The presence of surface-active elements was found to be mainly responsible in determining the deposit geometry of single-track beads. The activity of oxygen and sulfur affect the magnitude and direction of liquid metal flow during additive manufacturing.
- Although all powder blends contain roughly the same concentrations of total oxygen and sulfur, the activity of surface-active elements varies depending on the chemical composition of the alloy. The activity of oxygen decreases with increasing amounts of deoxidizing elements, like aluminum, titanium, and silicon. Consequently, material with higher amounts of 800H are calculated to contain less amounts of oxygen in solution since 800H is the source of deoxidizing elements. The activity of sulfur is largely unchanged as a function of alloy composition.
- Oxygen and sulfur decrease the surface tension near the liquidus temperature, causing the temperature coefficient of surface tension to change from positive to negative with increasing temperature. The critical temperature, or the temperature where surface tension changes from positive to negative, increases with higher oxygen activity. As a result, the critical temperature is highest for the 10% 800H alloy and lowest for the 60% 800H alloy.
- The differences in the temperature coefficient of surface tension for various alloy compositions was found to have a pronounced effect on the molten pool geometry. A strong inward flow was simulated in alloys with low amounts of 800H while outward flow

dominated as the percentage of 800H increased. Accordingly, the width of the deposit increased with increasing amounts of 800H and the penetration depth decreased.

## 5.8 Reference

- [1] T. Mukherjee, T. DebRoy, A digital twin for rapid qualification of 3D printed metallic components, *Applied Materials Today*, 14 (2019) 59-65.
- [2] T. DebRoy, H. Wei, J. Zuback, T. Mukherjee, J. Elmer, J. Milewski, A. Beese, A. Wilson-Heid, A. De, W. Zhang, Additive manufacturing of metallic components—process, structure and properties, *Prog. Mater. Sci.*, 92 (2018) 112-224.
- [3] A.E. Wilson-Heid, T.C. Novak, A.M. Beese, Characterization of the Effects of Internal Pores on Tensile Properties of Additively Manufactured Austenitic Stainless Steel 316L, *Exp. Mech.*, (2018).
- [4] A.M. Beese, B.E. Carroll, Review of Mechanical Properties of Ti-6Al-4V Made by Laser-Based Additive Manufacturing Using Powder Feedstock, *JOM*, 68(3) (2015) 724-734.
- [5] E. Wycisk, A. Solbach, S. Siddique, D. Herzog, F. Walther, C. Emmelmann, Effects of Defects in Laser Additive Manufactured Ti-6Al-4V on Fatigue Properties, *Phys. Procedia*, 56 (2014) 371-378.
- [6] Q.C. Liu, J. Elambasseril, S.J. Sun, M. Leary, M. Brandt, P.K. Sharp, The Effect of Manufacturing Defects on the Fatigue Behaviour of Ti-6Al-4V Specimens Fabricated Using Selective Laser Melting, *Advanced Materials Research*, 891-892 (2014) 1519-1524.
- [7] L.D. Bobbio, R.A. Otis, J.P. Borgonia, R.P. Dillon, A.A. Shapiro, Z.-K. Liu, A.M. Beese, Additive manufacturing of a functionally graded material from Ti-6Al-4V to Invar: Experimental characterization and thermodynamic calculations, *Acta Mater.*, 127 (2017) 133-142.
- [8] L.D. Bobbio, B. Bocklund, R. Otis, J.P. Borgonia, R.P. Dillon, A.A. Shapiro, B. McEnerney, Z.-K. Liu, A.M. Beese, Characterization of a functionally graded material of Ti-6Al-4V to 304L stainless steel with an intermediate V section, *J. Alloy. Comp.*, 742 (2018) 1031-1036.
- [9] N. Sridharan, E. Cakmak, B. Jordan, D. Leonard, W. Peter, R. Dehoff, D. Gandy, S. Babu, Design, fabrication, and characterization of graded transition joints, *Weld. J.*, 96(8) (2017) 295S-306S.
- [10] B. Onuik, A. Bandyopadhyay, Additive manufacturing of Inconel 718 – Ti6Al4V bimetallic structures, *Addit. Manuf.*, 22 (2018) 844-851.
- [11] G.R. Belton, Langmuir adsorption, the Gibbs adsorption isotherm, and interfacial kinetics in liquid metal systems, *Metall. Mater. Trans. B*, 7(1) (1976) 35-42.
- [12] P. Sahoo, T. Debroy, M.J. McNallan, Surface tension of binary metal—surface active solute systems under conditions relevant to welding metallurgy, *Metallurgical Transactions B*, 19(3) (1988) 483-491.
- [13] Z. Li, K. Mukai, M. Zeze, K.C. Mills, Determination of the surface tension of liquid stainless steel, *J. Mater. Sci.*, 40(9) (2005) 2191-2195.
- [14] C.H. Lupis, *Chemical thermodynamics of materials*, New York, NY, 1983.
- [15] Z.-K. Liu, Y. Wang, *Computational thermodynamics of materials*, Cambridge University Press, Cambridge, UK, 2016.
- [16] N. Saunders, Z. Guo, X. Li, A. Miodownik, J.-P. Schille, *Modelling the material properties and behaviour of Ni-based superalloys*, *Superalloys*, Warrendale, PA, 2004, pp. 849-858.
- [17] Z. Fan, P. Tsakiroopoulos, A.P. Miodownik, A generalized law of mixtures, *J. Mater. Sci.*, 29(1) (1994) 141-150.

- [18] S. Patankar, Numerical heat transfer and fluid flow, 1st ed., Hemisphere Publishing Corporation, Boca Raton, FL, 1980.
- [19] C.S. Wu, L. Dorn, Computer simulation of fluid dynamics and heat transfer in full-penetrated TIG weld pools with surface depression, *Comp. Mater. Sci.*, 2(2) (1994) 341-349.
- [20] C.-H. Kim, W. Zhang, T. DebRoy, Modeling of temperature field and solidified surface profile during gas-metal arc fillet welding, *J. Appl. Phys.*, 94(4) (2003) 2667-2679.
- [21] M.F. Gouge, J.C. Heigel, P. Michaleris, T.A. Palmer, Modeling forced convection in the thermal simulation of laser cladding processes, *The International Journal of Advanced Manufacturing Technology*, 79(1) (2015) 307-320.
- [22] I. Taberero, A. Lamikiz, E. Ukar, L.N. López de Lacalle, C. Angulo, G. Urbikain, Numerical simulation and experimental validation of powder flux distribution in coaxial laser cladding, *J. Mater. Process. Technol.*, 210(15) (2010) 2125-2134.
- [23] J.C. Haley, J.M. Schoenung, E.J. Lavernia, Observations of particle-melt pool impact events in directed energy deposition, *Addit. Manuf.*, 22 (2018) 368-374.
- [24] X. Lou, P.L. Andresen, R.B. Rebak, Oxide inclusions in laser additive manufactured stainless steel and their effects on impact toughness and stress corrosion cracking behavior, *J. Nucl. Mater.*, 499 (2018) 182-190.
- [25] J.H. Martin, B.D. Yahata, J.M. Hundley, J.A. Mayer, T.A. Schaedler, T.M. Pollock, 3D printing of high-strength aluminium alloys, *Nature*, 549 (2017) 365.
- [26] W. Pitscheneder, T. Debroy, K. Mundra, R. Ebner, Role of sulfur and processing variables on the temporal evolution of weld pool geometry during multikilowatt laser beam welding of steels, *Weld. J.*, 75(3) (1996).
- [27] S. Mishra, T.J. Lienert, M.Q. Johnson, T. DebRoy, An experimental and theoretical study of gas tungsten arc welding of stainless steel plates with different sulfur concentrations, *Acta Mater.*, 56(9) (2008) 2133-2146.
- [28] Z. Gan, G. Yu, X. He, S. Li, Surface-active element transport and its effect on liquid metal flow in laser-assisted additive manufacturing, *Int. Commun. Heat Mass*, 86 (2017) 206-214.
- [29] G.K. Sigworth, J.F. Elliott, The thermodynamics of liquid dilute iron alloys, *Metal Science*, 8(1) (1974) 298-310.
- [30] E.T. Turkdogan, Physical chemistry of high temperature technology, Academic Press, Inc., New York, NY, 1980.
- [31] J.W. Elmer, G. Gibbs, The effect of atmosphere on the composition of wire arc additive manufactured metal components, *Sci. Technol. Weld. Joi*, (2019) 1-8.

## Chapter 6

# THE IMPACT OF COMPOSITION ON PRECIPITATE FORMATION IN AN ADDITIVELY MANUFACTURED NICKEL BASE SUPERALLOY

### 6.1 Introduction

Nickel base superalloys generally exhibit excellent corrosion resistance and creep strength, which make them suitable for high temperature environments in aerospace and marine applications [1]. These alloys are popular materials for the fabrication of functionally graded materials. Two common superalloys, Inconel® 625 and 718, have been combined with a variety of dissimilar alloys, like SS316L [2, 3], SS304L [4], Ti-6Al-4V [5, 6], and copper alloy GRCop-84 [7], using additive manufacturing. However, the combination of many alloying elements can often lead to the formation of deleterious secondary phases that can promote cracking during processing [8] and impact the mechanical and corrosion properties and performance [9]. For example, Figure 6.1 shows a crack in a Laves phase particle in an Inconel® 625 part fabricated using laser-based directed energy deposition additive manufacturing.

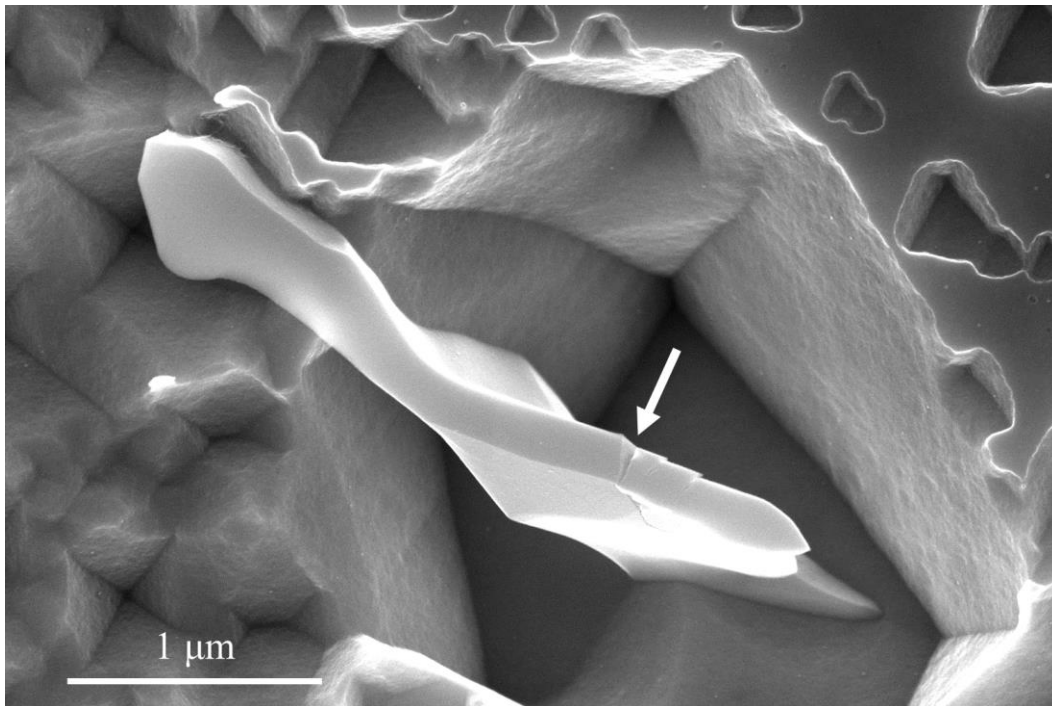


*Figure 6.1. Some precipitates in Inconel® 625 are undesirable in terms of mechanical properties due to their brittle nature, where can initiate cracks as shown by the white arrow in a Laves phase precipitate in low Fe Inconel® 625.*

Although Inconel® 625 is designed to be a solid-solution strengthened nickel-base superalloy, multiple secondary phases can form during solidification in fusion-based process such as welding [10, 11] and additive manufacturing [12-16]. It is well-established that the initial chemical composition of Inconel® 625 is an important driver for secondary phase formation, such as Laves and MC, in fusion welding [10]. However, the impact of chemical composition variations on secondary phase formation in Inconel® 625 fabricated by AM is not understood. Recently, Khayat and Palmer [17] found that differences in the Fe composition at the extremes of the Inconel® 625 specification [18] produced strikingly different grain sizes and tensile properties in structures fabricated using a powder based DED-L process, as described in Figure 6.2. Although different precipitate morphologies were observed, the underlying quantitative connections between chemical composition and secondary phases were not studied.

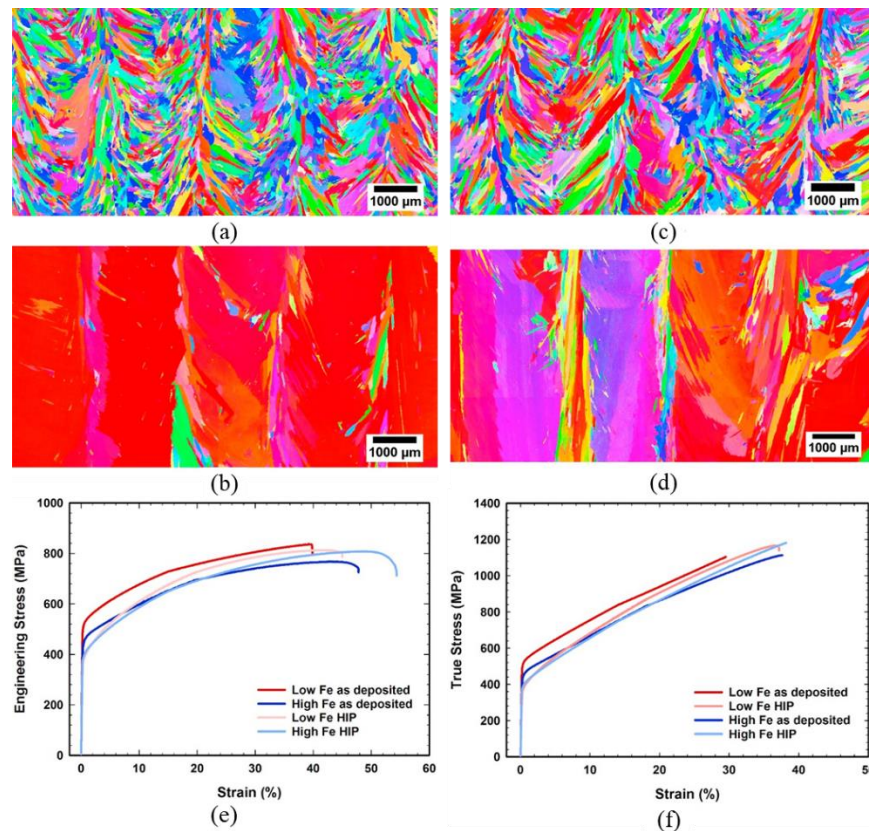


Figure 6.2. Small variations in chemistry can lead to significant differences in grain structures in as-deposited (a) low Fe and (b) high Fe Inconel® 625 and the corresponding grain structures after HIP in the (c) low Fe and (d) high Fe materials. Consequently, uniaxial tension tests and resulting (e) engineering and (f) true stress-strain curves for each material and condition show significant differences in material properties. Reprinted with permission from Elsevier.

This chapter<sup>4</sup> builds on the previous work of Khayat and Palmer [17] to understand the impact of chemical composition on precipitate morphology in additively manufactured Inconel® 625 materials. The segregation of alloying elements and secondary phases in these materials are characterized in greater detail using electron microscopy techniques. Measured partition coefficients of alloying elements are used to describe the differences in local chemical composition in regions where precipitates were located. A computational thermodynamic approach is utilized to probe the effects of small changes in the concentration of minor alloying elements on precipitate formation. In both alloys, a complex interplay of Fe, Si, and Ti drive the formation of different precipitate types and morphologies. The unexpected presence of some precipitates after hot isostatic are explained through equilibrium thermodynamic calculations. The results in this chapter are useful for tailoring chemical composition to provide control over the amount and type of precipitates in additively manufactured nickel base superalloys.

## 6.2 Materials and methods

Two nitrogen atomized Inconel® 625 powders (Carpenter Powder Products, Inc) with chemical compositions summarized in Table 6.1 were previously used as powder feedstocks to evaluate the impact of Fe composition (low vs. high) on the structure and properties of AM fabricated Inconel® 625. The powders were sieved to a size range between 53 and 125  $\mu\text{m}$  in diameter, and a laser-based DED system was used to deposit four L-shaped walls measuring approximately 100 mm in height and 13 mm in width on wrought Inconel® 625 plates with dimensions of 150 mm x 150 mm x 13 mm. Two builds were fabricated with the low Fe powder and the remaining with the high Fe powder using a laser power of 2000 W, a scanning speed of 10.6 mm/s, a mass flow rate of 0.23-0.27 g/s, and a beam diameter of approximately 4 mm. One of the L-shaped deposits fabricated from each material underwent a standard HIP treatment at a temperature of  $1163 \pm 25$  °C and a pressure of 101 MPa for 14400 seconds (Bodycote, Andover, MA). More information on the experimental setup and equipment details can be found elsewhere [17].

---

<sup>4</sup> Portions of this chapter are reproduced from J.S. Zuback, P. Moradifar, Z. Khayat, N. Alem, T.A. Palmer, ‘Impact of chemical composition on precipitate morphology in an additively manufactured nickel base superalloy’, *J. Alloy Comp.*, 798 (2019) 446-457

Using the chemical composition of each alloy, thermodynamic and kinetic calculations were performed using the JMatPro® V8 software with the Ni-superalloy database [19]. The software employs the calculation of phase diagram (CALPHAD) technique [20] to parameterize the Gibbs energy function for each individual phase using various multicomponent sublattice models. Initial chemical compositions of the bulk alloys, given in Table 6.1, were used as inputs. Phase equilibria in both the as-deposited and HIP conditions were investigated through equilibrium and Scheil solidification calculations. All available phases in the thermodynamic database were considered in calculations, unless noted otherwise.

*Table 6.1. Chemical composition (wt%) of Inconel® 625 powder feedstock.*

Material	Ni	Cr	Fe	Mn	Mo	Nb	Si	Ti	C
Low Fe	64.8	21.0	1.02	0.31	8.73	3.43	0.37	0.019	0.008
High Fe	61.3	21.3	4.34	0.01	8.70	3.83	0.035	0.19	0.005

Metallographic specimens for microstructure examination were extracted along an orientation parallel to the build direction at a location approximately 60 mm above the substrate. Each specimen was mounted in epoxy for metallurgical characterization and prepared by first grinding with a series of silicon carbide media followed by polishing sequentially with 3 µm and 1 µm polycrystalline diamond suspensions. A mirror finish was achieved via polishing with 0.05 µm colloidal silica for approximately 10 minutes. Selected samples were electrolytically etched in a 10% oxalic acid solution at a potential of 2 V for approximately 2 s for optical microscopy. A Nikon Epiphot camera was used to capture the solidification structure and precipitate distributions in the as-deposited and HIP conditions for both compositions. Scanning electron microscopy (SEM) was used to examine elemental segregation through a series of quantitative line scans using a FEI Helios NanoLab 660 FEG-SEM coupled with an Oxford Instruments X-Max X-ray energy dispersive spectroscopy (XEDS) detector.

Additional specimens for transmission electron microscopy (TEM) characterization were extracted from these same build locations using a FEI Helios 660 focused ion beam (FIB) and thinned to a thickness of approximately 70-80 nm (FIB lamella). An FEI Talos F200X TEM was operated at an accelerating voltage of 200 kV for high angle annular dark field scanning TEM (HAADF-STEM) imaging. Elemental compositions of precipitates were obtained using a superX-XEDS detector using both composition maps and line scans. Qualitative composition maps and

quantitative precipitate compositions were analyzed using ESPRIT software (Bruker Nano GmbH, Berlin, Germany). Approximately 50 precipitates were analyzed in total and the results presented are chosen to be representative.

### 6.3 Solidification structure and segregation behavior

Secondary phases tend to form in the interdendritic regions as a result of the segregation of alloying elements during solidification. Understanding variations in the local composition in Inconel® 625 materials can provide insight into the observed differences in precipitate morphologies. In Figure 6.3 (a) and (b), XEDS line scans are shown for the major alloying elements across multiple dendrites in the as-deposited low and high Fe materials, respectively. Regions between dendrites are enriched in Mo and Nb, while the dendrite cores are depleted in these same elements but enriched in Ni, Cr, and Fe. The measured chemical compositions (in wt%) for Ni, Fe, Cr, Mo, and Nb in the dendrite core ( $C_{core}$ ), interdendritic regions ( $C_{ID}$ ), and alloy ( $C_{avg}$ ), are extracted from the XEDS line scans taken across multiple dendrites and summarized in Table 6.2. At selected locations in the interdendritic regions, the degree of Mo and Nb enrichment reached maximum values that fall outside the allowable composition ranges, matching observations during fusion welding [11, 21] and PBF AM [22] of Inconel® 625.

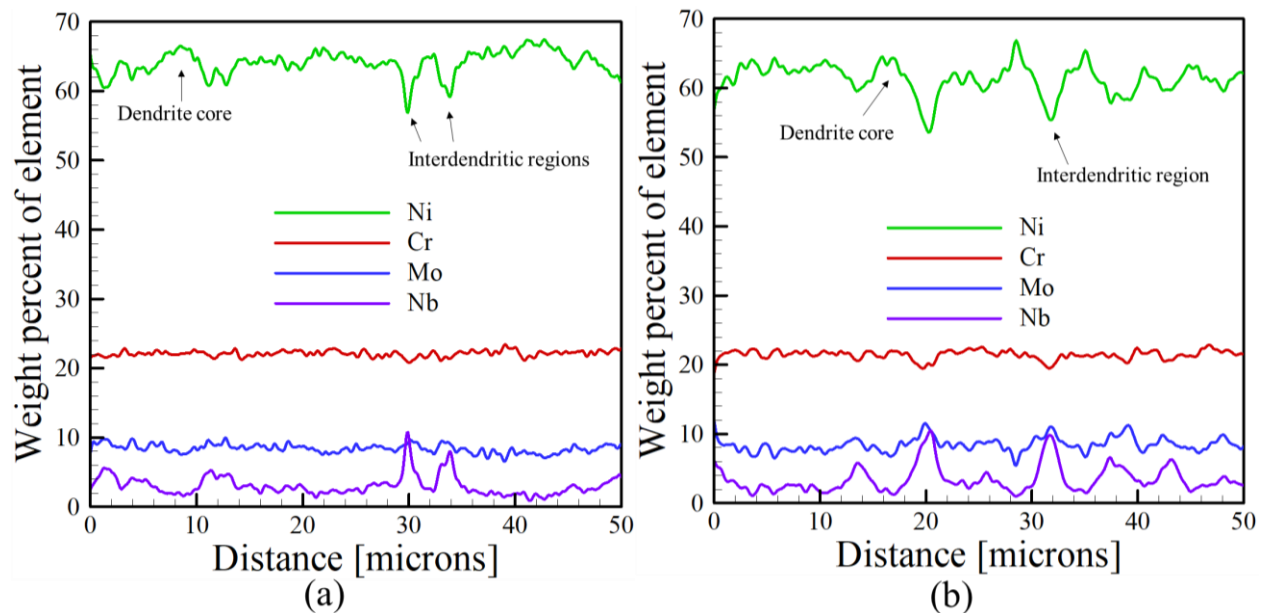


Figure 6.3. The measured chemical compositions in XEDS line scans across multiple dendrites in the as-deposited (a) low Fe and (b) high Fe Inconel® 625 show the spatial enrichment and depletion of alloying elements.

Table 6.2. A comparison between measured and predicted chemical compositions (wt %) of the dendrite core ( $C_{core}$ ), interdendritic region ( $C_{ID}$ ), initial alloy composition ( $C_{avg}$ ) or instantaneous liquid composition ( $C_L$ ), and partition coefficients ( $k_i$ ) during solidification for low and high Fe Inconel® 625.

Element	Measured				Simulated			
Low Fe Inconel® 625	$C_{core}$	$C_{ID}$	$C_{avg}$	$k_i$	$C_{core}$	$C_{ID}$	$C_L$	$k_i$
Ni	67.3	60.6	64.1	1.05	68.9	58.4	65.1	1.06
Fe	0.93	0.82	0.90	1.03	1.34	0.48	1.02	1.31
Cr	22.2	21.6	22.1	1.00	21.51	17.29	21	1.02
Mo	8.1	10.7	8.27	0.90	6.92	12.32	8.73	0.79
Nb	2.33	8.77	3.27	0.71	0.99	10.29	3.43	0.29
Si	-	-	-	-	0.25	0.61	0.37	0.68
Ti	-	-	-	-	0.011	~0	0.019	0.58
High Fe Inconel® 625	$C_{core}$	$C_{ID}$	$C_{avg}$	$k_i$	$C_{core}$	$C_{ID}$	$C_L$	$k_i$
Ni	67.4	58.3	61.8	1.09	64.8	55.6	61.6	1.05
Fe	4.40	3.70	4.12	1.07	5.52	2.07	4.35	1.27
Cr	21.8	20.7	21.5	1.01	21.9	15.9	21.3	1.03
Mo	6.99	11.6	8.22	0.85	6.67	12.27	8.71	0.77
Nb	1.64	8.72	3.25	0.51	0.97	13.78	3.83	0.25
Si	-	-	-	-	0.021	0.067	0.035	0.60
Ti	-	-	-	-	0.050	0.074	0.096	0.52

The ability to predict segregation levels is important for understanding the connection between elemental segregation and the observed differences in precipitate morphology. The segregation of an alloying element ( $i$ ) at a specific temperature during solidification can be assessed by the Scheil equation [23]:

$$C_{s,i} = k_i C_{0,i} (1 - f_s)^{k_i - 1} \quad (6.1)$$

where  $C_{s,i}$  is the composition of the solid at the solidifying interface,  $C_{0,i}$  is the initial alloy concentration,  $f_s$  is the fraction of the solid, and  $k_i$  is the partition coefficient of element  $i$  defined

as the ratio of the solid composition ( $C_{s,i}$ ) to the liquid composition ( $C_{l,i}$ ). The Scheil formulation relies on the following assumptions:

- Diffusion of alloying elements in the liquid phase is infinitely fast. This implies that the chemical composition of the liquid is homogeneous and changes only as a function of temperature.
- No diffusion occurs in solid phases during solidification and these phases can be thought of as ‘frozen’. In other words, there is no transport of alloying elements away from a solid phase once solidified.
- Thermodynamic equilibrium exists at the solid/liquid interface, which allows for equilibrium phase compositions and fractions calculations at a specific temperature to be valid.

At the start of solidification ( $f_s \approx 0$ ), the partition coefficient can be expressed as:

$$k_i = \frac{C_{s,i}}{C_{l,i}} = \frac{C_{s,i}}{C_{0,i}} \quad (6.2)$$

The partition coefficient in Equation (6.2) serves as a metric to experimentally compare the degree of segregation for each element. When  $k$  is approximately equal to unity, the alloying element concentration across the dendrites in the solidification structure remains nearly uniform. Alloying elements that partition to the interdendritic regions, which are the last to solidify, have partition coefficients less than unity, while elements with coefficients greater than unity are soluble in the matrix and are among the first to solidify.

The partition coefficients for Ni, Fe, Cr, Mo, and Nb in each material were calculated using the  $C_{core}$  and  $C_{avg}$  values obtained from the XEDS measurements and are shown in Table 6.2. Although most elements have similar calculated partition coefficients when comparing materials, the  $k_{Nb}$  values show significant differences. The measured values indicate that, under similar processing conditions, the segregation of Nb to the interdendritic regions is more pronounced in the high Fe material than the low Fe material. Since  $C_{avg}$  for Nb is similar for both alloys, this difference arises from the measured  $C_{core}$  values, which were approximately 2.33 and 1.64 wt% Nb for the low and high Fe Inconel® 625 materials, respectively.

The composition of the liquid ( $C_L$ ) at the beginning of solidification can be determined in Scheil simulations and therefore is used to calculate  $k_i$  values according to Equation (6.2). The changes in the predicted partition coefficients in, owing to the differences in chemical composition between the low and high Fe Inconel® 625, are insignificant. However, the differences in the amounts of solute segregating to the interdendritic regions ( $C_{ID}$ ), where precipitates are observed, are pronounced for Fe and Si. In the low Fe Inconel® 625, the amount of Si ( $C_{ID} = 0.61$  wt%) is an order of magnitude higher than that predicted in the high Fe material ( $C_{ID} = 0.067$  wt%). Also, the interdendritic Fe composition in the low Fe material (0.48 wt%) is about four times lower than that in the high Fe material (2.07 wt%). Since Ti is consumed by nitrides during solidification, which will be discussed later, the Ti concentration in the interdendritic regions is negligible in both materials. These differences in the interdendritic composition are driven by the variations of the initial alloy composition leading to the different observed precipitate morphologies.

#### **6.4 Precipitate characterization in as-deposited condition**

In AM processes, the as-deposited solidification structures depend on processing conditions that affect the temperature gradient and velocity of the solid/liquid interface [24, 25]. In general, the relatively large molten pools and low scanning speeds prevalent in DED processes lead to low temperature gradients and slow solidification velocities which favor the formation of columnar dendritic solidification structures [8]. In both the low and high Fe Inconel® 625 materials, shown in Figure 6.4 (a) and (b), respectively, columnar dendritic solidification structures comprised of elongated primary dendrites and smaller secondary dendrite arms were prevalent. The measured secondary dendrite arm spacings, which can be correlated to cooling rates during solidification [25, 26], were  $4.43 \pm 0.22$   $\mu\text{m}$  in the low Fe and  $4.12 \pm 0.38$   $\mu\text{m}$  in the high Fe Inconel® 625. The negligible differences observed in the scale of solidification structures between the two Inconel® 625 materials indicate that both materials experienced roughly similar thermal histories. Secondary phase precipitates, which are shown as dark particles after etching in Figure 6.4, are present primarily in the interdendritic regions in both materials.

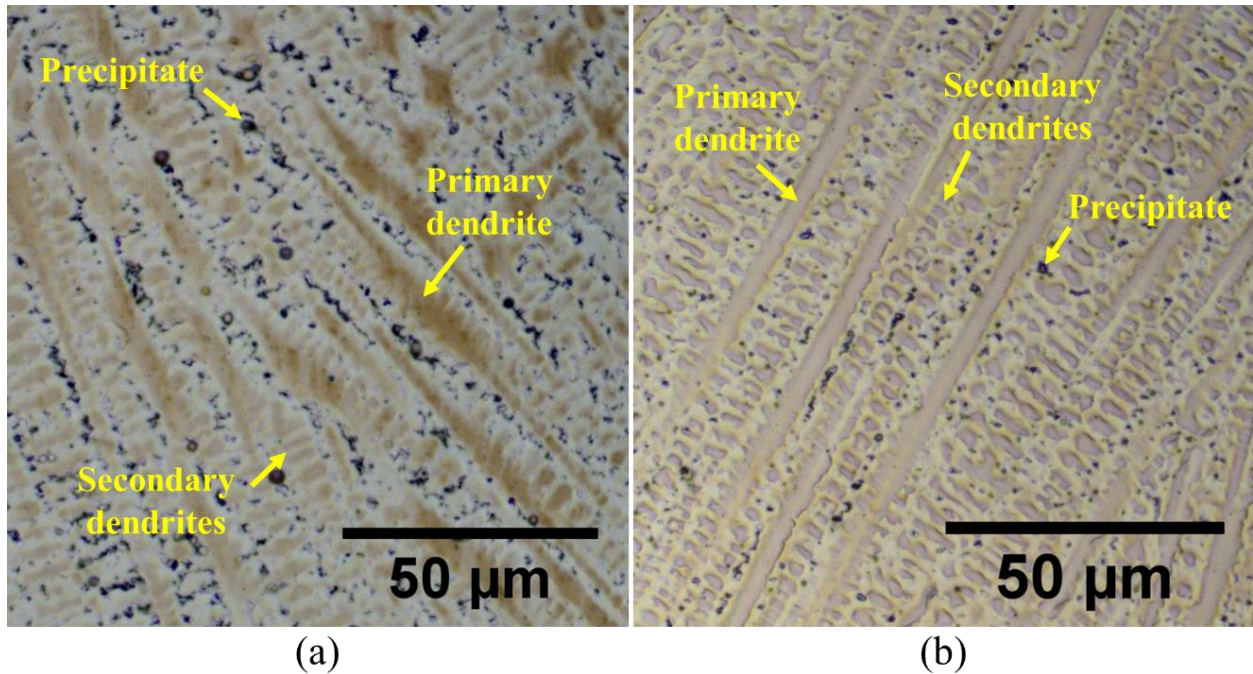
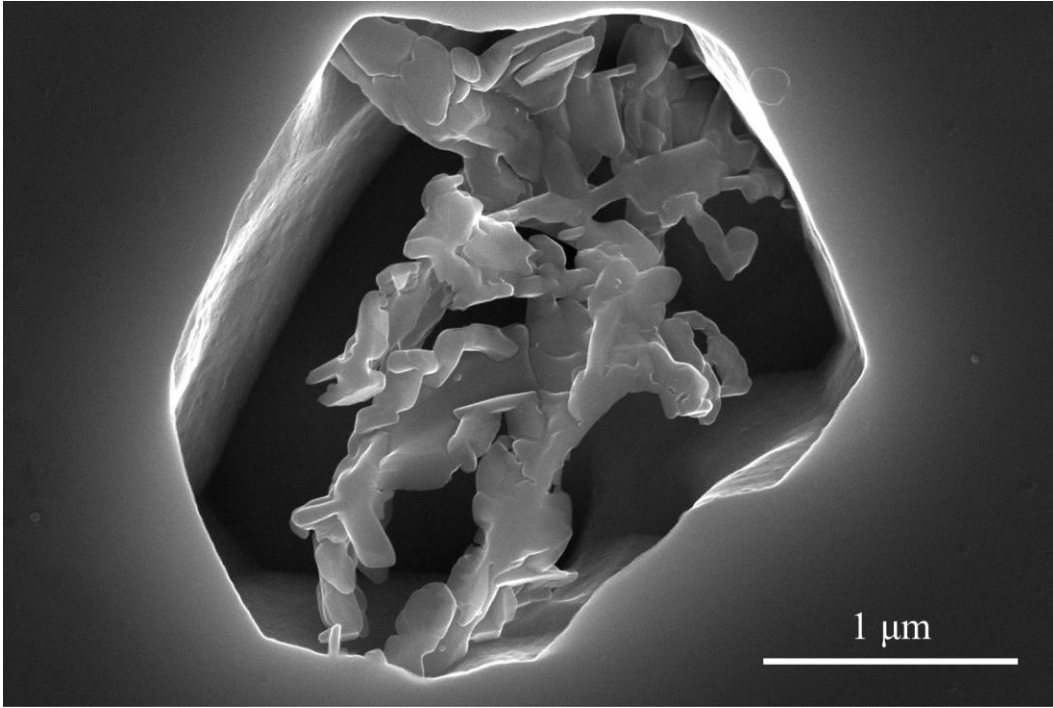


Figure 6.4. The optical micrographs of as-deposited (a) low Fe and (b) high Fe Inconel® 625 show the columnar dendritic solidification structures and secondary phase precipitates in interdendritic regions.

Although similarities were observed in solidification structure and secondary phase distribution, the differences in precipitate morphology for the two compositions were pronounced. The precipitates in the as-deposited low Fe Inconel® 625 exhibited a relatively large, irregular shape that formed elongated chains of particles in the interdendritic regions, as shown in Figure 6.5. A more detailed high magnification HAADF-STEM image of a characteristic secondary phase in the low Fe Inconel® 625 is shown in Figure 6.6, which formed around a small oxide inclusion. These oxides commonly observed in microstructures produced with gas atomized powder feedstocks [27]. The corresponding composition maps of the secondary phases in Figure 6.6 show that the precipitate is enriched in Mo, Nb, and Si and depleted in Ni, Fe, and Cr. The average chemical compositions measured in multiple secondary phases in the alloy presented in Table 6.3 are characteristic of Laves phase reported in both welding [28] and AM [29] studies of Inconel® 625. The irregular morphology of the Laves phase is derived from a eutectic-like transformation occurring near the end of solidification where the remaining liquid in the interdendritic regions transforms to a combination of an enriched  $\gamma$  matrix and Laves phase.



*Figure 6.5. Laves phase in Inconel® 625 exhibits an irregular morphology derived from a eutectic transformation near the end of solidification, such as the cluster shown in as-deposited low Fe Inconel® 625.*

In contrast, no Laves phase was found in the as-deposited high Fe Inconel® 625, and a different precipitate morphology is prominent, as shown in Figure 6.7. The particles in the high Fe material are rich in both Nb and Ti, with compositions characteristic of MN nitrides. Generally, the composition of MX type precipitates, where M is a metallic element and X signifies carbon or nitrogen, are dominated by Nb and C in Inconel® 625 alloys [11, 21]. However, the high Ti concentration in the powder feedstock alters the composition of these nitrides, which became more enriched in Ti. In fact, Ti constitutes a larger fraction, by weight, than Nb in the nitrides, as shown in Table 6.3. Complex carbonitrides of the (Nb,Ti)(C,N) type have been found in Inconel® 625 weld overlays [30] and compositional fluctuations have been shown to arise from the formation of Nb-rich shells forming around Ti-rich nitrides during solidification.

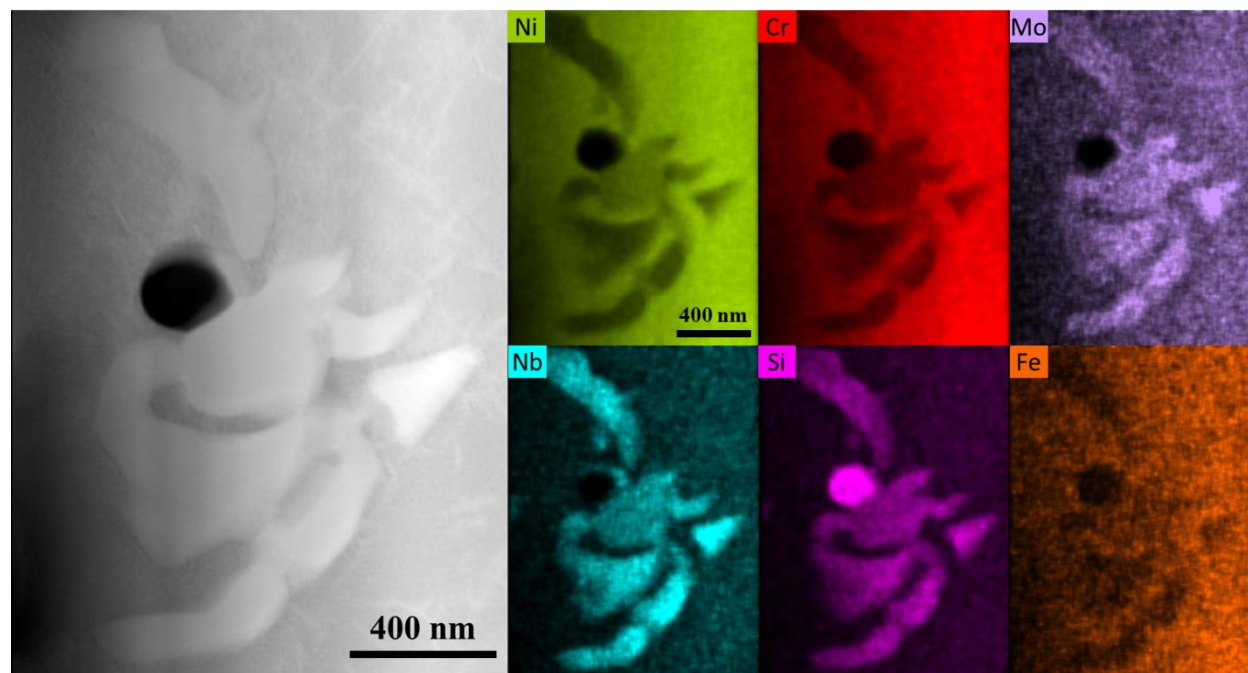


Figure 6.6. HAADF-STEM micrograph of the precipitate morphology in the as-deposited low Fe sample along with the corresponding XEDS maps of Ni, Cr, Mo, Si, Nb and N.

Table 6.3. Comparison between the average measured chemical compositions (wt%) of secondary phases in Inconel® 625.

Material	Condition	Phase	Ni	Cr	Fe	Mo	Nb	Si	Ti
LowFe	As-deposited	Laves	39.0	14.0	0.59	16.2	24.6	2.81	0.24
LowFe	HIP	Laves	34.3	14.8	0.58	18.4	25.8	2.51	0.23
LowFe	HIP	M <sub>2</sub> N	2.38	21.9	0.27	21.0	50.1	0.42	0.19
HighFe	As-deposited	MN	28.3	12.4	2.61	3.42	20.6	0.15	26.3
HighFe	HIP	MN	21.5	8.92	2.54	3.73	16.4	0.25	35.9

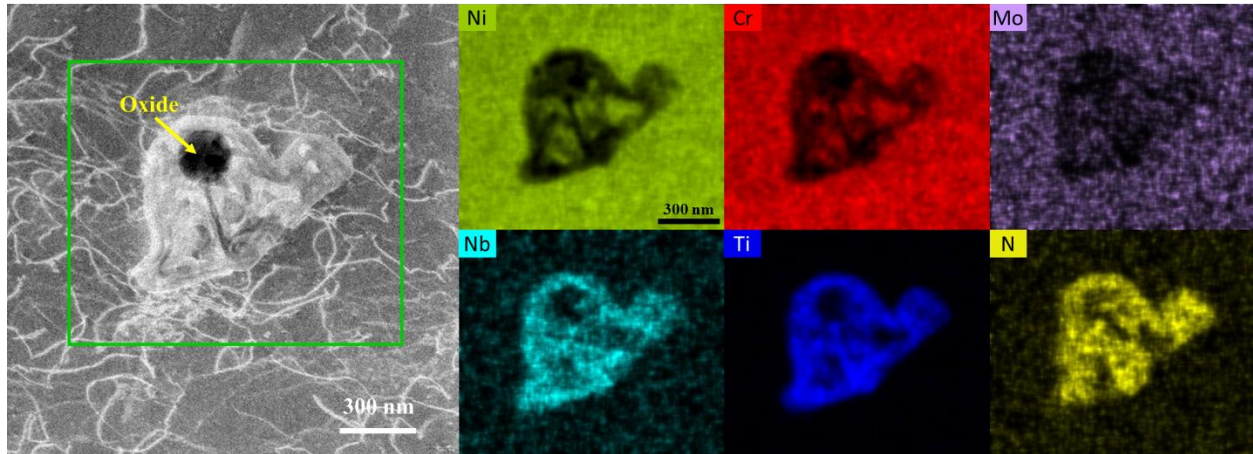


Figure 6.7. HAADF-STEM micrograph showing the precipitate morphology in the as-deposited high Fe Inconel® 625 sample along XEDS maps corresponding to the enclosed area showing enrichment in Ti, Nb, and N and depletion in Ni, Cr, and Mo.

### 6.5 Predicting precipitate morphology from chemical composition

The variations in alloy composition for the Inconel® 625 materials lead to changes in the predicted secondary phase formation during solidification under Scheil conditions. Figure 6.8(a) and (b) show the volume fraction of solidified phases as a function of temperature for the low and high Fe Inconel® 625 materials, respectively. The largest differences are observed in the volume fractions of Laves phase and the temperature at which the MN nitride forms. The low Fe Inconel® 625 material displays a Laves volume fraction ( $\sim 1.0 \times 10^{-2}$ ) that is an order of magnitude greater than that predicted in the high Fe Inconel® 625 material ( $\sim 7.8 \times 10^{-4}$ ). The temperature at which Laves phase forms is also suppressed by roughly  $16^\circ\text{C}$  in the high Fe Inconel® 625 when compared to the low Fe material.

The differences in nitride formation in the two materials are pronounced. The nitrides form by a eutectic reaction ( $L \rightarrow \gamma + MN$ ) in the low Fe Inconel® 625 at a temperature of approximately  $1295^\circ\text{C}$ . In contrast, the same nitride forms in the liquid phase in the high Fe Inconel® 625 material. The increased stability of the nitride in the high Fe material is due to the increase in Ti, which is a well-known nitride former [28, 30]. The formation of nitrides is also supported, in part, by the measured Nb partition coefficient. At the beginning of solidification, calculations indicate that all available Nb is present in the low Fe Inconel® 625 liquid. However, the formation of nitrides in the high Fe Inconel® 625 liquid consumes some Nb, lowering the amount of Nb in the dendrite core and thus decreases  $k_{Nb}$ .

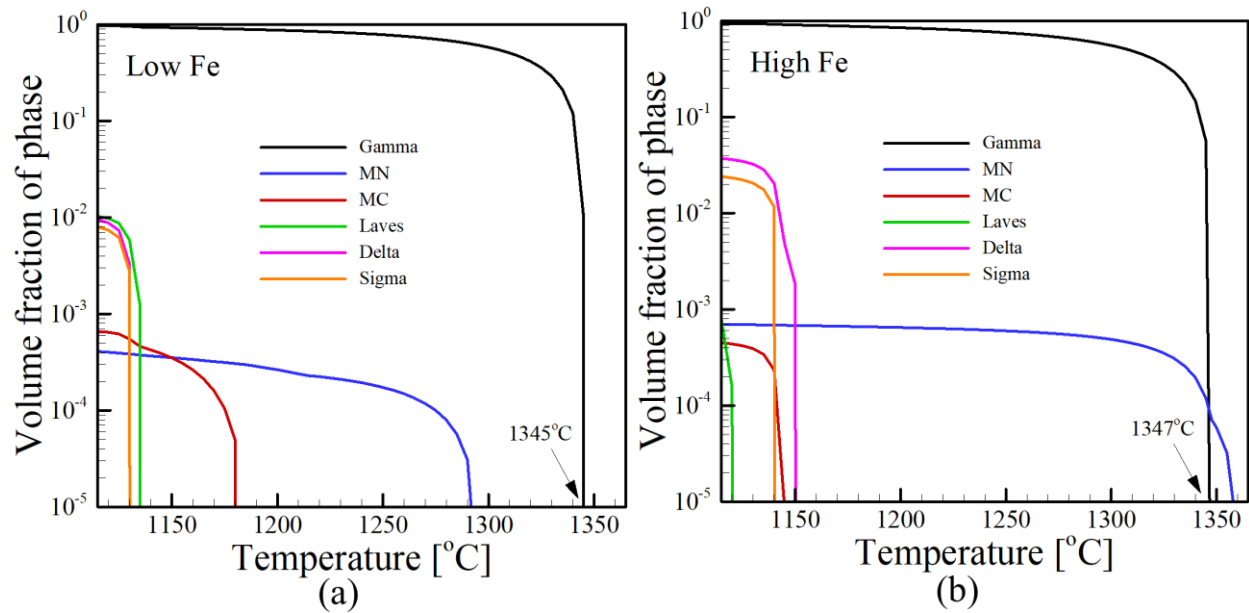


Figure 6.8. Significant differences in the fractions of secondary phases as a function of temperature are predicted for the (a) low Fe and (b) high Fe Inconel® 625 during Scheil solidification.

Although Figure 6.8 shows that variations in Fe, Si, and Ti indeed affect precipitate morphology, it does not elucidate the complex interplay between these alloying elements and the resulting impact on precipitates formation. To investigate the effects of these minor alloying element additions on the formation of Laves phase, Scheil simulations were performed for Fe, Si, and Ti concentrations spanning the allowable ranges for each alloying element. Nominal compositions of Ni-0.2Al-21.5Cr-0.25Mn-9.0Mo-3.65Mo-0.01C-0.01N (in wt%) were used and kept constant for all calculations to account for the other alloying elements.

The contour plot in Figure 6.9 represents the volume fraction of Laves phase as a function of Fe and Si content in the initial alloy composition when no Ti is added. In all cases, Laves phase is not predicted to form in appreciable quantities until a Si composition of at least 0.05 wt% is reached. With this level of Si, the volume fraction of Laves phase increases with increasing Fe concentrations, which is consistent with the findings from DuPont et al. [31]. Although Ti has a negligible effect on the volume fraction of Laves phase, Ti additions can affect the temperature at which Laves phase forms, as shown in Figure 6.10. At low Si concentrations (~0.05 wt%), additions of 0.4 wt% Ti can suppress the Laves formation temperature by approximately 15-20°C compared to an alloy with no Ti. As more Si is added to the alloy, however, Ti has less influence and Si begins to dominate the Laves formation temperature.

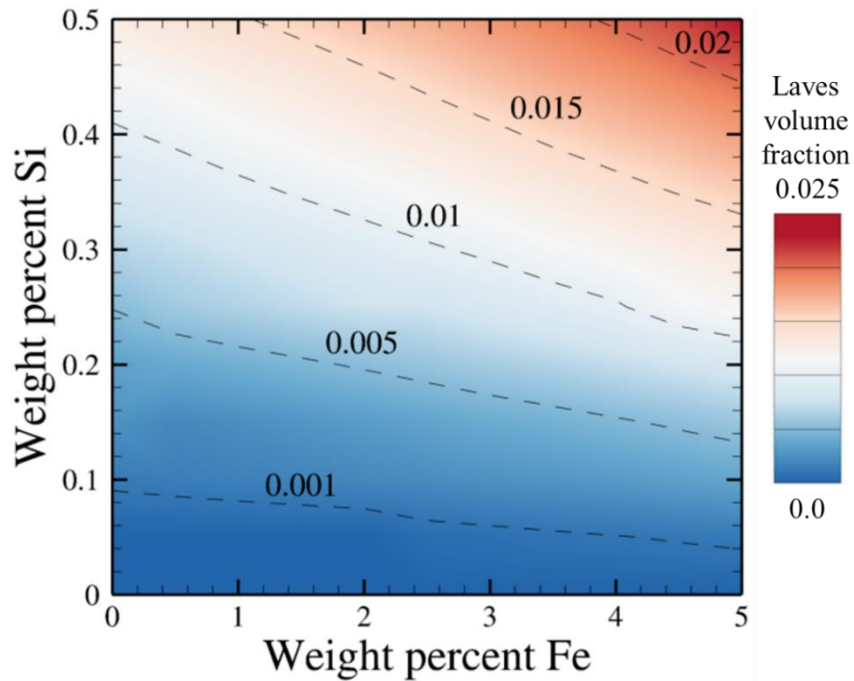


Figure 6.9. The Laves phase volume fraction under Scheil solidification conditions is influenced by the amount of Fe and Si in the alloy composition as shown by the contour plot. The dotted lines represent constant volume fractions with values indicated by labels.

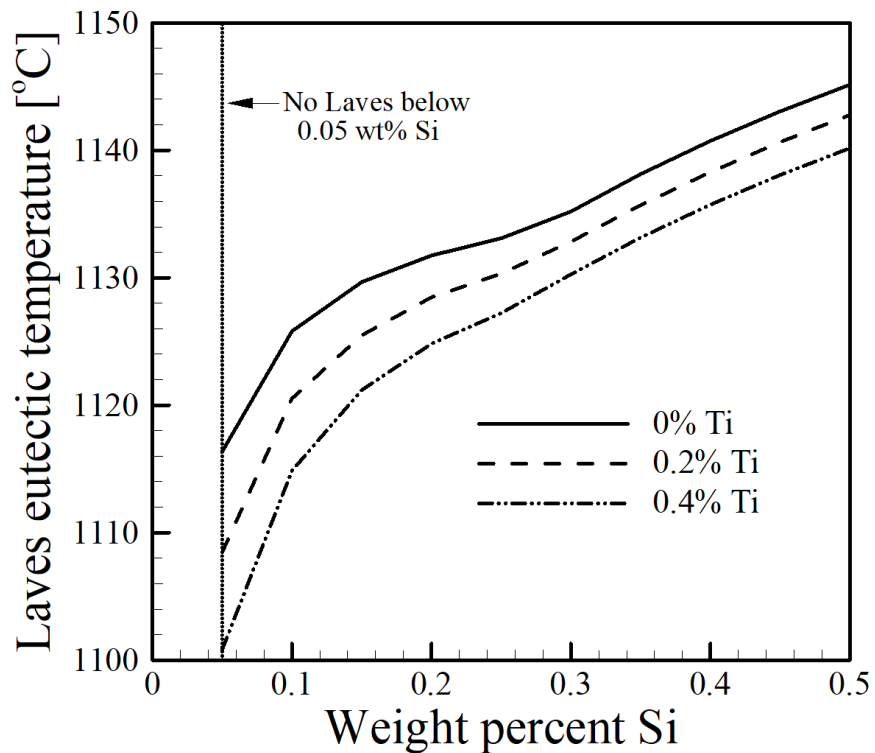


Figure 6.10. The effects of Si and Ti contents on the temperature at which Laves phase forms in Inconel® 625 with a constant Fe concentration of 2.5 wt%.

## 6.6 Effects of HIP on precipitate morphology

Although HIP is used primarily as a thermomechanical process to close internal voids, the high temperatures used in the process can also induce microstructural changes of the as-deposited material. Temperatures of approximately 1150-1200°C, similar to the HIP temperature of 1160°C, have been used as a solutionizing heat treatment for AM nickel base alloys [13, 29, 32-34]. At these temperatures, alloying elements can diffuse quickly and eliminate the concentration gradients formed during solidification in the as-deposited microstructure. The diffusion coefficients of various alloying elements in nickel are plotted as a function of temperature in Figure 6.11. Of all elements, Mo has the lowest diffusivity ( $9.5 \times 10^{-15} \text{ m}^2/\text{s}$ ) in Ni at the HIP temperature of 1160C.

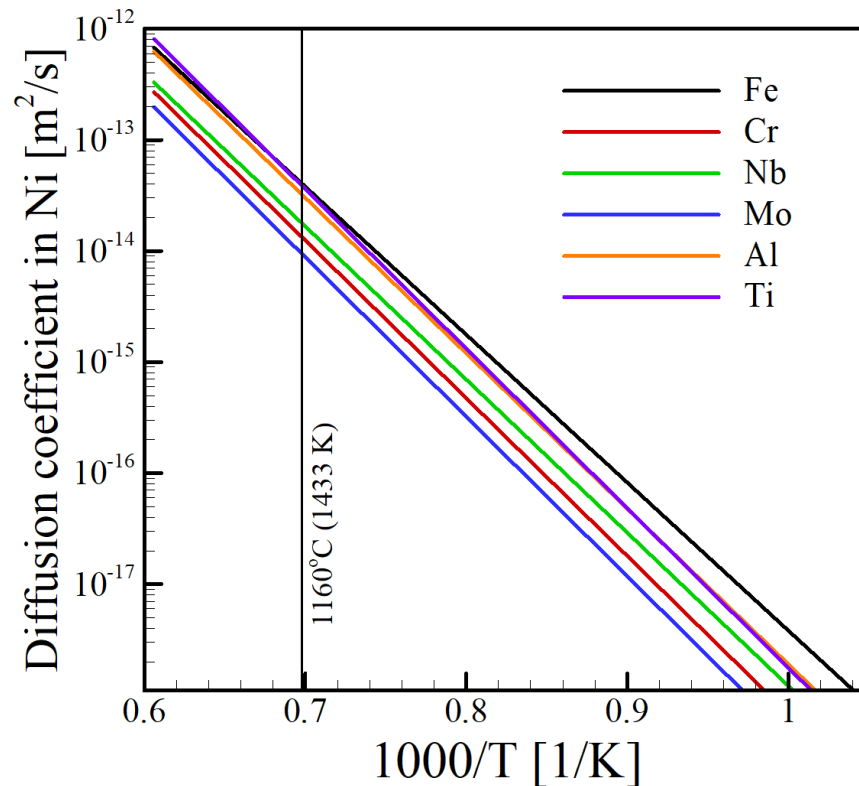


Figure 6.11. The binary diffusion coefficients [1] of various alloying elements in FCC nickel as a function of temperature.

To evaluate the homogenization behavior of the segregated Inconel® 625 matrix, the time needed to eliminate concentration gradients present from elemental segregation was calculated. A domain of  $2 \mu\text{m}$ , corresponding to half of the secondary dendrite arm width ( $\sim 4 \mu\text{m}$ ), was used to solve the one-dimensional diffusion equation. The concentration profiles of alloying elements

from Scheil solidification calculations were used as inputs, since they provide a conservative estimate of the segregation in the as-deposited material. The concentration profiles of Mo, the slowest diffusing element in Inconel® 625 at 1160°C, are plotted in Figure 6.12 as a function of distance and time. In both Inconel® 625 alloys, the concentration gradients of Mo are eliminated after just 180 seconds, indicating that the composition of the matrix phase in the alloy is quickly homogenized during HIP.

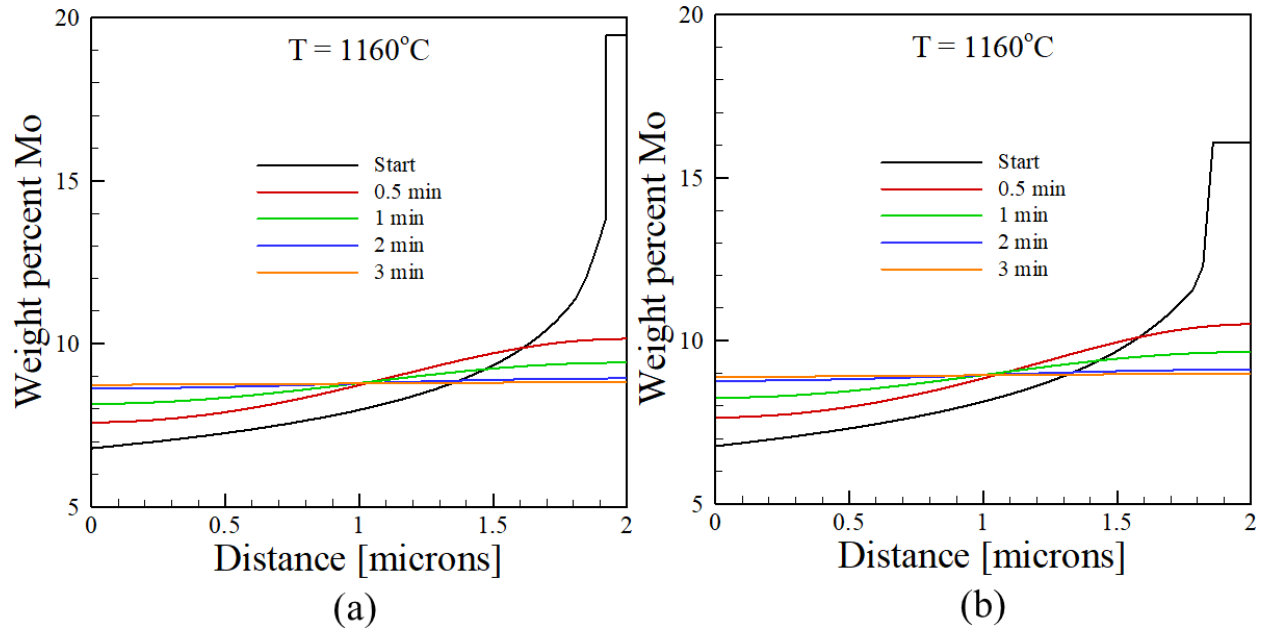
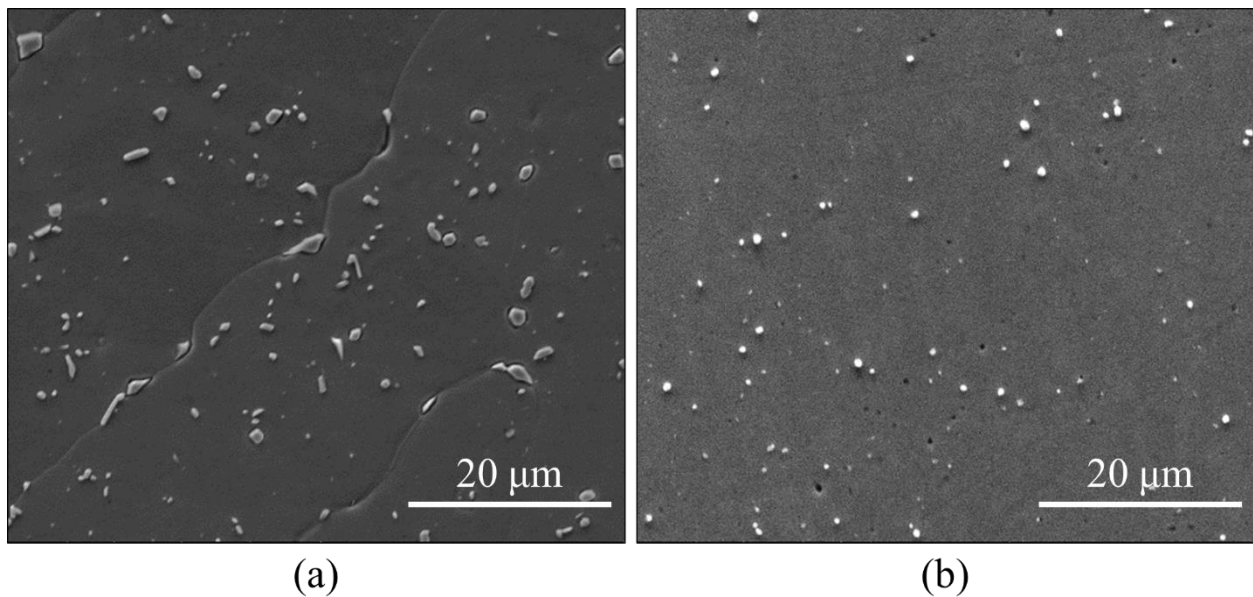


Figure 6.12. The calculated concentration profiles as a function of distance and time show that the spatial variation of Mo, the slowest diffusing element, quickly homogenizes in both the (a) low Fe and (b) high Fe Inconel® 625 at the HIP temperature (1160°C). The starting concentration profile is calculated from Scheil solidification and the domain corresponds to half a secondary dendrite.

Assuming that no nucleation occurs during the initial 180 seconds of homogenization, further equilibrium calculations can be performed to investigate secondary phase stability. When using the initial compositions for both alloys, only a small fraction (~0.03) of MN is predicted to be in equilibrium with the matrix at a temperature of 1160°C. However, a distinct difference in chemical compositions of the MN phase between the two materials is calculated at equilibrium. In the low Fe Inconel® 625, the Ti to Nb composition ratio in the MN phase is approximately 3.0 (58.36Ti-19.39Nb) and rises to a level of approximately 24.2 (74.51Ti-3.08Nb) in the high Fe material. These differences are largely due to the variations in Ti concentration, with the high Fe material containing an order of magnitude more Ti.

The precipitate dispersions throughout the  $\gamma$  matrix in the low and high Fe materials are shown in Figure 6.13(a) and (b), respectively. In the low Fe material, secondary phases were distributed along grain boundaries as well as within the grains. The average precipitate size after HIP was  $1.36 \pm 0.12 \mu\text{m}$ , which is nearly twice the size of the precipitates observed in the as-deposited condition ( $0.88 \pm 0.21 \mu\text{m}$ ). In contrast, the secondary phases in the high Fe Inconel® 625 showed no tendency to locate near grain boundaries and were uniformly distributed throughout the matrix. The average precipitate size ( $0.66 \pm 0.29 \mu\text{m}$ ) after HIP was similar to the average precipitate size in the as-deposited condition ( $0.56 \pm 0.08 \mu\text{m}$ ). Although the columnar dendritic solidification structure was eliminated after HIP, the precipitates showed a similar distribution to the as-deposited condition for both materials.



*Figure 6.13. Precipitate distribution in (a) low Fe and (b) high Fe Inconel® 625 after HIP at 1160C for 4 h.*

After HIP, the precipitates in the low Fe Inconel® 625 microstructure displayed significant deviations from the irregular Laves particles observed in the as-deposited condition. Many precipitates developed a blocky morphology with measured chemical compositions characteristic of a  $M_2N$  phase, as shown in Table 6.3. Figure 6.14 shows a discontinuous chain of these precipitates located at a grain boundary in the low Fe material. In other precipitates, such as those shown in Figure 6.15, the  $M_2N$  was found to coexist with Laves phase on a grain boundary, which has also been observed in as-deposited IN625 [35]. Although the Laves and  $M_2N$  phases share a similar hexagonal close packed crystal structure, the distinct differences in measured chemical

compositions in Table 6.3 were used to distinguish the two phases. The Si-rich Laves phase was found to be on the fringes or fully surround the  $M_2N$  nitrides. The regions characterized as Laves had compositions with significant amounts of Ni and Si nearly identical to the precipitates found in the as-deposited condition, while the  $M_2N$  phase contained only small amounts of Ni and Si. This finding is consistent with studies in welding of Inconel® 625 in which various types of carbides form without significant amounts of Si, while the Laves phase is enriched in Si [21]. The similarities in precipitate morphology indicate that  $M_2N$  nucleates and grows inside the Laves phase as a function of time, as some precipitates completely transformed (Figure 6.14) while others only partially transformed (Figure 6.15).

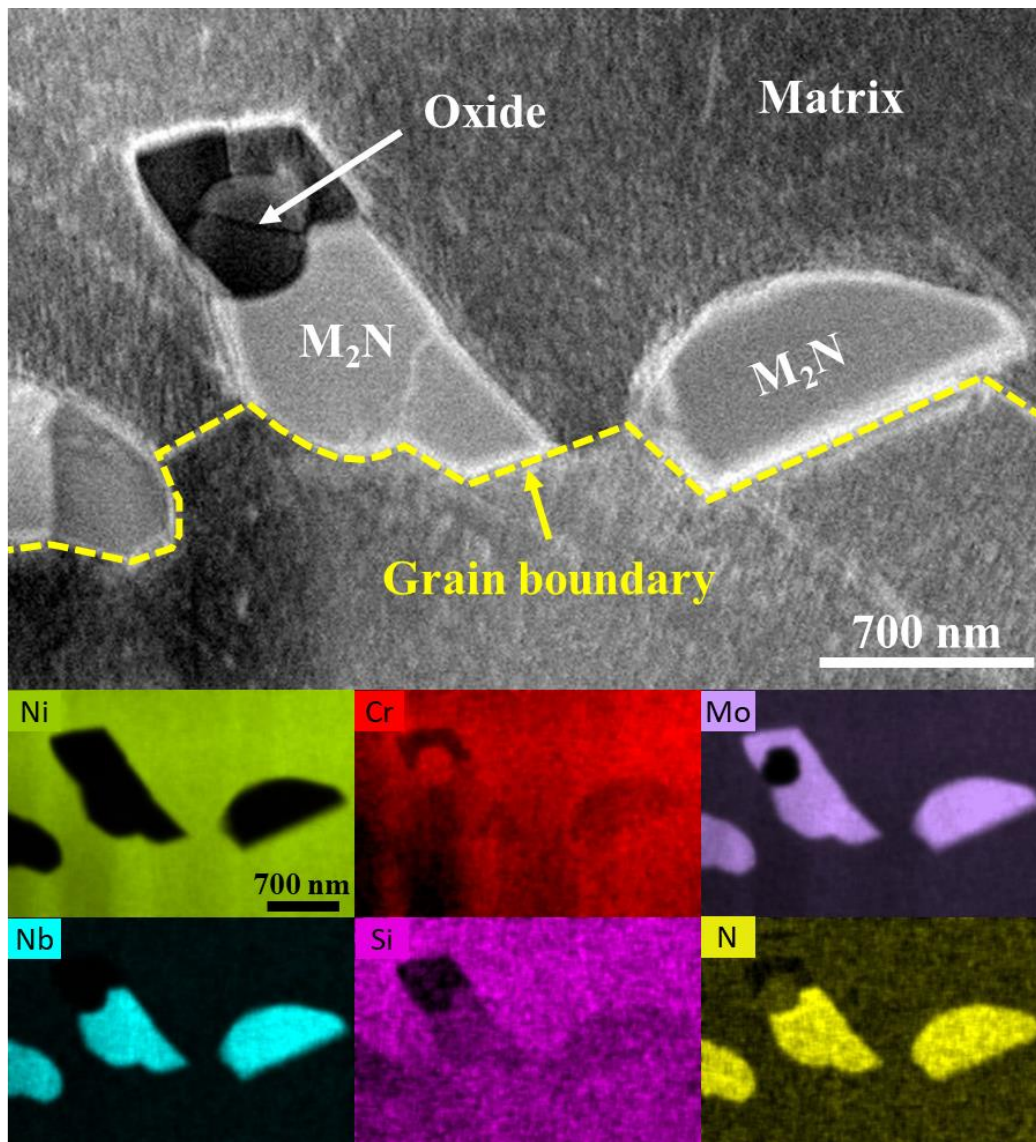


Figure 6.14. HAADF-STEM micrograph of precipitates rich in Mo, Nb, and N along a grain boundary in the low Fe Inconel® 625 sample after HIP.

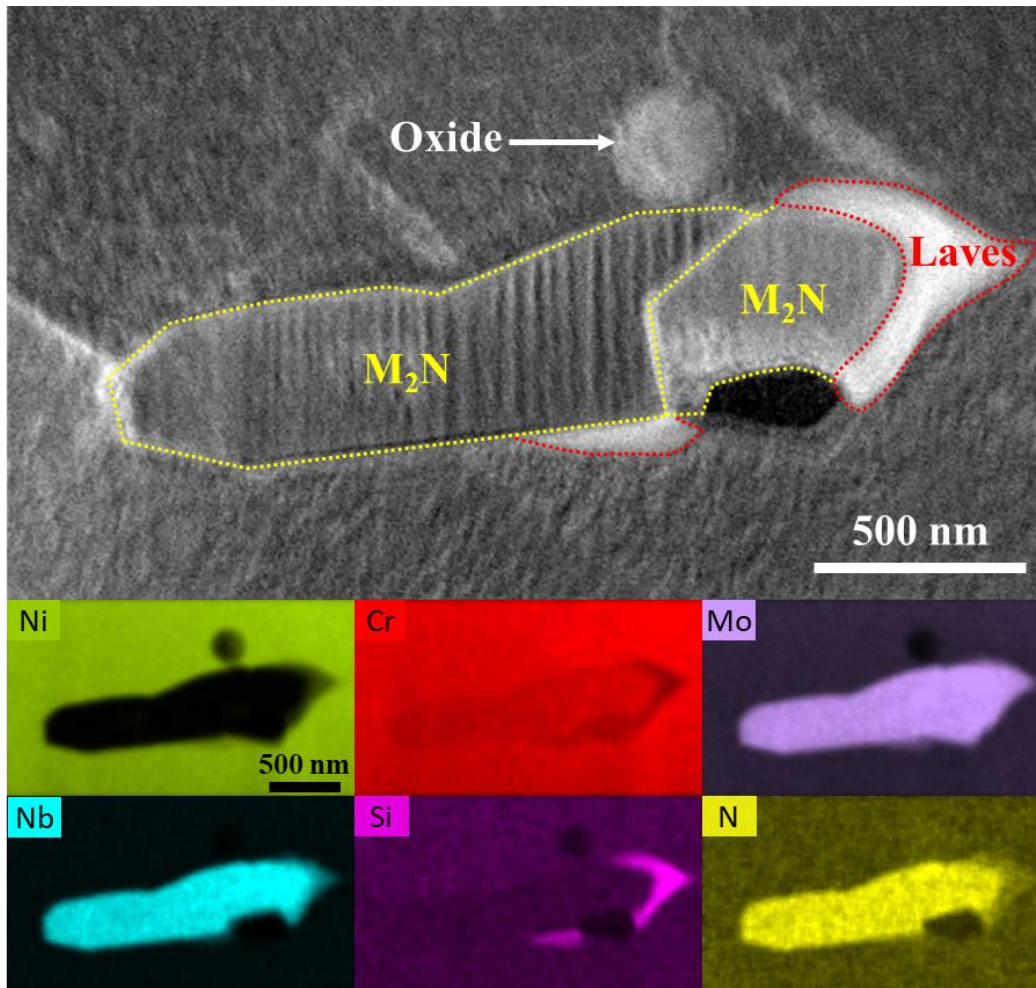


Figure 6.15. HAADF-STEM micrograph and corresponding XEDS composition maps showing the combination of  $M_2N$  and Laves precipitates at a grain boundary in the low Fe Inconel® 625 after HIP.

Since Laves phase is not an equilibrium phase at the HIP temperature for Inconel® 625 alloy compositions, it should theoretically dissolve into the  $\gamma$  matrix. However, local equilibrium may be achieved within a metastable phase by transformation to a more energetically favorable structure or composition. Using the average measured composition of the Laves phase as input, the equilibrium phase fractions, considering all available phases in the thermodynamic database, at the HIP temperature are shown in Figure 6.16(a). The Laves phase is at equilibrium in a substantial weight fraction of the compositions considered. Keller et al. [36] showed that along with the MC carbide,  $M_2(C,N)$  also has a high driving force for nucleation at 1150°C in an enriched interdendritic region. If MC precipitates are unable to form due to unfavorable conditions,

$M_2(C,N)$  is the next energetically favorable phase to form. When the  $M(C,N)$  phase is suspended in the calculations, Figure 6.16(b) shows that the  $M_2(C,N)$  phase is predicted to exist at equilibrium. Therefore, multiple secondary phases are predicted to be in equilibrium during HIP within a volume that was initially a Laves particle in the as-deposited condition, which supports experimental findings.

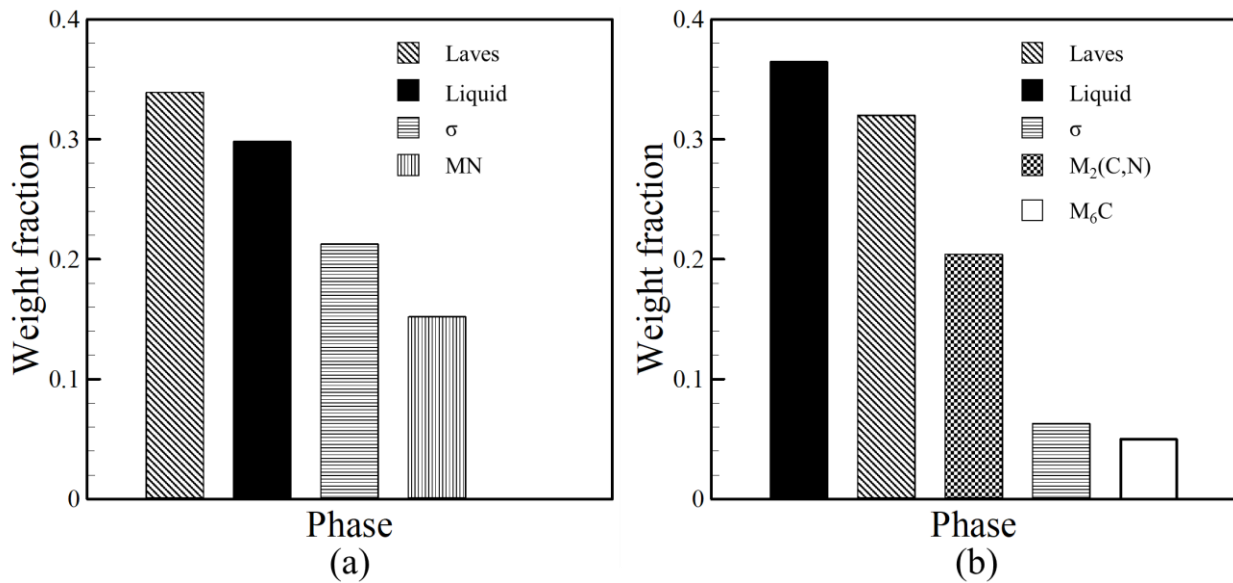
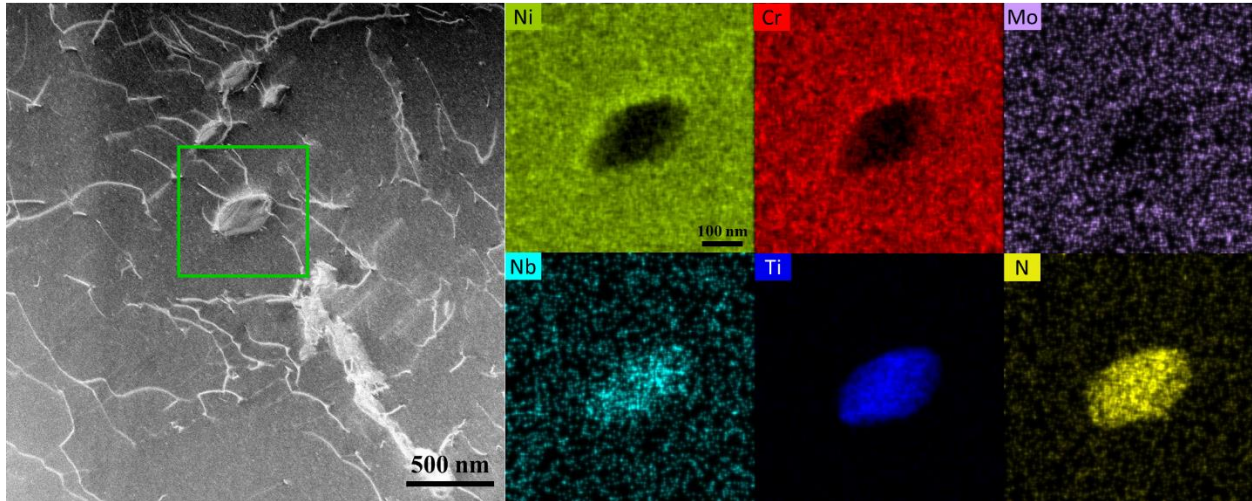


Figure 6.16. The calculated phase equilibria at 1160°C for a chemical composition corresponding to the measured Laves phase chemistry (a) considering all available phases in the Ni-superalloy database of JMatPro® V8 and (b) suspending the  $M(C,N)$  phase.

The presence of MN nitrides in the high Fe Inconel® 625 after HIP can be expected since this phase is stable at the HIP temperature. Consequently, the precipitates in the high Fe Inconel® 625 showed only minor changes in morphology and distribution throughout the alloy after HIP. Figure 6.17 shows a HAADF-STEM micrograph of nitrides in the high Fe material after HIP. Compared to the precipitates in the as-deposited material (Figure 6.7), the nitrides became slightly elliptical and were uniformly distributed throughout the sample. However, a noticeable change in composition of the nitrides was measured. As shown in Table 6.3, the nitrides became more enriched in Ti and depleted in Nb during HIP, and compositional variations within the precipitates were eliminated, as shown in the composition maps in Figure 6.17.



*Figure 6.17. HAADF-STEM micrograph of a Ti and Nb rich nitride in the high Fe Inconel® 625 sample after HIP.*

## 6.7 Summary and conclusions

Along with changes in the grain size, strength, ductility, and strain hardening response, small variations in chemical composition within the allowable limits of Inconel® 625 specifications have a pronounced effect on precipitate morphology. Laves phase was the prominent precipitate observed in the low iron material (1 wt%), while MN nitrides and no Laves phase were observed at high iron levels (4 wt%). Computational thermodynamic calculations coupled with an in-depth characterization of the individual precipitates has shown that a complex interplay between iron, silicon, and titanium drives the changes in the precipitates observed with different iron levels. Specifically, silicon contents in excess of 0.05 wt% are required to promote the formation of Laves phase, regardless of the iron level. On the other hand, increases in the titanium concentration suppress the formation of Laves phase and promote the precipitation of nitrides rich in titanium and niobium in the liquid phase. With hot isostatic post processing, the precipitate types and morphologies in both materials evolved. In the low iron material, the Laves phase originally in the as-deposited material partially transformed to a complex nitride rich in niobium, molybdenum, and chromium. In the high iron Inconel® 625, the nitrides remained similar in size to those present in the as-deposited condition but became more enriched in titanium and depleted in niobium. The following are the main conclusions:

- The segregation of alloying elements to interdendritic regions causes secondary phases to precipitate during solidification. Different precipitates were characterized in each Inconel®

625 alloy owing to the variations in chemical composition of the powder feedstock. The alloy with low iron content developed a microstructure dominated by continuous Laves phase particles while the high iron material contained only MN nitrides.

- The differences in secondary phases are linked to the silicon and titanium concentrations of the initial alloy compositions. High amounts of silicon (0.37 wt%) found in the low iron material promote the formation of Laves, while the silicon poor (0.035 wt%) and high iron alloy did not form any Laves phase.
- The high amounts of titanium (0.19 wt.%) in the high iron Inconel® 625 promote nitride formation in the liquid alloy before solidification. The measured composition of the nitride indicates that significant amounts of niobium were consumed from the liquid prior to solidification. This phenomenon is manifested in the measured niobium partition coefficient ( $k_{Nb} = 0.51$ ), which is significantly lower than that measured in the low iron material ( $k_{Nb} = 0.71$ ) where precipitates form near the end of solidification.
- After HIP, precipitates in both materials remain but change in type, composition and morphology. The Laves phase in the low Fe alloy developed a blocky morphology and partially transformed to a nitride rich in niobium, chromium, and molybdenum after HIP. While the size and distribution of the nitrides in the high Fe material did not change, the composition became more enriched in Ti and depleted in Nb.

## 6.8 References

- [1] J.N. DuPont, J.C. Lippold, S.D. Kiser, *Welding metallurgy and weldability of nickel-base alloys*, John Wiley & Sons, 2011.
- [2] K. Shah, I. ul Haq, A. Khan, S.A. Shah, M. Khan, A.J. Pinkerton, Parametric study of development of Inconel-steel functionally graded materials by laser direct metal deposition, *Mater. Des.*, 54 (2014) 531-538.
- [3] D. Wu, X. Liang, Q. Li, L. Jiang, *Laser Rapid Manufacturing of Stainless Steel 316L/Inconel718 Functionally Graded Materials: Microstructure Evolution and Mechanical Properties*, *International Journal of Optics*, 2010 (2010) 802385.
- [4] B.E. Carroll, R.A. Otis, J.P. Borgonia, J.-o. Suh, R.P. Dillon, A.A. Shapiro, D.C. Hofmann, Z.-K. Liu, A.M. Beese, Functionally graded material of 304L stainless steel and inconel 625 fabricated by directed energy deposition: Characterization and thermodynamic modeling, *Acta Mater.*, 108 (2016) 46-54.
- [5] M. Domack, J. Baughman, Development of nickel-titanium graded composition components, *Rapid Prototyp. J.*, 11(1) (2005) 41-51.
- [6] K. Shah, I.U. Haq, S.A. Shah, F.U. Khan, M.T. Khan, S. Khan, Experimental Study of Direct Laser Deposition of Ti-6Al-4V and Inconel 718 by Using Pulsed Parameters, *The Scientific World Journal*, 2014 (2014) 841945.

- [7] B. Onuiké, B. Heer, A. Bandyopadhyay, Additive manufacturing of Inconel 718—Copper alloy bimetallic structure using laser engineered net shaping (LENS<sup>TM</sup>), *Addit. Manuf.*, 21 (2018) 133-140.
- [8] T. DebRoy, H. Wei, J. Zuback, T. Mukherjee, J. Elmer, J. Milewski, A. Beese, A. Wilson-Heid, A. De, W. Zhang, Additive manufacturing of metallic components—process, structure and properties, *Prog. Mater. Sci.*, 92 (2018) 112-224.
- [9] W.J. Sames, F.A. List, S. Pannala, R.R. Dehoff, S.S. Babu, The metallurgy and processing science of metal additive manufacturing, *Int. Mater. Rev.*, 61(5) (2016) 315-360.
- [10] M. Cieslak, The welding and solidification metallurgy of alloy 625, *Weld. J.*, 70(2) (1991) 49-58.
- [11] J.N. DuPont, Solidification of an alloy 625 weld overlay, *Metall. Mater. Trans. A*, 27(11) (1996) 3612-3620.
- [12] Y.L. Hu, X. Lin, X.B. Yu, J.J. Xu, M. Lei, W.D. Huang, Effect of Ti addition on cracking and microhardness of Inconel 625 during the laser solid forming processing, *J. Alloy. Comp.*, 711 (2017) 267-277.
- [13] Y.L. Hu, X. Lin, X.F. Lu, S.Y. Zhang, H.O. Yang, L. Wei, W.D. Huang, Evolution of solidification microstructure and dynamic recrystallisation of Inconel 625 during laser solid forming process, *J. Mater. Sci.*, 53(22) (2018) 15650-15666.
- [14] L.E. Murr, E. Martinez, S. Gaytan, D. Ramirez, B. Machado, P. Shindo, J. Martinez, F. Medina, J. Wooten, D. Cisel, Microstructural architecture, microstructures, and mechanical properties for a nickel-base superalloy fabricated by electron beam melting, *Metall. Mater. Trans. A*, 42(11) (2011) 3491-3508.
- [15] M. Rombouts, G. Maes, M. Mertens, W. Hendrix, Laser metal deposition of Inconel 625: Microstructure and mechanical properties, *J. Laser Appl.*, 24(5) (2012) 052007.
- [16] G. Marchese, X. Garmendia Colera, F. Calignano, M. Lorusso, S. Biamino, P. Minetola, D. Manfredi, Characterization and comparison of Inconel 625 processed by selective laser melting and laser metal deposition *Adv. Eng. Mater.*, 19(3) (2017) 1600635.
- [17] Z. Khayat, T. Palmer, Impact of iron composition on the properties of an additively manufactured solid solution strengthened nickel base alloy, *Mater. Sci. Eng., A*, 718 (2018) 123-134.
- [18] ASTM International, ASTM F3056-14e1 Standard Specification for Additive Manufacturing Nickel Alloy (UNS N06625) with Powder Bed Fusion, West Conshohocken, PA, 2014, <https://doi.org/10.1520/F3056-14E01>.
- [19] N. Saunders, Phase diagram calculations for Ni-based superalloys, in: R.D. Kissinger (Ed.) TMS, Warrendale, PA, 1996.
- [20] N. Saunders, A.P. Miodownik, CALPHAD (calculation of phase diagrams): a comprehensive guide, Elsevier, 1998.
- [21] M.J. Cieslak, T.J. Headley, A.D. Romig, T. Kollie, A melting and solidification study of alloy 625, *Metall. Trans. A*, 19(9) (1988) 2319-2331.
- [22] F. Zhang, L.E. Levine, A.J. Allen, M.R. Stoudt, G. Lindwall, E.A. Lass, M.E. Williams, Y. Idell, C.E. Campbell, Effect of heat treatment on the microstructural evolution of a nickel-based superalloy additive-manufactured by laser powder bed fusion, *Acta Mater.*, 152 (2018) 200-214.
- [23] E. Scheil, Bemerkungen zur schichtkristallbildung, *Z. Metallkd.*, 34(3) (1942) 70-72.
- [24] V. Manvatkar, A. De, T. DebRoy, Spatial variation of melt pool geometry, peak temperature and solidification parameters during laser assisted additive manufacturing process, *Mater. Sci. Tech.*, 31(8) (2015) 924-930.

- [25] G.L. Knapp, T. Mukherjee, J.S. Zuback, H.L. Wei, T.A. Palmer, A. De, T. DebRoy, Building blocks for a digital twin of additive manufacturing, *Acta Mater.*, 135 (2017) 390-399.
- [26] J.J. Blecher, T.A. Palmer, T. DebRoy, Solidification map of a nickel-base alloy, *Metall. Mater. Trans. A*, 45(4) (2014) 2142-2151.
- [27] B.M. Morrow, T.J. Lienert, C.M. Knapp, J.O. Sutton, M.J. Brand, R.M. Pacheco, V. Livescu, J.S. Carpenter, G.T. Gray, Impact of defects in powder feedstock materials on microstructure of 304L and 316L stainless steel produced by additive manufacturing, *Metall. Mater. Trans. A*, 49(8) (2018) 3637-3650.
- [28] C.C. Silva, V.H.C. De Albuquerque, E.M. Miná, E.P. Moura, J.M.R. Tavares, Mechanical properties and microstructural characterization of aged nickel-based alloy 625 weld metal, *Metall. Mater. Trans. A*, 49(5) (2018) 1653-1673.
- [29] Y.L. Hu, X. Lin, S.Y. Zhang, Y.M. Jiang, X.F. Lu, H.O. Yang, W.D. Huang, Effect of solution heat treatment on the microstructure and mechanical properties of Inconel 625 superalloy fabricated by laser solid forming, *J. Alloy. Comp.*, 767 (2018) 330-344.
- [30] C.C. Silva, H.C. De Miranda, M.F. Motta, J.P. Farias, C.R.M. Afonso, A.J. Ramirez, New insight on the solidification path of an alloy 625 weld overlay, *J. Mater. Res. Technol.*, 2(3) (2013) 228-237.
- [31] J.N. DuPont, A.R. Marder, M.R. Notis, C.V. Robino, Solidification of Nb-bearing superalloys: Part II. Pseudoternary solidification surfaces, *Metall. Mater. Trans. A*, 29(11) (1998) 2797-2806.
- [32] C. Li, R. White, X. Fang, M. Weaver, Y. Guo, Microstructure evolution characteristics of Inconel 625 alloy from selective laser melting to heat treatment, *Mater. Sci. Eng., A*, 705 (2017) 20-31.
- [33] S. Li, Q. Wei, Y. Shi, Z. Zhu, D. Zhang, Microstructure characteristics of Inconel 625 superalloy manufactured by selective laser melting, *J. Mater. Sci. Technol.*, 31(9) (2015) 946-952.
- [34] L. Qin, C. Chen, M. Zhang, K. Yan, G. Cheng, H. Jing, X. Wang, The microstructure and mechanical properties of deposited-IN625 by laser additive manufacturing, *Rapid Prototyp. J.*, 23(6) (2017) 1119-1129.
- [35] A.M. Beese, Z. Wang, A.D. Stoica, D. Ma, Absence of dynamic strain aging in an additively manufactured nickel-base superalloy, *Nature Communications*, 9(1) (2018) 2083.
- [36] T. Keller, G. Lindwall, S. Ghosh, L. Ma, B.M. Lane, F. Zhang, U.R. Kattner, E.A. Lass, J.C. Heigel, Y. Idell, M.E. Williams, A.J. Allen, J.E. Guyer, L.E. Levine, Application of finite element, phase-field, and CALPHAD-based methods to additive manufacturing of Ni-based superalloys, *Acta Mater.*, 139 (2017) 244-253.

## Chapter 7

### CONCLUDING REMARKS

The combination of multiple types of structural alloys are essential for the safe and efficient operation of power generation facilities. Inevitably, these materials need to be joined, and fusion welding with selected filler metals is widely used. However, the fusion welding of dissimilar materials, such as ferritic and austenitic alloys, often encounter metallurgical challenges that compromise structural integrity after years of service at elevated temperatures. These issues can lead to premature failures that occur years or even decades before the designed lifetime of the facility. The repair and replacement of failed parts can be costly due to capital losses from plant outages. Although efforts have been made to improve weld design, current solutions have only prolonged the time to failure without solving the root problems.

In fusion welds between ferritic and austenitic alloys, variations in chemical composition, microstructure, and properties occur over distances on the order of tens to hundreds of microns. Consequently, these abrupt changes can lead to carbon migration, selective oxidation, mismatches in thermal expansion coefficients, localized plastic deformation, and internal stresses near the weld interface, which is where most premature failures occur. A potential solution for mitigating the metallurgical issues of these dissimilar metal joints is to introduce a functionally graded material in which the chemical composition and resulting microstructure vary gradually from one alloy to the other over much larger distances. Additive manufacturing is an attractive technology suitable for fabricating functionally graded materials, where the chemical composition can be varied in a layer-by-layer manner. These chemical composition profiles can be tightly controlled to achieve designed functions that enhance properties and performance of dissimilar metal joints

Carbon diffusion away from ferritic steels in dissimilar ferritic-to-austenitic welds is a major factor leading to premature failure of structural materials in nuclear and fossil power generation facilities. A solution to the problem involves the reduction of the thermodynamic driving force for diffusion through tailoring the chemical composition profiles. The spatial variation of the carbon chemical potential was controlled through compositional grading between 2.25Cr-1Mo steel and Alloy 800H through computational thermodynamic calculations. The functionally graded transition joints with the designed composition profiles were then fabricated using laser-based directed energy deposition additive manufacturing. The effectiveness of the

functionally graded material for reducing carbon diffusion was tested experimentally and directly compared to the performance of its dissimilar weld counterpart. The major findings are summarized as follows:

- Changes in chemical composition in dissimilar metal welds causes an abrupt decrease in the carbon chemical potential gradient, resulting in a large thermodynamic driving force for carbon diffusion. In contrast, a functionally graded material significantly lowers the carbon chemical potential gradient and reduces the driving force for carbon diffusion.
- The ferritic steel becomes depleted in carbon and while the austenitic filler becomes enriched after 20 years at 500°C in a dissimilar weld. In contrast, the initial carbon concentration profile in the functionally graded material remains virtually unchanged after the same exposure. The negligible carbon diffusion in the functionally graded material is a result of the lowered thermodynamic driving force.
- Experimentally measured carbon concentration profiles show that a functionally graded material between 2.25Cr-1Mo steel and Alloy 800H is highly effective in reducing carbon diffusion compared to a dissimilar weld. While depletion in the ferritic steel and accumulation in the filler metal were observed in the dissimilar weld, negligible changes in the carbon concentration profile were observed in the functionally graded material before and after heat treatment.
- Functionally graded materials with overall lengths as small as 5 cm can be effective for reducing the carbon chemical potential gradient. For an optimized material, benefits from increasing in length beyond this point are marginal.

For a comprehensive design of functionally graded material between 2.25Cr-1Mo steel and Alloy 800H, consideration of microstructure is essential. The spatial variations of microstructure, chemical composition, and hardness were characterized in the as-deposited functionally graded material using a suite of experimental characterization tools. Single alloy specimens representing discrete regions of the functionally graded material were also fabricated to investigate phase composition and transformations. Comparisons between experimental measurements and theoretical predictions were made to understand the effects of chemical composition on microstructure. The following are the main findings:

- Although the as-deposited functionally graded material was expected to produce a martensitic to austenitic transition, an abrupt decrease in microhardness was observed in the 10% 800H region followed. As more of the austenitic alloy was added to the joint, a gradual change from a martensitic to a fully austenitic structure was observed.
- A bainitic microstructure was found to exist in the 10% 800H region of the joint, causing the decrease in microhardness which was followed by high hardness levels in the martensitic 20% 800H region. If the 10% 800H region of the graded joint is excluded to avoid bainite formation and eliminate sudden variations in hardness, an increase in the driving force for carbon migration results.
- No benefits are gained in compositional grading after 70% 800H, where the microstructure is fully austenitic. Further changes in composition cause negligible changes in the driving force for carbon diffusion. The functionality of the FGM can be achieved by joining 2.25Cr-1Mo steel to Alloy 800H with a composition gradient ranging from 10 to only 70% 800H.

Variations in molten pool geometry caused by changes in chemical composition led to lack of fusion defects during the additive manufacturing of functionally graded materials. A combined experimental and theoretical approach was used to understand these changes in molten pool behavior for alloy compositions relevant to a transition from 2.25Cr-1Mo steel to Alloy 800H. Thermodynamic calculations coupled with a numerical heat transfer and fluid flow model were then used to explain the experimentally observed variations in deposit geometry. The following are the main conclusions:

- Changes in major alloying elements small effects on the shape and size of the molten pool for the alloy compositions investigated. Surface-active elements were found to be mainly responsible in determining the deposit geometry of single-track beads. The activity of oxygen and sulfur affect the magnitude and direction of liquid metal flow during additive manufacturing.
- The activity of oxygen decreases with increasing amounts of deoxidizing elements, like aluminum, titanium, and silicon. Consequently, material with higher amounts of 800H contain less oxygen in solution because 800H is the source of deoxidizing elements. The activity of sulfur is largely unchanged as a function of alloy composition.

- Oxygen and sulfur suppress the surface tension near the liquidus temperature, causing the temperature coefficient of surface tension to change from positive to negative with increasing temperature. The temperature where surface tension changes from positive to negative, referred to as the critical temperature, increases with higher oxygen activity. As a result, the critical temperature is highest for the 10% 800H alloy and lowest for the 60% 800H alloy.
- The differences in the temperature coefficient of surface tension for various alloy compositions was found to have a pronounced effect on the molten pool geometry. A strong inward flow was simulated in alloys with low amounts of 800H while outward flow dominated as the percentage of 800H increased. Accordingly, the width of the deposit increased with increasing amounts of 800H and the penetration depth decreased.

Composition grading often leads to the formation of unexpected secondary phases when functionally graded materials are fabricated using additive manufacturing. The effects of chemical composition on precipitate formation were investigated in two additively manufactured Inconel® 625 alloys with small differences in chemical composition. Computational thermodynamic calculations coupled with an in-depth characterization of the individual precipitates has shown that a complex interplay between iron, silicon, and titanium drives the changes in the precipitates observed with different iron levels. With hot isostatic post processing, the precipitate types and morphologies in both materials evolved. The following are the main conclusions:

- Secondary phases precipitate during solidification due to the segregation of alloying elements to interdendritic regions, however different precipitates were characterized in each Inconel® 625 alloy. The alloy with low iron content developed a microstructure dominated by continuous Laves phase particles while the high iron material contained only MN nitrides.
- The differences in secondary phases are linked to the silicon and titanium concentrations of the initial alloy compositions. High amounts of silicon (0.37 wt%) found in the low iron material promote the formation of Laves, while the silicon poor (0.035 wt%) and high iron alloy did not form any Laves phase.
- The high amounts of titanium (0.19 wt.%) in the high iron Inconel® 625 promote nitride formation in the liquid alloy before solidification. The measured composition of the nitride

indicates that significant amounts of niobium were consumed from the liquid prior to solidification. This phenomenon is manifested in the measured niobium partition coefficient ( $k_{\text{Nb}} = 0.51$ ), which is significantly lower than that measured in the low iron material ( $k_{\text{Nb}} = 0.71$ ) where precipitates form near the end of solidification.

- After HIP, precipitates in both materials remain but change in type, composition and morphology. The Laves phase in the low Fe alloy developed a blocky morphology and partially transformed to a nitride rich in niobium, chromium, and molybdenum after HIP. While the size and distribution of the nitrides in the high Fe material did not change, the composition became more enriched in Ti and depleted in Nb.

## VITA

James S. Zuback II was born in Lock Haven, PA on January 3<sup>rd</sup>, 1992. He enrolled in the Physics program at Lock Haven University in August of 2010 and received his Bachelor of Science degree in May of 2014. In August of 2014, James was accepted into the graduate school at Pennsylvania State University and began his Ph.D. studies in the department of Materials Science and Engineering under the direction of Prof. T. DebRoy and Dr. Todd Palmer in January 2015. James served as a teaching assistant each semester during his graduate career and was awarded the Beaver Award for Excellence as a Teaching Assistant in April 2019. He has coauthored the following publications:

- H.L. Wei, G.L. Knapp, J.S. Zuback, T. Mukherjee, W. Zhang, A. De, T. DebRoy, Verifiable mechanistic models in additive manufacturing of metallic materials, *Prog. Mater. Sci.*, *Submitted for publication*.
- J.S. Zuback, P. Moradifar, Z. Khayat, N. Alem, T.A. Palmer, Impact of chemical composition on precipitate morphology in an additively manufactured nickel base superalloy, *J. Alloy Comp.*, 798 (2019) 446-457.
- J.S. Zuback, T. DebRoy, The hardness of additively manufactured alloys, *Materials*, 11 (2018) 2070.
- S.D. Meredith, J.S. Zuback, J.S. Keist, T.A. Palmer, Impact of composition on the heat treatment response of additively manufactured 17-4PH grade stainless steel, *Mater. Sci. Eng. A*, 738 (2018) 44-56.
- J.S. Zuback, T.A. Palmer, T. DebRoy, Additive manufacturing of functionally graded transition joints between ferritic and austenitic alloys, *J. Alloy Comp.*, 770 (2019) 995-1003.
- T. Mukherjee, J.S. Zuback, W. Zhang, T. DebRoy, Residual stresses and distortion in additively manufactured compositionally graded and dissimilar joints, *Comp. Mater. Sci.*, 150 (2018) 369-380
- T. DebRoy, H.L. Wei, J.S. Zuback, T. Mukherjee, J.W. Elmer, J.O. Milewski, A.M. Beese, A. Wilson-Heid, A. De, W. Zhang, Additive manufacturing of metallic components – process, structure and properties, *Prog. Mater. Sci.*, 92 (2018) 112-224.
- G.L. Knapp, T. Mukherjee, J.S. Zuback, H.L. Wei, T.A. Palmer, A. De, T. DebRoy, Building blocks for a digital twin of additive manufacturing, *Acta Mater.*, 135 (2017) 390-399.
- T. Mukherjee, J.S. Zuback, A. De, T. DebRoy, Heat and fluid flow modeling to examine 3D-printability of alloys, *7<sup>th</sup> International Symposium on High-Temperature Metallurgical Processing*, (2017) 471-478.
- T. Mukherjee, J.S. Zuback, A. De, T. DebRoy, Printability of alloys for additive manufacturing, *Sci. Rep.*, 6 (2017) 19717.